Investigating the kinetochore complex in *Schizosaccharomyces pombe* using advanced fluorescence microscopy techniques

KUMULATIVE
DISSERTATION

zur Erlangung des Grades eines
Doktor der Naturwissenschaften
(Dr. rer. nat.)
des Fachbereichs Biologie
der Phillips-Universität Marburg

vorgelegt von
Ilijana Vojnovic
aus
Bad Mergentheim, Deutschland

Marburg 2022

Die vorliegende Dissertation wurde von April 2017 bis November 2022 am Fachbereich Biologie der Philipps-Universität Marburg unter Leitung von Prof. Dr. Ulrike Endesfelder angefertigt.

Vom Fachbereich Biologie der Philipps-Universität Marburg (Hochschulkennziffer 1180) als Dissertation angenommen am 19.12.2022.

Erstgutachterin: Prof. Dr. Ulrike Endesfelder
Zweitgutachter: Prof. Dr. Martin Thanbichler

Eidesstattliche Erklärung

Hiermit versichere ich, dass ich meine Dissertation mit dem Titel 'Investigating the kinetochore complex in *Schizosaccharomyces pombe* using advanced fluorescence microscopy techniques' selbstständig, ohne unerlaubte Hilfe angefertigt und mich dabei keiner anderen als der von mir ausdrücklich bezeichneten Quellen und Hilfsmittel bedient habe.

Diese Dissertation wurde in der jetzigen oder einer ähnlichen Form noch bei keiner anderen Hochschule eingereicht und hat noch keinen sonstigen Prüfungszwecken gedient.

Ilijana Vojnovic

Marburg, der 30.11.2022

Erklärung zur kumulativen Dissertation

Ich versichere, dass die im kumulativen Teil der Dissertation mit dem Titel 'Investigating the kinetochore complex in *Schizosaccharomyces pombe* using advanced fluorescence microscopy techniques' aufgeführten Anteile der Autoren an den verfassten Publikationen und Manuskripten korrekt und vollständig dargelegt sind.

Der kumulative Teil umfasst die Kapitel:

- Unterkapitel 1.2.2 and 1.2.3
- Kapitel 2
- Kapitel 3
- Appendix A.1

Marburg, den 30.11.2022

Unterschrift Doktorand/in	Unterschrift Betreuer/in
Name: Ilijana Vojnovic	Name: Prof. Dr. Ulrike Endesfelder

Contents

Summary

Major insights into various biological processes and structures could be achieved using fluorescence microscopy, which is a non-invasive, live- and fixed cell compatible, high contrast imaging technique. Here, the molecule of interest can be specifically labeled with a fluorescent marker using a multitude of different labeling techniques, best suited for the individual biological research question. The location of the molecule of interest can be deduced from the emitted fluorescent signal of the marker due to their immediate proximity.

However, structures smaller than the diffraction limit of light of about 200 nm can not be resolved by conventional fluorescence microscopy. Other techniques, such as e.g. electron microscopy (EM) or X-ray crystallography allow for higher resolutions, but lack the target specific read-out or are not compatible with *in vivo* studies. Nevertheless, by utilizing advanced optical components and illumination patterns and designing fluorophores with tightly controllable photophysics, the diffraction limit of light could be circumvented leading to improved resolutions. From these super-resolution techniques, only single-molecule localization microscopy (SMLM) allows for a quantitative analysis of the target molecule due to the spatiotemporal detection of the fluorescent marker.

The segregation of sister-chromatids to the corresponding daughter cells is a vital and irreversible process, which needs to be tightly regulated. Here, a multi-protein complex called the kinetochore (KT), which serves as a force-sensing linker between the centromere in chromosomes and kinetochore microtubules (kMTs) originating from the spindle pole body (SPB), plays a pivotal role as errors in this process lead to aneuploidy or cell death. Thus, understanding the architecture and regulation of this complex is essential. However, even though certain subcomplexes of the KT could be resolved by EM or X-ray crystallography *in vitro*, the full KT nanostructure was not resolved *in vivo* yet.

Hence in chapter 2, the *in vivo* nanoscale structure of the fission yeast KT complex was investigated using SMLM. The fission yeast *Schizosaccharomyces pombe* was used as the model organism of choice, due to its small regional centromeres. It acts as an intermediate between the point centromere in the budding yeast *Saccharomyces cerevisiae*, on which only one KT assembles, and the larger regional centromeres in humans. To investigate the KT in fission yeast, a structure smaller than the diffraction limit of light, different SMLM imaging and labeling strategies in microbes were developed or applied fitting this research question. However, for the creation of the KT map at least two different super-resolved targets are required: one reference protein at the centromere and one protein of interest (POI) a time in the KT complex. As no combination of commonly used photoswitchable organic dyes for SMLM proved to be applicable in fission yeast, the focus was shifted towards photoactivatable and - convertable fluorescent proteins (FPs) as alternative fluorescent markers. Knowing this, the KT structure was investigated using a multi-color SMLM approach based on FPs utilizing an orthogonal

sequential illumination pattern and a KT protein database was generated. Developing novel image analysis tools and controls allowed for the extraction of intra- KT distances and POI copy numbers. Based on these parameters, first conclusions on the structure, preferred KT assembly pathways and stoichiometries were drawn and a model of the fission yeast KT was proposed.

Finally, to investigate the KT structure in even greater detail, a new imaging technique combining expansion microscopy (ExM) and SMLM, termed single-molecule expansion microscopy in fission yeast (SExY) was developed in chapter 3, which increases the imaging resolution of SMLM by the corresponding expansion factor (EF) of the sample. For this, the fixed sample was first embedded in a hydrogel and then expanded upon incubation in aqueous media. To achieve an even expansion, the proteins were covalently linked to the gel mesh and obstacles like protein connections, cell walls or membranes were dissolved in homogenization steps prior to expansion. Then, the sample was imaged using the SMLM based imaging technique photoactivated localization microscopy (PALM), which lead to single-digit nanometer resolutions. Since KT proteins are low abundant, we optimized for an increase in protein retention yield, which we could improve by half compared to the initial protocol. We also optimized for an isotropic expansion of the sample, which we controlled by determining the EFs of different cell organelles and the distribution of cytosolic FPs compared to non-expanded cells. With the final SExY protocol at hand we were than able to visualize KT proteins as well as other nuclear targets *in vivo* at a single digit nanometer range for the first time.

Zusammenfassung

Bedeutende Erkenntnisse unterschiedlicher biologischer Prozesse und Strukturen konnten mittels Fluoreszenzmikroskopie erlangt werden, die eine nicht-invasive, Lebend- und fixierte Zellen kompatible, kontrastreiche Bildgebung darstellt. Hierfür werden die Zielmoleküle mit einer Vielzahl an unterschiedlichen Markierungstechniken spezifisch mit einem Fluoreszenzmarker versehen, der für die individuelle biologische Fragestellung am Besten geeignet ist. Aufgrund der unmittelbaren Nähe kann die Lokalisierung des Zielmoleküls aus dem emittierten Fluoreszenzsigmal des Fluoreszenzmarkers abgeleitet werden.

Jedoch können Strukturen kleiner als das Auflösungslimit des Lichts von ungefähr 200 nm nicht über konventionelle Fluoreszenzmikroskopie aufgelöst werden. Andere Techniken, wie z.B. Elektronenmikroskopie oder Röntgenkristallstrukturanalyse ermöglichen bessere Auflösungen, erlauben jedoch keine zielmolekülspezifische Auslesung oder sind nicht kompatibel mit *in vivo* Studien. Nichtsdestotrotz, durch Anwendung von modernen optischen Komponenten und Ausleuchtungsmodellen und Herstellung von Fluorophoren mit strikt kontrollierbarer Photophysik, kann das Auflösungslimit umgangen werden und höhere Auflösungen konnten erreicht werden. Unter diesen hochauflösenden Techniken erlaubt nur die Einzelmolekül-Lokalizationsmikroskopie eine quantitative Analyse des Zielmoleküls aufgrund der räumlich und zeitlich aufgelösten Detektion des Fluoreszenzmarkers.

Die Trennung von Schwester-chromatiden zu den jeweiligen Tochterzellen ist ein lebensnotwendiger und irreversibler Prozess, der streng reguliert werden muss. Dabei spielt ein Multiproteinkomplex namens Kinetochor, der ein druckempfindliches Verbindungsstück zwischen dem Zentromer in Chromosomen und Mikrotubuli, die aus dem Spindelpol entstehen darstellt, eine wichtige Rolle, da Fehler in diesem Prozess zu Aneuploidie oder Zelltod führen. Folglich ist es essenziell die Struktur und Regulierung dieses Komplexes zu verstehen. Obwohl einzelne Subkomplexe des Kinetochors *in vitro* durch Elektronenmikroskopie und Röntgenkristallstrukturanalyse aufgelöst werden konnten, wurde die volle Struktur des Kinetochorkomplexes im Nanometerbereich noch nicht in lebenden Zellen aufgelöst.

Aufgrund dessen wurde in Kapitel 2 die *in vivo* Struktur des Kinetochorkomplexes im Nanometerbereich mittels Einzelmolekül-Lokalizationsmikroskopie untersucht. Die Spalthefe *Schizosaccharomyces pombe* wurde aufgrund ihres kleinen regionalem Zentromers als Modelorganismus gewählt. Sie dient als Bindeglied zwischen dem Punktzentromer der Bierhefe *Saccharomyces cerevisiae*, auf dem nur ein einzelnes Kinetochor augebaut wird und dem größeren regionalem Zentromer in Menschen. Um das Kinetochor in der Spalthefe zu untersuchen, das kleiner ist als das Auflösungslimit, wurden unterschiedliche Einzelmolekül-Lokalizationsmikroskopie Bildgebungen und Markierungsstrategien in Mikroben der Untersuchung passend entwickelt und angewendet. Um eine Mappe des Kinetochors

herzustellen werden jedoch mindestens zwei unterschiedliche hochaufgelöste Zielstrukturen benötigt: ein Referenzprotein am Zentromer und ein Zielprotein nach dem anderen im Kinetochorkomplex. Da keine Kombination von häufig verwendetem photoschaltbaren organischen Farbstoffen in der Einzelmolekül-Lokalizationsmikroskopie in der Spalthefe zielführend war, wurde der Fokus auf photoaktivierbare und -konvertierbare Fluoreszenzproteine als alternative Marker gelenkt. Danach wurde die Kinetochorstruktur mithilfe eines Mehrfarben Einzelmolekül-Lokalizationsmikroskopie Ansatzes basierend auf Fluoreszenzproteinen, die einen orthogonalen aufeinanderfolgendem Anregungsmuster nutzen, untersucht und eine Kinetochor-Datenbank generiert. Durch die Entwicklung neuer Werkzeuge für die Bildanalyse und Kontrollen war es möglich, Intrakinetochordistanzen und die Menge jedes Zielmoleküls zu extrahieren. Basierend auf diesen Parametern wurden erste Schlüsse bezüglich der Struktur, des bevorzugtem Aufbaus des Kinetochores und der Stöchiometrie gezogen und ein Model des Kinetochors in der Spalthefe wurde postuliert.

Schließlich wurde, um die Kinetochorstruktur im größeren Detail zu untersuchen, in Kapitel 3 eine neue Bildgebungstechnik namens single-molecule expansion microscopy in fission yeast (SExY) entwickelt, die expansion microscopy (ExM) und Einzelmolekül-Mikroskopie vereint und dadurch die Auflösung der Einzelmolekül-Mikroskopie um den entsprechenden Expansionsfaktor der Probe verbessert. Hierbei wird die fixierte Probe zunächst in einem Hydrogel eingebettet und dann nach Inkubation in wässrigem Medium expandiert. Um eine gleichmäßige Expansion zu gewähren, wurden Proteine kovalent an das Gelnetz gebunden und Hindernisse wie Proteinverbindungen, Zellwände und -membranen in Homogenisierungsschritten vor der Expansion aufgelöst. Danach wurde die Probe mithilfe von einer auf Einzelmolekül-Lokalizationsmikroskopie basierenden Bildgebungstechnik namens Photoaktivierbarer Lokalisierungsmikroskopie visualisiert, was zu Auflösungen im einstelligen Nanometerbereich führte. Da Kinetochorproteine nur spärlich vorhanden sind hatten wir auf die Ausbeute an verbleibendem Proteinsignal optimiert, die wir im Vergleich zum anfänglichen Protokoll um die Hälfte erhöhen konnten. Wir optimierten auch auf eine isotrope Expansion der Probe, die wir durch die Bestimmung des Expansionsfaktors in unterschiedlichen Organellen und der Verteilung von zytosolischen Fluoreszenzproteinen im Vergleich zu nicht expandierten Zellen kontrollierten. Mit dem finalen SExY-Protokoll konnten wir dann Kinetochorproteine sowie weitere nucleare Zielproteine *in vivo* zum ersten Mal im einstelligem Nanometerbereich visualisieren.

CHAPTER 1

Introduction

This introduction is divided into first a biological introduction (chapter 1.1) giving a general overview of the cell division stages (chapter 1.1.1) and key biological structures involved in the faithful capture, anchoring and segregation of chromosomes to the corresponding daughter cells during mitosis in chapters 1.1.2, 1.1.3 & 1.1.4. Here, the main focus lies on the assembly and architecture of a multi-protein complex called the kinetochore (KT) anchoring the centromere region in the sister-chromatids to the microtubules (MTs) nucleated from the spindle pole body (SPB). Along the way *Schizosaccharomyces pombe*, also called fission yeast, is introduced as the best suited model organism to investigate the KT in chapter 1.1.1.

This is then followed by a methodological introduction into super-resolution microscopy techniques in chapter 1.2 focusing on single-molecule localization microscopy (SMLM) and elaborating its advantages to unravel biological structures below 200 nm (chapter 1.2.1), such as the KT, which represents the main goal of this thesis. Afterwards, the differences of conventional widefield fluorescence and SMLM microscopes are highlighted and crucial hard- & softwares for single-molecule sensitivity as well as important measures for a successful sample preparation in SMLM are discussed (chapter 1.2.2). Next, in chapter 1.2.3 different state-of-the-art labeling and imaging strategies for multiple targets using SMLM in microbes are discussed and techniques best suited to resolve the KT nanostructure in fission yeast specifically are elaborated. Finally, a recently developed fluorescence imaging technique called expansion microscopy (ExM) is introduced in chapter 1.2.4, which physically expands the sample and thus yields a higher resolution compared to conventional fluorescence microscopy. By combining ExM with SMLM, the achievable resolution can be increased even further, allowing for the visualizing of the KT structure in greater detail.

Lastly, the overall goals of this thesis are summarized in chapter 1.3.

1.1 Cell divison

The transfer of genetic material is the foundation of life, yet its exact process and regulation remain a mystery. This transfer occurs in a vital biological process called cell division and is part of the cell cycle in which the mother cell divides into daughter cells by both nuclear and cytoplasmic fission. In eukaryotes, the cell division is based on a process termed mitosis, which produces genetically identical daughter cells during the vegetative, or alternatively on meiosis during the reproductive cell cycle. In meiosis, genetically different daughter cells are formed with half the set of chromosomes, due to one round of chromosome replication and two rounds of chromosome segregation (meiosis I and II), where genetic information is exchanged in a process called homologous recombination during the prophase of meiosis I. As both mitosis and meiosis are irreversible, any missegragation and -regulation of this process ultimately lead to aneupliody, various types of cancer or cell death.

1.1.1 The cell cycle of fission yeast

One key player in orchastrating the faithful segregation of sister-chromatids is the KT, which tethers the centromere to kMTs originating from the SPB. As a suitable model organism to investigate the KT structure we chose the fission yeast *Schizosaccharomyces pombe* as its KT shares a high homology to the human one. Yet, with its small regional centromere, which serves as an assembly platform for the KT, fission yeast presents an intermediate between the simplistic point-centromere in budding yeast, on which only a single KT assembles, and the large, complex regional centromere in humans. While fission yeast divides in a symmetrical fashion like mammalian cells, it only possesses three chromosomes compared to the 46 chromosomes in humans, which decrowdes the nucleus and reduces the risk of overlapping sister-chromosomes allowing for simultaneous visualization of all sister-chromosomes. Additionally to that, fission yeast possesses a fast generation time and a vast and easy to handle genetic toolbox [1]. Furthermore, fission yeast can enter both a diploid as well as a preferred haploid vegetative cell cycle, making a comparison of diploid and halpoid KT structures and stoichiometries possible. Both cycles are connected through zygotic or azygotic meiosis, which is triggered by nutrient starvation and mating pheromone exposure. In zygotic meiosis, recently separated haploid fission yeast cells of opposite mating types conjugate resulting in a fusion of both nuclei and thus form a diploid fission yeast cell [2]. Alternatively, in azygotic meiosis, diploid fission yeast cells form halpoid spores, which can enter the haploid vegetative cell cycle [2].

The fission yeast cell cycle consists of four main phases: G2, mitosis or meiosis, G1 and S phase (see figure 1.1 a). Recently divided cells replicate their chromatids in S phase resulting in two identical sister-chromatids. These sister-chromatids are then joined by cohesin in early G2 phase, which forms a ring-like structure around the two chromosome arms [3]. In addition to that cells grow in size from early to late G2, which takes up the majority of the cell cycle. After passing the G2/M checkpoint, which prevents cells from dividing chromosomes with damaged DNA, cells enter mitosis or alternatively meiosis, where the replicated chromosomes are segragated. For this, the interplay between multiple key protein complexes has to be tightly orchestrated. Here, the spindle apparatus is required to generate the force that is required to separate sister-chromatids.

Generally, mitosis and meiosis can be divided into four main phases: prophase, metaphase, anaphase and telophase. In prophase, the chromatin is partially condensed, by replacing cohesin at the sister-chromatid arms with the condensin II complex, which induces loop extursions [4]. Additionally, the spindle MTs capture the KT complex at the centromere in prophase. However, cohesin remains

attached to the centromere until an amphitelic attachment of the sister-chromosomes to the correct SPB could be confirmed by the spindle assembly checkpoint (SAC) in metaphase. In meiotic prophase I, genetic material between maternal and paternal homologous chromosomes is exchanged by at least one cross-over, also termed homologous recombination. Furthermore, fission yeast undergoes a closed mitosis leaving the nuclear envelope (NE) intact in prophase, which is in contrast to the open mitosis of humans.

Next, the sister-chromatids are oscillating between both poles until a proper attachment and bi-orientation is achieved in metaphase and the SAC is deactivated [5]. In metazoans a metaphase plate with aligned sister-chromosomes is formed at the equator of the cell, which is either absent or very short lived in fission yeast as bi-orientation is achieved before the duplicated SPBs are opposite of each other [6–8].

Consecutively, anaphase is entered upon the deactivation of SAC and consequently of activation of the anaphase promoting complex (APC), which promotes the cleavage of remaining cohesin and the binding of condensin I, resulting in a maximum condensation of chromatids [9]. This leads to fully separated sister-chromatids, which can then be pulled to the SPBs in anaphase A, while in anaphase B the SPBs are migrated to the poles of the mother cell by astral MTs leading to a deformation of the nucleus in a closed mitosis (see figure 1.1 a-b) [10].

Next, fission yeast cells enter telophase, where the narrow bridge between both daughter nuclei is dissassembled in closed mitosis [11]. Finally, chromatin is decondensed in telophase and the mother cell is split into daughter cells upon cytokinesis, which in case of fission yeast takes place in G1 phase, where a primary and secondary septum is formed. In preparation for segregation of sister-chromatids in the next cell cycle, the SPB in fission yeast is then duplicated in G1 to S phase as well as the recently segregated DNA checked for damages before DNA replication (G1/S checkpoint) [12–14].

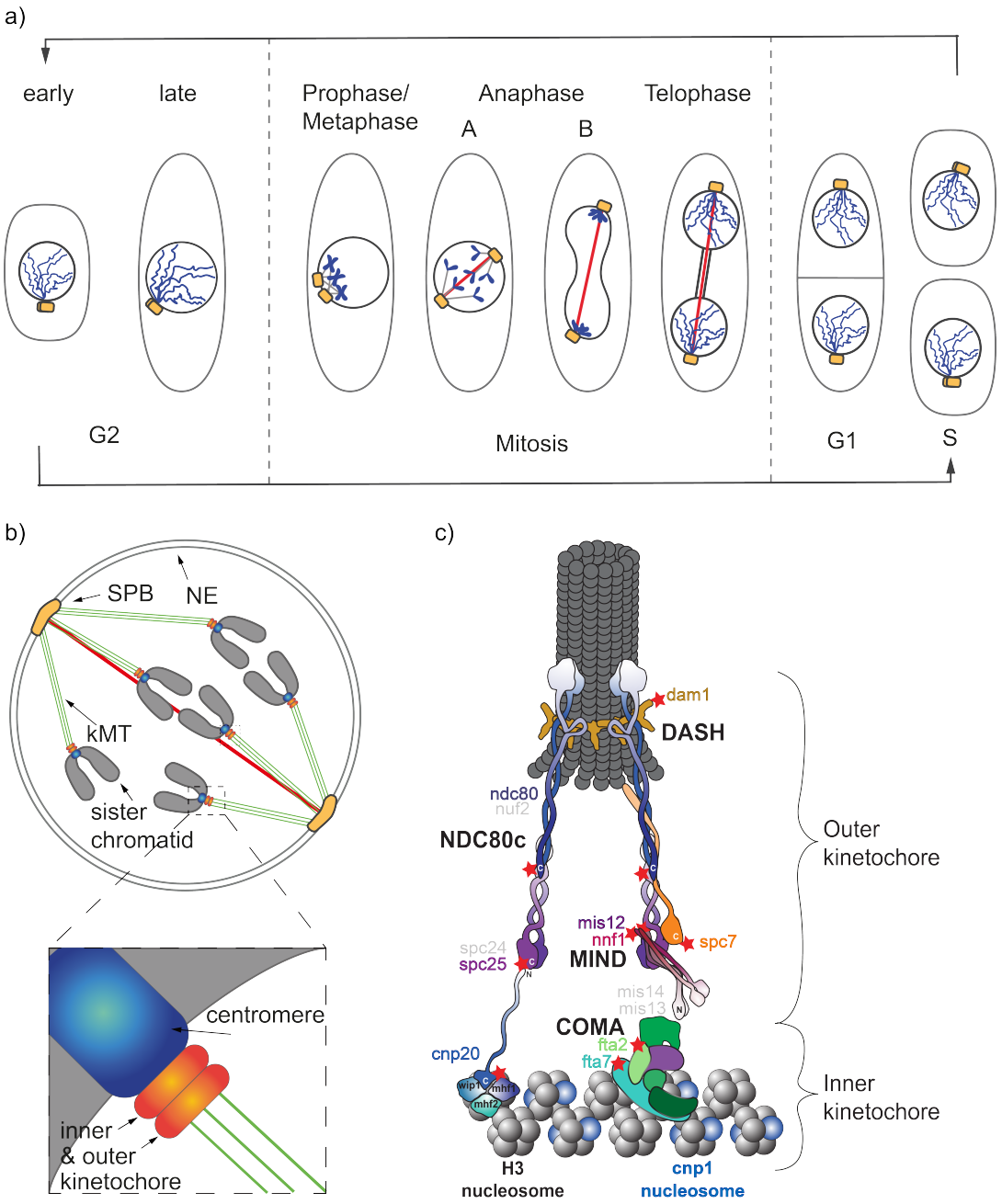

Figure 1.1: Progression and key players in mitotic chromosome division in fission yeast. a) Vegetative cell cycle in fission yeast consisting of G2, mitosis, G1 and S phase. Cell wall and NE as well as the kMTs are depicted in dark grey, the SPB in yellow, the chromosomes or chromatids in blue and the thick interpolar MT-bundle in red, b) Spindle formation during anaphase A and zoom in to the contact site of kMTs and the centromere, c) KT model based on biochemical pull-down assays, EM and X-ray crystallography data. Figure parts adapted from [15].

1.1.2 Microtubules and kinetochore capture

Microtubule organizing centers (MTOCs) are structures that nucleate MTs from γ-tubulin complexes and are involved in various processes such as cell division, cellular trafficking and motility. The MTOCs involved in cell division are the SPB in fission and budding yeast or centrosome in metazoans. Though they are functionally related, their architecture is vastly different [16]. While the budding yeast SPB is embedded into the NE throughout the whole cell cycle, the fission yeast SPB is connected to the cytoplasmic site of the NE in interphase, migrates into the NE in metaphase and is once again ejected from the NE in anaphase [12, 17–20].

In general, MTOCs are defined as the minus-end of MT and the growing or shrinking MT tip, is defined as plus-end. MTs consist of 13 heterodimers composed of α- and β-tubulin that are arranged in a hollow cylinder with a 23-27 nm outer and 11-15 nm inner diameter [21, 22]. MT polymerisation is favoured when both α- and β-tubulin bind one GTP each, while MT depolymerization, occurs when β-tubulin is bound to GDP, leading to a more accessible dimer, that is more likely to depolymerize [23, 24]. Stable MTs form a so called GTP-cap at the plus-end that prevents depolymerization of the MT.

Additionally, MTs can randomly search for one another and upon contact form bundles, which are then cross-linked by special MT binding proteins. Various proteins interact with MT, such as microtubule-associated proteins (MAPs), which stabilize single MTs upon binding or facilitate MT cross-linking, plus-end tracking proteins (TIPs), which remain associated to the growing tip of the MT and serve as linkers to other structures, such as the KT or membranes and motor proteins, which are molecular machines that can pull cargo along the MT towards either end of the MT. MTs originating from opposite SPBs form antiparallel bundles, which are involved in pushing the SPBs apart, while MTs from the same SPB form parallel bundles that can bind KTs anchored to centromeres, then termed kMTs or k-fibers, and pull them towards the SPB [25, 26]. It is highly disputed how kMTs search for KTs, as simulations have shown that chance encounters alone would take longer then the mitotic time frame [27]. There are different theories as to how the likelihood of capture can be increased. This includes, but is not limited to, a larger searching surface at the MT-bundle as KTs were shown to also bind to the GTP-cap and then are transferred to the MT-tip as well as additional MT growth originating from the KT, which can then form a bundle with SPB-MTs and subsequently transfer the KT [28–31].

For a successful chromosome segregation each sister-chromatid needs to form an attachment to a kMT-bundle of one opposite SPB. Once this amphitelic MT-KT attachment is formed and the appropriate tension is built up, the SAC is deactivated and the sister-chromatids are separated [32]. However, different types of MT-KT attachment can be formed in the meantime such as a monotelic attachment, where only one SPB is connected to one sister-chromatid, a syntelic attachment, where one SPB is connected to both sister-chromatids or a merotelic attachment, where one sister-chromatid is connected to both SPBs, while the other sister-chromatid has only one connection. Fortunately, these incorrect attachment types can not build up the necessary tension triggering chromosome segregation most of the time, which leads the active SAC to detach the MT-KT attachment.

1.1.3 Centromere regions

In eukaryotes, DNA is wrapped around octameric nucleosomes that consist of two copies of each H2A, H2B, H3 and H4 histone proteins that make up the histone core and the histone linker H1, which may assist in chromatid compaction [33]. Most centromeres, which serve as a landmark for KT assembly, are defined as the DNA region containing most of the H3 histone variant (CENP-A in humans, cse4

in budding and cnp1 in fission yeast), where the nucleosomes have either one or both copies of H3 replaced by the H3 variant (see figure 1.2) [34, 35]. These cnp1$^{\text{CENP-A}}$-containing nucleosomes are intersparsed by regular H3 nucleosomes [36]. Tables 1.1 and 1.2 present the organism specific homolog names of all structural KT proteins as well as their subcomplex classification for a better understanding of the following chapters. For future reference all KT proteins will be written using the fission yeast nomenclature in regular script with the human homologue, if it exists, in superscript, an example being cnp1$^{\text{CENP-A}}$.

It was shown that the biggest difference between cnp1$^{\text{CENP-A}}$ and the regular H3 is the N-terminal histone tail, where most of the lysine residues are replaced by arginine in cnp1$^{\text{CENP-A}}$, which renders the histone tail more basic [37]. The histone-tail also contains the CENPA targeting domain (CATD), which serves as a recognition site for cnp1$^{\text{CENP-A}}$ loading factors as well as the inner KT proteins mis15$^{\text{CENP-N}}$ [38, 39] from the mis6/sim4 complex and mal2$^{\text{CENP-O}}$ and fta2$^{\text{CENP-P}}$ from the COMA complex [40]. Additionally, the inner KT protein cnp3$^{\text{CENP-C}}$, which links the centromere to the outer KT, recognizes six amino acids in the C-terminal end of cnp1$^{\text{CENP-A}}$ [38].

The centromere was shown to greatly vary in sequence and size ranging from point centromers of barely 125 bp in size in budding yeast, over regional centromers of 0.5-4.0 Mbp in humans to holocentromeres that encompass the whole chromosome length of 13-20 Mb in *C. elegans* [41–43]. Fission yeast has three chromosomes with chromosome lengths of 3.7, 4.6 and 5.7 Mbp and possess small regional centromers with a length of 35-110 kb, which can serve as an intermediate between the simplistic point centromere and the more complex regional centromere of humans [44]. Furthermore, while the centromere lengths of fission yeast are inversely proportional to the respective chromosome length, the cnp1$^{\text{CENP-A}}$ copy number is proportional to the kMT [18, 36, 44]. This leads to the assumption that KTs at the fission yeast regional centromere are most likely repeats of single KTs. However, centromere establishment and maintenance as well as KT assembly in budding yeast is heavily dependant on the centromere sequence [41, 45, 46]. In contrast to that, fission yeast and humans rely on the epigenetic inheritance of post-translational modifications patterns like methylation, acetylation or phosphorylation of cnp1$^{\text{CENP-A}}$ and its flanking heterochromatin [47, 48].

Centromeres consist of different centromere elements. The budding yeast point centromere consists of the three centromere elements CDEI-III, which are wrapped around 1-2 cnp1$^{\text{CENP-A}}$ containing nucleosomes upon which only a single kinetochore, tethered to a single kMT, is assembled [49–52]. CDEI and CDEIII are palindromic repeats that flank an A/T-rich CDEII centromere core domain (cnt) that mainly interacts with cnp1$^{\text{CENP-A}}$ and cnp3$^{\text{CENP-C}}$, while the ndc10 homodimer of the CBF3 complex binds to the CDEI and CDEIII domain in order to loop the centromeric DNA around the nucleosome [53].

In contrast to that, the fission yeast centromere is divided into a non-repetitive cnt that harbours most of the available cnp1$^{\text{CENP-A}}$ and flanking outer repeats (otrs), where the histone H3 is either twice or thrice methylated at its 9th lysine residue yielding H3K9me2 and H3K9me3, respectively or histone H4 is thrice methylated at its 20th lysine residue yielding H4K20me3. These post-translational modifications in heterochromatin lead to chromatin compaction and thus silencing of the genes located in otrs [54]. Some residual cnp1$^{\text{CENP-A}}$ can be found at outer repeats, while basically none is located in the residual chromosome under normal circumstances [36]. The distinct H3K9me3 methylation pattern at otrs is recognized by the chromatin-associated protein swi6, which then recruits cohesin to otrs, while hardly any cohesin is present in the cnt [55]. It was also shown that a disturbed methylation pattern leads to less recruited swi6 and consequentially less cohesin at otrs [55]. The central domain is subdivided into a cnt domain with flanking imperfect repeat regions (imrs) domains, while the

outer repeats consist of dg or db domains. Using high-throughput DNA sequencing and PALM it was shown that the fission yeast centromere contains 20 nucleosomes containing 1-2 cnp1$^{\text{CENP-A}}$ molecules each that are tethered to 2-4 kMTs via the KT according to EM data [18, 36]. Over-expression of cnp1$^{\text{CENP-A}}$ was shown to form neocentromeres by additional deposition of cnp1$^{\text{CENP-A}}$ nucleosomes at telomere repeats [56, 57]. These neocentromeres however did not form functional centromeres as only a small amount of KT proteins were located at the new sites [58, 59]. This is most likely caused by cells actively removing non-centromeric loci by degradation, as cnp1$^{\text{CENP-A}}$ nucleosomes posses no post-translational modifications by cnp1$^{\text{CENP-A}}$ loading factors or the constitutive centromere associated network (CCAN) proteins in the inner KT [60]. The total loss of centromeres can lead to aneuploidy, which leads to severe disabilities such as e.g. trisomy, while the excess of centromeres was shown to yield chromosome breakage, most likely due to linkage to opposed pulling forces [61, 62].

The human centromere consists of multiple small repetitive DNA called α-satellite repeats with 171 bp units, roughly the size of one nucleosome, which are flanked by heterochromatin. The centromere is tethered to up to 20 kMTs with an average of 17 kMTs [63–66].

Centromere establishment and maintenance

A distinct methylation pattern in the otrs is required to establish a novel functional centromere, while the cnt alone is insufficient. Contrary to that, the loss of heterochromatin from established centromeres was not shown to affect cnp1$^{\text{CENP-A}}$ or KT maintenance in the cnt [47, 48]. This suggests that heterochromatin may, in an unknown mechanism, initially direct the site of cnp1$^{\text{CENP-A}}$ chromatin and thus KT assembly [67]. To redistribute old or load new cnp1$^{\text{CENP-A}}$ nucleosomes for centromere maintenance or assemble the KT, the centromere must be exposed to the surface of the chromosome, which is facilitated by chromatin rearrangement for which multiple models have been proposed [68, 69].

For centromere maintanance the mis16/18 and mis6/sim4 complexes are recruited to the otrs in early G1 phase at first, where both complexes are known to play a role in deacetylation of the cnt nucleosomes [70]. This deacetylation compacts chromatin due to positively charged histone tails that are attracted to the negatively charged DNA coiled around the histones. Afterwards, the histone chaperone homodimer smc3$^{\text{HJURP}}$ is recruited to the centromere and unbound cnp1$^{\text{CENP-A}}$ nucleosomes are loaded onto the histone chaperone sim3 in G1 phase [70–73]. After DNA replication, the cnp1$^{\text{CENP-A}}$-sim3 heterodimer interacts with the smc3$^{\text{HJURP}}$ homodimer and is incorporated equally into the cnt of both sister-chromatids via a still unknown mechanism, which may leave gaps in the cnt that may be temporally filled up by regular H3 nucleosomes [74]. Nevertheless, the human smc3$^{\text{HJURP}}$ was shown to bind to the CATD domain in cnp1$^{\text{CENP-A}}$ [75–77]. Furthermore, it was shown by quantitative PALM that cnp1$^{\text{CENP-A}}$ copy numbers double from early to late G2 phase in fission yeast [36], which is believed to replace the 'placeholder' H3 nucleosomes at cnt by nascent cnp1$^{\text{CENP-A}}$ nucleosomes [78]. While it is not known, why integration of new cnp1$^{\text{CENP-A}}$ is limited to G2 phase in fission yeast, other organisms such as *D. melanogaster* facilitate the cnp1$^{\text{CENP-A}}$ loading in G1 phase [79]. Finally, both the mis16/18 complex as well as smc3$^{\text{HJURP}}$ homodimer dissociate from the otrs in mitosis, while the mis6/sim4 complex remains centromere bound [80, 81].

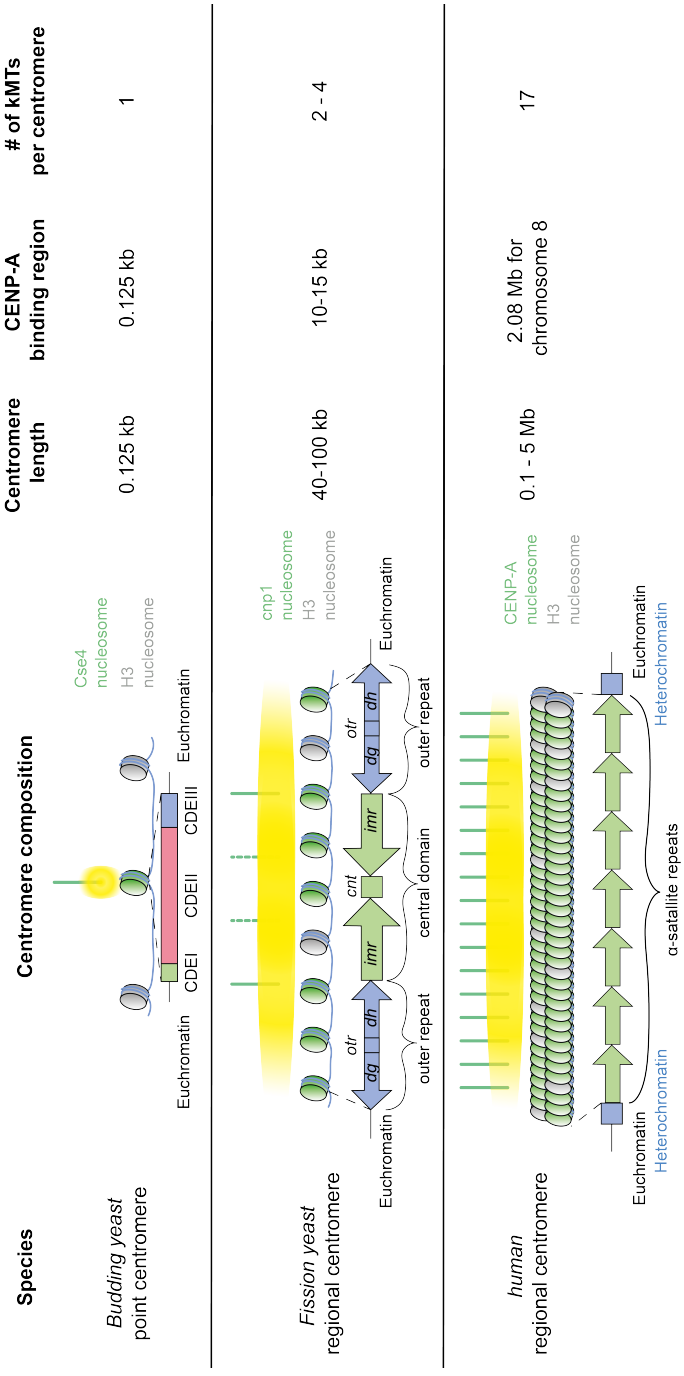

Figure 1.2: Schematic representation of different centromere organizations in different organisms.

1.1.4 Kinetochore structure

The KT is a multi-protein complex, which serves as a linker between the centromere in chromatids and kMTs of the spindle apparatus. Generally, the kinetochore structure can be divided into an inner KT, which assembles at the centromere, and an outer KT that builds upon the inner KT and tethers

kMTs (see tables 1.1 and 1.2 and figure 1.1c). Additionally, the inner and outer KT can be further divided into multiple main subcomplexes. Due to the parallel discovery of these subcomplexes in different organisms, the naming and classification is inconsistent in literature. This leads to several KT proteins being assigned to different subcomplexes at the same time.

The inner KT subcomplexes are the CCAN, which is a network of 16 KT proteins that were discovered by first cnp1$^{\text{CENP-A}}$ based pull-down experiments from mammalian extracts, the mis6/sim4 complex, which as previously mentioned, interacts with cnp1$^{\text{CENP-A}}$ and is involved in cnp1$^{\text{CENP-A}}$ loading at the centromere, the COMA complex named after the budding yeast homologs (Ctf19, Okp1, Mcm21 and Ame1), the CENP-TWSX complex and the budding yeast specific CBF3 complex. Next to these subcomplexes, some inner KT proteins remain unassigned to specific complexes, such as glm1$^{\text{GLMN}}$, cbp1$^{\text{CENP-B}}$ and cnp1$^{\text{CENP-A}}$. In contrast to that, the outer KT consists on one hand of the MIND, NDC80c and KNL1 complexes, which together make up the KNM network, and on the other hand of MT binding DASH complex found in budding and fission yeast, which is replaced by the SKA1 complex in humans.

A detailed description of integral inner and outer KT subcomplex, as well as their intra-KT interactions, regulations and variability between different organisms is given in the next subchapters.

Inner kinetochore

First studies, which focused on outer KT complexes, indicated a well-conserved and stable structure present in various species with only minor alterations [82–84]. However, recent studies using comparative genomics spotlighting the inner KT complexes indicate a loss of various proteins among different organisms [83]. Furthermore, it was shown that in contrast to regular histones, cnp1$^{\text{CENP-A}}$ is rapidly evolving [85–87], which is theorized to force the inner KT to also adapt. Currently, three major pathways for connecting the centromere to the outer KT complex have been identified: cnp3$^{\text{CENP-C}}$, cnp20$^{\text{CENP-T}}$ and the COMA complex [88–92].

A prominent representative for a cnp3$^{\text{CENP-C}}$ based inner KT is *D. melanogaster*, which only possesses cnp1$^{\text{CENP-A}}$ and cnp3$^{\text{CENP-C}}$ homologs [83, 93–95]. Here, cnp3$^{\text{CENP-C}}$ has been shown to physically bear the load of chromosome segregation by using Förster resonance energy transfer (FRET) and talin-vinculin based force sensors [96]. Generally, cnp3$^{\text{CENP-C}}$ was shown to have four functional domains: the N-terminus, which binds the mis12/nnf1 head domain of the MIND complex [97, 98], the central domain and CENP-C motif, which serve as nucleosome binding sites [38, 95, 99–102] and a cupin homodimerization domain at its C-terminus [103, 104]. Furthermore, it was proposed that in humans two copies of each cnp3$^{\text{CENP-C}}$ and mis15$^{\text{CENP-N}}$ symmetrically bind to one cnp1$^{\text{CENP-A}}$ bearing nucleosome [105]. Once the chromatid is condensed and the cnp1$^{\text{CENP-A}}$ nucleosomes are rearranged in a plate-like manner at the chromatid surface, rendering the centromere more accessible to KT proteins in mitosis, one of the two copies of mis15$^{\text{CENP-N}}$ detaches from the nucleosome, while both nucleosomal binding sites in cnp3$^{\text{CENP-C}}$ now form bonds [105].

In contrast to that, in budding yeast only Ame1, Okp1, which form one out of two heterodimers (Ame1/Okp1 and Mcm21/Cft19) in the COMA complex, and cnp3$^{\text{CENP-C}}$ are essential inner KT proteins from the three mentioned main pathways [106–109]. Both complexes bind to the N-terminal histone tail of cnp1$^{\text{CENP-A}}$ [40] and the outer KT complex MIND at their N-terminal mis12/nnf1 head domain through Ame1 or as previously mentioned through the cnp3$^{\text{CENP-C}}$ N-terminus [98]. All three proteins have been shown to transmit the necessary pulling force for chromosome segregation [110]. Interestingly, the deletion of the MIND binding N-terminus in cnp3$^{\text{CENP-C}}$ is nonessential, whereas

deletion of the MIND binding domain in Ame1 is essential [111]. These findings indicate that for budding yeast the primary pathway for the inner KT is the COMA complex, whereas cnp3$^{\text{CENP-C}}$ appears to represent a secondary and thus backup pathway, in case COMA-MIND binding is hindered. Furthermore, van Hoff *et al.* have shown that the COMA complex is evolutionary an relatively new addition to the inner KT, as its appearance is essential in various species, but unessential in their ancestors [83].

The third pathway for inner KT assembly is based on cnp20$^{\text{CENP-T}}$, which is part of the stable heterotertameric CENP-TWSX complex, that can induce DNA super-coils, form a histone fold [91], has a MIND [112–114] as well as a NDC80c binding domain [112, 115–118] and is independent of cnp1$^{\text{CENP-A}}$ unlike the cnp3$^{\text{CENP-C}}$ and COMA based pathways [119]. This is supported by the fact that two types of cnp20$^{\text{CENP-T}}$-based inner KTs exist, one in the presence of cnp1$^{\text{CENP-A}}$, which is the case for Chicken DT40 cells and one in the absence of cnp1$^{\text{CENP-A}}$ homologs, which is the case for *B. mori* [120]. This leads to the assumption that cnp20$^{\text{CENP-T}}$ might replace the function of cnp1$^{\text{CENP-A}}$ for KT assembly in *B. mori*. Whereas the regulation of the KT assembly has been studied in various organisms, the KT dissassembly remains mostly elusive. However, it is general consens that the CCAN remains present throughout the cell cycle, while the outer KT complexes MIND and NDC80c detach from the CENP-TWSX complex upon mitotic exit, which is most likely caused by dephosphorylation of cnp20$^{\text{CENP-T}}$ contact sites [114]. While cnp20$^{\text{CENP-T}}$ is nonessential in budding yeast [109, 121–123], it has been shown that deletions of either NDC80c and MIND binding domains in cnp20$^{\text{CENP-T}}$ are essential in Chicken DT40 cells, whereas the MIND binding N-terminus in cnp3$^{\text{CENP-C}}$ is nonessential [114]. Using a talin sensor system Hara *et al.* showed that cnp20$^{\text{CENP-T}}$ bears the major pulling force in chromosome segregation, while mutations, that prevent CENP-TWSX complex tertramerization prevent successful mitosis in humans and Chicken DT40 [114]. Thus, it is assumed that Chicken DT40 cells primarily utilize the cnp20$^{\text{CENP-T}}$ pathway, whereas the cnp3$^{\text{CENP-C}}$ pathway acts as a secondary backup pathway.

In human cells cnp3$^{\text{CENP-C}}$ and cnp20$^{\text{CENP-T}}$ are essential for viability [124], whereas the COMA complex has been shown to be a) nonessential in HeLa cells and b) unable to bind to the MIND complex [125, 126]. Similarly, to the Chicken DT40 cells, the cnp20$^{\text{CENP-T}}$ appears to be the load bearing factor in chromosome segregation as it was shown by increased cnp20$^{\text{CENP-T}}$ stretching upon deletion of cnp3$^{\text{CENP-C}}$ as well as the fact that the N-terminus of cnp3$^{\text{CENP-C}}$ does not localize close to MIND in HeLa cells [127]. Thus, it is hypothesized that humans utilize cnp20$^{\text{CENP-T}}$ as the primary inner KT pathway and the cnp3$^{\text{CENP-C}}$ as a secondary backup pathway [120].

For fission yeast the preferred inner KT pathway has not been identified yet [120]. From previous studies it is known that the deletion of cnp3$^{\text{CENP-C}}$ is viable in fission yeast [101, 103, 108] whereas the deletion of cnp20$^{\text{CENP-T}}$ is nonviable [101], which is the opposite in budding yeast [106–109, 121–123]. Although budding and fission yeast evolutionary diverged around 420 million years ago [128], the fission yeast homologs of Ame1 (mis17$^{\text{CENP-U}}$) and Okp1 (fta7$^{\text{CENP-Q}}$) are essential as well [108, 129]. Furthermore, the deletions of the remaining COMA proteins fta2$^{\text{CENP-P}}$ and mal2$^{\text{CENP-O}}$ are nonviable, rendering the whole COMA complex essential in fission yeast [108, 130].

Outer kinetochore

On top of the inner KT, the outer KT is assembled, which consists of four major subcomplexes. One of these subcomplexes is the previously mentioned heterotetrameric MIND complex consisting of the two heterodimers mis12$^{\text{MIS12}}$/nnf1$^{\text{PMF1}}$ and mis13$^{\text{DSN1}}$/mis14$^{\text{NSL1}}$ [98]. As mentioned before,

the MIND complex interacts with the inner KT trough the N-terminal mis12^{MIS12}/nnf1^{PMF1} head domain with Ame1 (mis17^{CENP-U}) of the COMA complex and with the N-terminus of cnp3^{CENP-C} as well as with the N-terminus of cnp20^{CENP-T} through the C-terminus of mis12^{MIS12}/nnf1^{PMF1}. In the yeast *Kluyveromyces lactis* it was shown that the C-terminus of mis13^{DSN1} is wrapped around the mis12^{MIS12}/nnf1^{PMF1} head domain, blocking the binding sites of COMA and cnp3^{CENP-C} in the MIND complex [98]. After phosphorylation of the mis13^{DSN1} C-terminus by Aurora B kinase, the C-tail unwraps from the mis12^{MIS12}/nnf1^{PMF1} head domain, which is then accessible to COMA and cnp3^{CENP-C} [98]. On the other hand MIND establishes connections to the other outer KT subcomplexes KNL1c and NDC80c through the C-terminus of mis14^{NSL1} with the spc7^{KNL1} RWD-C domain at the C-terminus [131, 132] and the C-termini of both mis12^{MIS12}/nnf1^{PMF1} and mis13^{DSN1}/mis14^{NSL1} heterodimers with the C-terminal head domain of the spc24^{SPC24}/spc25^{SPC25} heterodimer of NDC80c, respectively [98, 133]. This suggests that the MIND complex competes with cnp20^{CENP-T} for the binding site in NDC80c, while MIND and cnp20^{CENP-T} can also form a connection.

The KNL1c complex consists of a spc7^{KNL1}/sos7^{ZWINT} heterodimer, where the humans spc7^{KNL1} was shown to have a globular head consisting of a tamden RWD domain, divided into RWD-N and RWD-C domains connected by a helix, and a predicted coiled-coil domain at the N-terminus, which was shown to interact with sos7^{ZWINT}, ndc80^{NDC80} and mis12^{MIS12} in biochemical pull-down assays [131].

One of the most studied KT subcomplexes is the highly conserved heterotetrameric NDC80c complex, which consists of two heterodimers (ndc80^{NDC80}/nuf2^{NUF2} and spc24^{SPC24}/spc25^{SPC25}) [134, 135]. Both heterodimers posses a globular head domain (calponin homology (CH) domain at the N-terminus of ndc80^{NDC80}/nuf2^{NUF2} and RING finger, WD repeat, DEAD-like helicases (RWD) domain at the C-terminus of spc24^{SPC24}/spc25^{SPC25}), as well as a coiled coil domain at the ndc80^{NDC80}/nuf2^{NUF2} C-terminus and spc24^{SPC24}/spc25^{SPC25} N-terminus [136, 137]. Through interaction of the coiled coil domains of both heterodimers, the full dumbbell-shaped NDC80c is assembled [136, 137]. The ndc80^{NDC80}/nuf2^{NUF2} dimer tethers the KT to the kMT, whereas the spc24^{SPC24}/spc25^{SPC25} dimer forms previously described connections to the inner KT via MIND and cnp20^{CENP-T}. So far only modified NDC80c complexes could be crystalized, where either the coiled coil domain was shortened or the heterodimers were bound together by forming covalent bonds at the tetramerization site [136, 137]. Nevertheless, the crystal structures revealed a 57 nm long head-to-head domain NDC80c [134, 135] that has an unstructured 80 amino acid long N-terminal tail in ndc80^{NDC80}, which interacts with kMT and as well as other NDC80c as well as a ndc80^{NDC80} loop region within the coiled-coil domain that is an important interaction hub for KT-kMT interaction stabilizing MAP and TIP proteins and integral for force sensing during chromosome bi-orientation [138, 139]. The NDC80c-kMT binding is regulated by Aurora B kinase, which is a member of the SAC that phosphorylates several amino acids in the CH domain and N-terminal tail of ndc80^{NDC80} upon sensing a faulty chromosome bi-orientation [140, 141]. This neutralizes the positive charge needed for kMT interaction leading to a kMT release.

Another kMT binding subcomplex is the DASH complex in fission and budding yeast, which is believed to have been replaced by the SKA1 complex in mammalians. Crystal structures of the budding yeast DASH complex showed T-shaped heterodecamers, where 17 units are arranged in a ring-like structure around the kMT with an inner and outer diameter of 39 nm or 56 nm respectively [142]. Furthermore, *in vitro* EM data revealed that NDC80c can bridge two DASH rings on MTs with a rigorous 35 nm distance between both rings, while protein cross-linking and mass spectrometry data determined the two DASH interaction sites with one being close to the ndc80^{NDC80}-loop and the

second close to the head domain in the ndc80^{NDC80}/nuf2^{NUF2} heterodimer [143]. Since mutations at the head region interaction site of ndc80^{NDC80} proved to be more severe than in the ndc80^{NDC80} loop region, it is believed to bear the main contact site to the DASH complex [143]. Similar to the kMT release in NDC80c, phosphorylation of dam1, ask1 and spc34 C-termini by Aurora B kinase disrupts the interaction between the NDC80c and DASH complex and initiates the release [144]. Additionally, MT bound NDC80c was shown to withstand higher pulling forces in presence of single DASH complex proteins, which is attributed to a more stable bound between NDC80c and the MT as well as to a redistrubution of the load between NDC80c and the DASH complex [144]. However, while DASH rings could be detected *in vitro*, no evidence has been found yet that the DASH complex forms rings *in vivo*. Contrary to the DASH complex, the SKA1 complex consists of SKA1-3 that form a heterotrimere [145]. Two of these heterotrimers form a W-shaped dimer with the C-termini facing outside while the N-termini establish the interaction. In crystal data ten W-shaped dimers form the complete SKA complex with a coiled-coil core, where the N-termini face the core and the C-termini bind the kMT at two sites [145]. Similar to the DASH complex, no ring-like structure of the SKA1 complex could be found *in vivo*.

fission yeast	*budding yeast*	*human*	**subcomplex**
cnp1	Cse4	CENP-A	centromeric chromatin
cbp1, cbh1, cbh2	x	CENP-B	
cnp20	Cnn1	CENP-T	CCAN network, CENP-TWSX complex
wip1 alias new1	Wip1	CENP-W	
mhf1	Mhf1	CENP-S	
mhf2	Mhf2	CENP-X	
cnp3	Mif2	CENP-C	CCAN network
x	x	CENP-M	
x	x	CENP-R	
mis15	Chl4	CENP-N	Mis6/Sim4 complex, CCAN network
fta1	Iml3 alias Mcm19	CENP-L	
fta3	Mcm16	CENP-H	
mis6	Ctf3	CENP-I	
sim4	Mcm22	CENP-K	
mal2	Mcm21	CENP-O	COMA complex, Mis6/Sim4 complex, CCAN network
fta2	Ctf19	CENP-P	
fta7	Okp1	CENP-Q	
mis17	Ame1	CENP-U	
cnl2	Nkp2	x	Mis6/Sim4 complex
fta4	Nkp1	x	
fta6	x	x	
x	cep3	x	CBF3 complex
skp1	Skp1	SKP1	
x	Ctf13	x	
x	Cbf2 alias Ndc10	x	
glm1 paralog to glm2	Ybp2 paralog to Ybp1	GLMN	Central kinetochore associated protein

Table 1.1: Structural components of the inner kinetochore complex present during mitosis in different organisms

fission yeast	*budding yeast*	*human*	**subcomplex**
nnf1	Nnf1	PMF1	MIND complex, KMN complex
mis12	Mtw1	MIS12	
mis13	Dsn1	DSN1	
mis14	Nsl1	NSL1	
spc7	Spc105	KNL1	KMN complex, KNL1 complex
sos7	Kre28	ZWINT	
ndc80	Ndc80	NDC80	NDC80c complex, KMN complex
nuf2	Nuf2	NUF2	
spc24	Spc24	SPC24	
spc25	Spc25	SPC25	
spc34	Spc34	x	DASH compex
ask1	Ask1	x	
dad1	Dad1	x	
dad2	Dad2	x	
dad3	Dad3	x	
dad4	Dad4	x	
dad5	Hsk3	x	
dam1	Dam1	x	
duo1	Duo1	x	
spc19	Spc19	x	
x	x	SKA1	SKA1 complex
x	x	SKA2	
x	x	SKA3	

Table 1.2: Structural components of the outer kinetochore complex present during mitosis in different organisms

1.2 Super-resolution microscopy

1.2.1 The limits of conventional fluorescence microscopy

Super-resolution microscopy (SRM) evolved into a powerful tool during the last decades for studying biological structures and processes at the low nanometer scale. In comparison to conventional fluorescence microscopy, which is constrained by the diffraction limit of light, SRM circumvents this limit by utilizing sophisticated illumination patterns, special fluorophores with tightly controllable photophysics or physically expanding the sample itself.

The diffraction limit of light was postulated by Ernst Abbe in 1873 to be the maximum achievable resolution using conventional optical systems, which is given by the numerical aperture (NA) of the objective and half of the utilized wavelength, as depicted in formula 1.1 [146]. The NA of the objective can be calculated from the refractive index of the medium (n) and the half opening angle $\alpha$of the objective. A single emitter appears as a circular spot with a bright maximum and a series of concentric rings of decreasing intensity, also called point spread function (PSF). In 1879 Lord Rayleigh then described the maximum achievable resolution between two overlapping emitters (see formular 1.2) to be the distance, where the maximum of one PSF coincides with the first minimum of the second PSF, causing a drop in intensity of about 20% (see figure 1.3) [147]. Hence, in conventional fluorescence microscopy, lateral and axial resolutions of about 200 nm and 500 nm can be achieved, respectively.

$$d = \frac{\lambda}{2 \cdot n \cdot \sin\alpha} = \frac{\lambda}{2 \cdot NA} \tag{1.1}$$

$$d_{Rayleigh} = \frac{0.61 \cdot \lambda}{NA} \tag{1.2}$$

Different strategies to circumvent the diffraction limit have been developed and can be classified into roughly three groups of SRM techniques: the first group relies on modulation of the excitation light pattern, such as stimulated emission depletion (STED) [148] or structured illumination microscopy (SIM) [149]. The second group is based on the detection and localisation of single fluorescent emitters over time, also termed SMLM [150–152]. In contrast to that, the final group expands the sample in water after anchoring the target molecules to a hydrogel mesh, which yields higher magnification and thus resolution of the sample also called ExM [153]. Although all SRM techniques yield higher resolutions than conventional fluorescence microscopy, a quantification of the target molecule is only possible in SMLM techniques due to the output of a localization list from which the detections per cluster can be deduced. Due to this, SMLM was selected as the method of choice to create a map of the kinetochore nanoscale structure based on inter-protein distances and protein stoichiometries.

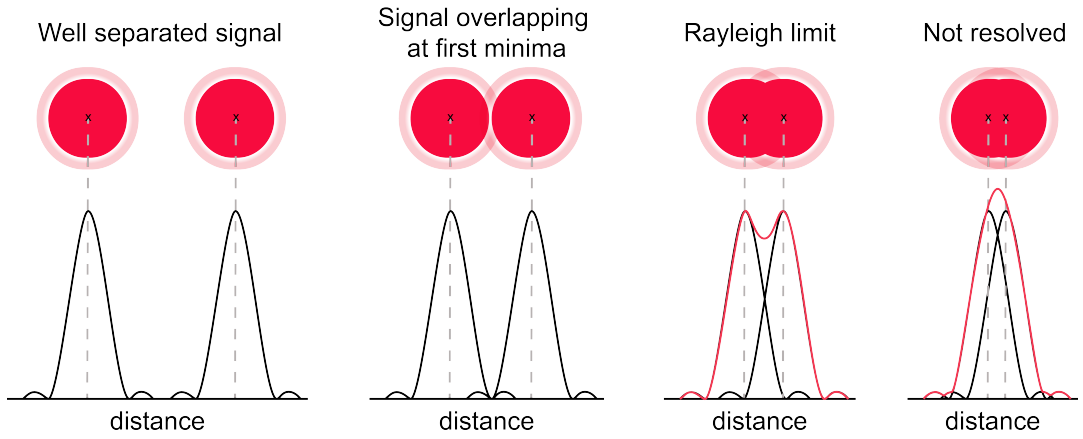

Figure 1.3: The resolution limit of light explained by two single point emitters gradually getting closer until their signal can not be discerned anymore.

1.2.2 Introduction into SMLM imaging

This part of the thesis is written in the style of a manuscript and was published as a review in *The Biochemist* in 2020. For this manuscript I conducted the literature research and prepared the figures with input from Prof. Dr. Ulrike Endesfelder. The manuscript text was written together with Prof. Dr. Ulrike Endesfelder.

Here, we first describe the principle of fluorescence microscopy and highlight the differences between conventional widefield and SMLM microscopes. We discuss three critical optical components that are pivotal to achieve single-molecule sensitivity and can be easily implemented in basic widefield microscope setups. However, as true single-molecule fidelity is not solely dependent on the hardware of the microscope setup, we also discuss required parameter optimizations in the sample preparation such as labeling efficiency and specificity as well as imaging controls such as drift-control and correction.

Beginner's guide to producing super-resolved images on a widefield fluorescence microscope

Ilijana Vojnovic and **Ulrike Endesfelder** (Max Planck Institute for Terrestrial Microbiology and LOEWE Center for Synthetic Microbiology (SYNMIKRO), Germany)

The development of super-resolution microscopy techniques, which are able to achieve resolutions in the nanometre range and as such allow the visualization of subcellular structures and dynamics, has considerably expanded the possibilities of fluorescence microscopy in the life sciences. While a majority of these techniques require highly specialized hardware, *single-molecule localization microscopy* (SMLM) can be implemented on conventional widefield fluorescence microscopes. Here, we describe what technical upgrades are necessary and discuss some of the difficulties that can be encountered during sample preparation and imaging.

Visualizing life with fluorescence microscopy

Fluorescence microscopy sheds light on all areas of life. It visualizes the embryonic development of large multicellular organisms as well as the molecular organization within tiny microbes. The molecules of interest are labeled with fluorophores, which reveal their positions through their emitted fluorescence, producing colourful and contrast-rich images.

The development of super-resolution techniques has expanded the possibilities of fluorescence microscopy even further. These techniques are not restricted by the diffraction limit of light, and thus are able to attain resolutions of only a few nanometres. This has in many cases revealed unexpected, spectacular new biology. The demand for super-resolution setups, access to imaging facilities and collaborations with research groups operating such systems is, therefore, high.

Whilst some super-resolution techniques work with complex illumination patterns and require highly specialized hardware, the class of *single-molecule localization microscopy* (SMLM) techniques relies on special fluorophores that can be photoswitched between a non-emitting 'dark state' and a fluorescent 'on-state' to achieve sub-diffraction resolution. They are modulated in such a way that only few of them fluoresce at the same time. Fluorophores, therefore, appear as distinct fluorescence spots on the detector whose centres can be localized with high precision.

As a consequence, SMLM, in its simplest form, can be implemented on a widely available widefield fluorescence microscope. This makes it ideal for anyone wishing to explore the possibilities of super-resolution microscopy at a relatively low cost. In the following sections, we describe how you can equip your conventional widefield microscope for SMLM and what needs to be considered during sample preparation and imaging.

Preparing your microscope

The basic design of a widefield fluorescence microscope is depicted in Figure 1a. The excitation light, depicted in green, is reflected by a dichroic mirror onto the objective to illuminate the sample. The emitted fluorescence, depicted in orange, is collected by the same objective and now passes the dichroic mirror due to its Stokes shift to longer wavelengths. The fluorescence image is then recorded by a light-sensitive detector.

Unfortunately, most conventional widefield microscopes are not sensitive enough to detect the signal of single fluorophores, which is essential for SMLM. However, this can be remedied by upgrading three core components – the light sources, the objective and the detector.

Conventional fluorescence microscopes typically employ gas discharge lamps or an array of *light-emitting*

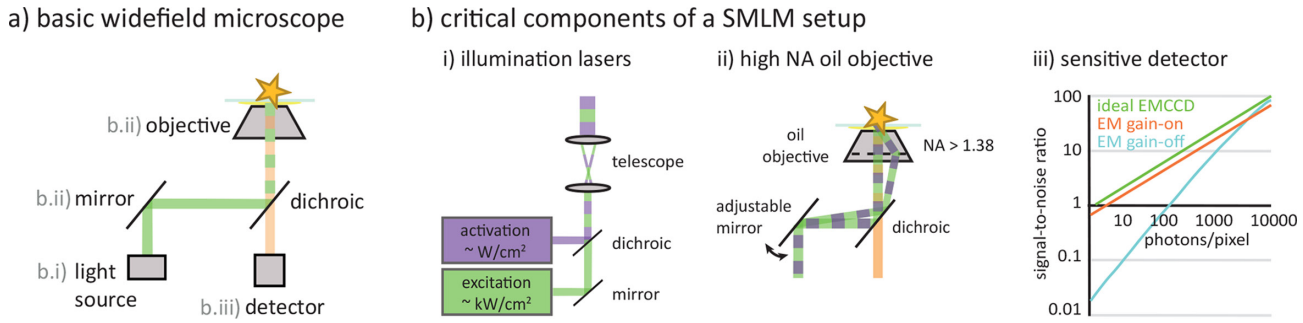

Figure 1. Adapting a widefield microscope for SMLM imaging. In order to adapt an epifluorescence widefield microscope system as depicted in (**a**) for SMLM imaging, three components are necessary: illumination lasers (**b.i**), an immersion oil objective with high numeric aperture (**b.ii**) and a sensitive detector such as an EMCCD camera (**b.iii**). Together, these allow for single-molecule sensitivity.

diodes (LEDs) as light sources, thereby accommodating a wide range of fluorophores with diverse excitation spectra and allow for straightforward multicolour imaging. For SMLM imaging, these light sources need to be replaced by lasers. Unlike ensemble fluorescence microscopy, which records the joint signal of all fluorescent molecules, SMLM relies on the ability to detect individual fluorophores. This is only possible if a minimum of several hundred to a few thousands of photons per fluorophore reach the detector in a single imaging frame. As each emission of a photon requires the absorption of an excitation photon, fluorophores have to be excited as efficiently as possible to maximize the emitted fluorescence per time. Lasers provide the strong, coherent illumination to achieve this (Figure 1b.i).

Typically, small diode lasers or diode-pumped solid state lasers with wavelengths matching the absorption spectra of common SMLM fluorophores are used. By means of a telescope, the laser beams' diameters are adjusted in such a way that the illuminated area within the sample covers the field of view of the detector. In an efficient setup, lasers with powers of 100–500 mW are sufficient to achieve an illumination intensity of 0.5–2 kW/cm^2 that is needed for SMLM imaging. This requires that the expansion of the laser beams is not larger than necessary and that about 50% of the lasers' original power reaches the sample (this is typically only possible with open laser paths).

In addition to the excitation lasers, a so-called activation laser is needed to modulate the photoswitching fluorophores. Most fluorophores suitable for SMLM are photoswitched by near-UV laser illumination of ~400 nm wavelength. Typically, intensities of a few W/cm^2 of a 405-nm diode laser are sufficient (Figure 1b.i). Additionally, variants exist of many commonly used fluorescent proteins that can be photoswitched via so-called *primed photoconversion*, which uses a combination of 488 nm and near-infrared illumination. Primed photoconversion can be useful to reduce phototoxicity and (in combination with a near-UV switchable fluorophore) for dual colour imaging. Another very convenient add-on is the fast mechanical shutters or an *acousto-optic tunable filter* (AOTF) to modulate the activation and excitation lasers for fast temporal illumination control.

The second crucial prerequisite for the detection of single fluorophores is an objective that collects as much fluorescence as possible from the sample (Figure 1b.ii). As the fluorescence emitted by a fluorophore is typically isotropic, an objective with a large light collection angle (also called aperture angle) is essential. However, light hitting the glass surface of the objective at a sharp angle will simply be reflected away if it comes from a less-dense medium. The space between cover slip and objective, therefore, needs to be filled with an immersion oil with a refractive index matching that of glass (about 1.51). This also prevents photon loss due to refraction at the boundary of cover slip and immersion medium. Aperture angle and the refractive index of the immersion liquid are, therefore, the key performance indicators of any objective. Together, they determine the so-called *numerical aperture* (NA) of an objective, which is defined as the product of the refractive index and the sinus of the half aperture angle. The higher the NA, the better the ability of the objective to collect light. For SMLM imaging, an objective with an NA of 1.45 or higher is typically necessary.

High NA objectives also come with a second advantage: they allow for objective-based *total internal reflection fluorescence* (TIRF) microscopy. The TIRF geometry creates an evanescent light field of only 100–200 nm width at the cover slip surface. It only excites molecules close to the surface, and as such drastically improves the signal-to-noise ratio when imaging small objects. An adjustable mirror can be installed in the optical path of the illumination lasers to easily switch between widefield and TIRF imaging modes (Figure 1b.ii).

The last critical component is a detector sensitive enough to detect the weak signal of single fluorophores. As a widefield microscopy technique, SMLM records images with a two-dimensional array detector, e.g., a *charge-coupled device* (CCD) sensor. CCD chips consist of an array of photodiodes that detect incident fluorescence photons by means of the photoelectric effect. To attain single-molecule sensitivity, CCDs are enhanced by electron multipliers (EMCCDs), which cause photoelectrons to trigger an avalanche of secondary electrons through impact ionization. The strength of this amplification can be adjusted through the EM gain of the detector, which can make even the signal of only a few photons detectable (Figure 1b.iii). Apart from EMCCD cameras, the new generation of *scientific Complementary Metal Oxide Semiconductor* (sCMOS) sensors are sensitive enough for SMLM imaging.

Labelling and imaging performance at single-molecule fidelity

The right hardware, however, is only part of the story. Due to the delicate nature of nanoscale imaging, special care needs to be taken during sample preparation and imaging. Single-molecule–sensitive microscopes provide single-molecule resolution. This means that factors that are hardly noticeable in conventional widefield images can have a large impact on the quality of an SMLM image.

One important aspect of fluorescence microscopy is the notion that one always only visualizes the fluorophores, not the molecules of interest themselves. As such, fluorescence microscopy techniques strongly depend on the fidelity of the chosen fluorescence label. Good labeling will have a high efficiency, i.e., a large part of the target molecules carry a label, and a high specificity, i.e., most other things do not.

In Figure 2a, we showcase a high-quality image of vimentin filaments in a mammalian HeLa cell at widefield (left), as well as SMLM resolution (right). In this specific example, the vimentin structures are labeled by a small, only a few nanometres, sized single-chain antibody, a so-called nanobody, which yields high labeling efficiency and specificity. The labels densely populate the filaments which are thoroughly stained. The nanobody carries an organic dye, Alexa Fluor 647, in a quantitative one-to-one labeling ratio, which is one of the best performing fluorophores in the SMLM field. It is a bright probe, its photoswitching is well-controlled and reliable, and its bleaching rate in SMLM buffers is low.

Using this SMLM data set, we simulate typical problems of labeling and imaging procedures.

In Figure 2b, we use only a fraction of our data set to visualize how low labeling efficiencies impact image quality. While the labeling efficiency is still acceptable for widefield resolution (Figure 2b.i), prominent gaps are visible in the vimentin structures in the SMLM image (Figure 2b.ii). In general, low labeling efficiencies can have many different causes: for affinity tags such as antibodies, their affinity could just not be sufficiently high or the targeted epitopes cannot be reliably reached (e.g., labels physically too big, epitopes partially buried in the structure). For transient expressions of genetic labels, the filaments simply could be a mixture of native and labeled proteins of interest. It is also possible for the sample preparation protocols to be too harsh, quenching fluorescence or destroying the epitopes of extrinsic labels.

The quality of SMLM images can also be impacted by false-positive signals caused by unspecific staining or autofluorescence. This is especially critical if the native abundance of the molecules of interest is low. We simulate unspecific, false-positive signals in the data set for our example by distributing random data points throughout the field of view (Figure 2c). Even though vimentin is a highly structural, filamentous protein, the interpretation of the image becomes ambiguous. It is difficult to evaluate if a registered signal results from specific staining, e.g., a pool of vimentin monomers, or from an unspecific, non–target-bound fluorophore (Figure 2c.ii). In general, autofluorescence can be mostly attributed to colourful metabolites or pigments within the specific organism, or to uptakes from the growth media. Unspecific staining originates from non–target-bound labels that were not washed out during sample preparation, e.g., sticking by charge. Genetic labels can be troublesome as well: overexpression can produce a large pool of non-physiological monomers which are not integrated into native structures, or tags can disturb the biological function of the protein of interest.

It is easy to imagine how the quantitative evaluation of SMLM data quickly becomes unfeasible for less-structured or low copy number targets if labeling efficiency and specificity are low. For example, a staining efficiency of 75% for a homotrimeric structure will, on average, result in only about 50% of labeled structures actually appearing as trimers – under otherwise ideal imaging conditions. In practice, the underlying structure would be further obscured by random noise and signals lost due to insufficient brightness, premature bleaching or improper photoswitching control. All in all, ensuring high labeling efficiency and specificity is essential in every SMLM project. It will often be necessary to modify or completely replace the chosen labeling strategy if, after some test runs, no satisfactory results are obtained. It is not uncommon to pursue two, three or even four different approaches before being successful.

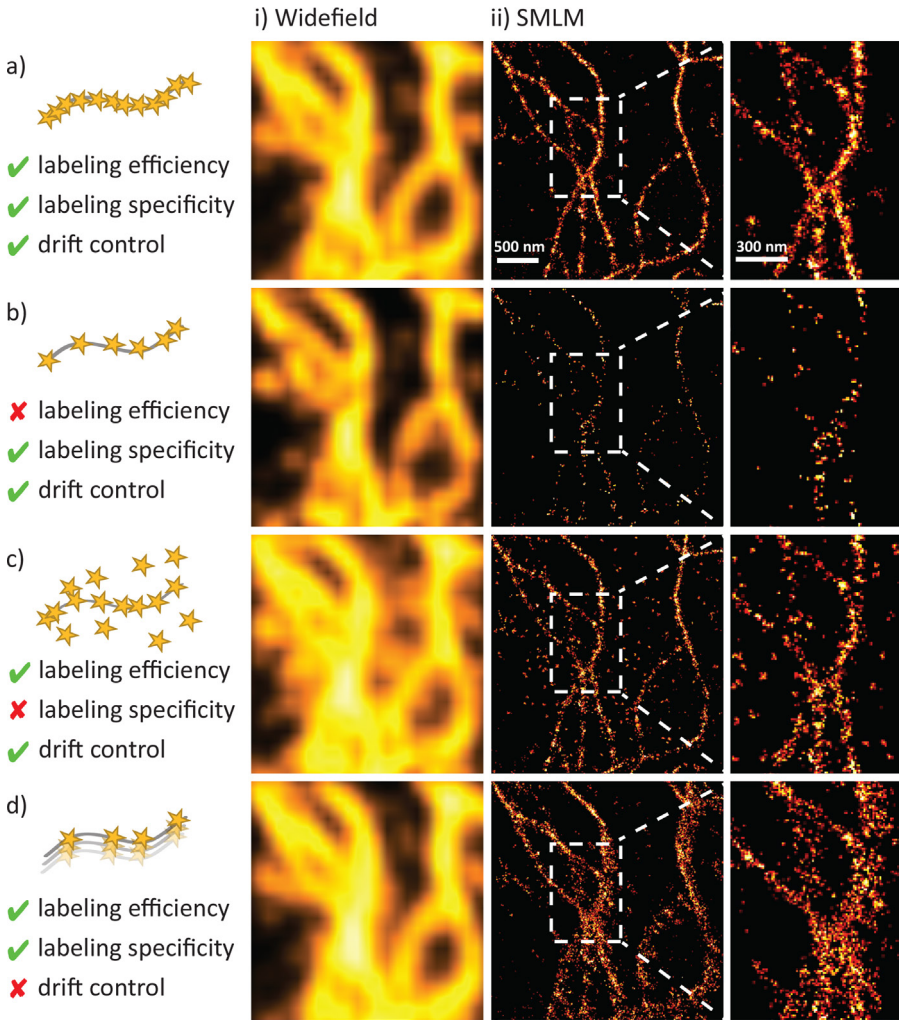

Figure 2. Labeling and imaging performance at single-molecule fidelity. (**a**) SMLM image of vimentin structures in a HeLa cell. Cells were stained using nanobodies carrying the SMLM-suitable photoswitching fluorescent dye, Alexa Fluor 647. This original recording (taken from Virant et al., Nat Commun, 2018. 9(1)) illustrates a good practice example for SMLM imaging with high labeling efficiency and specificity and robust drift control. In (**b**)–(**d**), we used this data set to simulate typical problems in labeling and imaging performance. These include low labeling efficiency (**b**), unspecific signal (**c**) and drift during image acquisition (**d**). In all cases, shortcomings in fluorescence labeling and imaging performance are clearly visible in the SMLM images (**i**), and as such limit their quality. At the same time, they are hardly noticeable in the corresponding widefield fluorescence images (**ii**).

Last but not least, a robust drift correction is needed. Recording SMLM images takes time, which increases the chance for substantial sample drift accumulating over minutes of imaging (Figure 2d). Most microscope setups are built in a heavy, mechanically stable fashion which passively prevents large drift. Additionally, most commercial systems actively stabilize the focal plane to suppress axial drift, detecting shifts via the reflection of infrared lasers from the cover slip on quadrant photodiodes. However, these measures usually do not suffice to achieve nanometre precise drift control as is required for SMLM imaging. Thus, SMLM images are typically post-processed to remove residual drift, e.g., by means of trajectories of fiducial markers measured with the sample or by calculating spatiotemporal cross-correlations using the sample data itself. Most SMLM software supports such corrections.

To illustrate the severity of residual drift in SMLM imaging, we added an artificial linear shift of 0.02 nm per imaging frame to our data set. This small drift sums up to 200 nm of total drift over the 10,000 imaging frames – hard to spot in the widefield image (Figure 2d.i) but clearly visible in the SMLM image (Figure 2d.ii).

To gather some initial experience with SMLM imaging and to test the setup, it is a good idea to first image a well-known test sample. Cytoskeletal structures such as microtubules, actin or vimentin filaments are often used as visualized standards. For all of them, well-tested commercial antibodies – pre-labeled with Alexa Fluor 647 – are available. Microtubules have the additional advantage that they are hollow, have a well-defined diameter of 25 nm and do not form higher-order filaments bundling together several fibres. In high-quality SMLM images, a cross-section through a microtubule should, therefore, show two clear peaks separated by 25 nm plus two times the size of the label and can serve as a good control for successful staining and imaging.

Conclusion

We hope that this beginners' guide has been able to convince you that the first steps towards SMLM imaging are not too difficult. Requirements are a widefield setup equipped for single-molecule sensitivity and careful sample preparation and imaging routines. For further steps, e.g., towards quantitative or live cell SMLM imaging, please have a look at the (open access) overview articles listed below. Happy imaging. ■

Further reading

Introduction into the technical details of light microscopy

- Wegerhoff, R., Weidlich, O., Kässens, M. (2006) *Basics of Light Microscopy & Imaging*, GIT Verlag GmbH & Co. https://analyticalscience.wiley.com/do/10.1002/imaging.1654

Introduction into suitable fluorophores and their photoswitching. This review includes several overview tables.

- Turkowyd, B., Virant, D. and Endesfelder, U. (2016) From single molecules to life: microscopy at the nanoscale. *Anal. Bioanal. Chem.* **408**, 6885–6911 10.1007/s00216-016-9781-8

Strategies for multicolor labeling in SMLM imaging. This review includes an experimental design guideline and a troubleshooting table.

- Vojnovic, I., Winkelmeier, J. and Endesfelder, U. (2019) Visualizing the inner life of microbes: practices of multi-color single-molecule localization microscopy in microbiology. *Biochem. Soc. Trans.* **47**, 1041–1065. 10.1042/bst20180399

The example vimentin data set of Figure 2 is taken from this publication. It introduces a new nanobody label for SMLM imaging.

- Virant, D., Traenkle, B., Maier, J., et al. (2018) A peptide tag-specific nanobody enables high-quality labeling for dSTORM imaging. *Nat. Commun.* **9**, 930 10.1038/s41467-018-03191-2

Ilijana Vojnovic studied chemistry at the Goethe University in Frankfurt, Germany, and is now a PhD student at the Department for Systems and Synthetic Microbiology at the Max Planck Institute for Terrestrial Microbiology in Marburg, Germany. She applies super-resolution methods for structural studies in microbes, investigating multi-protein complexes. Email: ilijana.vojnovic@synmikro.mpi-marburg.mpg.de

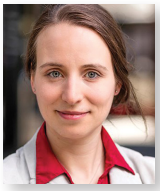

Ulrike Endesfelder studied physics and has been a group leader at the Max Planck Institute for Terrestrial Microbiology in Marburg since 2014. She is a member of the German Young Academy. In summer 2020, she and her group will move to Carnegie Mellon University in Pittsburgh, USA, where she accepted a professorship position for Experimental Biophysics. Email: ulrike.endesfelder@synmikro.mpi-marburg.mpg.de

1.2.3 Multi-color SMLM in microbiology

This part of the thesis is written in the style of a manuscript and was published as a review in *Biochemical Society Transactions* in 2019. For this manuscript Jannik Winkelmeier, Prof. Dr. Ulrike Endesfelder and me conducted the literature research and created the tabular overviews of multi-color SMLM studies conducted in bacteria and fungi. The figures were designed by Jannik Winkelmeier and me and the manuscript text was written together by Prof. Dr. Ulrike Endesfelder and me with the help of Jannik Winkelmeier.

In the following review we explain the principle of SMLM along with the structure and photophysical behavior of commonly used fluorescent markers as well as various labeling methods to target different cellular components such as proteins, carbohydrates, lipids or nucleotides. Furthermore, the review goes into detail about which parameters are of importance when establishing SMLM studies in microbes as well as what difficulties can arise when imaging multiple targets. Then, a detailed review of all multi-color SMLM studies in microbes is given along with an analysis of possible fluorophore combinations and imaging schemes used in bacteria and fungi to date. Finally, the review concludes with a guideline on how to design multi-color SMLM experiments with a concrete practical example on how to solve the KT nanostructure in fission yeast, which is the main goal of this thesis, (see figure 5 of chapter 1.2.3) as well as lists possible pitfalls along the way (see table 3 of chapter 1.2.3).

Biochemical Society Transactions (2019) **47** 1041–1065
https://doi.org/10.1042/BST20180399

PORTLAND PRESS

Review Article

Visualizing the inner life of microbes: practices of multi-color single-molecule localization microscopy in microbiology

Ilijana Vojnovic, Jannik Winkelmeier and Ulrike Endesfelder

Single-Molecule Microbiology Group, Department of Systems and Synthetic Microbiology, Max Planck Institute for Terrestrial Microbiology and LOEWE Center for Synthetic Microbiology (SYNMIKRO), Marburg, Germany

Correspondence: Ulrike Endesfelder (ulrike.endesfelder@synmikro.mpi-marburg.mpg.de)

In this review, we discuss multi-color single-molecule imaging and tracking strategies for studying microbial cell biology. We first summarize and compare the methods in a detailed literature review of published studies conducted in bacteria and fungi. We then introduce a guideline on which factors and parameters should be evaluated when designing a new experiment, from fluorophore and labeling choices to imaging routines and data analysis. Finally, we give some insight into some of the recent and promising applications and developments of these techniques and discuss the outlook for this field.

Introduction

The emerging field of Single-Molecule Localization Microscopy (SMLM) allows to resolve biological structures at the nanometer scale and to monitor molecular interactions in the millisecond range. To tackle the diverse biological and technical demands of specific research questions, a growing number of practical SMLM tools have been developed over the last years. This is nicely illustrated by recent general reviews on super-resolution microscopy developments [1–3] as well as by reviews focusing on photoswitchable fluorophores needed for SMLM techniques [4–6].

However, since each research field has its own particularities, only a subset of the overall SMLM toolbox matches the given, field-specific requirements. An example of such a specific research area is the field of microbiology. Technical demands are largely shared by this field of biology, which encompasses all known microorganisms. Robust SMLM tools for studying microbial cell biology all face the challenges that microorganisms, in general, are (1) small and densely packed single-cell organisms protected by robust cell walls, (2) show rather low protein copy numbers often combined with specific autofluorescence or background of colorful pigments when compared with, e.g. mammalian cells and (3) possess rather fast growth rates accompanied by rapid metabolism rates. However, many model organisms provide widely established genetic modification tool sets facilitating genetic target labeling.

While current (microbial) SMLM studies mostly examine the dynamic and structural properties of a single target [7–9], one could argue that biological processes, in general, rely on interactions of multiple components. Therefore, establishing reliable methods for multi-color SMLM is becoming increasingly more important.

Hence, in this review, we exclusively focus on the multi-color single-molecule imaging and tracking studies on microbial cell biology published to date and discuss their utilized tools' advantages and disadvantages as well as possible pitfalls. Moreover, we highlight recent and potential future developments within the field.

Received: 2 December 2018
Revised: 22 April 2019
Accepted: 26 April 2019

Version of Record published:
11 July 2019

PORTLAND PRESS

Biochemical Society Transactions (2019) **47** 1041–1065
https://doi.org/10.1042/BST20180399

Principle of SMLM techniques

Fluorescence microscopy is a powerful tool to investigate biological systems as it allows to monitor the spatio-temporal behavior of virtually any, fluorescently labeled biomolecule of interest at high specificity. Nevertheless, even for specifically chosen, labeled molecules, details below 200 nm remain unresolved due to the diffraction barrier of light microscopy (Figure 1a, left).

Basic working principle of SMLM imaging

SMLM techniques achieve a higher resolution than conventional fluorescence microscopy methods by controlling the fluorescent emission of individual fluorophores. By a 'blinking signal' strategy, images of varying, small subsets of fluorophores can be acquired over time and the centroid of each, individual fluorescent signal can be localized at high precision to create detailed molecular maps and super-resolved SMLM images at the nanometer scale (Figure 1a, right).

Fluorophores for SMLM imaging

The most commonly used fluorophores in SMLM imaging are fluorescent proteins (FPs) and organic dyes. FPs offer the advantage of genetic labeling and consist of a β-barrel protein structure protecting the chromophore in its middle (Figure 1b, left). Organic dyes, on the other hand, usually offer higher fluorescence quantum yields than FPs and can be customized during their chemical synthesis, e.g. fine-tuning their spectral properties by a distinct delocalized π-electron system design and increasing their solubility and photostability by additional groups flanking the chromophore. Furthermore, their application is highly flexible as variable labeling groups can be added (Figure 1b, right).

Strategies in fluorophore photoswitching

Most critical in SMLM imaging is the tight control of fluorophore blinking in order to resolve individual fluorescent signals. In general, all SMLM methods can be categorized into reversible and irreversible blinking strategies (Figure 1c). For reversible blinking, two main strategies exist: fluorophores can either be imaged while reversibly binding and unbinding their targets (such as in Points Accumulation for Imaging in Nanoscale Topography (PAINT) microscopy [10]), or they can be photophysically or photochemically switched between a fluorescence-emitting and a dark state by specific light illumination and/or imaging buffers (such as in direct STochastic Optical Reconstruction Microscopy (dSTORM) [11] or by several Dark State Pumping and Recovery methods [12–16] (to which we, for simplicity, refer to by using the acronym DaStPuRe) (Figure 1c, left).

The second type of fluorophores (such as FPs used in photoactivated localization microscopy (PALM) [17]) is irreversibly photoactivated or -converted from a dark or initial fluorescent state of different color into a fluorescent state of desired read-out color (Figure 1c, right). The majority of irreversible photoactivating/converting fluorophores require UV-light illumination for changing their state. Nevertheless, recently, a novel mechanism called primed photoconversion was discovered where a special class of FPs was found to be photoconvertible via an intermediate dark state upon irradiation with less phototoxic blue and infra-red (IR) light [18,19]. Detailed reviews focusing on the photophysical and/or photochemical specifics to blink fluorophores in SMLM imaging can be found elsewhere [2,4–6].

Systematic review of multi-color SMLM studies conducted in microbes

Most studies introducing new multi-color SMLM tools are conducted in mammalian cell systems, as they contain defined and accessible nanostructures (such as cytoskeletal networks [20,21], clathrin-coated pits [22], nuclear pores [23,24] or the human glycine receptor [25]) to benchmark the tools (e.g. SMLM-suitable fluorophores such as in [2], table 2). Since a direct technology transfer to microbial targets—also from our own experience—often proves to be challenging, we compiled a systematic review of all multi-color SMLM work on microbial targets which are published to date and summarized them in Table 1 for bacteria and Table 2 for fungi. Furthermore, we assembled two visual collections of 'best-practice' examples: one for structural studies (Figure 2) and one for dynamic single-particle tracking (SPT) studies (Figure 3).

We use this systematic summary as a basis to discuss and compare the strengths, similarities and differences between current approaches and with respect to the inherent requirements for specific microorganisms. As one of the most crucial decisions when planning a new SMLM study is the choice of label and labeling technique

Biochemical Society Transactions (2019) **47** 1041–1065
https://doi.org/10.1042/BST20180399

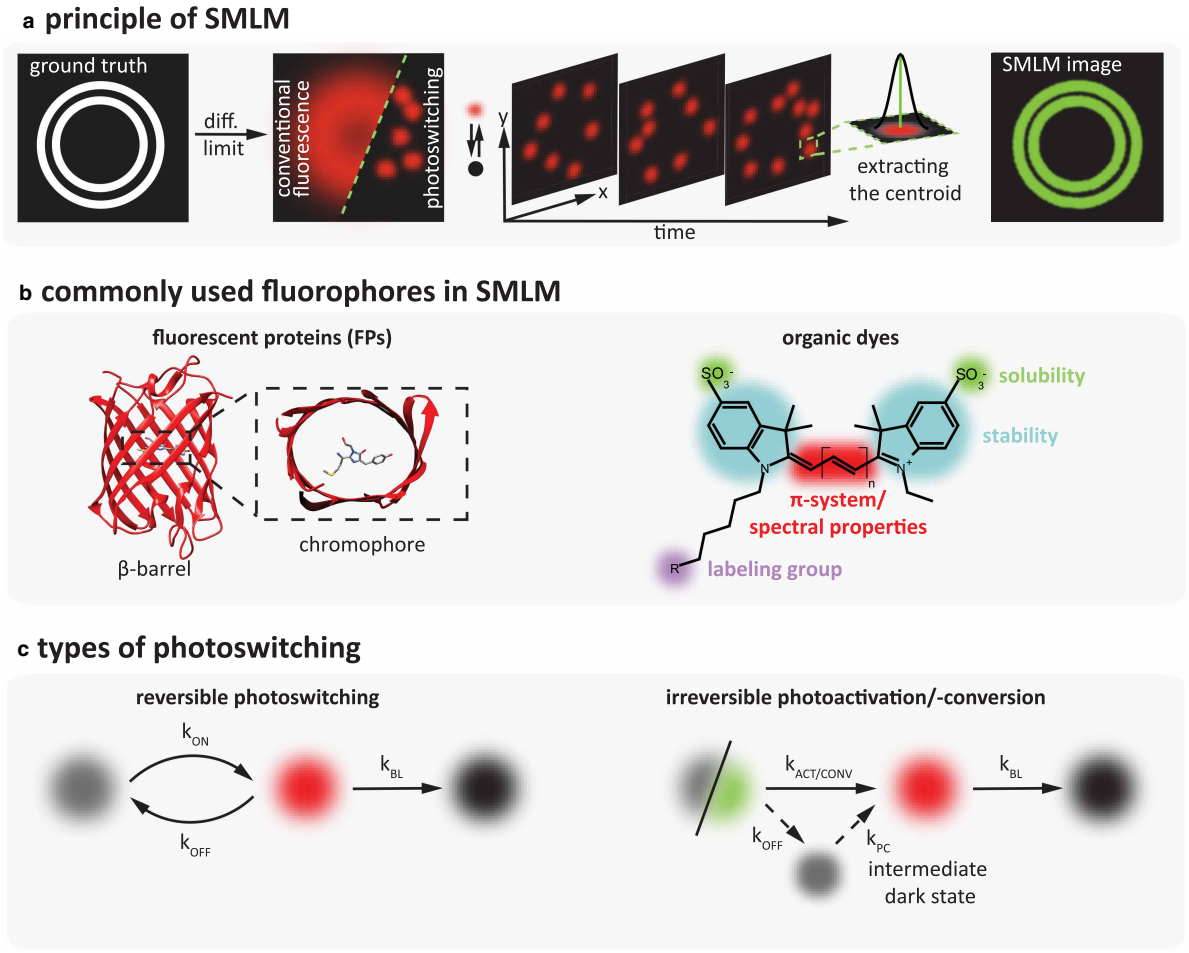

Figure 1. Principles of SMLM imaging.

(**a**) Schematic representing the basic working principle of SMLM imaging. The example ground truth of two rings is masked by diffraction in conventional fluorescence microscopy (left). The spatiotemporal separation of fluorophores by photoswitching allows to image only a subset (middle). After recording different subsets of fluorescent signals over time, their centroids are extracted and a super-resolved SMLM image can be reconstructed (right). (**b**) Commonly used fluorophores in SMLM imaging are FPs (left) and organic dyes (right). FPs consist of a β-barrel protein structure protecting a chromophore formed by three amino acid residues in its middle (left). Organic dyes are chemically synthesized to form a delocalized π-electron system (red) which, dependent on their design, can emit fluorescence at customized wavelengths (right). Additionally, the dyes are photostabilized and improved for solubility by structures flanking the chromophore. Due to variable labeling groups (violet), organic dyes can be used to specifically and flexibly label different target molecules. (**c**) Fluorophores in SMLM imaging need to possess a precisely controlled photoswitching mechanism. Some fluorophores are reversibly photoswitched between a dark state and a fluorescence emitting state (left). Here, the fluorophore either photoswitches back to the dark state or irreversibly photobleaches. Photoactivatable fluorophores irreversibly switch from a dark state to a fluorescent state by UV-light illumination, photoconvertible fluorophores switch from one fluorescent state to another (right). Certain photoconvertible fluorophores can, alternatively to the UV-light-mediated pathway, be transferred to an intermediate dark state by blue light to then subsequently convert into the fluorescent read-out state by IR light (primed photoconversion). In all cases, the fluorophores eventually photobleach.

and the available options are one of the most limiting factors in current study designs, we additionally compiled a figure introducing and explaining them for the different classes of biomolecules—proteins, carbohydrates, lipids and nucleotides—and discuss them along with our literature review below (Figure 4). The references in the caption of Figure 4b–d link the interested reader to original literature which uses those methods for targets in microorganisms.

Table 1 Multi-color SMLM studies conducted in bacteria

Part 1 of 3

	Organism	Live/ fixed	Probes	Biological target	Targeting method	Technique	Imaging routine	Ref.
Triple-colored SMLM	*Caulobacter crescentus*	Live	eYFP PAmCherry NileRed	CreS PopZ Cell membrane	Chromosomal ectopic addition Dynamic on-/off-binding	DaStPuRe PALM PAINT	Parallel read-out of eYFP and PAmCherry, NileRed was added and read-out after a full read-out of PAmCherry	[14]*
	Escherichia coli	Fixed	PAmCherry NileRed, R6G AF647	RNA polymerase Cell membrane DNA	Chromosomal replacement Dynamic on-/off-binding Supplied EdU, click chemistry	PALM PAINT dSTORM	Full read-out of PAmCherry, then NileRed was added and read-out, last DNA-incorporated EdU was stained with AF647 and read-out	[26]*
			PAmCherry NileRed AF647	OmpR Cell membrane DNA	Chromosomal ectopic addition Dynamic on-/off-binding Supplied EdU, click- chemistry	PALM PAINT dSTORM	Sequential read-out, see [26] above	[27]
			mEos3.2-A69T PAmCherry NileRed SYTOX Orange	RNA polymerase FtsZ Cell membrane DNA	Chromosomal replacement Plasmid Dynamic on-/off-binding Nucleic acid-binding dye	PC-PALM PALM PAINT Diff. limited	Sequential read-out: mEos3.2-A69T, PAmCherry, subsequent addition and read-out of NileRed and SYTOX Orange	[28]*
			JF503-Hoechst NileRed AF647	DNA Cell membrane Nascent DNA	Dynamic on-/off-binding Supplied EdU, click chemistry	PAINT dSTORM	DNA-incorporated EdU was stained with AF647 and read-out, subsequent addition and read-out of NileRed and JF503-Hoechst	[29]
			PAmCherry JF503-Hoechst Potomac Red	HisB, RNAP DNA Cell membrane	Chromosomal ectopic addition Dynamic on-/off-binding	PALM PAINT	Full read-out of PAmCherry, subsequent read-out of Potomac Red and JF503-Hoechst. PAINT dyes can be applied before imaging	
Dual-colored SMLM	*Bacteroides thetaiotaomicron*	Live	TMR AF488	SusG Maltoheptose, amylopectin	Protein tag, chromosomal replacement Supplied fluorescently labeled compounds	dSTORM	Parallel read-out	[30]
		Fixed	TMR AF488	SusG SusG, -D, -E, -F	Protein tag, chromosomal replacement Immunofluorescence			
	Caulobacter crescentus	Live	eYFP PAmCherry	ParB, ParA-G16V PopZ	Plasmid	DaStPuRe PALM	Alternating read-out in two channels	[31]
			eYFP NileRed, DCDHF-Tail	CreS Cell membrane	Chromosomal ectopic addition Dynamic on-/off-binding	DaStPuRe PAINT	Read-out of eYFP, addition and read-out of membrane-binding dye	[32]
		Fixed	eYFP PAmCherry	RNase E PopZ	Plasmid	DaStPuRe PALM	Parallel read-out	[12]*
			eYFP Rhodamine Spirolactam 9	RNase E cell surface	Plasmid Dynamic on-/off-binding	DaStPuRe PAINT		
	Escherichia coli	Live	Dronpa PAmCherry	ZapA, ZapB FtsZ, ZapA	Plasmid	PALM	Parallel read-out	[33]*
			mEos3.2-A69T PAmCherry	RNA polymerase FtsZ	Chromosomal replacement Plasmid	PC-sptPALM sptPALM	Sequential read-out: mEos3.2-A69T, then PAmCherry	[28]
		Live, fixed	PAmCherry AF647	RNA polymerase DNA	Chromosomal replacement Supplied EdU, click chemistry	sptPALM dSTORM	Read-out of PAmCherry, then fixation and labeling of DNA-incorporated EdU with AF647 followed by read-out	[26]
			GFP	Fis, ParB	Chromosomal ectopic addition; FROS: chromosomal ectopic addition of parS at ori/ter	Diff. limited	Sequential read-out of first GFP then subsequent addition of both NileRed and JF646-Hoechst and imaging	[29]*
			NileRed JF646-Hoechst	Cell membrane DNA	Dynamic on-/off-binding	PAINT		

Continued

Biochemical Society Transactions (2019) **47** 1041–1065
https://doi.org/10.1042/BST20180399

Biochemical Society Transactions (2019) **47** 1041–1065
https://doi.org/10.1042/BST20180399

Table 1 Multi-color SMLM studies conducted in bacteria Part 2 of 3

Organism	Live/ fixed	Probes	Biological target	Targeting method	Technique	Imaging routine	Ref.
	Fixed	PAmCherry NileRed	OmpR, RNA polymerase Cell membrane	Chromosomal ectopic addition (OmpR), replacement (RNAP) Dynamic on-/off-binding	PALM PAINT	Read-out of PAmCherry, then addition and imaging of NileRed	[27]
		AF647 AF568	SgrS ptsG mRNA	smFISH	dSTORM	Sequential read-out of AF647, then AF568	[34]
		ATTO655 TMR	FlgE FliO	Protein tag, chromosomal replacement	dSTORM	Parallel read-out	[35]*
		AF647, mEos3.2-N mEos3.2-C	EF-Tu MreB	Protein tag, plasmid Chromosomal replacement	dSTORM BiFC-PALM BiFC-PALM	Sequential read-out of AF647, then mEos3.2 mEos3.2-N-EF-Tu and MreB-mEos3.2-C can be used for live cell sptPALM of MreB-EF-Tu interactions	[36]
		mEos2 AF647	EF-Tu MreB	Chromosomal replacement Immunofluorescence	PALM dSTORM	Sequential read-out of AF647, then mEos2	
		AF647 AF488 Propidium iodide	FtsZ Cell surface DNA	Immunofluorescence Supplied fluorescently labeled WGA Nucleic acid-binding dye	dSTORM Diff. limited	Sequential read-out	[37]
		AF555 TOTO-3	FtsZ DNA	Immunofluorescence Nucleic acid-binding dye	dSTORM		
		JF503-/JF549-/ JF646-Hoechst Potomac Gold	DNA Cell membrane	Dynamic on-/off-binding	PAINT	Sequential addition and read-out of PAINT dyes	[29]
Salmonella typhimurium	Live	ATTO655 TMR-Star	CheZ CheY	Protein tag, plasmid	dSTORM	parallel read-out	[38]
	Fixed	TMR ATTO655	FliM FliC	Protein tag, chromosomal replacement Immunofluorescence	dSTORM	Sequential read-out of TMR and ATTO655, parallel read-out of TMR-Star and ATTO655/SiR	[39]
		ATTO655 TMR-Star	SpaS, FliN FliN, SpaS	Protein tag, chromosomal replacement			
		SiR TMR-Star	SiiF SiiC	Protein tag, plasmid			
		mEos3.2 AF647	PrgH, SpaO SipD	Chromosomal replacement immunofluorescence	PALM dSTORM	Sequential read-out of AF647, then mEos3.2	[40]*
Vibrio cholerae	Live	AF405-Cy5 Cy3-Cy5 DAPI	RbmC Vibrio polysaccharide DNA	Protein tag, chromosomal replacement Supplied fluorescently labeled WGA Nucleic acid-binding dye	STORM Diff. limited	Alternating activation of acceptor dyes (AF405 or Cy3) with a continuous read-out of receptor dye Cy5, then DAPI read-out	[41]*

Continued

Table 1 Multi-color SMLM studies conducted in bacteria

	Organism	Live/ fixed	Probes	Biological target	Targeting method	Technique	Imaging routine	Ref.
Single-colored SMLM + 1 diff. limited color	*Bacillus subtilis*	Live	SytoxGreen FM4-64 mMaple	DNA cell membrane SpoIIIE	Nucleic acid-binding dye Membrane-binding dye Chromosomal ectopic addition in ΔSpoIIIE strain	Diff. limited PALM	Sequential read-out of SytoxGreen, then Maple, last addition and read-out of FM4-64	[42]
			PAmCherry mCitrine	MutS DnaX	chromosomal replacement (MutS), ectopic addition (DnaX)	sptPALM Diff. limited	Sequential read-out of mCitrine and then PAmCherry	[43]*
			FM5-95 Dendra2, tdEos	cell membrane SpoIIIE	membrane-binding dye chromosomal replacement	Diff. limited PALM	Sequential read-out of FM5-95, then Dendra2 or tdEos	[44,45]
	Caulobacter crescentus	Live, fixed	eYFP CFP, mCherry	ParA ParB	Chromosomal ectopic addition	DaStPuRe Diff. limited	Read-out of mCherry/CFP spot, followed by a high laser illumination forcing most eYFP molecules into a dark state allowing to read-out single spots	[16]
	Escherichia coli	Live	eYFP mEos2	hdeA, hchA, lacZ genes H-NS	FROS: chromosomal ectopic addition of TetR-eYFP and TetO array next to targets Chromosomal replacement	Diff. limited PALM	Sequential read-out of mEos2 and eYFP	[46]
			PAmCherry Syto-16	UvrA, UvrB DNA	Chromosomal replacement Nucleic acid-binding dye	sptPALM Diff. limited	Sequential read-out of Syto-16, then PAmCherry	[47]*
			PAmCherry SytoxGreen	RNA polymerase DNA	chromosomal replacement Nucleic acid-binding dye	PALM Diff. limited	Sequential read-out of SytoxGreen, then PAmCherry	[48]
			PAmCherry GFP	lacO array malO array	FROS: chromosomal ectopic addition of 6× tandem lacO and lacI-PAmCherry FROS: chromosomal ectopic addition of 20× malO next to lacO array, MalI-GFP: plasmid	PALM Diff. limited	Sequential read-out of PAmCherry, then GFP	[49]*
		Fixed	AF647 YOYO-1	FtsZ DNA	Immunofluorescence Nucleic acid-binding dye	dSTORM Diff. limited	Sequential read-out of YOYO-1, then AF647	[50,51]
			mKate2 YPet	UmuC LacY	Chromosomal replacement Plasmid	Diff. limited DaStPuRe	Sequential read-out of mKate2, followed by a high laser illumination forcing most eYFP molecules into a dark state allowing to read-out single spots	[52]

The table is structured as follows (left to right): (1) number of (SMLM) colors used, (2) investigated microorganism in alphabetical order, (3) live, live/fixed or fixed study, (4) applied fluorophore combination sorted by sequential read-out order or excitation wavelength for parallel read-out, (5) biological targets, (6) targeting method; ectopic addition: an additional copy of the POI gene with tag sequence is introduced into the organism by chromosomal integration at another locus, replacement: fusion replaces the POI gene at original locus under the original promoter, (7) SMLM method; DaStPuRe: dark state pumping and recovery, illumination with high laser power forces the fluorophores into a dark state, (8) comments to imaging procedure, (9) references (* highlights studies that are represented in Figures 2 and 3).

Biochemical Society Transactions (2019) **47** 1041–1065
https://doi.org/10.1042/BST20180399

Biochemical Society Transactions (2019) **47** 1041–1065
https://doi.org/10.1042/BST20180399

Table 2 Multi-color SMLM studies conducted in fungi

Part 1 of 2

	Organism	Live/ fixed	Probes	Biological target	Targeting method	Technique	Imaging routine	Ref.
Dual-colored SMLM	*Saccharomyces cerevisiae*	Live	mKate2 YPet	Pil1 Sur7, Lyp1, Can1	Chromosomal replacement	DaStPuRe	A high laser illumination forces most mKate2 molecules into a dark state which allows to read-out single spots, then same procedure for YPet	[13]*
			mCardinal	Can1, Nha1, Pma1	Chromosomal replacement (Can1), plasmid (Can1, Nha1, Pma1)	SPT	First SPT using mCardinal, then YPet read-out as above	
			YPet	Sur7	Chromosomal replacement	DaStPuRe		
		Fixed	AF647	Cdc11	Chromosomal replacement (GFP fusion), immunofluorescence (anti-GFP nanobody)	dSTORM	Parallel spectral demixing read-out	[53]*
			AF700	α-linked mannose	Fluorescently labeled concanavalin A			
			AF647	α-linked mannose	Fluorescently labeled concanavalin A	dSTORM	Sequential (AF647 then tdEos) on a multifocus microscope	[54]*
			tdEos	α-tubulin	Chromosomal replacement (one of two α-tubulin genes of diploid)	PALM		
			AF647 AF750	Tub4 Tub1	mCherry (γ-tubulin) and GFP (α-tubulin) fusions, immunofluorescence (anti-GFP/ RFP nanobodies)	dSTORM	Parallel spectral demixing read-out	[55]
			AF647	Las17, Myo5	Protein tag, chromosomal replacement	dSTORM	Parallel read-out	[56]*
			mMaple	Sla2, Abp1, Las17	Chromosomal replacement	PALM		
			AF647	Sla2	Chromosomal replacement (GFP fusion), immunofluorescence (anti-GFP nanobody)	dSTORM		
			mMaple	Ede1	Chromosomal replacement	PALM		

Continued

Table 2 Multi-color SMLM studies conducted in fungi Part 2 of 2

	Organism	Live/ fixed	Probes	Biological target	Targeting method	Technique	Imaging routine	Ref.
	Schizosaccharomyces pombe	Live, fixed	Dendra2 PAmCherry DAPI	cbp1 cnp1 DNA	Chromosomal replacement Nucleic acid-binding dye	PC-sptPALM sptPALM Diff. limited	Sequential read-out of Dendra2, PAmCherry, then fixation, addition and read-out of DAPI	[28]*
		Fixed	mMaple3 ATTO647N	19 structural, 10 signaling contractile ring POIs, lifeact, Acyl Cell membrane	Chromosomal replacements (contractile ring proteins), plasmid (Acyl, lifeact) Fluorescently labeled mCling	PALM DaStPuRe	Sequential read-out of Atto647N and either AF488 (for both dyes, PALM-like read-out with 405 nm activation without imaging buffer was used) or one of the mMaple3 tagged ring components.	[15]
			AF488 ATTO647N	Actin Cell membrane	Fluorescently labeled phalloidin Fluorescently labeled mCling	DaStPuRe		
			mScarlet-I mEos3.2-A69T PAmCherry	sad1 spc25 cnp1	Chromosomal replacement	Diff. limited PC-PALM PALM	Full read-out of mScarlet-I, mEos3.2-A69T, then PAmCherry	Unpub#*
Single-colored SMLM + 1 diff. limited color	*Saccharomyces cerevisiae*	Fixed	mEos2 GFP	PI3P Chc1, Clc1, Vps21, Ypt7	Plasmid ([FYVE]$_2$ domain of EEA1 targeting PI3P) Plasmid	PALM Diff. limited	Sequential read-out of mEos2, then GFP	[57]
			mMaple GFP	Las17, Ede1, Pam1, Abp1 Abp1, Sla2, Rvs167	Chromosomal replacement Chromosomal replacement	PALM Diff. limited	Sequential read-out of mMaple, then GFP	[56]
	Ustilago maydis	Live	tdEosFP GFP	Num1 Tub1	Chromosomal replacement Chromosomal ectopic addition	PALM Diff. limited	Sequential read-out of GFP, then tdEosFP	[58]
		Fixed	tdEosFP GFP	Num1 Rab5a	Chromosomal replacement Chromosomal ectopic addition	PALM Diff. limited		
	Aspergillus nidulans	Live	mEosFPthermo GFP	TeaR tubA, SecC	Chromosomal ectopic addition	PALM Diff. limited	Parallel read-out	[59]

See the explanation of Table 1, #unpublished work from our group [60]. *highlights studies that are represented in Figures 2 and 3.

Biochemical Society Transactions (2019) **47** 1041–1065
https://doi.org/10.1042/BST20180399

Biochemical Society Transactions (2019) **47** 1041–1065
https://doi.org/10.1042/BST20180399

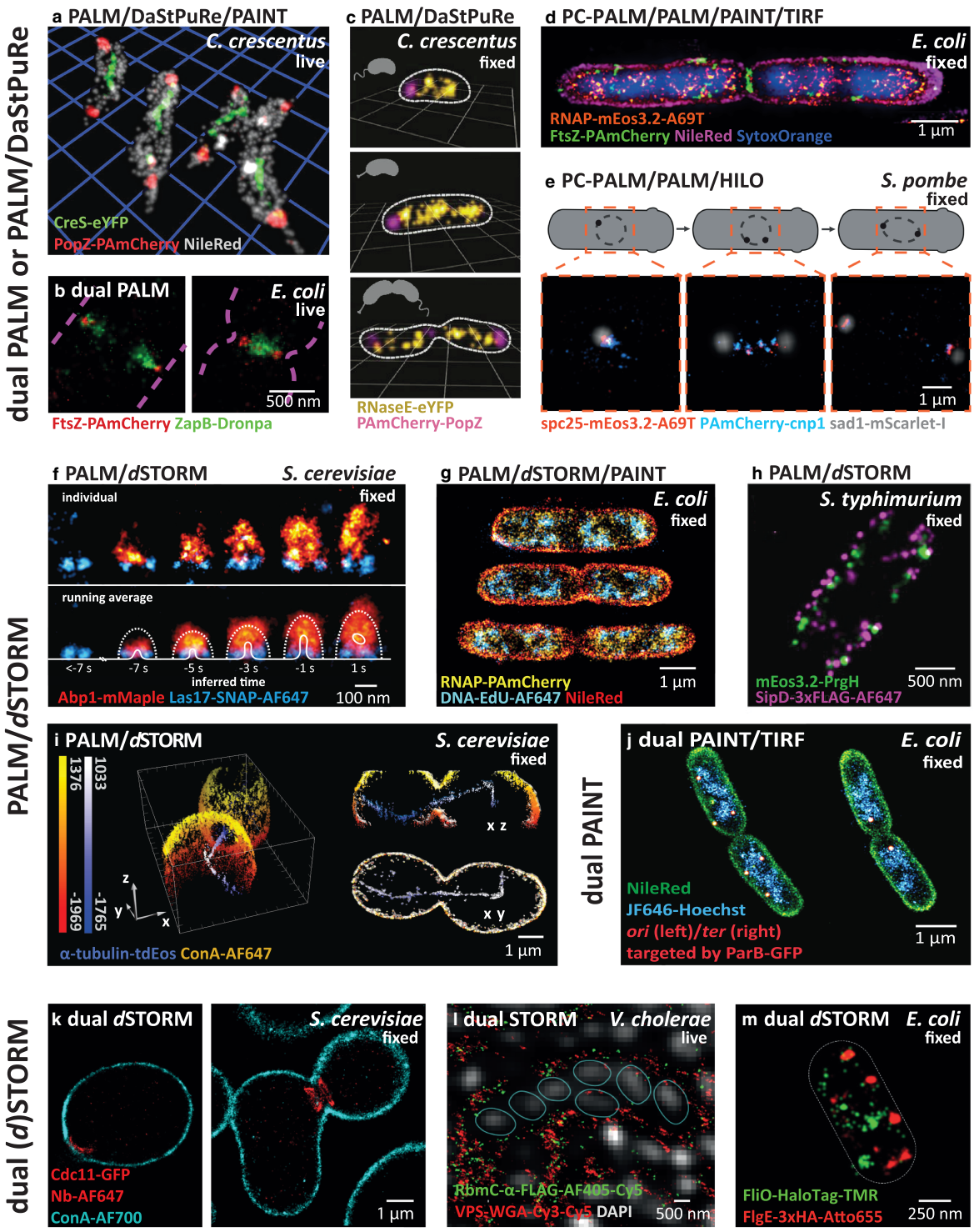

Figure 2. Examples of structural multi-color SMLM studies in microorganisms. Part 1 of 2

(**a**) Co-localization of filament-like fiber and pole-organizing protein structures in live *Caulobacter crescentus*. Grid segments: 1 µm adapted with permission from [14]. Copyright 2013 American Chemical Society, (**b**) Divisome elements during different cell cycle stages in live *E. coli* cells. Adapted from [33]. Copyright CC BY 4.0, (**c**) RNA degradosome and pole-organizing protein structures in fixed *C. crescentus* cells undergoing different cell cycle stages. Grid segments: 1 µm. Adapted from [12]. Copyright CC BY 4.0, (**d**) Co-localization of a transcriptome machinery compartment, a divisome element and the nucleoid in fixed *E. coli*. [28]. Copyright CC BY 4.0, (**e**) Spindle pole and kinetochore components during different cell cycle stages in

Biochemical Society Transactions (2019) **47** 1041–1065
https://doi.org/10.1042/BST20180399

Figure 2. Examples of structural multi-color SMLM studies in microorganisms. Part 2 of 2

fixed *Schizosaccharomyces pombe* (Unpublished work, [60]), (**f**) Endocytosis machinery compartments in fixed *S. cerevisiae* cells. Adapted from [56]. Copyright CC BY 4.0, (**g**) Transcriptome co-localized with nucleoid structure in fixed *E. coli*. © IOP Publishing. Adapted with permission from [26]. All rights reserved. (**h**) Type III protein secretion machinery compartments in fixed *Salmonella typhimurium*. Adapted from [40]. Copyright CC BY 4.0. (**i**) Yeast microtubules during cell division in fixed *S. cerevisiae*. Adapted from [54]. Copyright CC BY 4.0. (**j**) Nucleoid structure in fixed *E. coli* cells. Adapted from [29]. Copyright CC BY 4.0. (**k**) Septin ring component co-localized with the membrane in fixed *S. cerevisiae*. Adopted by permission from [53], (**l**) Extracellular polysaccharide and protein distributions in live *Vibrio cholerae* biofilms. Adapted from [41] with permission from AAAS. (**m**) Flagellar-specific type III secretion system components in fixed *E. coli*. Adapted from [35]. Copyright CC BY 4.0.

Multi-color microbial SMLM studies are still rare

At a first glance, our compilation demonstrates that multi-color SMLM work is still exceptional in microbiology as we count only 40 studies (Tables 1 and 2). Most multi-color studies either investigate only one target at high resolution accompanied by a diffraction-limited structural reference such as the nucleoid, cell membrane or a single-spot-forming protein cluster (15 studies, examples are Figure 3a–c[43,47,49]) or two targets at high resolution (20 studies, examples are Figures 2b,c,f,h–k,m and 3d,f [12,13,26,29,33,35,40,53,54,56]) also often supported by a reference (Figures 2e,l and 3e [28,41,60]). Three targets in SMLM resolution are rare (five studies, examples are Figure 2a,d,g [14,26,28]), and studies aiming at four or more targets are non-existent (to our knowledge).

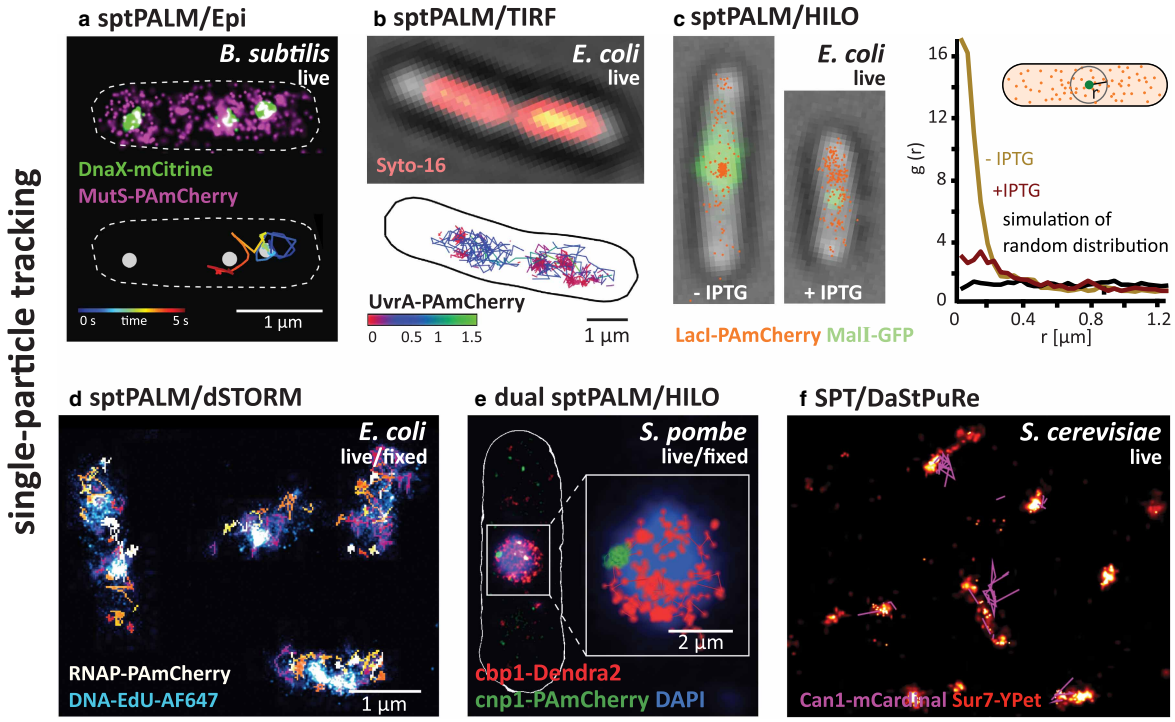

Figure 3. Examples of multi-color SPT studies in microorganisms.

(**a**) Co-localization of a DNA repair component and a DNA replication gene in live *B. subtilis*. Adapted from [43]. Copyright CC BY 4.0. (**b**) Nucleotide excision repair components in live *E. coli*. Adapted from [47]. Copyright CC BY 4.0. (**c**) Transcription factor distributions at specific gene locations in live *E. coli*. Adapted from [49]. Copyright CC BY 4.0., (**d**) Transcriptome co-localized with nucleoid structure in live *E. coli*. © IOP Publishing. Adapted with permission from [26]. All rights reserved. (**e**) Co-localization of centromeres and kinetochore-associated DNA binding proteins. Adapted from [28]. Copyright CC BY 4.0. (**f**) Membrane compartments and proteins in live *S. cerevisiae*. Adapted from [13]. Copyright CC BY 4.0.

Biochemical Society Transactions (2019) **47** 1041–1065
https://doi.org/10.1042/BST20180399

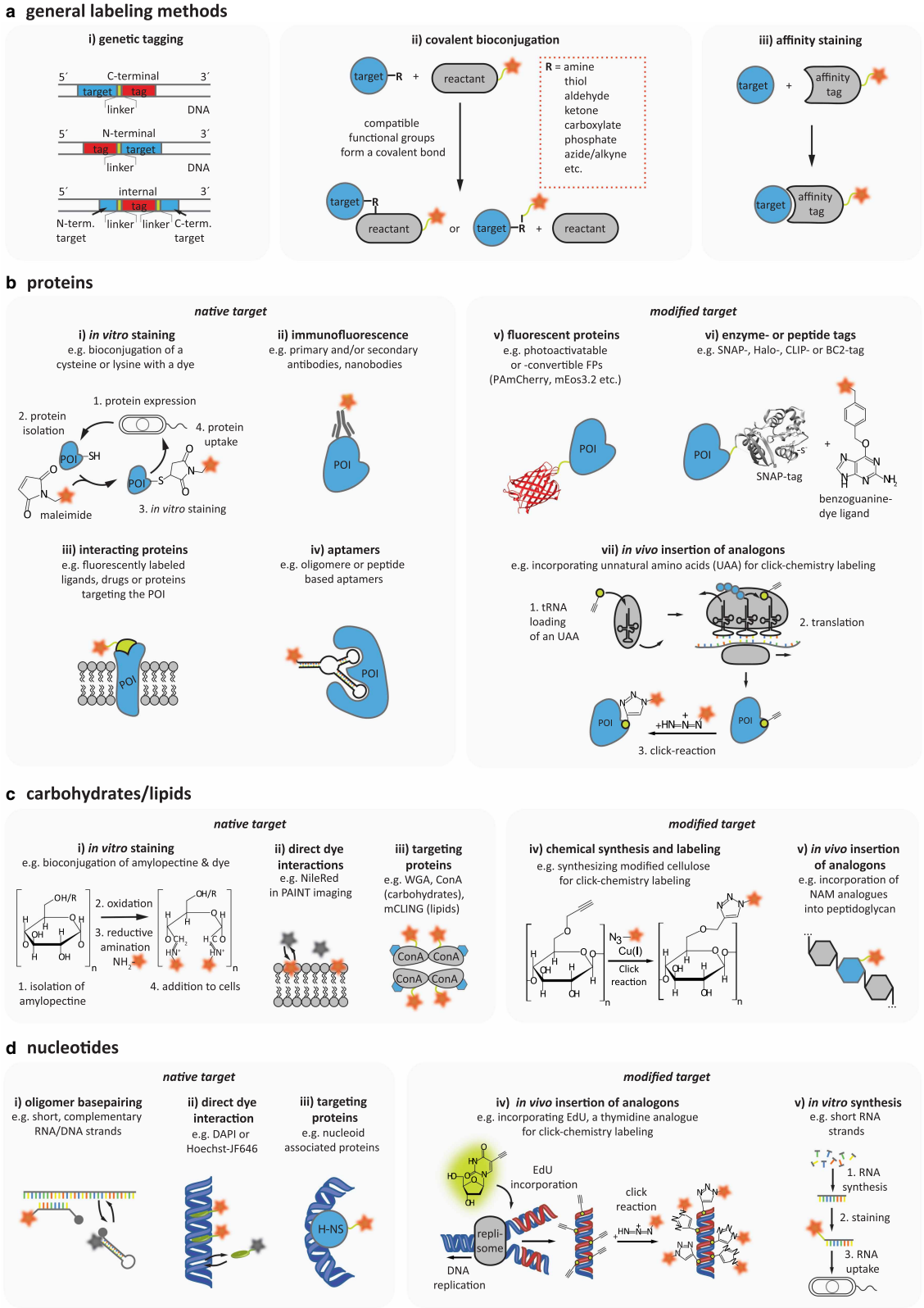

Figure 4. SMLM-suitable labeling methods targeting proteins, carbohydrates, lipids and nucleotides. Part 1 of 2

(**a**) Target molecules can be genetically modified (i) or stained by covalent bioconjugation (ii) or by affinity staining (iii). For genetic labeling, the chosen gene (blue) is extended by a tag sequence, e.g. encoding for an FP, enzyme- or peptide tag (red).

Biochemical Society Transactions (2019) **47** 1041–1065
https://doi.org/10.1042/BST20180399

Figure 4. SMLM-suitable labeling methods targeting proteins, carbohydrates, lipids and nucleotides. Part 2 of 2

It can be inserted at the 3′- or 5′-end or directly into the target sequence, e.g. replacing or extending an internal loop structure. In each case, a small linker sequence (green) is inserted in between to ensure the undisturbed biological function of the target protein (i). For labeling a molecule by covalent bioconjugation, a functional group (e.g. amines, thiols, etc.) of the target is exploited for forming a covalent bond with a fluorescently labeled reactant (ii). Molecules can also be targeted using fluorescently labeled affinity tags which bind them by van der Waals bonds or ionic attractions (iii). (**b**) Native POIs (blue) are either stained *in vitro* after their expression and isolation before being taken up again into cells [61,62] or *in situ* by adding a fluorescently labeled interacting compound, e.g. by immunofluorescence using anti- or nanobodies [36,37,39,40,50,51,53,56] (ii), by fluorescently labeled ligands, drug molecules or targeting proteins [15] (iii) or by aptamers (iv). Furthermore, the POI can be modified, either by a FP (v, PAmCherry (pdb 3KCT)) [13,14,28,40,43,58,59] or by an enzyme/peptide tag (vi, SNAP (pdb 3L00)) [21,30,35,36,38,39,41,56,63] or by insertion of an unnatural amino acid into the primary structure of the protein (vii), which after protein folding is coupled to a dye by a click chemistry reaction [64,65]. (**c**) Staining of native carbohydrates or lipids can be facilitated in a similar fashion as for proteins. In vitro staining is showcased using isolated amylopectin [30] (i). Furthermore, specific lipophilic, fluorogenic dyes can directly visualize the native membrane by reversible on- and off-binding in PAINT microscopy (ii) [14,26,28,29,42]. Also carbohydrates-targeting proteins like WGA and ConA or lipid-targeting probes like mCLING or FYVE can be used (iii) [15,37,41,53,54,57]. Synthetic carbohydrates or lipids can be customized *in vitro* (iv). Finally, also analogues of native building blocks can be inserted into newly synthesizing polymers *in vivo* (v) [66]. (**d**) Specific nucleotide sequences are labeled by single-molecule fluorescence *in situ* hybridization (smFISH) using short, complementary DNA/RNA oligomers (often designed as fluorogenic hairpins in a fluorophore–quencher combination) (i) [34]. DNA, in general, can be either visualized by the reversible on- and off-binding of fluorogenic DNA intercalator-dye constructs using DNA-PAINT (ii) [29] or by nuclear-associated proteins decorating it (iii) [46]. A method to label nascent DNA is by incorporation of the alkyne-modified thymidine analog EdU during DNA replication combined with subsequent click labeling (v) [26,27,29]. Short oligomers can also be synthesized and stained *in vitro* to then be transferred into cells, e.g. by electroporation [67,68].

Most studies investigate microbial model organisms

The vast majority was conducted in bacteria (30 studies with 18 studies at least dual color and 12 studies single-color SMLM imaging plus a diffraction-limited reference, Table 1), with the model organism *Escherichia coli* having the biggest share (13 studies). In contrast, only 12 studies focused on fungi biology (eight at least dual color, four are single-color plus reference, Table 2), among which the studies on *Saccharomyces cerevisiae* dominated by number (seven studies).

In general, for both fungi and bacteria, the great majority of studies is conducted in model organisms where laboratory cultivation techniques are well established and for which a large number of tools, e.g. genetic manipulation strategies have been developed. Multi-color SMLM studies under more complex culturing conditions (e.g. under medical relevant conditions or using non-model strains and exploring, e.g. biofilms or co-cultures like the human microbiome) are scarce (Figure 2l) [30,41].

Structural multi-color SMLM studies are established whereas SPT studies are rare

Furthermore, the studies are largely focusing on structural SMLM imaging exploring spatial molecular organizations (126 targets in total), mostly conducted in chemically fixed cells (102 fixed versus 24 live targets, Figure 2 and Tables 1 and 2). Multi-color SPT studies are rare (eight targets in total, Figure 3 and Tables 1 and 2). These SPT studies investigating molecular interactions were mostly conducted using single-color sptPALM accompanied by a diffraction-limited reference [43,47] and in one case super-resolving the nucleosome via dSTORM [26]. Investigating the dynamics of two targets was conducted by either orthogonal photoactivation modes in a subsequent manner [28] or bimolecular fluorescence complementation-PALM (BiFC-PALM), where two biological targets were each labeled with one component of a split FP [36].

Most studies record the different targets sequentially in time

Reviewing the imaging routines, fluorophore combinations were either imaged in parallel by splitting the signals of appropriate fluorophore pairs onto two areas of the camera chip (14 studies), or more commonly in a sequential imaging mode using the same detection path (28 studies). For the latter, also fluorophores of similar emission spectra can be used when separating them either by different photoactivation/conversion modes [28] or by sequential addition or exchange of probes (e.g. sequentially added dyes for PAINT imaging

[26–28] or 5-ethynyl-2′-deoxyuridine (EdU) staining of DNA [26,27]. For both methods, this brings the advantage of avoiding chromatic aberrations. When adding fluorophores sequentially, a position-stabilizing autofocus system or a robust position-refinding routine (by, e.g., re-recognizing unique landmarks) is required.

Among the diverse labeling options, genetic labeling, in particular, FP fusions, are dominant

A successful experimental multi-color design needs a thought-out choice of fluorophore combinations and labeling methods. Well-established genetic tools (Figure 4a(i)), which include powerful methods like exploiting the microbes' own homologous repair mechanism for chromosomal recombinant replacements of native target genes, exist for most model microorganisms [69]. Also, while being densely packed into the small microbial volume, absolute copy numbers of microbial protein of interests (POIs) can be rather low [70] which demands for highly specific labeling approaches. Performing statistics on all published studies summarized in Tables 1 and 2, it is thus not surprising that chromosomal tags were used for 90 out of 154 targets, 72 of which as recombinant replacements at the original locus under the original promoter and 15 as ectopic additional copies, integrated into the chromosome at another locus. These are FP fusions to a large extent (77 POIs, Figure 4b(v)) with only a minor portion of protein tags (10 chromosomal replacements, Figure 4b(vi)) and fluorescent repressor–operator system (FROS) arrays (4 ectopic additions). Additional 22 genetic fusions were introduced into the cells by plasmids carrying recombinant genes. Other targeting methods are only seldom applied: We find 14 immunofluorescence stainings (10 antibody stainings targeting native epitopes and 4 anti-GFP/-RFP nanobody probes, Figure 4a(iii) and b(ii)), 17 uses of on- and off-binding PAINT probes (Figure 4c(ii) and d(ii)), and 12 incubations with target-specific and fluorescently labeled compounds (Figure 4a(ii), b(ii–iv), c(i–iii), d(i–iii)). For the latter, various labeling methods were used, such as (1) *in vitro*-labeled compounds (e.g. *in vitro*-labeled carbohydrates specific for the cell wall (Figure 4c(i)) [30], target-specific drugs like WGA [37,41] and concanavalin A (Figure 4c(iii)) [53,54], actin-binding phalloidin or lifeact (Figure 4b(iii)) [15] or smFISH oligonucleotides (Figure 4d(i)) [34]), (2) target-binding fluorophores (e.g. TOTO-3 targeting DNA (Figure 4d(ii)) [37]), and (3) analogs carrying, e.g. alkene or azide groups that can be stained by click chemistry approaches afterwards (Figure 4b(ii,v), c(iv), d(iv)). For the latter, the most often used one is the thymidine analog EdU incorporating into nascent DNA (Figure 4d(iv)) [26,27,29]).

Either the DsRed-derived FP PAmCherry or an FP from the Kaede family are part of almost every multi-color labeling strategy

Turning the perspective to the selected molecules of interest, FPs strongly dominate the chosen combinations when imaging protein targets. Here, PAmCherry fulfills a special role: it is the only commonly applied photoactivatable FP of the DsRed family [5]. These photoactivatable FPs photoactivate from an initial dark, premature chromophore state into their fluorescent state in the 'red' part of the visible spectrum (~580–660 nm wavelength range). In a multi-color experiment, PAmCherry thus stands out from the RFPs from the Kaede family (e.g. mEos2 or 3, Dendra2 or mMaple(3)) as these green-to-red photoconverting FPs fluoresce in the 'green' part of the visible spectrum (~490–560 nm wavelength range) in their initial GFP-like form [5]. This makes PAmCherry an almost obligatory choice for (1) green/red dual FP pairings (being either paired with eYFP (Figure 2a,c) [12,14,31] or Dronpa (Figure 2b) [33]) and for (2) dual red FP pairings which are separated by orthogonal illumination modes when photoactivating PAmCherry by UV-light and photoconverting a FP from the Kaede family by primed photoconversion (only possible for threonine 69 variants [18], e.g. using mEos3.2-A69T (Figure 2d,e) [28,60], or Dendra2 (Figure 3e) [28]).

Another commonly used combination is far-red (~650–730 nm wavelength range) dyes together with red FPs (10 studies). Here both PAmCherry and the Kaede-like proteins are equally popular choices as the green spectral channel can be neglected (Figures 2f,g,h,i and 3d). The choice of the far-red dye is dominated by AF647—also incredibly popular in single-color dSTORM experiments (see [2], table 2)—and leads to a remarkable count of 9 out of 10 studies (examples in Figures 2f,g,h,i,k and 3d).

Target biomolecules other than proteins are mainly imaged by dSTORM and PAINT techniques

Cellular components other than proteins are usually reliant on non-genetic targeting tools and thus are mostly investigated by dSTORM and PAINT studies. In case of dual dSTORM experiments relying on organic

Biochemical Society Transactions (2019) **47** 1041–1065
https://doi.org/10.1042/BST20180399

dyes, it becomes apparent that the membrane-permeable, spectrally distinct red/far-red dye combination TMR (-Star)/ATTO655 (Figure 2m, four out of six red/far-red pairings [35,38,39]) were preferred over AF647 paired with spectrally close dyes in a spectral demixing imaging mode (AF700 (Figure 2k) [53] or AF750 [55]) or green/red [30], green/far-red [15,37] or STORM activator/acceptor (Figure 2l) [41] dye combinations.

SMLM visualization of the cell membrane was mainly conducted by using the dynamic on- and off-binding of NileRed for PAINT imaging (8 out of 17 studies of the cell membrane, Figures 2a,d,j,g and 4c(ii)[14,26–29,32]), while labeling of DNA was performed using either (a) transiently binding dyes (e.g. JF646-/JF549- or JF503-Hoechst (Figures 2j and 4d(ii)) [29], (b) EdU stainings with AF647 (Figures 2g, 3d and 4d(iv)) [26,27], (c) blinking intercalator TOTO-3 (Figure 4d(ii)) [37]) or (d) diffraction-limited fluorescent probes (DAPI (Figures 2l and 3e) [28,41], Sytox Green [42,48] or Orange (Figure 2d) [28], Syto-16 (Figure 3b) [47] or propidium iodide [37]). The most popular diffraction-limited reference is DNA (nine times), while the co-imaged SMLM probe in most cases was a red FP (seven times, out of which four times PAmCherry was chosen [28,47,48]). One study combined membrane and DNA probes for dual-PAINT, accompanied by either a FROS array spot or a PAmCherry-labeled POI (Figure 2j) [29].

For the few triple-color studies, until now dual-FP/PAINT (Figure 2a,d) [14,28], dual-PAINT/PALM [29] or PALM/PAINT/dSTORM (Figure 2g) [26,27] approaches were established.

Design of a multi-color SMLM experiment investigating microbial cell biology

Based on our observations while comparing the 40 publications applying multi-color SMLM studies in microbiology, we compiled a best practice guideline (Figure 5a and Table 3). Whereas the rationale behind this guideline can be generally used to design multi-color SMLM experiments for any organism, our examples are focused on studying microbes. Importantly, single-molecule imaging and tracking methods can yield a manifold of detailed answers about individual molecules and their interactions at a high spatiotemporal resolution *in situ*, but they are not every-samples techniques. Experimental factors such as single-molecule sensitivity beyond (low) background, tight photoswitching control of fluorophores or reliable corrections for drift and chromatic aberrations are strong determinants for image quality. Achieving good results for several channels in multi-color imaging is multiplying the overall efforts to be undertaken. To further illustrate our general scheme, we thus as well added a practical example of study design based on our own experience (Figure 5b).

Formulating the biological question

First of all, it is worthwhile to invest a lot of resources into the study's design and to precisely formulate and specify the biological question one aims to answer. This entails a profound knowledge of the underlying biological system and often goes in hand with a strong hypothesis about observations to be expected (Figure 5a, upper box). It should be clear whether the observation of a structure and/or the dynamics of how many targeted molecules leads to a relevant investigation and which spatiotemporal resolution is required to acquire the data aimed for (Figure 5a, TASK 1 and 2).

Here, a higher temporal resolution or measuring the axial position often goes hand in hand with the trade-off of a lowered lateral spatial resolution due to lowered signal-to-noise (S/N) ratio of individual single-molecule fluorescence [1]. Often, one can already 'guestimate' from the target characteristics and its cellular environment where some technical hurdles might appear, e.g. thick cell walls might hinder staining, low pH, e.g. in the periplasm, lowers fluorescence read-out or colorful microbial pigments (e.g. carotenoids, melanins or flavins [73]) can superpose fluorescence in certain spectral ranges. In cases where both target protein termini are functional domains (as often encountered for membrane receptors), genetic tagging of either of them will most likely interfere with the proteins' biology. In such cases, internal loop structures could be a better-suited spot for recombinant fusions, as has been done for, e.g., MreB in *E. coli* [74–76].

Furthermore, reflecting target abundances, their replenishment and accessibility can be of large importance: Is a native expression from the native gene locus possible and favorable (e.g. for measuring stoichiometry and cellular organization) or is an ectopic expression better suited for the planned investigation (e.g. exploring the DNA binding affinities of proteins in large statistics facilitated by overexpression and irrespective of their native copy number)? Is the time of POI folding or POI lifetime known? Too fast protein turn-over can prevent the use of FPs due to their typically rather long maturation time needed to properly arrange their chromophore and thus their ability to fluoresce [77,78]. In case of low molecular abundances or co-localization studies of

Biochemical Society Transactions (2019) **47** 1041–1065
https://doi.org/10.1042/BST20180399

Figure 5. Guideline for designing a multi-color SMLM experiment. Part 1 of 2

(**a**) General scheme. For a successful study design, first, the biological specifications have to be determined (upper box). For this, the general biological research question needs to be translated into specific targets and measures (TASK 1). By answering

Biochemical Society Transactions (2019) **47** 1041–1065
https://doi.org/10.1042/BST20180399

Figure 5. Guideline for designing a multi-color SMLM experiment. Part 2 of 2

several target- and organism/system-related questions (TASK 2), possible measurement strategies can be identified (TASK 2) and the targets can be arranged into groups based on their imaging priority (TASK 3). If no solution can be found, the choice of measures and/or targets should be reassessed by repeating TASK 1. After a successful target grouping, the technical study design can be approached (lower box). First, a suitable fluorophore–label combination should be chosen for each target in the group, taking limitations set by groups with higher priority or setup limitations into account (TASK 4). If multiple strategies seem possible, they can be ranked based on their applicability and can be readjusted if initial test experiments show major obstacles. If none of the options yields a suitable experimental strategy, the choice of measures and/or targets has to be reassessed by repeating TASK 1. After a successful proof of principle experiment, the biological study can be started. (**b**) Practical example. To illustrate the general scheme, we added an example based on our own experience. Here, our interest in investigating the kinetochore architecture of the fission yeast *S. pombe*, a multi-protein complex linking microtubules and centromeric DNA during mitosis, led us to a triple-color imaging strategy as depicted in Figure 2e. Specifically, our aim was to measure protein copy numbers as well as cluster distances of POIs in the kinetochore to build a molecular kinetochore map (TASK 1). Aside from labeling each POI, we thus needed a reference to identify cells in meta- to anaphase A as well as the orientation of the mitotic spindle and a centromeric reference serving as a landmark for kinetochore assembly in relation to the POIs. Therefore, we planned a triple-color strain library in which each strain contained the same two labeled reference proteins and a varying POI: As the reference proteins should have sufficient abundance, a defined organization and be present throughout the cell cycle, this led us to choose sad1, a protein from the spindle pole body (SPB) and the centromere-specific histone protein cnp1 (TASK 2) as references. From our imaging priority (TASK 3) and a mix of literature knowledge, a priori experience and several test strains and experiments we could deduce several measurement strategies solely relying on FPs (TASK 4), excluding blue and green fluorophores, some self-aggregating FPs as well as labeling strategies based on extrinsic labels or showing decreased S/N ratio or cross-talk problems (TASK 5). In our final, experimental study (manuscript in preparation) we use mScarlet-I [71], a bright red FP for the SPB reference and the UV-photoactivatable FP PAmCherry [72] as centromeric reference. Our highest priority on quantitative read-out of the POIs led us to choose the primed photoconvertible FP mEos3.2-A69T as POI-label [18,28].

several partners, highly efficient and specific labeling becomes a key factor. For example, two interaction partners, both labeled with a realistic efficiency of 50% would yield at best—when forming a permanent, static complex—only maximal 25% of positive co-localization (here we think of co-localization in an SMLM-specific definition of molecules being co-localized within an 'interaction radius' that takes localization precision and post-processing errors, labeling linkage distances, protein sizes and position of label attachment into account [79,80]). This observed co-localization of molecular partners easily drops further, e.g. for dynamic on/off-binding interaction equilibria dependent on different molecular conformations or when being misled by unspecific staining artifacts or lowered by slow FP maturation times. Here, counteractive knowledge on how to accumulate or arrest target molecules in certain molecular states by environmental changes (e.g. pH, temperature and nutrition), specific drug treatments (e.g. antibiotics compromising transcription, replication and cell wall organization) or by protein mutation might help the experiment. Additionally, target density easily restricts label choices. A clustered target in dense substructures demands for a high spatial resolution and tighter control of fluorophore read-out. Clustered targets can also be more challenging to label due to steric hindrances or label-dependent artificial aggregation artifacts as compared with an evenly distributed target within the cytoplasm [21,78,81–83].

When imaging living microorganisms, the shortest possible and least disturbing read-out option is desirable to avoid an excess of phototoxicity effects or changes in observed biology, e.g., the sensitivity of the investigated organism for specific wavelengths should be tested. Fast dynamics (e.g. free cytosolic Brownian diffusion or fast active transport) need a high temporal sampling to be resolved and to avoid confinement effects of the small microbial volumes. Contrarily, POIs slowed down by interactions with other cellular components (e.g. nucleoid-associated proteins or larger protein complexes) or by the viscosity of a certain compartment (e.g. in the membrane) allow for higher spatial resolution by the improved S/N of fluorescence read-out of slower acquisitions. Thus, it remains challenging but important to identify suitable sampling rates and read-out densities to correctly separate overlapping trajectories, to avoid confinement effects and to ensure being faster in read-out than biological alterations.

Transferring all mentioned requirements that can interfere with each other as best as possible into a practical experimental plan (Figure 5a, TASK 3) is the crucial key for a successful single-molecule sensitive microscopic

Biochemical Society Transactions (2019) **47** 1041–1065
https://doi.org/10.1042/BST20180399

Table 3 Important factors to consider for a successful SMLM experiment Part 1 of 3

Labeling considerations	
Type of fluorophore	- **Control wild-type strain for specific autofluorescence in different spectral read-out channels** - **Evaluate the illumination intensities for different wavelengths for your specific organism. Which wavelengths and doses are tolerated, what are signs of phototoxicity? Generally, fluorophores of long wavelength and with low level of ROS production are favorable** - ***Evaluate your targets applicable orthogonal multi-targeting methods which go alongside with some fluorophore choices, e.g. FP utility depends on biologically undisturbed genetic fusions, dyes are extrinsic labels which are often not membrane-permeable and thus often need fixation protocols, etc.*** Signal detection at longer wavelengths typically improves S/N ratio, lowers phototoxicity and increases maximal imaging depth - ***Check for fluorophore-pair photophysics, e.g. brightness, bleaching rate, reversible blinking rates, preferably in the environment of your organism; check dye pairs for compatible switching buffers*** - Check FPs for compatible maturation times (e.g. faster than POI replenishment) and possible oligomerization tendencies (commonly dependent on POI abundance and density)
Functionality controls	- Control for biological function and localization of POIs by growth and functionality assays, western blot, tagging of POI by different fluorophore tags, C- or N-terminal or in-loop tagging variants, etc. - **Minor growth and functionality deficiencies might be compensated for by slower growth at lower temperatures**
Sample preparation	
Growth	- Use transparent, defined, sterile filtered medium to avoid background. If possible, avoid fluorescent supplements in medium - **Harvest cells in exponential growth phase, not in stationary phase** - **The optimal temperature for growth is not necessarily the optimal temperature for imaging, growth at lower temperatures might lead to less background in cells (but needs additional assays controlling for altered functionality)**
Ectopic induction of POI	- **Prepare fresh inducer stock from powder to avoid degradation effects ensuring reproducible induction conditions** - **Use only minimal concentrations of inducer (typically only a fraction of amounts from standard protocols) as overexpression of POI might cause high background fluorescence, inclusion bodies, aggregates or phenotype artifacts** - **After induction, allow for sufficient FP maturation time before imaging**
Fixation	- Optimal fixation conditions are target-, fluorophore- and organism-dependent. In general, fixation with 1–4% formaldehyde (final concentration) for 15–30 min is a good start. Addition of 0.05%–1% glutaraldehyde (final concentration) can improve the fixation results. Alternatively, also ice-cold methanol fixation can be tested - To quench excess formaldehyde, the first washing step with PBS should contain sodium borohydride or ammonium chloride - Several washing steps are needed to remove all excess formaldehyde - Carefully check if the fluorescence of the label or the spatial organization of your target is impaired by fixation
Staining	- Charge and size of dyes can lead to unspecific or insufficient staining - Blocking with neutral or charge masking compounds and/or intense washing with buffers containing higher salt concentrations (>100 mM) and low concentrations of detergent might reduce unspecific staining - Cell membrane permeabilization and **cell wall digestion improves staining** - **Prolonged staining combined with low (up to 1000-fold lower than conventional immunofluorescence) covalent dye/label concentrations can improve S/N ratio** - Use only minimal dye concentrations for live cell staining by electroporation/membrane-permeable dyes to avoid remaining free dyes - Perform a control staining of a sample without the target epitope to evaluate the degree of non-specific staining
Post-fixation	- For non-covalent labels with fixable groups, a finalizing post-fixation step following staining and washing prevents detachment of labels over time, which can be caused by the addition of thiol-containing imaging buffers
Cover glass slides	- Use high-precision cover glasses with defined thickness and matching the specifications of your objective - Clean thoroughly, prepare fresh - **For agarose pads, use high purity grade low gelling agarose to minimize heat degradation effects of the media which causes background and growth impairments**

Continued

Biochemical Society Transactions (2019) **47** 1041–1065
https://doi.org/10.1042/BST20180399

Table 3 Important factors to consider for a successful SMLM experiment Part 2 of 3

	- **For multi-well cover glasses, immobilize sample firmly onto a cover glass surface using poly-L-lysine (or organism-specific substances, e.g. ConA for targeting the α-linked mannose residues of the *S. cerevisiae* polysaccharides)**
General buffers	- Use high-quality chemicals with high purity grade for minimizing contaminants causing background - Prepare fresh and sterile filtered buffers - Use buffer with high salt concentration to wash out unwanted fluorescence (e.g. fluorescent metabolites, free fluorophores)
Fiducial markers	- Sonicate thoroughly prior to loading onto the sample to avoid fiducial aggregates - Adjust concentration to a density of at least three fiducials in focus in a typical ROI - Match fiducial brightness with sample brightness to prevent superposing the single-molecule signals during imaging - ***For imaging in two parallel channels: calibration slide (e.g. a fine spatial grid) of multi-colored fiducials for channel overlay***
Storage	- Check if sample quality (sample appearance, S/N and photoswitching efficiencies) is preserved after (long-term) storage at 4°C - Addition of sodium azide to fixed samples prevents the growth of contaminants
Imaging conditions	
Laser power	- Control laser power post-objective before each experiment - Adjust laser power (e.g. activation illuminations) for constant fluorophore blinking at sufficiently low density - Check for fluorophore bleaching
Illumination mode	- Laser power and background in the target plane change with applied imaging mode (epifluorescence, light sheet, HILO, TIRF) - Pulsing of the photoactivating lasers can reduce possible phototoxicity and offers temporal control for fluorophore activation
Switching buffers	- Quality demands as for general buffers above - ***Switching buffers have to be adjusted to both dyes of the selected dye combination*** - pH or redox components influence fluorophore switching behavior - Apply oxygen removing buffers directly before imaging and tightly seal the sample to prevent uptake of new atmospheric oxygen - Replace buffer regularly as enzymatic buffer exhaust themselves over time and might cause pH changes (e.g. GLOX buffer drops pH)
Imaging conditions and parameters	- Use appropriate immersion oil for your objective and avoid air bubbles in the oil - If implemented, use a focus-stabilizing system to avoid *z*-drift - ***Image fluorophores with excitation maxima at longer wavelengths first to avoid photobleaching and cross-talk*** - Camera frame rate should be fast enough to temporally resolve the molecule of interest kinetics - For structural studies, single fluorophore blinks should be recorded in only a few camera frames for maximal S/N - For 3D read-out: match the spatial resolution needed to answer your biological question with a compatible 3D technique. Read-out range and sensitivity is different for each 3D method
Imaging controls	- Negative: to check autofluorescence/background in all spectral channels used, a wild-type strain, a without correct epitope stained sample, for drug studies check non-treated strains - Positive: easy-to-image "standard strain" to control for stable setup configuration and thus constant read-out quality (S/N, photoswitching efficiencies) and to check for proper sample preparations. - Check for phototoxicity effects in live cell studies - **When imaging dynamics: prepare controls for (i) the freely diffusive cytosolic fluorophore(s) used as labels to benchmark the purely diffusive signal distribution (e.g. for confinement effects of small microbial volumes, possible inclusion bodies for overexpression) and (ii) a fixed control to access the immobile signal distribution (where the apparent movement is only determined by the acquired localization precision)**

Continued

Biochemical Society Transactions (2019) **47** 1041–1065
https://doi.org/10.1042/BST20180399

Table 3 Important factors to consider for a successful SMLM experiment Part 3 of 3

Post-processing prior data analysis	
Localization routine	- Check if the chosen localization algorithm fits fluorescent spots reliably - Determine the experimentally achieved localization precision - Check for fluorophore recall rates and false positives
Drift correction	- Use fiducial markers to correct for *x*–*y*-drift (by bead traces or cross-correlation) or apply cross-correlation on the target directly if possible (needs high fluorophore densities per frame, typically only possible for large ROIs and samples with highly abundant target molecule)
Channel alignment	- ***Parallel read-out: use a dense, ideally fine spatial grid as calibration sample for channel alignment before your experiment*** - ***For sequential read-out in the same spectral channel, fiducial markers are sufficient to overlay the image sequences***
Visualization	- Choose a visualization reflecting your achieved resolution to avoid interpretation errors (in co-localization, clustering analysis, etc.) - Choose a visualization with well-adjusted intensity scaling to mimic real fluorescence images one is used to
Data analysis	
Counting	- Characterize and quantify for over- and undercounting bias/error in your measurements
Clustering	- Optimize clustering algorithm thresholds/parameters to identify clusters properly while at the same time avoiding merging clusters into one cluster and omitting sparse molecules - Check and correct for self-clustering artifacts of blinking probes
Co-localization	- ***For live cell samples measured for long observation times (e.g. in sequential imaging modes or for long parallel read-out), control for possible target movements during the read-out time***
Dynamics	- Consider filtering trajectories for sufficient length (e.g. >6 steps) to provide enough statistics to extract robust diffusion characteristics

The table gives an overview of common tips and tricks and discusses the pitfalls of an SMLM experiment sorted by the different stages from study design over sample preparation to data analysis. Factors explicitly relevant for microbial samples are marked in bold; factors relevant for multi-color imaging in italics and bold.

study displaying its full potential. Thus, the more *a priori* knowledge of the measures needed to answer a specific biological question and of the characteristics of the target and its environment we have, the more straightforward is the selection of an appropriate combination of single-molecule targeting and read-out methods as discussed in the next paragraph (and in Figure 5a, lower box).

Selecting a suitable multi-color imaging strategy

When imaging multiple targets by multi-color SMLM one first has to choose groups of targets being imaged in parallel so that the signal of two sorts of fluorophores is detected at the same time, and/or sequential imaging, where the different targets are measured independently from each other and fluorescent signals are detected in a successive manner. For structural studies conducted in fixed samples which can be regarded as 'frozen biology' snapshots of immobile targets, this choice is only dependent on the selected fluorophore and labeling combination. Here, sequential imaging allows for subsequent addition of fluorophores which reduces channel cross-talk and prevents preterm photobleaching of only later read-out fluorophores. Furthermore, chromatic aberration can be circumvented by 'reusing' the same color channel [14,26–28]. Parallel imaging, on the other hand, reduces imaging times and allows for parallel drift correction. Chromatic aberrations can also be avoided by spectral demixing [53,55]. Next to the extremes of sequential and parallel imaging modes also an alternating read-out mode by orthogonal activation schemes can be applied, either using one [41] or several color channels [31,79].

When imaging living samples, parallel imaging is the primary choice for highly dynamic samples but technically highly limited. Here, dual-color sptPALM of interaction partners in microbes has been achieved by

Biochemical Society Transactions (2019) **47** 1041–1065
https://doi.org/10.1042/BST20180399

BiFC [36]. When using sequential imaging, at least one target should be considered temporally invariant [13,14,28,32,39,54], forced to be immobile by fast fixation [26,29,31], or both targets have to be regarded to be in dynamic equilibria states for the time of the experiment [28].

Criteria for suitable fluorophore combinations

Next to the biological constraints, technical factors restrict the repertoire of available fluorophore combinations that can be reliably used in multi-color SMLM (Figure 5a, lower box). Transferring the ideal list of desired fluorophore and labeling properties to the, in reality, still rather limited number of existing multi-color combinations of well-performing strategies usually only leaves a few choices—if any at all—and often requires simplification of the original experimental plans (returning to the first phase of study design as depicted in the upper box of Figure 5a).

Generally, as already introduced in Figure 4a, a fluorescent marker can be brought into the biological system by genetic fusions or by staining using immunolabeling, specific drugs, analogons or oligonucleotides dependent on the type of molecule of interest (protein, lipid, nucleic acid, etc.). Genetic fusions provide specific labeling in a one-to-one ratio which allows to visualize low abundant POIs or to quantify protein numbers (correcting for under- and overcounting effects [84]), whereas staining bears the risk of insufficient or unspecific labeling (e.g. due to dye charges, probe sizes or hydrophobicity). Only a few fluorescent dyes suited for SMLM studies are cell membrane-permeable, such as TMR, ATTO655 or the JF dye family [29,30,35,38,39]. Consequently, introducing dyes at high staining efficiencies into the crowded microbial organisms is challenging and dye delivery, as well as residual dye removal, needs to be assisted by membrane permeabilization or electroporation and cell wall digestion. Genetic fusions should be checked for growth and functionality deficiencies as some FPs tend to oligomerize [21,78,81–83] or might sterically hinder the protein function(s), e.g. shown for MreB in *E. coli* [74–76]. Finally, fluorescent dyes are commonly brighter and more photostable than FPs, improving read-out, but require specific switching buffers for photoblinking, which can be tricky to apply to live samples or can be toxic (e.g. depleting oxygen or adding strong reductants [2,6]). Here, different dyes might require different switching buffers which prevent their combined use. Also, FPs are influenced by switching buffers, e.g. oxygen removal prevents folding and reductants induce increased blinking [85,86]. Clever pairings of fluorophores and molecules of interest can compromise some drawbacks, e.g. when labeling and imaging a low abundance POI tagged with an FP first and only then staining the structural reference with a dye or when imaging the most dynamic POI by the brightest fluorophore of a chosen combination.

Nevertheless, taken all these limitations and requirements, it is not surprising that only a few fluorophore combinations perform well and lead to a full biological study after successfully passing TASK 4 and 5 in Figure 5a. These working combinations appear repeatedly in our literature review and often are specifically tailored. For example, dye staining is preferred for outer cell staining such as the cell wall, or brightness is often traded for probe specificity when using an FP tag for otherwise difficult-to-label POIs. In this respect, Tables 1 and 2 give a good overview of current working strategies and at the same time highlight the need for further probe developments.

Perspectives

Applying multi-color single-molecule imaging and tracking strategies remains challenging but yields essential results for our understanding of biological processes

The direct visualization and *in situ* measurement of the inner life of cells is essential for our understanding of biological processes and has led to many profound discoveries in biological research. Nevertheless, adapting and applying multi-color single-molecule imaging and tracking techniques in the various research fields remains challenging to this day. Behind each of the current microbial studies with their remarkable results hide individually tailored and often complex experimental designs. All the used single-molecule tools work close to current technology limits, and each new technological development allows for method improvement.

Recent (and future) probe developments might shift current technology limits

Current advances with promising results are for example brighter, fluorogenic or photoactivatable/photoswitchable probes [87–90], implementations of dye labels for single-molecule tracking with prolonged and more precise trajectories of different targets in microorganisms than traditionally obtained using FP labels in sptPALM imaging [91,92] or smaller (genetic) labels not interfering with cellular biology and/or allowing for high labeling densities and efficiencies [21,93].

How to best follow dynamic, co-moving interaction partners using SMLM methods remains an open question

To this day, there are no efficient tools for observing the dynamics of molecular interactions at a single-molecule resolution. One reason for this is the stochastic photoswitching read-out of probes. To follow both partners, both fluorophores have to emit light simultaneously. Currently, read-out of molecular interactions was realized by designing split versions of photochromic FPs for BiFC-PALM [36,94–96] or by energy transfer pairs using a photochromic donor [97], which, except for [36], were all conducted in mammalian cells. Both techniques, however, suffer from several drawbacks: Problems in BiFC-PALM stem from the irreversibility of FP complementation interfering with the imaged biology and the slow maturation of the complemented FP chromophores, which both prevent the dynamic study of transient short-lived interactions. Additionally, split-FPs have unneglectable tendencies of self-assembly, generating false-positive read-out signals. Photochromic fluorescence resonance energy transfer (FRET) approaches as reported in [97], however, suffer from almost halved fluorescence intensity read-outs drastically decreasing single-molecule resolution, direct acceptor excitation and acceptor bleaching and depend on extrinsic staining by far-red organic dyes as acceptors. Finally, all current photochromic approaches use UV-mediated photoconversion schemes which can interfere with cellular biology [18,98]. Thus, a protein interaction detection method inheriting the abilities of these tools, but being able to (i) reversibly monitor interaction dynamics (ii) at fast time scales, (iii) for prolonged imaging times and (iv) overcoming the current imaging artifacts will have a major impact when studying various fields of biology.

Abbreviations

AF, Alexa Fluor; BiFC, bimolecular fluorescence complementation; DaStPuRe, dark state pumping and recovery, illumination with high laser power forces the fluorophores into a dark state; dSTORM, direct stochastic optical reconstruction microscopy; EdU, 5-ethynyl-2′-deoxyuridine; FP, fluorescent protein; FRET, fluorescence resonance energy transfer; FROS, fluorescent repressor–operator system; HILO, highly inclined and laminated optical sheet; JF, Janelia Fluor; PAINT, point accumulation for imaging in nanoscale topography; PALM, photoactivated localization microscopy; PC-PALM, PALM using primed photoconversion; POIs, protein of interests; ROI, region of interest; S/N, signal-to-noise ratio; smFISH, single-molecule fluorescent *in situ* hybridization; SMLM, single-molecule localization microscopy; SPT, single-particle tracking; sptPALM, single-particle tracking PALM; TIRF, total internal reflection fluorescence; UV-PALM, PALM using UV-light photoactivation/conversion.

Author Contribution

I.V., J.W. and U.E. performed the literature review and created the tabular overviews, I.V. and J.W. conceived the figures, I.V. and U.E. wrote the manuscript with the help of J.W.

Funding

The authors gratefully acknowledge the Max Planck Society, SYNMIKRO and the Fonds der Chemischen Industrie for financial support.

Acknowledgements

We sincerely hope that we did not overlook any multi-color SMLM study conducted in microorganisms and would like to apologize to the authors if we did not include them in this summary. We furthermore thank David

Biochemical Society Transactions (2019) **47** 1041–1065
https://doi.org/10.1042/BST20180399

Virant, Bartosz Turkowyd and Alexander Balinovic for discussions and critical reading of the manuscript. Finally, we would like to thank all authors that provided us with figure data from their original publications to compile the overview figures 2 and 3.

Competing Interests

The authors declare that there are no competing interests associated with the manuscript.

References

1 Liu, Z., Lavis, L.D. and Betzig, E. (2015) Imaging live-cell dynamics and structure at the single-molecule level. *Mol. Cell* **58**, 644–659 https://doi.org/10.1016/j.molcel.2015.02.033
2 Turkowyd, B., Virant, D. and Endesfelder, U. (2016) From single molecules to life: microscopy at the nanoscale. *Anal. Bioanal. Chem.* **408**, 6885–6911 https://doi.org/10.1007/s00216-016-9781-8
3 Sigal, Y.M., Zhou, R. and Zhuang, X. (2018) Visualizing and discovering cellular structures with super-resolution microscopy. *Science* **361**, 880–887 https://doi.org/10.1126/science.aau1044
4 van de Linde, S., Löschberger, A., Klein, T., Heidbreder, M., Wolter, S., Heilemann, M. et al. (2011) Direct stochastic optical reconstruction microscopy with standard fluorescent probes. *Nat. Protoc.* **6**, 991–1009 https://doi.org/10.1038/nprot.2011.336
5 Adam, V., Berardozzi, R., Byrdin, M. and Bourgeois, D. (2014) Phototransformable fluorescent proteins: future challenges. *Curr. Opin. Chem. Biol.* **20**, 92–102 https://doi.org/10.1016/j.cbpa.2014.05.016
6 Endesfelder, U. (2016) Photoswitching fluorophores in super-Resolution fluorescence microscopy. *Super Resolution Imaging Biomed.* p. 49, CRC Press
7 Sahl, S.J. and Moerner, W.E. (2013) Super-resolution fluorescence imaging with single molecules. *Curr. Opin. Struct. Biol.* **23**, 778–787 https://doi.org/10.1016/j.sbi.2013.07.010
8 Xiao, J. and Dufrêne, Y.F. (2016) Optical and force nanoscopy in microbiology. *Nat. Microbiol.* **1**, 16186 https://doi.org/10.1038/nmicrobiol.2016.186
9 Kapanidis, A.N., Lepore, A. and El Karoui, M. (2018) Rediscovering bacteria through single-Molecule imaging in living cells. *Biophys. J.* **115**, 190–202 https://doi.org/10.1016/j.bpj.2018.03.028
10 Sharonov, A. and Hochstrasser, R.M. (2006) Wide-field subdiffraction imaging by accumulated binding of diffusing probes. *Proc. Natl Acad. Sci. U.S.A.* **103**, 18911–18916 https://doi.org/10.1073/pnas.0609643104
11 Heilemann, M., van de Linde, S., Schüttpelz, M., Kasper, R., Seefeldt, B., Mukherjee, A. et al. (2008) Subdiffraction-resolution fluorescence imaging with conventional fluorescent probes. *Angew. Chem. Int. Ed. Engl.* **47**, 6172–6176 https://doi.org/10.1002/anie.200802376
12 Bayas, C.A., Wang, J., Lee, M.K., Schrader, J.M., Shapiro, L. and Moerner, W.E. (2018) Spatial organization and dynamics of RNase E and ribosomes in *Caulobacter crescentus*. *Proc. Natl Acad. Sci. U.S.A.* **115**, E3712–E3721 https://doi.org/10.1073/pnas.1721648115
13 Bianchi, F., Syga, Ł., Moiset, G., Spakman, D., Schavemaker, P.E., Punter, C.M. et al. (2018) Steric exclusion and protein conformation determine the localization of plasma membrane transporters. *Nat. Commun.* **9**, 501 https://doi.org/10.1038/s41467-018-02864-2
14 Gahlmann, A., Ptacin, J.L., Grover, G., Quirin, S., von Diezmann, A.R.S., Lee, M.K. et al. (2013) Quantitative multicolor subdiffraction imaging of bacterial protein ultrastructures in three dimensions. *Nano Lett.* **13**, 987–993 https://doi.org/10.1021/nl304071h
15 McDonald, N.A., Lind, A.L., Smith, S.E., Li, R. and Gould, K.L. (2017) Nanoscale architecture of the *Schizosaccharomyces pombe* contractile ring. *eLife* **6**, 28865 https://doi.org/10.7554/eLife.28865
16 Ptacin, J.L., Lee, S.F., Garner, E.C., Toro, E., Eckart, M., Comolli, L.R. et al. (2010) A spindle-like apparatus guides bacterial chromosome segregation. *Nat. Cell Biol.* **12**, 791–798 https://doi.org/10.1038/ncb2083
17 Betzig, E., Patterson, G.H., Sougrat, R., Lindwasser, O.W., Olenych, S., Bonifacino, J.S. et al. (2006) Imaging intracellular fluorescent proteins at nanometer resolution. *Science* **313**, 1642–1645 https://doi.org/10.1126/science.1127344
18 Turkowyd, B., Balinovic, A., Virant, D., Carnero, H.G.G., Caldana, F., Endesfelder, M. et al. (2017) A general mechanism of photoconversion of green-to-red fluorescent proteins based on blue and infrared light reduces phototoxicity in live-cell single-molecule imaging. *Angew. Chem. Int. Ed. Engl.* **56**, 11634–11639 https://doi.org/10.1002/anie.201702870
19 Mohr, M.A., Kobitski, A.Y., Sabater, L.R., Nienhaus, K., Obara, C.J., Lippincott-Schwartz, J. et al. (2017) Rational engineering of photoconvertible fluorescent proteins for dual-color fluorescence nanoscopy enabled by a triplet-state mechanism of primed conversion. *Angew. Chem. Int. Ed. Engl.* **56**, 11628–11633 https://doi.org/10.1002/anie.201706121
20 Lampe, A., Haucke, V., Sigrist, S.J., Heilemann, M. and Schmoranzer, J. (2012) Multi-colour direct STORM with red emitting carbocyanines. *Biol. Cell* **104**, 229–237 https://doi.org/10.1111/boc.201100011
21 Virant, D., Traenkle, B., Maier, J., Kaiser, P.D., Bodenhöfer, M., Schmees, C. et al. (2018) A peptide tag-specific nanobody enables high-quality labeling for dSTORM imaging. *Nat. Commun.* **9**, 930 https://doi.org/10.1038/s41467-018-03191-2
22 Dempsey, G.T., Vaughan, J.C., Chen, K.H., Bates, M. and Zhuang, X. (2011) Evaluation of fluorophores for optimal performance in localization-based super-resolution imaging. *Nat. Methods* **8**, 1027–1036 https://doi.org/10.1038/nmeth.1768
23 Löschberger, A., van de Linde, S., Dabauvalle, M.-C., Rieger, B., Heilemann, M., Krohne, G. et al. (2012) Super-resolution imaging visualizes the eightfold symmetry of gp210 proteins around the nuclear pore complex and resolves the central channel with nanometer resolution. *J. Cell Sci.* **125**, 570–575 https://doi.org/10.1242/jcs.098822
24 Szymborska, A., de Marco, A., Daigle, N., Cordes, V.C., Briggs, J.A.G. and Ellenberg, J. (2013) Nuclear pore scaffold structure analyzed by super-resolution microscopy and particle averaging. *Science* **341**, 655–658 https://doi.org/10.1126/science.1240672
25 Durisic, N., Laparra-Cuervo, L., Sandoval-Álvarez, Á., Borbely, J.S. and Lakadamyali, M. (2014) Single-molecule evaluation of fluorescent protein photoactivation efficiency using an in vivo nanotemplate. *Nat. Methods* **11**, 156–162 https://doi.org/10.1038/nmeth.2784
26 Spahn, C., Cella-Zannacchi, F., Endesfelder, U. and Heilemann, M. (2015) Correlative super-resolution imaging of RNA polymerase distribution and dynamics, bacterial membrane and chromosomal structure in *Escherichia coli*. *Methods Appl. Fluoresc.* **3**, 014005 https://doi.org/10.1088/2050-6120/3/1/014005

27 Foo, Y.H., Spahn, C., Zhang, H., Heilemann, M. and Kenney, L.J. (2015) Single cell super-resolution imaging of *E. coli* ompR during environmental stress. *Integr. Biol.* **7**, 1297–1308 https://doi.org/10.1039/c5ib00077g
28 Virant, D. Turkowyd, B., Balinovic, A. and Endesfelder, U. (2017) Combining primed photoconversion and UV-photoactivation for aberration-free, live-cell compliant multi-color single-molecule localization microscopy imaging. *Int. J. Mol. Sci.* **18**, E1524 https://doi.org/10.3390/ijms18071524
29 Spahn, C.K., Glaesmann, M., Grimm, J.B., Ayala, A.X., Lavis, L.D. and Heilemann, M. (2018) A toolbox for multiplexed super-resolution imaging of the *E. coli* nucleoid and membrane using novel PAINT labels. *Sci. Rep.* **8**, 14768 https://doi.org/10.1038/s41598-018-33052-3
30 Karunatilaka, K.S., Cameron, E.A., Martens, E.C., Koropatkin, N.M., Biteen, J.S. and Ruby, E.G. (2014) Superresolution imaging captures carbohydrate utilization dynamics in human gut symbionts. *mBio* **5**, e02172 https://doi.org/10.1128/mBio.02172-14
31 Ptacin, J.L., Gahlmann, A., Bowman, G.R., Perez, A.M., von Diezmann, A.R.S., Eckart, M.R. et al. (2014) Bacterial scaffold directs pole-specific centromere segregation. *Proc. Natl Acad. Sci. U.S.A.* **111**, E2046–E2055 https://doi.org/10.1073/pnas.1405188111
32 Lew, M.D., Lee, S.F., Ptacin, J.L., Lee, M.K., Twieg, R.J., Shapiro, L. et al. (2011) Three-dimensional superresolution colocalization of intracellular protein superstructures and the cell surface in live *Caulobacter crescentus*. *Proc. Natl. Acad. Sci. U.S.A.* **108**, E1102–E1110 https://doi.org/10.1073/pnas.1114444108
33 Buss, J., Coltharp, C., Shtengel, G., Yang, X., Hess, H., Xiao, J. et al. (2015) A multi-layered protein network stabilizes the *Escherichia coli* FtsZ-ring and modulates constriction dynamics. *PLoS Genet.* **11**, e1005128 https://doi.org/10.1371/journal.pgen.1005128
34 Fei, J., Singh, D., Zhang, Q., Park, S., Balasubramanian, D., Golding, I. et al. (2015) RNA biochemistry. Determination of in vivo target search kinetics of regulatory noncoding RNA. *Science* **347**, 1371–1374 https://doi.org/10.1126/science.1258849
35 Fabiani, F.D., Renault, T.T., Peters, B., Dietsche, T., Gálvez, E.J.C., Guse, A. et al. (2017) A flagellum-specific chaperone facilitates assembly of the core type III export apparatus of the bacterial flagellum. *PLoS Biol.* **15**, e2002267 https://doi.org/10.1371/journal.pbio.2002267
36 Liu, Z., Xing, D., Su, Q.P., Zhu, Y. Zhang, J., Kong, X. et al. (2014) Super-resolution imaging and tracking of protein-protein interactions in sub-diffraction cellular space. *Nat. Commun.* **5**, 4443 https://doi.org/10.1038/ncomms5443
37 Vedyaykin, A.D., Gorbunov, V.V., Sabantsev, A.V., Polinovskaya, V.S., Vishnyakov, I.E. Melnikov, A.S. et al. (2015) Multi-color localization microscopy of fixed cells as a promising tool to study organization of bacterial cytoskeleton. *J. Phys. Conf. Series* **643**, 012020 https://doi.org/10.1088/1742-6596/643/1/012020
38 Wille, T., Barlag, B., Jakovljevic, V., Hensel, M., Sourjik, V., Gerlach, R.G. et al. (2015) A gateway-based system for fast evaluation of protein-protein interactions in bacteria. *PLoS ONE* **10**, e0123646 https://doi.org/10.1371/journal.pone.0123646
39 Barlag, B., Beutel, O., Janning, D., Czarniak, F., Richter, C.P., Kommnick, C. et al. (2016) Single molecule super-resolution imaging of proteins in living *Salmonella enterica* using self-labelling enzymes. *Sci. Rep.* **6**, 31601 https://doi.org/10.1038/srep31601
40 Zhang, Y., Lara-Tejero, M., Bewersdorf, J. and Galán, J.E. (2017) Visualization and characterization of individual type III protein secretion machines in live bacteria. *Proc. Natl Acad. Sci. U.S.A.* **114**, 6098–6103 https://doi.org/10.1073/pnas.1705823114
41 Berk, V., Fong, J.C.N., Dempsey, G.T., Develioglu, O.N., Zhuang, X., Liphardt, J. et al. (2012) Molecular architecture and assembly principles of *Vibrio cholerae* biofilms. *Science* **337**, 236–239 https://doi.org/10.1126/science.1222981
42 Fiche, J.B., Cattoni, D.I., Diekmann, N., Langerak, J.M., Clerte, C., Royer, C.A. et al. (2013) Recruitment, assembly, and molecular architecture of the SpoIIIE DNA pump revealed by superresolution microscopy. *PLoS Biol.* **11**, e1001557 https://doi.org/10.1371/journal.pbio.1001557
43 Liao, Y., Schroeder, J.W., Gao, B., Simmons, L.A. and Biteen, J.S. (2015) Single-molecule motions and interactions in live cells reveal target search dynamics in mismatch repair. *Proc. Natl Acad. Sci. U.S.A.* **112**, E6898–E6906 https://doi.org/10.1073/pnas.1507386112
44 Fleming, T.C., Shin, J.Y., Lee, S.H., Becker, E., Huang, K.C., Bustamante, C. et al. (2010) Dynamic SpoIIIE assembly mediates septal membrane fission during *Bacillus subtilis* sporulation. *Genes. Dev.* **24**, 1160–1172 https://doi.org/10.1101/gad.1925210
45 Yen Shin, J., Lopez-Garrido, J., Lee, S.H., Diaz-Celis, C., Fleming, T., Bustamante, C. et al. (2015) Visualization and functional dissection of coaxial paired SpoIIIE channels across the sporulation septum. *eLife* **4**, e06474 https://doi.org/10.7554/eLife.06474
46 Wang, W., Li, G.-W., Chen, C., Xie, X.S. and Zhuang, X. (2011) Chromosome organization by a nucleoid-associated protein in live bacteria. *Science* **333**, 1445–1449 https://doi.org/10.1126/science.1204697
47 Stracy, M., Jaciuk, M., Uphoff, S., Kapanidis, A.N., Nowotny, M., Sherratt, D.J. et al. (2016) Single-molecule imaging of UvrA and UvrB recruitment to DNA lesions in living *Escherichia coli*. *Nat. Commun.* **7**, 12568 https://doi.org/10.1038/ncomms12568
48 Stracy, M., Lesterlin, C., Garza de Leon, F., Uphoff, S., Zawadzki, P. and Kapanidis, A.N. (2015) Live-cell superresolution microscopy reveals the organization of RNA polymerase in the bacterial nucleoid. *Proc. Natl Acad. Sci. U.S.A.* **112**, E4390–E4399 https://doi.org/10.1073/pnas.1507592112
49 Garza de Leon, F., Sellars, L., Stracy, M., Busby, S.J.W. and Kapanidis, A.N. (2017) Tracking low-copy transcription factors in living bacteria: the case of the lac repressor. *Biophys. J.* **112**, 1316–1327 https://doi.org/10.1016/j.bpj.2017.02.028
50 Vedyaykin, A.D., Vishnyakov, I.E. Polinovskaya, V.S., Khodorkovskii, M.A. and Sabantsev, A.V. (2016) New insights into FtsZ rearrangements during the cell division of *Escherichia coli* from single-molecule localization microscopy of fixed cells. *Microbiologyopen* **5**, 378–386 https://doi.org/10.1002/mbo3.336
51 Vedyaykin, A.D., Sabantsev, A.V., Vishnyakov, I.E. Morozova, N.E. and Khodorkovskii, M.A. (2017) Recovery of division process in bacterial cells after induction of SulA protein which is responsible for cytokinesis arrest during SOS-response. *Cell Tissue Biol.* **11**, 89–94 https://doi.org/10.1134/S1990519X17020080
52 Robinson, A., McDonald, J.P., Caldas, V.E.A., Patel, M., Wood, E.A., Punter, C.M. et al. (2015) Regulation of mutagenic DNA polymerase V activation in space and time. *PLoS Genet.* **11**, e1005482 https://doi.org/10.1371/journal.pgen.1005482
53 Ries, J., Kaplan, C., Platonova, E., Eghlidi, H. and Ewers, H. (2012) A simple, versatile method for GFP-based super-resolution microscopy via nanobodies. *Nat. Methods* **9**, 582–584 https://doi.org/10.1038/nmeth.1991
54 Hajj, B., Wisniewski, J., El Beheiry, M., Chen, J., Revyakin, A., Wu, C. et al. (2014) Whole-cell, multicolor superresolution imaging using volumetric multifocus microscopy. *Proc. Natl Acad. Sci. U.S.A.* **111**, 17480–17485 https://doi.org/10.1073/pnas.1412396111
55 Zhao, T., Wang, Y., Zhai, Y., Qu, X., Cheng, A., Du, S. et al. (2015) A user-friendly two-color super-resolution localization microscope. *Opt. Express* **23**, 1879–1887 https://doi.org/10.1364/OE.23.001879
56 Mund, M., van der Beek, J.A., Deschamps, J., Dmitrieff, S., Hoess, P., Monster, J.L. et al. (2018) Systematic nanoscale analysis of endocytosis links efficient vesicle formation to patterned actin nucleation. *Cell* **174**, 884–896.e17 https://doi.org/10.1016/j.cell.2018.06.032

Biochemical Society Transactions (2019) **47** 1041–1065
https://doi.org/10.1042/BST20180399

57 Puchner, E.M., Walter, J.M., Kasper, R., Huang, B. and Lim, W.A. (2013) Counting molecules in single organelles with superresolution microscopy allows tracking of the endosome maturation trajectory. *Proc. Natl Acad. Sci. U.S.A.* **110**, 16015–16020 https://doi.org/10.1073/pnas.1309676110

58 Zhou, L., Obhof, T., Schneider, K., Feldbrügge, M., Nienhaus, G.U. and Kämper, J. (2018) Cytoplasmic transport machinery of the SPF27 homologue Num1 in *Ustilago maydis*. *Sci. Rep.* **8**, 3611 https://doi.org/10.1038/s41598-018-21628-y

59 Ishitsuka, Y., Savage, N., Li, Y., Bergs, A., Grün, N., Kohler, D. et al. (2015) Superresolution microscopy reveals a dynamic picture of cell polarity maintenance during directional growth. *Sci. Adv.* **1**, e1500947 https://doi.org/10.1126/sciadv.1500947

60 Virant, D., Vojnovic, I., Winkelmeier, J., Rigl, M. and Endesfelder, U. Investigation of the kinetochore structure of *Schizosaccharomyces pombe* by quantitative single-molecule localization microscopy imaging. Manuscript in preparation

61 Sustarsic, M., Plochowietz, A., Aigrain, L., Yuzenkova, Y., Zenkin, N. and Kapanidis, A. (2014) Optimized delivery of fluorescently labeled proteins in live bacteria using electroporation. *Histochem. Cell Biol.* **142**, 113–124 https://doi.org/10.1007/s00418-014-1213-2

62 Di Paolo, D., Afanzar, O., Armitage, J.P. and Berry, R.M. (2016) Single-molecule imaging of electroporated dye-labelled CheY in live *Escherichia coli*. *Philos. Trans. R. Soc. Lond. B Biol. Sci.* **371**, 20150492 https://doi.org/10.1098/rstb.2015.0492

63 Saurabh, S., Perez, A.M., Comerci, C.J., Shapiro, L. and Moerner, W.E. (2016) Super-resolution imaging of live bacteria cells using a genetically directed, highly photostable fluoromodule. *J. Am. Chem. Soc.* **138**, 10398–10401 https://doi.org/10.1021/jacs.6b05943

64 Raulf, A., Spahn, C.K., Zessin, P.J.M., Finan, K., Bernhardt, S., Heckel, A. et al. (2014) Click chemistry facilitates direct labelling and super-resolution imaging of nucleic acids and proteins. *RSC Adv.* **4**, 30462–30466 https://doi.org/10.1039/C4RA01027B

65 Kipper, K., Lundius, E.G. Ćurić, V., Nikić, I., Wiessler, M., Lemke, E.A. et al. (2017) Application of noncanonical amino acids for protein labeling in a genomically recoded *Escherichia coli*. *ACS Synth. Biol.* **6**, 233–255 https://doi.org/10.1021/acssynbio.6b00138

66 Liang, H., DeMeester, K.E., Hou, C.-W., Parent, M.A., Caplan, J.L. and Grimes, C.L. (2017) Metabolic labelling of the carbohydrate core in bacterial peptidoglycan and its applications. *Nat. Commun.* **8**, 15015 https://doi.org/10.1038/ncomms15015

67 Crawford, R., Torella, J.P., Aigrain, L., Plochowietz, A., Gryte, K., Uphoff, S. et al. (2013) Long-lived intracellular single-molecule fluorescence using electroporated molecules. *Biophys. J.* **105**, 2439–2450 https://doi.org/10.1016/j.bpj.2013.09.057

68 Volkov, I.L., Lindén, M., Aguirre Rivera, J., leong, K.-W., Metelev, M., Elf, J. et al. (2018) tRNA tracking for direct measurements of protein synthesis kinetics in live cells. *Nat. Chem. Biol.* **14**, 618–626 https://doi.org/10.1038/s41589-018-0063-y

69 Muyrers, J.P., Zhang, Y. and Stewart, A.F. (2001) Techniques: recombinogenic engineering – new options for cloning and manipulating DNA. *Trends Biochem. Sci.* **26**, 325–331 https://doi.org/10.1016/S0968-0004(00)01757-6

70 Bremer, H. and Dennis, P.P. (1996) Modulation of chemical composition and other parameters of the cell by growth rate. In *Escherichia coli and Salmonella*, 2nd edn (Neidhardt, F.C., ed.), pp. 1553–1569, ASM Press, Washington, DC

71 Bindels, D.S., Haarbosch, L., van Weeren, L., Postma, M., Wiese, K.E., Mastop, M. et al. (2017) mScarlet: a bright monomeric red fluorescent protein for cellular imaging. *Nat. Methods* **14**, 53–56 https://doi.org/10.1038/nmeth.4074

72 Subach, F.V., Patterson, G.H., Manley, S., Gillette, J.M., Lippincott-Schwartz, J. and Verkhusha, V.V. (2009) Photoactivatable mCherry for high-resolution two-color fluorescence microscopy. *Nat. Methods* **6**, 153–626 https://doi.org/10.1038/nmeth.1298

73 Narsing Rao, M.P., Xiao, M. and Li, W.J. (2017) Fungal and bacterial pigments: secondary metabolites with wide applications. *Front. Microbiol.* **8**, 1113 https://doi.org/10.3389/fmicb.2017.01113

74 Bendezu, F.O., Hale, C.A., Bernhardt, T.G and de Boer, P.A.J. (2009) RodZ (YfgA) is required for proper assembly of the MreB actin cytoskeleton and cell shape in *E. coli*. *EMBO J.* **28**, 193–204 https://doi.org/10.1038/emboj.2008.264

75 Swulius, M.T. and Jensen, G.J. (2012) The helical MreB cytoskeleton in *Escherichia coli* MC1000/pLE7 is an artifact of the N-terminal yellow fluorescent protein tag. *J. Bacteriol.* **194**, 6382–6386 https://doi.org/10.1128/JB.00505-12

76 Lee, T.K., Tropini, C., Hsin, J., Desmarais, S.M., Ursell, T.S., Gong, E. et al. (2014) A dynamically assembled cell wall synthesis machinery buffers cell growth. *Proc. Natl Acad. Sci. U.S.A.* **111**, 4554–4559 https://doi.org/10.1073/pnas.1313826111

77 Wu, B., Piatkevich, K.D., Lionnet, T., Singer, R.H and Verkhusha, V.V. (2011) Modern fluorescent proteins and imaging technologies to study gene expression, nuclear localization, and dynamics. *Curr. Opin. Cell Biol.* **23**, 310–317 https://doi.org/10.1016/j.ceb.2010.12.004

78 Wang, S., Moffitt, J.R., Dempsey, G.T., Xie, X.S. and Zhuang, X. (2014) Characterization and development of photoactivatable fluorescent proteins for single-molecule-based superresolution imaging. *Proc. Natl Acad. Sci. U.S.A.* **111**, 8452–8457 https://doi.org/10.1073/pnas.1406593111

79 Malkusch, S., Endesfelder, U., Mondry, J., Gelléri, M., Verveer, P.J. and Heilemann, M. (2012) Coordinate-based colocalization analysis of single-molecule localization microscopy data. *Histochem. Cell Biol.* **137**, 1–10 https://doi.org/10.1007/s00418-011-0880-5

80 Aaron, J.S., Taylor, A.B. and Chew, T.L. (2018) Image co-localization – co-occurrence versus correlation. *J. Cell Sci.* **131**, jcs211847 https://doi.org/10.1242/jcs.211847

81 Landgraf, D., Okumus, B., Chien, P., Baker, T.A and Paulsson, J. (2012) Segregation of molecules at cell division reveals native protein localization. *Nat. Methods* **9**, 480–482 https://doi.org/10.1038/nmeth.1955

82 Zhang, M., Chang, H., Zhang, Y., Yu, J., Wu, L., Ji, W. et al. (2012) Rational design of true monomeric and bright photoactivatable fluorescent proteins. *Nat. Methods* **9**, 727–729 https://doi.org/10.1038/nmeth.2021

83 Stockmar, I., Feddersen, H., Cramer, K., Gruber, S., Jung, K., Bramkamp, M. et al. (2018) Optimization of sample preparation and green color imaging using the mNeonGreen fluorescent protein in bacterial cells for photoactivated localization microscopy. *Sci. Rep.* **8**, 10137 https://doi.org/10.1038/s41598-018-28472-0

84 Jung, S.R., Fujimoto, B.S. and Chiu, D.T. (2017) Quantitative microscopy based on single-molecule fluorescence. *Curr. Opin. Chem. Biol.* **39**, 64–73 https://doi.org/10.1016/j.cbpa.2017.06.004

85 Subach, F.V., Malashkevich, V.N., Zencheck, W.D., Xiao, H., Filonov, G.S., Almo, S.C. et al. (2009) Photoactivation mechanism of PAmCherry based on crystal structures of the protein in the dark and fluorescent states. *Proc. Natl Acad. Sci. U.S.A.* **106**, 21097–21102 https://doi.org/10.1073/pnas.0909204106

86 Endesfelder, U., Malkusch, S., Flottmann, B., Mondry, J., Liguzinski, P., Verveer, P.J. et al. (2011) Chemically induced photoswitching of fluorescent probes – a general concept for super-resolution microscopy. *Molecules* **16**, 3106–3118 https://doi.org/10.3390/molecules16043106

87 Grimm, J.B., English, B.P., Choi, H., Muthusamy, A.K., Mehl, B.P., Dong, P. et al. (2016) Bright photoactivatable fluorophores for single-molecule imaging. *Nat. Methods* **13**, 985–988 https://doi.org/10.1038/nmeth.4034

88 Ke, N., Landgraf, D., Paulsson, J. and Berkmen, M. (2016) Visualization of periplasmic and cytoplasmic proteins with a self-labeling protein tag. *J. Bacteriol.* **198**, 1035–1043 https://doi.org/10.1128/JB.00864-15
89 Lavis, L.D. (2017) Teaching old dyes new tricks: biological probes built from fluoresceins and rhodamines. *Annu. Rev. Biochem.* **86**, 825–843 https://doi.org/10.1146/annurev-biochem-061516-044839
90 Gautier, A. and Tebo, A.G. (2018) Fluorogenic protein-based strategies for detection, actuation, and sensing. *Bioessays* **40**, e1800118 https://doi.org/10.1002/bies.201800118
91 Yu, A. (2017) *Towards Resolving the Yeast Replisome In Vivo*, McGill University Libraries, Mc Gill University
92 Banaz, N., Mäkelä, J. and Uphoff, S. (2018) Choosing the right label for single-molecule tracking in live bacteria: Side-by-side comparison of photoactivatable fluorescent protein and halo tag dyes. *J. Phys. D Appl. Phys.* **52**, 064002 https://doi.org/10.1088/1361-6463/aaf255
93 Strauss, S., Nickels, P.C., Strauss, M.T., Jimenez Sabinina, V., Ellenberg, J., Carter, J.D. et al. (2018) Modified aptamers enable quantitative sub-10-nm cellular DNA-PAINT imaging. *Nat. Methods* **15**, 685–688 https://doi.org/10.1038/s41592-018-0105-0
94 Xia, P., Liu, X., Wu, B., Zhang, S., Song, X., Yao, P.Y. et al. (2014) Superresolution imaging reveals structural features of EB1 in microtubule plus-end tracking. *Mol. Biol. Cell* **25**, 4166–4173 https://doi.org/10.1091/mbc.e14-06-1133
95 Nickerson, A., Huang, T., Lin, L.-J. and Nan, X. (2015) Photoactivated localization microscopy with bimolecular fluorescence complementation (BiFC-PALM). *J. Vis. Exp.* **106**, e53154 https://doi.org/10.3791/53154
96 Chen, M., Liu, S., Li, W., Zhang, Z., Zhang, X., Zhang, X.-E. et al. (2016) Three-fragment fluorescence complementation coupled with photoactivated localization microscopy for nanoscale imaging of ternary complexes. *ACS Nano* **10**, 8482–8490 https://doi.org/10.1021/acsnano.6b03543
97 Basu, S., Needham, L.-M., Lando, D., Taylor, E.J.R., Wohlfahrt, K.J., Shah, D. et al. (2018) FRET-enhanced photostability allows improved single-molecule tracking of proteins and protein complexes in live mammalian cells. *Nat. Commun.* **9**, 2520 https://doi.org/10.1038/s41467-018-04486-0
98 Wäldchen, S., Lehmann, J., Klein, T., van de Linde, S. and Sauer, M. (2015) Light-induced cell damage in live-cell super-resolution microscopy. *Sci. Rep.* **5**, 15348 https://doi.org/10.1038/srep15348

1.2.4 Expansion microscopy

ExM is a novel imaging technique, which yields higher resolutions by physically expanding and thus magnifying the fixed sample (see figure 1.4, [153]). Using ExM or its various adjustments, it is possible to expand samples ranging from whole organs and tissues to single microbes and viruses with magnifications, also called EFs, ranging from 3x to 20x [153–171].

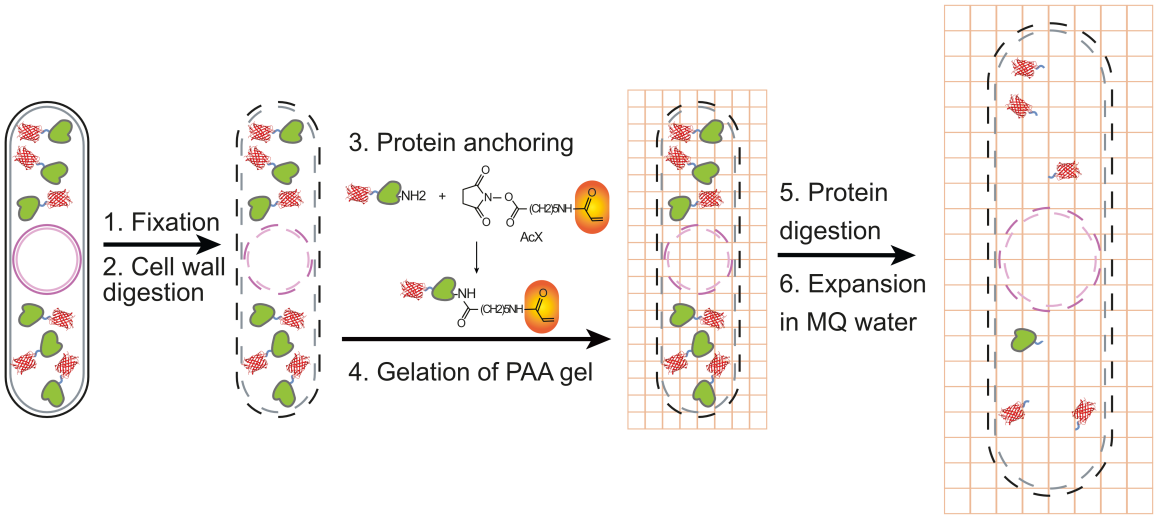

Figure 1.4: The principle of expansion microscopy.

In ExM the target molecules are anchored to a hydrogel mesh, mostly consisting of poly-acrylamide (PAA), and subsequently expanded upon contact with aqueous media. The resolution is hence increased by the corresponding EF of the sample. To obtain an even or so called isotropic expansion, which is inherent with the preservation of the biological target structure, the POI has to be fully anchored to the gel mesh and all obstructions such as cell walls and membranes and protein-protein linkages have to be efficiently severed. This is achieved in anchoring [172–174] or fixation [173] as well as cell wall removal [158, 159, 175, 176] and protein digestion [169, 177–180] steps in the ExM protocol. Implementing ExM in organisms with more complex cell walls compared to mammalian cells and tissues such as fission yeast is extremely demanding and has to be adjusted for every organism separately [157–159, 163, 165, 175, 176]. This became clear since various publications claimed differing detected expansion factors between the expanded gel, tissue, different organelles or regions within organelles in the same sample [180–184]. It was shown for instance that while ultrastructure expansion microscopy (U-ExM) preserves isolated centrioles from *Chlamydomonas reinhardtii* very well, this ExM method failed to evenly expand chromatin in barley root tips [181, 185].

Beside an isotropic expansion, the protein retention yield, a measure for the amount of POIs detected via fluorescent markers after expansion, plays a key role in ExM and is significantly decreased by harsh protein digestion and gelation and incomplete labeling of the POI. The sample is homogenized by cleaving proteins and protein-protein interactions not discriminating between POI and fluorophore via digestion with proteinase K or collagenase type II, heat denaturation or homogenization agents such as SDS so far [153, 169, 177–179]. Furthermore, free radicals during the chain polymerization reaction of PAA gels quench the fluorescence of organic dyes and fluorescent proteins [161]. Although,

non-radical gelation for ExM was established and shown to retain a higher protein yield, the custom synthesized monomers needed for gelation are hard to come by [161]. Additionally to that, incomplete and unspecific labeling can reduce the protein retention yield, yet up to date most ExM methods rely on organic dyes [172]. While this is a reliable method when staining highly abundant targets, it was shown that staining low abundant targets in organisms with high molecular crowding and heterogeneous charge such as fission yeast can introduce artefacts that can be falsely classified as real signal [15].

Combining ExM with SRM yields superior resolutions, yet fluorophore choice and labeling strategy must suit both techniques and survive the combined sample preparation protocol. To date ExM was successfully combined with SIM [186], STED [187] and direct stochastic optical reconstruction microscopy (dSTORM)[188, 189]. Those methods however, mainly rely on external staining of the target with organic dyes via immunofluorescence. As mentioned before, the SMLM techniques dSTORM and PALM achieve the highest resolution of about 20 nm and can additionally quantify the target molecules by counting the detected localizations [190]. However, photoswitching of dSTORM compatible organic dyes is induced by strong ionic switching buffers, which were shown to shrink expanded gels [189]. Therefore, one implementation of dSTORM in combination with ExM, called expansion single-molecule localization microscopy (Ex-SMLM), directly expands the sample in ionic buffers, so that the expanded gel does not change during imaging with switching buffers, which however yields smaller expansion factors compared to expansions in deionized water [189]. In another implementation expansion stochastic optical reconstruction microscopy (ExSTORM) reembeds the expanded gel, which was previously expanded 4x in deionized water, with an uncharged secondary gel [188]. While this second gel shrinks the original gel to about ~3x, it does not change upon incubation in ionic switching buffers. On the flipside, in PALM, POIs are labeled in a 1:1 POI to FP ratio by inserting the FP DNA sequence into the genetic locus of the POI and has no need for any switching buffers. Thus, the protein retention yield in PALM is not affected by external labeling as dSTORM. Hence, establishing a method that combines ExM with PALM (ExPALM) can circumvent these issues. Especially microbes, which possess greater molecular crowding and a highly charged cytosol that make staining more difficult, should benefit most from ExPALM as an implementation host. Additionally, SRM studies combining ExM are rare as only two studies using expansion structured illumination microscopy (ExSIM) of fungi and bacteria were successfully conducted so far, making an implementation of ExPALM in microbiology even more attractive [175, 191]. As the kinetochore is a small structure that can establish protein-protein interactions below the resolution limit of PALM and is a multi-protein complex with very low protein copy numbers, yet densely located proteins, it is the perfect target structure to establish ExPALM.

1.3 Aim of the thesis

The KT plays a crucial role during cell division and has thus been the focus of numerous studies. However, due to its complexity and flexibility, only the *in vitro* structures of certain subcomplexes were successfully investigated at high resolustions so far. Previous attempts to study the complete KT structure *in vivo* based on conventional fluorescence microscopy were not able to resolve single KTs, as the structure is smaller than the diffraction limit of light. With the development of SMLM techniques, higher resolutions were achievable *in vivo*, while also allowing for a quantitative read-out of the fluorescent marker linked to the target protein. Nevertheless, the number of KT studies applying SMLM is still scarce and also only limited to single targets.

Therefore, the goal of this thesis was to create a map of the native *in situ* KT architecture in the fission yeast *Schizosaccharomyces pombe* at a nanometer resolution using, and if necessary developing, advanced SMLM techniques. To build an accurate map of the KT, the positions and orientations of the KT POIs have to be measured in relation to reference proteins, and the number of available POIs per KT complex have to be determined. Therefore, to study the human-like KT in fission yeast, a robust multi-target SMLM imaging scheme had to be implemented by identifying suitable reference proteins, evaluating possible fluorophore combinations, creating a stable and functionally undisturbed strain library, and establishing a SMLM sample preparation, imaging and analysis routine.

CHAPTER 2

Examining the fission yeast kinetochore complex using multi-color SMLM

This chapter is written in the style of a manuscript and was accepted as a report in *Journal of Cell Biology* in 2022. For this publication, the experiments were designed by Dr. David Virant, Jannik Winkelmeier, Dr. Dave Lando, Prof. Dr. Ulrike Endesfelder and me, the experiments were conducted by Dr. David Virant, Jannik Winkelmeier and me, the manuscript figures and tables were designed by Jannik Winkelmeier and me and the manuscript text was written by Prof. Dr. Ulrike Endesfelder with the input from all co-authors. The analysis pipeline was established by Dr. David Virant, Dr. Bartosz Turkowyd, Marc Endesfelder and Prof. Dr. Ulrike Endesfelder. While the initial data analysis was performed by Jannik Winkelmeier, Dr. David Virant, Dr. Bartosz Turkowyd, Marc Endesfelder, Prof. Dr. Ulrike Endesfelder and me, the final data analysis included in the manuscript was performed by Jannik Winkelmeier, Marc Endesfelder, Prof. Dr. Ulrike Endesfelder and me. The supplementary information of this work can be found in this chapter subsequently to the main publication and the code for the determination of KT-POI distances can be found online on GitHub (https://github.com/Endesfelder-Lab/Kinetochore_Distances).

In this publication, we investigate several KT inter-protein distances and copy numbers by using a multi-color SMLM approach, where two reference proteins, one at the spindle pole and one at the centromere were visualized along with one KT - POI a time. Using this, we created a KT model for fission yeast, that while confirming previous assumptions also gives new insights into the organization of the inner KT of fission yeast.

Unraveling the kinetochore nanostructure in *Schizosaccharomyces pombe* using multi-color SMLM imaging

David Virant[1,†], Ilijana Vojnovic[1,2,3,†], Jannik Winkelmeier[1,2,3,†], Marc Endesfelder[4], Bartosz Turkowyd[1,2,3], David Lando[5] and Ulrike Endesfelder[1,2,3*]

[1]Department of Systems and Synthetic Microbiology, Max Planck Institute for Terrestrial Microbiology and LOEWE Center for Synthetic Microbiology (SYNMIKRO), Marburg, Germany

[2]Department of Physics, Carnegie Mellon University, Pittsburgh, Pennsylvania, US

[3]Institute for Microbiology and Biotechnology, Rheinische-Friedrich-Wilhelms-Universität Bonn, Bonn, Germany

[4]Institute for Assyriology and Hittitology, Ludwig-Maximilians-Universität München, Germany

[5]Department of Biochemistry, University of Cambridge, Cambridge CB2 1EW, UK

[†] authors contributed equally

*corresponding author, email: endesfelder@uni-bonn.de

Abstract

The key to ensuring proper chromosome segregation during mitosis is the kinetochore (KT), a tightly regulated multiprotein complex that links the centromeric chromatin to the spindle microtubules and as such leads the segregation process. Understanding its architecture, function and regulation is therefore essential. However, due to its complexity and dynamics, only its individual subcomplexes could be studied in structural detail so far.

In this study we construct a nanometer-precise *in situ* map of the human-like regional KT of *Schizosaccharomyces pombe* using multi-color single-molecule localization microscopy. We measure each protein of interest (POI) in conjunction with two references, cnp1^{CENP-A} at the centromere and sad1 at the spindle pole. This allows us to determine cell cycle and mitotic plane, and to visualize individual centromere regions separately. We determine protein distances within the complex using Bayesian inference, establish the stoichiometry of each POI and, consequently, build an *in situ* KT model with unprecedented precision, providing new insights into the architecture.

Introduction

The proper segregation of chromosomal DNA during cell division is one of the most crucial processes in the cell cycle of living organisms. Aneuploidy, caused by chromosome maldistribution, leads to cancer, birth defects and cell death (Pfau and Amon, 2012; Santaguida and Amon, 2015; Yuen et al., 2005). During chromosome segregation, sister chromatids are separated by the microtubules of the spindle apparatus. Here, the kinetochore (KT), a multiprotein complex, acts as the link between the centromeric DNA and the microtubules emerging from the spindle (Musacchio and Desai, 2017; Roy et al., 2013).

In budding yeast *Saccharomyces cerevisiae*, the KT appears as a structure of about 126 nm in diameter (Gonen et al., 2012). A single KT connects one single microtubule to a 125 base-pair region, a so-called point centromere of defined sequence (Clarke, 1998; Winey et al., 1995). In contrast, in the fission yeast *Schizosaccharomyces pombe,* the KT complex links 2-4 KT microtubules (kMTs) to a regional centromere in the kilobase-pair range (Chikashige et al., 1989; Ding et al., 1993). In higher eukaryotes, the structure is even more extensive. For human chromosomes, the centromeric region spans 0.5-1.5 megabases (Wevrick and Willard, 1989; Zinkowski et al., 1991). Accordingly, the human KT structure connects to about 20 kMTs (McEwen et al., 1998; McEwen et al., 1997).

Despite these differences in centromere length and number of kMTs, the general KT architecture is highly conserved (Drinnenberg et al., 2016; van Hooff et al., 2017). The centromeric region is epigenetically defined by a H3 histone variant, cnp1^{CENP-A}, which replaces one or both H3 in the centromeric nucleosomes (Dunleavy et al., 2011; Lando et al., 2012). (In this report, we use the terminology of *S. pombe* and the human homolog in superscript, if different.) cnp1^{CENP-A} provides the scaffolding for the KT, which consists of several subcomplexes: the CCAN network, the Mis12/MIND complex (MIS12c/MINDc), the KNL1 complex (KNL1c), the NDC80 complex (NDC80c) and the DAM1/DASH complex (DAM1/DASHc or Ska complex in humans) (Kixmoeller et al., 2020; Musacchio and Desai, 2017).

The structures of these subcomplexes have been made available by cryo-EM and x-ray crystallography, e.g. of the CENH3 nucleosome (Migl et al., 2020; Tachiwana et al., 2011), the CCAN network (Hinshaw and Harrison, 2019a; Hinshaw and Harrison, 2019c; Yan et al., 2019), the MIND/Mis12c (Dimitrova et al., 2016; Petrovic et al., 2016), the NDC80c (Ciferri et al., 2008; Valverde et al., 2016) and the Dam1/DASHc (Jenni and Harrison, 2018). Despite advances in reconstituting large sub-complexes, e.g. resolving the 13-subunit Ctf19c/CCAN (Hinshaw and Harrison, 2019a), the assignment of KT proteins to specific subcomplexes within the fully assembled KT has not been successful so far (Gonen et al., 2012; Walstein et al., 2021).

Fluorescence microscopy visualizes proteins of interest (POIs) using fluorescent labels such as fluorescent proteins (FPs) (Tsien, 1998). Quantitative fluorescence measurements provide KT protein copy numbers (Coffman et al., 2011; Dhatchinamoorthy et al., 2017; Joglekar et al., 2008; Joglekar et al., 2006; Johnston et al., 2010; Lawrimore et al., 2011; Schittenhelm et al., 2010; Suzuki et al., 2015) and intra-complex distances (Aravamudhan et al., 2014; Haase et al., 2013; Joglekar et al., 2009; Schittenhelm et al., 2007; Suzuki et al., 2014; Suzuki et al., 2018; Wan et al., 2009). However, the spatial resolution is not sufficient to resolve individual KTs (Tournier et al., 2004). Here, super-resolution microscopy (SRM) bridges the resolution gap between conventional fluorescence microscopy and electron microscopy. The kinetochore has been studied SIM (Dhatchinamoorthy et al., 2019; Schubert et al., 2020; Venkei et al., 2012; Wynne and Funabiki, 2016; Zielinska et al., 2019) and STED microscopy (Drpic et al., 2018; Zielinska et al., 2019). Both provided detailed pictures of the structure at about 100 nm resolution. Only a handful of studies have been carried out at single molecule resolution, so far. Two *in situ* studies each targeted a single protein, cnp1^{CENP-A} (Lando et al., 2012) and Ndc80 (Wynne and Funabiki, 2016), and one study focused on two-color pairs *in vitro* (Ribeiro et al., 2010).

In this study, we investigate the architecture of the regional KT of the fission yeast *S. pombe*. We created a strain library of fluorescent fusions of key proteins of the inner and outer KT. Using quantitative multi-color single-molecule localization microscopy (SMLM) and Bayesian inference, we report *in situ* inner-KT distances and protein copy numbers. Based on those numbers, we can determine the KT architecture during mitosis and build an *in situ* model at a nanometer resolution. Our study confirms *in vitro* studies on reconstituted KT subcomplexes and adds new *S. pombe* specific insights to our current KT knowledge.

Results & discussion

A strategy to unravel the kinetochore structure

To investigate the KT architecture during mitosis, we first designed a robust and quantitative multi-color SMLM imaging strategy which did not exist before (Vojnovic et al., 2019). Specifically, our aim was to measure protein stoichiometries and distances between different POIs to build a molecular KT map (Fig. 1A, B). We set up a triple-color strain library of two labeled reference proteins and a varying POI: A spindle reference to identify cells in metaphase/early anaphase and the orientation of the mitotic plane and a second, centromeric reference as the landmark for KT assembly. To be a reliable reference, the chosen proteins need a defined organization, sufficient abundance and to be present throughout the cell cycle.

This led us to choose sad1, a protein from the spindle pole body (SPB) (Vojnovic, 2016) and the centromere-specific histone cnp1^{CENP-A} (Lando et al., 2012).

From our imaging priority (1. registering the mitotic plane, 2. quantitative read-out of POI stoichiometry and distribution, 3. quantitative read-out of cnp1^{CENP-A} as reference for stoichiometry and for distances), experience on autofluorescence and labeling (Fig. S1), we derived alternative imaging strategies (Materials & Methods) and finally decided on using dual-color PALM imaging by UV- and primed photoconversion (Turkowyd et al., 2017; Virant et al., 2017) together with a diffraction-limited SPB reference as third color (Fig. 1C). For the FP labels, we chose mScarlet-I (Bindels et al., 2017) as SPB reference and UV-photoactivatable PAmCherry1 (Subach et al., 2009) as centromeric reference and created a dual-color reference strain. For the POIs, we chose primed photoconvertible mEos3.2-A69T (Turkowyd et al., 2017), whose read-out we calibrated using a FtnA 24mer standard (Fig. 2 B, C) and built, using the dual-color strain as a template, a triple-color (3C) strain library targeting in total 10 different key POIs of the inner and outer KT at their C-terminus (Fig. 1 C, Fig. S2, Table S1).

Health assessment of the strain library

The integration of FPs may reduce protein functionality and alter cell physiology. Performing spot tests, we checked for temperature sensitivity (25, 32 and 37°C) and for KT-MT attachment defects using thiabendazole (TBZ, 2.5, 5.0, 7.5 and 10.0 mg/mL), a MT depolymerizing drug (Tang et al., 2013). Via flow cytometry, we tested all strains for a wildtype-like phenotype. The 3C strains showed no deviations from the parental h^{+}/WT strain except for two strains, cnp3^{CENP-C}-3C and dam1-3C (Fig. S2 C-E). cnp3^{CENP-C}-3C exhibited both, a TBZ sensitivity and a notably larger cell size, and was excluded from further analyses. Interestingly, cnp3^{CENP-C} interacts with the N-terminal CATD region of cnp1^{CENP-A} via its C-terminus (Black et al., 2007; Carroll et al., 2010; Guse et al., 2011). Thus, FP tagging of both, the cnp1^{CENP-A} N-terminus and cnp3^{CENP-C} C-terminus might have caused the observed effects. This hypothesis is supported by measurements using a 1C strain where only the cnp3^{CENP-C} C-terminus was tagged, as Cnp3^{CENP-C}-1C did not show any modified phenotype (data not shown). Dam1-3C appeared to be more stable in TBZ spot tests. Interestingly, similar results were obtained before: a dam1 deletion mutant was hypersensitive to TBZ, whereas a C-terminal truncation (dam1-127) led to higher TBZ resistance (Sanchez-Perez et al., 2005). Dam1 with two C-terminal mutations also proved to be more resistant to TBZ (Griffiths et al., 2008). This suggests that the dam1 C-terminus is important for controlling kMT stability which might increase by C-terminal tags. As dam1-3C showed no mitotic delay or altered phenotype, it was included in the study.

Determining kinetochore distances and protein stoichiometry

All 3C strains were prepared and imaged by a strict protocol that was repeated on different days using biological replicates (Materials & Methods). Since single centromeres can only be resolved during metaphase/early anaphase (Fig. S3, (Tournier et al., 2004)), the fraction of cells in this phase was increased by cell cycle synchronization (Fig. S2). All SMLM data was post-processed and annotated by several manual and automated analysis steps and stored in a SQL database (Fig. 2 A). For this work, we focused on i) the distances of the POIs to the centromeric region marked by cnp1^{CENP-A} and ii) their copy numbers. For the distances, we used Bayesian inference and derived the posterior probability distribution for each POI-cnp1^{CENP-A} distance (Fig. 2 F, G, Materials & Methods). In our Bayesian model (Fig. 2 F), we explicitly accounted for the angular offset between the kMT and spindle axes (Fig. 2 F, S3). We calibrated the measured localization counts per POI cluster using bacterial ferritin FtnA, an established homo-oligomer protein standard consisting of 24 subunits (Fig. 2 B, C).
In Fig. 3, we summarize all POI distances to cnp1^{CENP-A} and stoichiometries (statistics in Tables 1, 2). Our *in-situ* measurements are consistent with work based on conventional fluorescence microscopy (these studies, however, show considerable variation between them) and very accurately confirm structural data from *in vitro* EM and crystallography considering that i) typically tens to hundreds of amino acids long sequences of termini are unstructured and therefore missing from structural data, which ii) also do not carry FP tags of 2-3 nm barrel size. We will discuss the KT structure in the order of inner to outer KT POIs below.

Fta2^{CENP-P} and fta7^{CENP-Q} are part of the COMAc/CCAN network in a strict 1:1 stoichiometry. Their C-termini are close to each other, oriented in the same direction (Hinshaw and Harrison, 2019b; Pesenti et al., 2022). Our *in situ* distances of 11.4 ± 1.9 nm for fta2^{CENP-P} and 11.7 ± 2.9 nm for fta7^{CENP-Q} and the copy numbers of 55.1 ± 3.3 and 57.4 ± 4.1 reflect these properties and are consistent with cryo-EM data from reconstituted *S. cerevisiae* COMAc (Yan et al., 2019), with distances of N-cnp1^{CENP-A} to fta2^{CENP-P}-C and to fta7^{CENP-Q}-C being 9.7 nm and 10.7 nm, respectively.
Mis12 and nnf1^{PMF1} are both part of the MINDc in a 1:1 ratio (Maskell et al., 2010; Petrovic et al., 2010). Our distances are 28.0 ± 1.6 nm for mis12 and 27.1 ± 1.4 nm for nnf1^{PMF1}. They confirm fluorescence data where all C-termini of the MINDc proteins line up (Joglekar et al., 2009) and show FRET proximity signal (Aravamudhan et al., 2014) as well as EM data positioning all C-termini near each other (Petrovic et al., 2014). For spc7^{KNL1}, we find 25.9 ± 1.2 nm. Whereas full-length spc7^{KNL1} has not been purified (Maskell et al., 2010), its C-terminus has been resolved by EM (Petrovic et al., 2014) and to be close to the C-termini of mis12 and nnf1 (Petrovic et al., 2016). In fluorescence microscopy, the spc7^{KNL1} C-terminus

colocalized with the spc24 C-terminus within the NDC80c (reflected by our spc25 data below) (Joglekar et al., 2009). Interestingly, in our hands, the MINDc and spc7^{KNL1} proteins' stoichiometry amounts to 1 : 1.3 : 1.3 (copy numbers of 73.1 ± 3.1 mis12: 92.6 ± 3.6 nnf1^{PMF1}: 95.4 ± 3.3 spc7^{KNL1}). This differs from the reported 1 : 1 ratio for mis12 : nnf1^{PMF1} but posits a 1 : 1 ratio for nnf1^{PMF1} and spc7^{KNL1}. From reconstitution and cross-linking experiments, it is known that the MINDc binds spc7^{KNL1} via mis14^{NSL1} (Petrovic et al., 2010). This binding site, i.e. the C-termini of spc7^{KNL1} and mis14^{NSL1}, is conserved (Petrovic et al., 2014). This places our *in situ* measured 1 : 1 ratio of nnf1^{PMF1} and spc7^{KNL1} in agreement with the *in vitro* literature and demands for future work on mis12.

Whereas the structure of the outer KT is conserved (D'Archivio and Wickstead, 2017; Meraldi et al., 2006; van Hooff et al., 2017), several strategies exist for bridging centromere and outer KT and the importance of the different inner KT structures, i.e. either based on cnp20^{CENP-T}, cnp3^{CENP-C} or fta7^{CENP-Q} (COMAc), varies between organisms (Hamilton and Davis, 2020; van Hooff et al., 2017). While the inner KT of *Drosophila melanogaster* is defined by cnp3^{CENP-C} (Ye et al., 2016), *S. cerevisiae* relies on COMAc with cnp3^{CENP-C} as a backup (Hamilton et al., 2020; Hornung et al., 2014). Furthermore, while cnp20^{CENP-T} is non-essential in *S. cerevisiae* (Bock et al., 2012; De Wulf et al., 2003; Giaever et al., 2002; Schleiffer et al., 2012), it is the primary strategy in chicken (Hara et al., 2018) and humans (Suzuki et al., 2014) which also rely on cnp3^{CENP-C} as backup (Hamilton and Davis, 2020). To date, the preferred inner KT pathway of *S. pombe* is unknown (Hamilton and Davis, 2020). The deletion of cnp3^{CENP-C} in *S. pombe* is viable (Chik et al., 2019; Kim et al., 2010; Tanaka et al., 2009) whereas deletion of cnp20^{CENP-T} is not (Tanaka et al., 2009). This is inverted for *S. cerevisiae* (Bock et al., 2012; De Wulf et al., 2003; Giaever et al., 2002; Kim et al., 2010; Meeks-Wagner et al., 1986; Schleiffer et al., 2012). This organismal difference is also reflected in protein copy numbers as mif2 (cnp3^{CENP-C}) is more abundant than cnn1 (cnp20^{CENP-T}) in S. c*erevisiae*, chicken and humans (Cieslinski et al., 2021; Johnston et al., 2010; Suzuki et al., 2015). For the COMAc, fta7^{CENP-Q} (Ame1) and mis17 (Okp1) are essential for both yeasts (Hayles et al., 2013; Kim et al., 2010) and deletions of fta2^{CENP-P} and mal2^{CENP-O} are non-viable in *S. pombe*.

In our measurements, cnp20^{CENP-T} has a distance of 8.3 ± 2.4 nm to cnp1^{CENP-A}, similar to the MIND proteins fta7^{CENP-Q} and fta2^{CENP-P}. Furthermore, we measure a 1: 0.9 ratio of cnp20^{CENP-T} to the COMAc (Table S4). This underlines the importance of cnp20^{CENP-T} for *S. pombe* KTs as an essential protein (Tanaka et al., 2009) and suggests that *S. pombe* relies on the COMAc and cnp20^{CENP-T} in equal measures - unlike *S. cerevisiae*, which relies on COMAc and cnp3^{CENP-C}.

To map the Ndc80c, we measured ndc80^{HEC1} and spc25 and obtained distances of 36.2 ± 1.5 nm and 21.9 ± 2.2 nm and copy numbers of 107.2 ± 4.3 and 119.1 ± 6.2, respectively. The

shorter distance of spc25-C to cnp1^{CENP-A} in comparison to the distances of the MIND proteins to cnp1^{CENP-A} might reflect a spatial overlap of the POIs termini to interlock and stabilize the contact sites of the two sub-complexes and is in agreement with cross-linking data (Kudalkar et al., 2015). Furthermore, the order of increasing C-terminal distances from spc25 to spc7^{KNL1}, nnf1^{PMF1}, mis12 and ndc80^{HEC1} correlates with a study that measured decreasing FRET signal between spc25 and the POIs (Aravamudhan et al., 2014). In another study, an increase of Ndc80c and MINDc copy numbers from metaphase to anaphase was shown (Dhatchinamoorthy et al., 2017). For our data, we only selected and analyzed cells in metaphase/early anaphase. Comparing the mitotic spindle length and corresponding localization counts of POI and cnp1^{CENP-A} clusters, we did not detect any interdependence of spindle length and copy numbers, which confirms our cell cycle selection (data not shown).
For dam1 within the DAM1/DASHc, we find a distance of 64.2 ± 1.3 nm and a copy number of 63.7 ± 2.4. Comparing the positions of ndc80^{HEC1} and dam1, dam1 is closer than one would expect when colocalizing with the N-term/globular head of ndc80^{HEC1} (Aravamudhan et al., 2014; Roscioli et al., 2020). Dam1 possesses a highly variable length for different fungi and whereas its C-terminus has been shown to interact with the globular head of ndc80^{HEC1} in *S. cerevisiae,* it is predicted to be too short (155 aa in *S. pombe,* 343 aa in *S. cerevisiae*) to do so in *S. pombe* (Jenni and Harrison, 2018). Furthermore, deleting dam1 is viable for *S. pombe* (Zahedi et al., 2020) but inviable for *S. cerevisiae* (Giaever et al., 2002). Consistent with these observations, we hypothesize that *S. pombe* dam1 indeed interacts and colocalizes with the ndc80^{HEC1}-loop region. To explore this further, imaging the position of the N-terminus and loop region of ndc80^{HEC1} or imaging dad1 (localizing at the DASH ring within the ndc80^{HEC1} loop (Jenni and Harrison, 2018)) will be targeted in the future.
In contrast to the proteins of the outer KT complexes, which exhibit higher protein abundance, dam1 shows a similarly low copy number as the inner KT COMAc proteins. This was already seen in fluorescence measurements before (Joglekar et al., 2008), where protein abundance increased from the inner to the outer KT for both, *S. pombe* and *S. cerevisiae*, and a substantial drop was measured for *S. pombe* dam1 but not for *S. cerevisiae*.

Summary

We used quantitative SMLM imaging to map the KT architecture at a nanometer resolution. It is the first holistic SMLM study of a multi-protein complex in *S. pombe* with which we were able to drastically improve the positioning and stoichiometry accuracy of 10 KT proteins and uniquely, within the full, native KT structure. Our work thus fills in the gap between the highly resolved *in vitro* studies and previous *in vivo* experiments and provides *in situ* nanometer-

precise distances between the individual proteins and their copy numbers. Our measurements confirm the conserved structure of the outer KT and add knowledge on *S. pombe* specific outer KT details, e.g. on dam1 localization at the DASH ring. For the inner KT, strategies vary in between different organisms, i.e. being based on either cnp20^{CENP-T}, cnp3^{CENP-C} or fta7^{CENP-Q}. While other studies have reported the generally different use and importance of the inner KT structures between organisms, the *S. pombe* inner KT architecture so far remained unexplored (Dimitrova et al., 2016; Hamilton and Davis, 2020; Petrovic et al., 2016; Przewloka et al., 2011; Screpanti et al., 2011). We quantify the stoichiometry of the inner KT pathways for *S. pombe*, and show the *S. pombe* specific equal importance of COMAc and cnp20^{CENP-T}.

The SMLM study on the *S. cerevisiae* KT (Cieslinski et al., 2021), carried out in parallel to our work, is a perfect complement. Comparing the phylogenetically quite distant yeasts, the data consistently shows that KTs generally possess similar architecture despite *S. cerevisiae* maintaining a point centromere and *S. pombe* a regional structure (Table S4, S5). Importantly, one substantial difference for the inner KT surfaced: The ratio of cnp20^{CENP-T} to COMAc is 1:0.9 in *S. pombe* and 1:2.0 in *S. cerevisiae*. This is a strong indication that cnp20^{CENP-T} organization indeed differs between the two organisms. Furthermore, the positioning of *S. cerevisiae* ask1 is consistent with the position of *S. pombe* dam1 and thus supports our reasoning that the C-terminus of *S. pombe* dam1 is localized at the DASH ring and not at the ndc80 globular heads (like for *S. cerevisiae)*.

In the outlook, our strain library and results provide an excellent platform for quantitative SMLM work on the KT that goes beyond copy numbers and distances, and we will – by further dissecting our *S. pombe* KT data – focus on structural shapes and changes during the cell cycle, as well as extend our work to medically relevant mutants.

Author Contributions

D.Lando and U.Endesfelder designed research; D.Virant, I.Vojnovic, J.Winkelmeier, D.Lando and U.Endesfelder designed experiments; D.Virant, I.Vojnovic and J.Winkelmeier performed experiments; D.Virant, B.Turkowyd, M.Endesfelder and U.Endesfelder developed analysis procedure and software; I.Vojnovic, J.Winkelmeier, M.Endesfelder and U.Endesfelder performed the all-data final analysis, D.Virant and U.Endesfelder acquired funding; I.Vojnovic and J.Winkelmeier designed figures and tables; U.Endesfelder wrote the paper with input from all authors.

Funding
This work was supported by funds from the Max Planck Society, a travel grant to D. Virant by the Boehringer Ingelheim Fonds for a research-stay with D. Lando, funds at Carnegie Mellon University, the NSF AI Institute: Physics of the Future, NSF PHY- 2020295 and funds at Bonn University.

Acknowledgements
We are grateful to E. Laue for discussions and advice, to M. Rigl, K. Schmidt and B. Aybey for their help in the laboratory, and to S. González Sierra and V. Sourjik for their help with flow cytometry.

Competing financial interests
The authors declare no competing financial interests.

Code availability
The Stan code and our raw data on the posterior distributions of KT protein distances can be found in File S1.

Materials and methods

Choosing a labeling strategy for quantitative SMLM in *S. pombe*

While the number of SRM studies in fission yeast being published has been increasing in recent years, the majority of them are single color studies that target individual proteins (Akamatsu et al., 2017; Bell et al., 2014; Etheridge et al., 2014; Etheridge et al., 2021; Lando et al., 2012; Laplante et al., 2016; Matsuda et al., 2015), and only a few are dual-color studies visualizing several targets at the same time (Bestul et al., 2021; McDonald et al., 2017; Virant et al., 2017). Among those studies, SMLM imaging takes on a special role, as this technique does not only offer increased resolution, but also allows the determination of protein stoichiometries (Akamatsu et al., 2017; Lando et al., 2012; Laplante et al., 2016). Due to the limited number of working fluorophore/labeling combinations for SMLM imaging in microbial organisms, developing a successful multicolor single-molecule localization microscopy strategy can be challenging (Vojnovic et al., 2019).

To construct a nanoscale map of the KT in *S. pombe*, we labeled three proteins, the protein of interest, the centromeric reference cnp1^{CENP-A} and the spindle pole protein sad1. Imaging the spindle poles enabled us to a) easily identify and read out the correct cell cycle stage and focal plane and to b) drastically improve the accuracy of our distance calculations. The latter is possible as all three protein(-clusters) can be assumed to lie on a straight line, which allows a direct estimation of the size of the measurement errors from the deviation of that line (see data analysis and File S1).

As all organisms and targets have different requirements and specifics, SMLM labeling strategies, which need to be highly optimized to produce satisfying results, must be specifically adapted and tested for the actualities of each biological system (Vojnovic et al., 2019). In *S. pombe*, we avoided the green and blue color channels, due to increased phototoxicity as well as the fact that we found high levels of autofluorescence in those channels, as *S. pombe* is easily stressed by unstable or insufficient pH, temperature or aeration.

Furthermore, we found a high level of autofluorescence due to a selection marker in standard laboratory *S. pombe* strains which works by interrupting the adenine biosynthesis pathway to accumulate a precursor molecule – a bright red pigment which can be easily seen in screening colonies (Allshire, 1995; Levenberg and Buchanan, 1957; Lukens and Buchanan, 1959). These adenine deficient laboratory strains (most common are ade6-M210 and ade6-M216), even when grown under full adenine supply, possess a background level of metabolites which strongly disturb sensitive SMLM measurements even when colonies or liquid cultures remain inconspicuously colorless (Fig. S1 and (Winkelmeier, 2018)). We thus “cured” the adenine gene using a wildtype strain template for all strains in this study.

For three labels we were in need for three fluorophores with mutually supporting SMLM imaging properties: In general, *in situ* targeting of proteins can be achieved extrinsically by using dyes (e.g. using immunofluorescence and enzyme or peptide tags) or intrinsically by using FPs as genetic tags. On the one hand, organic dyes are brighter and therefore have a higher signal-to-noise ratio and localization precision, but on the other hand they bring two disadvantages: a) extrinsic staining is accompanied by non-specific staining and has unknown and possibly even heterogeneous staining efficiency, and b) SMLM imaging of organic dyes requires imaging buffers and might exhibit heterogeneous switching behavior. These drawbacks significantly affect *any* quantitative SMLM study but become especially severe for low copy number targets and for multi-color studies. While evaluating different labeling and imaging strategies, we tested different dyes. Surprisingly, the "golden SMLM standard" Alexa Fluor 647 does not work reliably in *S. pombe* (highly heterogeneous blinking to even non-blinking behavior - which we not only found for live cells but also for fixed cells and for all buffers tested (see buffer table in (Turkowyd et al., 2016)) for reasons unknown to us and exhibits extraordinary high nonspecific staining levels under even rigorous staining protocols due to its unmasked charges (Fig. S1). Other dyes yielded the desired low nonspecific staining and controlled blinking behavior. Nevertheless, dyes with masked charges (e.g. CF680) never achieved high labeling efficiencies, which may be partially attributed to their increased size (e.g. CF680 has about 2.3 times the molecular weight of Alexa Fluor 680 due to the masking groups) and the high molecular crowding of *S. pombe* cells (Fig. S1). Among all tested dyes, the best working ones available to us were JF549 and CF647 (Fig. S1). Nevertheless, for all labeling strategies involving dyes, achieving reliable and high labeling efficiencies as well as quantitative dual-color SMLM read-outs without any channel crosstalk or a high miss rate of events (we tested chromatic dual-color, spectral demixing and dye-FP-mixture strategies) remained problematic. Thus, all measurement strategies in our final selection solely relied on direct FP fusions and were all in the orange-red part of the visual spectrum. As mEos2, our first FP of choice induced conspicuous phenotypical anomalies for several POIs (and is known to artificially aggregate and self-oligomerize at higher densities interfering with POI positioning and function (Wang et al., 2014)), we carefully tested different FPs and ultimately decided to utilize a dual-color approach published in Virant et al. (Virant et al., 2017), which relies on mEos3.2-A69T and PAmcherry1 and added mScarlet-I as the label for the SPB reference.

Strain construction

To construct a dual-color reference strain with both a reference at the centromere and at the SPB, we added a spindle reference to the *S. pombe* strain DL70, which already carries a PAmCherry1-cnp1^{CENP-A} N-terminal fusion (Lando et al., 2012). To tag the SPB protein sad1

with mScarlet-I (Bindels et al., 2017) at its C-terminus, we adapted a cloning strategy from Hayashi et al. (Hayashi et al., 2009): DL70 cells were made chemically competent (Frozen-EZ Yeast Transformation II Kit, Zymo Research, #T2001) and were transformed with a linear DNA fragment consisting of the mScarlet-I sequence and a hygromycin resistance cassette flanked by 500-600 bp of homology arms on both sides for homologous recombination into the genome downstream of the native sad1 gene. Additionally, we inserted the terminator ADH1 from *S. cerevisiae* (Curran et al., 2013) between POI-FP and resistance genes to ensure native protein expression independent from the resistance gene. Cells were streaked on a YES agar plate, incubated overnight at 32°C and replica-plated on a YES agar plate containing 100 mg/L hygromycin B (Roche, #10843555001). The hygromycin plates were incubated for 1-2 days at 32°C until colonies had formed. Colonies were checked for successful integration of the mScarlet-I ADH1 hygromycin cassette by colony PCR and subsequent sequencing. When we tested the resulting strain SP129 for single-molecule imaging, we noted a high level of autofluorescence that we could attribute to an accumulating precursor in the interrupted adenine biosynthesis pathway due to the ade6-210 mutation, which is as bright as the single-molecule FP intensities and therefore severely compromises the SMLM read-out (Fig. S1 and Materials & Methods) (Allshire, 1995; Levenberg and Buchanan, 1957; Lukens and Buchanan, 1959). We thus repaired the ade6 gene using a wildtype strain template. Transformed cells were streaked on EMM 5S agar plates and grown overnight at 32°C, replica-plated on EMM agar plates containing 225 mg/L of histidine, leucine, lysine and uracil each, but only 10 mg/L of adenine and incubated for 1-2 days at 32°C. Cells that still possessed the truncated ade6 gene turned pink due to accumulation of the precursor (which is also used as a selection marker in the literature (Allshire, 1995)). Colonies with a successfully integrated wildtype ade6 gene stayed white and were checked by sequencing. This new strain (SP145) was used as the parent strain for the construction of a three-color KT library: Here, each POI was tagged with the FP mEos3.2-A69T using the same procedure as for sad1-tagging but using a kanamycin resistance cassette (Fig. S2 a). Successful transformants were selected on YES agar plates containing 100 mg/L geneticin (Roche, #4727894001) and checked with colony PCR and sequencing. Sequencing was done with the Mix2Seq kit (Eurofins Genomics, Germany). A colony was picked for each newly generated strain, cultured to early stationary phase in rich YES medium, mixed in a 1:1 ratio with sterile 87% glycerol and stored at -80°C. All strains used in this study can be found in Table S1 and all primers used for strain construction can be found in Table S2.

Spot tests

To assess the effect of the FP tags on the POIs and reference proteins, spot tests were conducted to compare the temperature and thiabendazole (TBZ, inducing mitotic defects by microtubule depolymerization) sensitivity to the parental h^+ WT strain (Fig. S2). For this, *S. pombe* strains from cryostocks were streaked on YES agar plates and incubated at 32°C for two days. After growing the overnight cultures in YES medium at 25°C to an OD_{600} of 1-2, all cultures were adjusted to an OD_{600} of 1.0 and 2 µL each of a serial dilution of 1:1, 1:10, 1:100 and 1:1000 were plated either on YES agar plates and incubated at 25, 32 or 37°C for three days for temperature sensitivity testing, or on YES agar plates containing 2.5, 5.0, 7.5 or 10.0 µg/mL TBZ (Cayman Chemical Company, #23391) and incubated at 25°C for three days.

Flow Cytometry

To assess the effect of the fluorescent protein tags on the phenotype of cells, flow cytometry was conducted (Fig. S2). Cells were streaked from cryostocks on YES agar plates and grown at 32°C for 2-3 days until colonies were visible. A single colony was picked, inoculated in 10 mL rich YES medium and grown overnight (25°C, 180 rpm). Subsequently, the OD_{600} for each strain was measured and an appropriate cell amount was used to inoculate 10 mL of EMM 5S to the same starting OD_{600}. Cells were grown overnight (25°C, 180 rpm) and the OD_{600} was measured again the next morning to verify that cells were in logarithmic growth phase. Light scattering (FSC and SSC) was measured with a BD LSRFortessa flow cytometer (BD Biosciences, Germany). Before each measurement, samples were mixed thoroughly to disperse cell aggregates. For each strain, 10.000 cells were recorded using the FACSDiva software (BD Biosciences, Germany). Data was analyzed and plotted with the software FlowJo (BD Biosciences, Germany).

Sample preparation for SMLM imaging

After streaking *S. pombe* strains from cryostocks on YES agar plates and incubating them at 32°C until colonies were visible, overnight cultures were inoculated in rich YES media at 25°C and grown to an OD_{600} of 1-2. Next, 2x 50 mL night cultures were inoculated in freshly prepared EMM 5S media starting at OD_{600} 0.1 and grown at 25°C for around 16 h to OD_{600} 1.0-1.5. Cultures were centrifuged at 2000 rpm at 25°C for 5 min, the supernatant was discarded, and the pellets were resuspended in 200 µL fresh EMM 5S each. Meanwhile, for cell synchronization, two previously prepared and frozen 15 mL falcons containing 20% lactose (Carl Roth #6868.1) were thawed at 30°C and the cell suspension was carefully added on top of the still cold lactose gradient (Fig. 2). The falcons were then centrifuged at 1000 rpm for 8

min and 1 mL of the resulting upper cell layer, which consists of cells in early G2 stage, was extracted, added to 1 mL fresh EMM 5S and centrifuged at 4000 x g for 1 min. The pellets were resuspended in 500 µL EMM 5S, combined and the OD_{600} was measured. The cell suspension was inoculated in fresh EMM 5S at a starting OD_{600} of 0.6 and grown for 60, 70 or 80 min at 25°C. At each time point, 2 mL aliquots were taken from the main culture for chemical fixation with 3% paraformaldehyde (PFA, Sigma-Aldrich, #F8775) at 20 min at RT. The fixed cells were centrifuged at 4000xg for 2 min and washed six times with 1 mL washing buffer alternating between 1xPBS, pH 7.5 (Gibco, #70011-036) and 50 mM Tris-HCl, pH 8.5 (Carl Roth, #AE15.2) with each 10 min of incubation. The cells were resuspended in 500 µL Tris-HCl after the last wash, a 1:1000 dilution of previously sonicated dark red (660/680) FluoSpheres (Molecular probes, #F8807) was added to serve as fiducial markers for drift correction (Balinovic et al., 2019) and incubated for 10 min in the dark. Ibidi 8-well glass bottom slides (Ibidi, #80827) were cleaned by incubating 1M KOH for 30 min, coated with poly-L-lysine (Sigma-Aldrich, #P8920-100ML) for 20 min and air dried thereafter. Next, 200 µL of the bead/cell mix were added to each well and were incubated for 10 min in the dark. Meanwhile, a 0.5% w/v low gelling agarose solution (Sigma-Aldrich, #A9414-100G) was melted in 50 mM Tris-HCl at 70°C for 1-2 min, a 1:1000 dilution of dark red (660/680) FluoSpheres was added, and the mix was kept at 32°C until further use. The supernatant of the bead/cell mix incubating in the Ibidi 8-well glass bottom slide was carefully removed on ice and six drops of the agarose mix were carefully added on each well and incubated for 5 min for proper gelation. Finally, 200 µL 50 mM Tris-HCl, pH 8.5 were added to each well. Samples were stored at 4°C for a maximum of one day until being imaged.

Microscope setup and SMLM Imaging

A custom built setup based on an automated Nikon Ti Eclipse microscopy body including suitable dichroic and emission filters for SMLM imaging using Photoactivated Localization Microscopy imaging by primed photoconversion (PC-PALM) (ET dapi/Fitc/cy3 dichroic, ZT405/488/561rpc rejection filter, ET610/75 bandpass, all AHF Analysentechnik, Germany) and a CFI Apo TIRF 100× oil objective (NA 1.49, Nikon) was used for multi-color imaging experiments as described earlier (Virant et al., 2017). The Perfect Focus System (PFS, Nikon, Germany) was utilized for z-axis control and all lasers (405 nm OBIS, 488 nm Sapphire LP, 561 nm OBIS, Coherent Inc. USA) except the 730 nm laser (OBIS, Coherent Inc. USA) were modulated by an acousto-optical tunable filter (AOTF) (TF525-250-6-3-GH18, Gooch and Housego, USA) in combination with the ESio AOTF controller (ESImaging, UK). Single-molecule fluorescence was detected using an emCCD camera (iXON Ultra 888, Andor, UK)

at a pixel size of 129 nm and the image acquisition was controlled by a customized version of µManager (Edelstein et al., 2010). All imaging was done at room temperature.

Movie acquisition of all triple-color strains was performed sequentially in HILO mode (Tokunaga et al., 2008). First, the sample was illuminated at low intensity 561 nm with 0.1-1 $W*cm^{-2}$ at the sample level to identify fields of view containing a good number of cells with two SPB spots (metaphase and early anaphase A cells) aligned in parallel to the focal plane. The sad1-mScarlet-I signal was read-out by taking 100 images of 60 ms exposure time with the 561 nm laser at 200 $W*cm^{-2}$ (at the sample level). Residual mScarlet-I signal was photobleached using 1 $kW*cm^{-2}$ of 561 nm laser light for 30-60 s. Next, the green-to-red photoconvertible FP mEos3.2-A69T was imaged in the same spectral channel using primed photoconversion by illuminating the sample with 488 (at every 10th frame) and continuous 730 nm laser light (6 - 70 & 450 $W*cm^{-2}$ respectively) and read-out by 561 nm at 1 $kW*cm^{-2}$ for 15.000 frames of 60 ms exposure. An additional post-bleaching step with 488 nm laser light (210 $W*cm^{-2}$ for 20 s) was performed to ensure that no residual mEos3.2-A69T signal was detected in the next acquisition step. Finally, PAmCherry1-cnp1^{CENP-A} was photoactivated by illumination with 10 - 20 $W*cm^{-2}$ of 405 nm laser light and read-out by 561 nm at 1 $kW*cm^{-2}$ for 10.000 frames of 60 ms exposure. Keeping the field of view well defined, we ensured homogeneous illumination.

Staining of samples with organic dyes

The construction of the N-terminal Halo-cnp1 strain is described in (Vojnovic, 2016). An overnight Halo-cnp1 YES culture was harvested by centrifugation, resuspended in fresh YES and fixed with 3.7% PFA at room temperature (RT) for 10 min. Afterwards, the sample was washed 3x and residual PFA was quenched using 1x PEM (100 mM PIPES (Sigma-Aldrich, #P1851-100G), pH 6.9, 1 mM EGTA (Sigma-Aldrich, #EDS-100G), 1 mM $MgSO_4$ (Sigma-Aldrich, #M2643-500G)) containing 50 mg/mL NH_4Cl (Carl Roth, #P726.1). Next, the sample was permeabilized using 1.25 mg/mL Zymolyase (MP Biomedicals, #320921) in 1x PEM at 37°C for 10 min and subsequently washed 3x with 1x PEM for 10 min. The sample was incubated using a few drops of Image-iT FX signal enhancer (Invitrogen, #I36933) at RT for 1 h to prevent non-specific staining and afterwards stained with 50 nM Halo-CF647 in PEMBAL buffer (1x PEM containing 3% BSA (Sigma-Aldrich, #A8549-10MG), 0.1% NaN_3 (Carl Roth, #4221.1), 100 mM lysine hydrochloride (Sigma-Aldrich, #L5626)) at RT for 3 h. The stained cells were then washed four times for 10 min with alternating 1x PEM and 1x PBS and incubated at RT for 15 min on a previously washed and with poly-L-lysine coated Ibidi 8-well glass bottom slide. Finally, the attached cells were washed twice with 1x PEM for 10 min.

SMLM imaging and post-processing of dye-stained samples

The stained Halo-cnp1 strains were imaged in a redox buffer (100 mM MEA (Sigma-Aldrich, #MG600-25G) with an oxygen scavenger system (van de Linde et al., 2011) in 1x PEM) and illuminated with a 637 nm laser (OBIS, Coherent Inc. USA) at 1.4 kW*cm^{-2} at the sample level with an exposure time of 50 ms for 10.000 frames on the same setup as described before, except that a different dichroic (ZET 405/488/561/640, Chroma) and longpass filter (655 LP, AHF) were used. Single-molecule localizations were obtained by the open-source software Rapidstorm 3.2 (Wolter et al., 2012). In order to track localizations that appeared in several frames and thus belong to the same emitting molecule, the NeNA localization precision value (Endesfelder et al., 2014) was calculated in the open-source software Lama (Malkusch and Heilemann, 2016).

Reconstruction of SMLM images

For visualization, we aimed to reconstruct SMLM images that neither over- nor under-interpret the resolution of the SMLM data and resemble fluorescence images as closely as possible. Localizations were tracked together using the Kalman tracking filter in Rapidstorm 3.2 with two sigma, and the NeNA value used as sigma (dSTORM data), or using kd-tree tracking (3D-color strain library data, described in detail in the data analysis section below). Images were then reconstructed in Rapidstorm 3.2 or 3.3 with a pixel size of 10 nm. Rapidstorm linearly interpolates the localizations and fills neighboring pixels based on the distance between the localization and the center of the main subpixel bin to avoid discretization errors (Wolter et al., 2012). These images were then processed with a Gaussian blur filter based on their NeNA localization uncertainty in the open-source software ImageJ 1.52p (Schindelin et al., 2012). Importantly, images were only used for image representation purposes, all data analysis steps were conducted on the localization data directly (see data analysis).

Construction of the FtnA protein standard

The pRSETa-FtnA backbone was amplified from pRSETa BC2-Ypet-FtnA (Virant et al., 2018), the mEos3.2-A69T fragment was amplified from pRSETa-mEos3.2-A69T (Turkowyd et al., 2017) with a 18 and 23 bp overlap to the pRSETa-FtnA backbone respectively. Purified DNA fragments (Clean & Concentrator-5 Kit, Zymo Research, #D4013) were merged by Overlap-Extension PCR in a 1:2 ratio of backbone to insert. The resulting plasmid was purified and transformed into competent DH5α cells and incubated on LB AmpR agar plates at 37°C overnight. Plasmids were isolated from individual colonies (Monarch Plasmid Miniprep Kit,

New England Biolabs, #T1010L) and sequenced (Mix2Seq Kit NightXpress, Eurofins genomics). The confirmed construct was transformed into competent Rosetta DE3 cells.

Sample preparation and imaging of the FtnA protein standard

Rosetta DE3 containing pRSETa mEos3.2-A69T-FtnA were grown over night at 37°C and 200 rpm in 50 mL AIM (autoinducing medium containing freshly added 25 g/L glucose (Carl Roth, #X997.2) and 100 g/L lactose (Carl Roth, #6868.1)). Cells were harvested by centrifugation at 4000 x g and 4°C for 30 min and the pellet was resuspended in 2 mL 50 mM Tris HCl (Carl Roth, #AE15.2) containing 25 mM NaCl (Sigma-Aldrich, #S3014-500G) at pH 8.5. The bacterial cell wall was digested by incubation with 50 mg/mL Lysozyme (Sigma-Aldrich, #L2879) for 2 h at 4°C. The sample was homogenized (Tough micro-organism lysing tubes (Bertin, #VK05) with 0.5 mm glass beads in Precellys 24 tissue homogenizer at 3x 15 s and 5000 rpm at RT). The cell lysate was centrifuged at 4000 x g for 30 min at 4°C and the supernatant was transferred into a clean Eppendorf tube. The centrifugation and transfer were repeated to ensure a debris-free supernatant. For long-term storage 30% glycerol (Sigma-Aldrich, #G5516) was added and the stock was kept at -20°C until further use.

In order to prepare the FP-FtnA oligomer surfaces, the mEos3.2-A69T-FtnA stock was diluted 1:5000 in 50 mM Tris HCl containing 25 mM NaCl at pH 8.5 and incubated with a sonicated 1:1000 dilution of dark red (660/680) FluoSpheres (Molecular probes, #F8807) on a clean, poly-L-lysine coated Ibidi 8-well glass bottom slide for 10 min. The sample was washed twice using 50 mM Tris HCl containing 25 mM NaCl at pH 8.5 and 0.5% w/v low gelling agarose solution (Sigma-Aldrich, #A9414-100G) was carefully added to the top to ensure proper immobilization. After gelation for 5 min on ice 300 µL of 50 mM Tris HCl containing 25 mM NaCl at pH 8.5 were added to the imaging well.

The same microscope setup and imaging routine that was used for imaging the triple-color strain library was utilized to image the isolated mEos3.2-A69T-FtnA oligomers. To simulate the mScarlet-I imaging & bleaching step prior to mEos3.2-A69T imaging, the sample was first illuminated with the 561 nm laser at 1 $kW*cm^{-2}$ for 1 min before the PC-PALM read-out of mEos3.2-A69T was recorded.

Data analysis

An overview of the workflow can be found in Fig. 2.

Localization, drift correction and filtering

First, all movies were localized using ThunderSTORM (Ovesny et al., 2014) with the B-spline wavelet filter with a scale of 2.0 pixel and order of 3, a 8 pixel neighborhood and threshold of 1.5*std(wavelet), the integrated Gaussian PSF model with a sigma of 1.4 pixel and a weighted least squares optimization with a fit radius of 4 pixel. The fluorescent beads embedded in the sample were used for drift correction. The combined drift trace as well as the drift trace for each bead were saved and checked for inconsistencies. In those instances, the localization file was manually drift corrected using a custom script written in Python 3 that allowed the selection of individual beads.

A nearest neighbor tracking algorithm based on kd-tree (Jones et al., 2001) was run on the localization files. For each localization, the nearest neighboring localization in a 150 nm radius was identified in the first subsequent frame. Neighbor identifiers were stored and used to connect localizations into tracks. Tracks were then merged by averaging the coordinates, intensity and PSF width of all localizations in a track. Averaged localizations were filtered based on these parameters to discard statistical outliers (Q1 - 1.5*IQR, Q3 + 1.5*IQR) in intensity and chi-square goodness of fit. For the PSF width, a set threshold of a sigma of 70-200 nm was used.

Visualization and Manual Analytics

For several manual steps, localizations were visualized in a custom software able to flexibly zoom in/out and to switch between/overlay sad1/POI/ cnp1^{CENP-A} channels. Using this tool, individual localizations could be selected and classified. For channel alignment, localizations belonging to the same fiducial marker in all three channels were grouped together. Cells with visible KT protein clusters in the focal plane were selected and classified as individual region of interests (ROIs) and all clusters were annotated. cnp1^{CENP-A} clusters were paired together with corresponding POI clusters. Whenever there was any doubt whether two clusters belonged to the same KT or whether a cluster represented a single centromere region or several, the clusters were discarded. Two exemplary data sets can be found in the zip-file Supplementary data S1. The annotation work was quality-checked by cross-checking the annotation of two different persons.

Channel alignment

The alignment between two channels along a given axis was calculated as the inverse-variance weighted mean displacement of beads present in both channels. The position of a bead in each channel was calculated as the mean position of all localizations associated with the given bead in this channel. The variance of the displacement is then given by the sum of the squared standard errors of the two positions. The alignment of two channels was deemed viable if it was based on at least two beads and a minimum of 15000 (channels 1 & 2) or 180 (channel 3) localizations. Initially, only beads with $e^{-|\log(FWHM_x/FWHM_y)|} > 0.9$ were used.
For all movies, where this did not result in a viable alignment, this threshold was successively lowered to 0.8, 0.7, 0.6, and 0.5 until a viable alignment was found. Movies for which no viable assignment could be found using this procedure were not taken into consideration when estimating the $cnp1^{CENP\text{-}A}$-POI distances.

Distance calculation

We used Bayesian inference to determine the real distance between $cnp1^{CENP\text{-}A}$ and the POI from the measured centers of their respective clusters, assuming Gaussian measurement errors of uncertain size. To improve accuracy, we also took the position of the associated spindle pole into account, as the three points (centers of POI, $cnp1^{CENP\text{-}A}$ and corresponding sad1 cluster) can be assumed to lie on a straight line. As it is not possible to reliably determine which spindle pole a centromere is attached to, we built a mixture model to take both possibilities into account. (The SPB closest to a KT is not necessarily the SPB to which the KT is attached to. The reasons for this are that *S. pombe* undergoes closed mitosis where the nuclear envelope doesn't break up before chromosomes separate and, furthermore, KTs oscillate back and forth along the mitotic spindle until DNA segregation takes place (Rieder et al., 1986)). To formalize the idea that a centromere is more likely to be attached to the closer spindle pole, we calculated a mixture coefficient $\lambda = 1 / (1 + (d_2/d_1)^{-3})$, where d_1 and d_2 are the measured distances between $cnp1^{CENP\text{-}A}$ and the first and second spindle pole, respectively. The coefficient then corresponds to the prior probability that the centromere is attached to the first spindle pole. We visualize the model in Fig. 2.

We considered three types of Gaussian measurement errors: the measurement error of the spindle, the measurement error of the center of the POI and $cnp1^{CENP\text{-}A}$ clusters, and the error of the alignment of the different channels. As the localizations belonging to a single spindle pole are (approximately) normally distributed, the variance of their mean can be estimated with high precision from the sample variance in *x* and *y*. The variances of the errors of the clusters and the alignment are more difficult to estimate directly and were therefore estimated together with the $cnp1^{CENP\text{-}A}$-POI distances, using a scaled inverse χ^2 distribution as prior.

Whereas the measurement error can be different for each individual cluster, the alignment error was assumed to be identical for all clusters in a movie. For the alignment error, we estimated the scale parameter r^2 of the prior distribution from the position of the beads in different channels (although this is likely to be an underestimation, as the same beads were used to calculate the alignment) and the degrees of freedom v from the number of beads used in the movie. We used constant values r^2 = 100 nm^2 and v = 4 for the error of the cluster centers, as they seemed to work reasonably well upon visual inspection. A more objective estimation of this error is difficult, as it results mainly from errors in the clustering, which was performed manually.

We used the Hamiltonian Monte Carlo algorithm as implemented by Stan (Carpenter et al., 2017; Stan Development Team, 2021) and the CmdStanPy python package (Stan Development Team, 2019) to approximate the posterior distribution of the cnp1^{CENP-A}-POI distances according to our model (code in Supplementary File S1 and on GitHub: https://github.com/Endesfelder-Lab/Kinetochore_Distances). Posterior distributions are shown in Fig. 2, means are plotted in Fig. 3 and summarized in Table 1.

Protein Stoichiometry

SMLM localization counts do not directly reflect on the real POI copy numbers due to several over- and undercounting factors (e.g. incomplete FP maturation or photoconversion or FP blinking (Turkowyd et al., 2016)). A robust way to acquire statistically correct average POI copy numbers is to calibrate the localization count data with corresponding data of a protein standard of known stoichiometry using the same sample, imaging and analysis protocols as for imaging the POI. We utilized the *Escherichia coli* protein ferritin (FtnA), a homo-oligomeric protein standard of 24 subunits labeled by mEos3.2-A69T to calibrate our POI localization counts (Finan et al., 2015; Virant et al., 2018). FtnA assembles from monomers into dimers to form 8mers which then arrange into the final 24mer structure. As depicted in Fig. 2, FtnA assembly intermediates (FtnA monomers, dimers, 8mers), full 24mers as well as aggregates can be identified by eye and their intrinsic stoichiometric differences are sufficient to discriminate them by fluorescence intensities. We manually selected 1458 8mers and 725 24mers from 29 imaging ROIs from two imaging days. Their localization count distribution yields a mean of 7.27 ± 2.72 STD and 21.68 ± 10.2 STD counts per 8mer and 24mer cluster, respectively (Fig. 2). Thus, both give a correction factor of about 0.9 to translate localization counts into POI counts. With the help of this factor, all POI counts were translated into POI copy numbers per centromeric cluster as given in Table 2.

Verifying the reliability of measured localizations counts and distances

In all measurements, we quantitatively assessed not only the localization counts for the POI clusters, but also the counts of the corresponding PAmCherry1-cnp1^{CENP-A} cluster. We use these reference counts to identify possible inconsistencies in the sample preparations and imaging routines of the different experiments. The PAmCherry1 localization counts for the cnp1^{CENP-A} reference remained constant independent of individual sample preparations, imaging days and different strains as can be seen in Fig. 2, where the data is exemplarily sorted into the different strain categories. The POI protein copy numbers as given in Table 2 show a large coefficient of variation. To assess to which extend this variability reflects a technical inability to measure protein levels accurately or some flexibility in KT protein stoichiometry (e.g. due to differing numbers of kMTs per KT), we can use the data of the FtnA oligomer counting standard: The FtnA oligomer is a biologically highly defined structure. Thus, our FtnA measurements can directly serve as a proxy for the contribution of the technical inaccuracy of our PALM imaging and analysis strategy to the variance. Using the results of 21.68 counts ± 10.2 STD for the 24mers and of 7.27 counts ± 2.72 STD for the 8mers, we can estimate that the technical inaccuracy causes a coefficient of variance of 0.35 to 0.5, thus almost completely explaining the experimentally seen coefficient of ~ 0.5 for our POI data (Table 2). Due this high technical inaccuracy, we cannot resolve sub-populations of possibly different KT structures (and thus POI copy numbers) on 2-4 kMTs in our current counting data (Fig. S3).

For distances, we examined whether the POI-cnp1^{CENP-A} distance depends on the mitotic spindle length, e.g. due to different phases in chromosome separation or different forces. As seen in Fig. S3 for the POI dam1 (but being true for all our measurements (data not shown)), we do not detect any dependence of the centroid distance to the mitotic spindle length and therefore conclude that the KTs, as we analyze them, all show the same layers and stretching. This is further validated by the posterior distributions of POI-cnp1^{CENP-A} distances in Fig. 2, which consistently show only a single, well defined peak. Furthermore, using a nup132-GFP strain in early G2 phase, we measured the average nuclear diameter of *S. pombe* to be 2.4 µm ± 0.19 µm (data not shown), in agreement with the literature (Maclean, 1964; Toda et al., 1981). The spindles included in our analysis have spindle lengths well below the nuclear diameter, thus excluding anaphase B cells (Fig. S3). Of additional note: While for *S. pombe* we assume - based on literature data and atb2 MT imaging (data not shown) that cnp1, POI and one spindle indeed lie on a line in metaphase/early anaphase, this has to be revisited for higher eukaryotes, where the outer kinetochore domain has been observed to swivel around the inner kinetochore/centromere, an effect thought to facilitate kMT attachment and which only reduces in anaphase (Smith et al., 2016).

Online supplemental material

Fig. S1 shows autofluorescence of metabolites and dye staining in *S. pombe*, related to Materials and Methods.

Fig. S2 shows the cloning strategy, sample preparation and strain health assessment used in this study, related to Materials and Methods.

Fig. S3 shows the independence of the centroid distances from the mitotic spindle length and the angular offset of kMTs and spindle axes, related to Materials and Methods.

Table S1 shows a list of *S. pombe* and *E. coli* strains used in this study, related to Materials and Methods.

Table S2 shows a list of oligonucleotides used in this study, related to Materials and Methods.

Table S3 shows the weighted mean of localization counts for POIs belonging to the same kinetochore subcomplex.

Table S4 shows a comparison of POI copy number ratios between different kinetochore subcomplexes with the literature

Table S5 shows a comparison of protein cluster distances of this study and Cieslinski et al.

Supplementary Data and File 1 contain the STAN code and raw distance data for distance analysis.

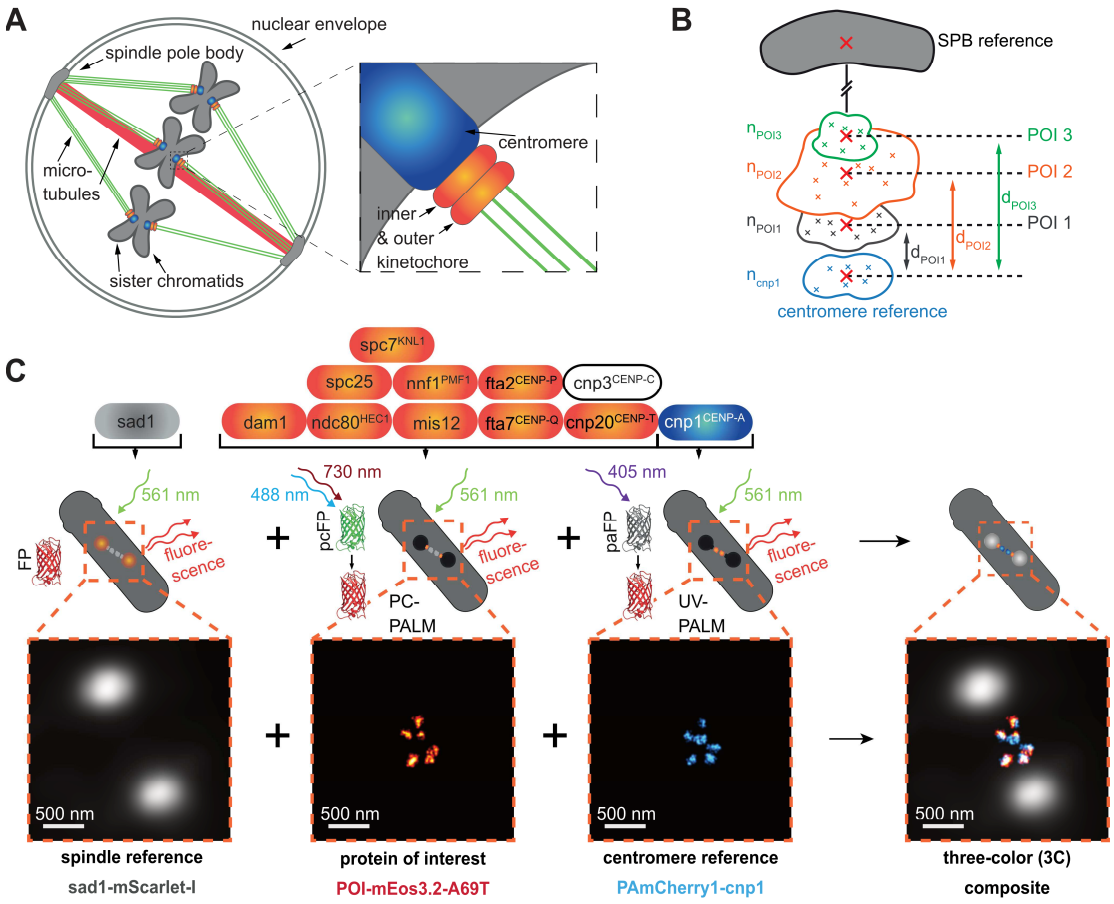

Fig. 1: Imaging strategy for measuring the kinetochore nanostructure

(A) During mitosis, the three sister chromatid pairs in *S. pombe* are attached to the two spindle pole bodies (SPBs) by tethering microtubules (green), and the SPBs are pushed apart by a bundle of spindle microtubules (red). The attachment between the centromeric region of each chromatid (blue) and the microtubules is facilitated by the KT-protein complex (orange), which consists of an inner and outer part.

(B) Each protein of interest (POI) in the KT complex can be mapped into the KT nanostructure by localizing it in relation to two references, a centromere and an SPB reference. Information about its copy number n_{POI} and its orientation and distance d_{POI} to the reference proteins is obtained.

(C) Imaging strategy: First, the SPB protein sad1-mScarlet-I fusion is imaged by conventional epifluorescence microscopy to map the mitotic spindle. Then, both the POI and the centromere reference cnp1^{CENP-A} are measured by super-resolution microscopy: Here, each POI-mEos3.2-A69T fusion (here spc7) is imaged by primed photoconversion PALM (PC-PALM),

followed by a read-out of PAmCherry1-cnp1^{CENP-A} fusion using UV-activation PALM (UV-PALM). Scale bar 500 nm.

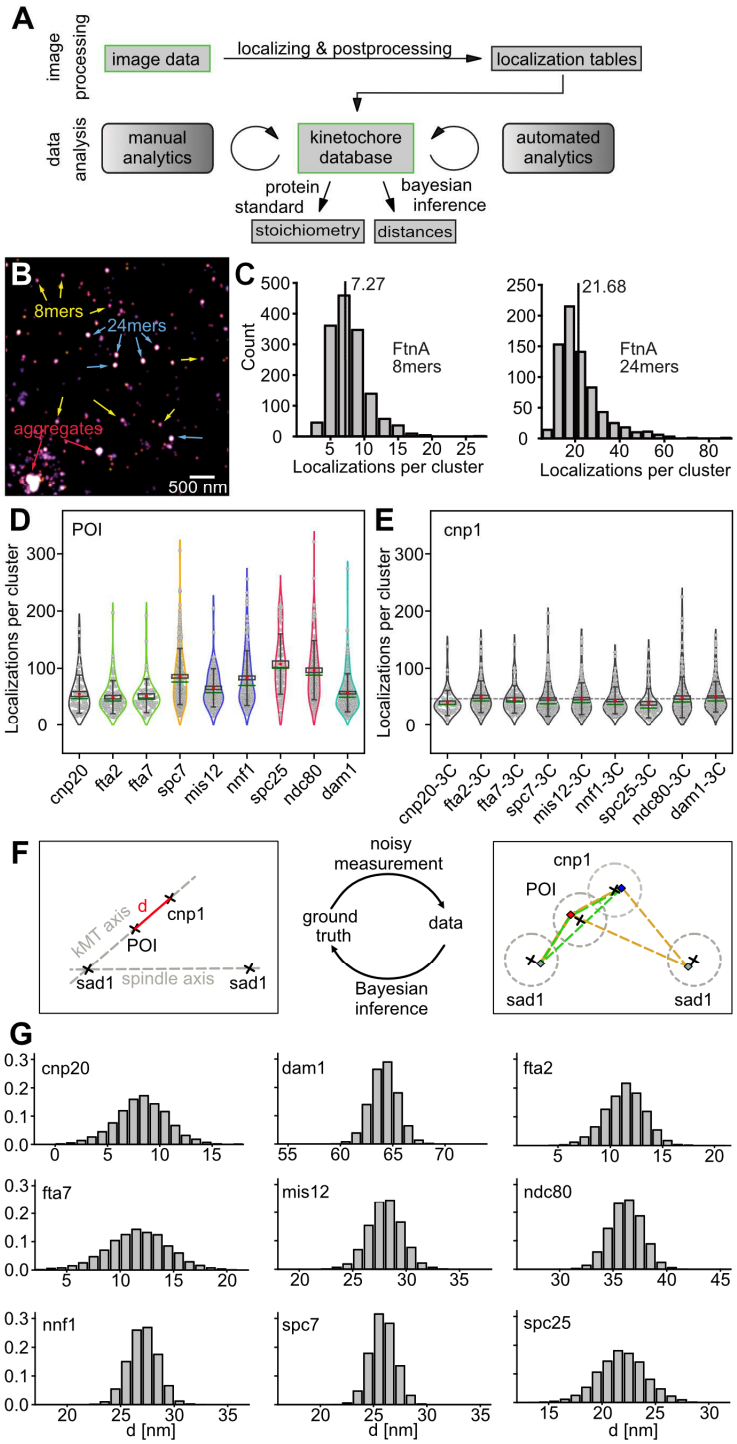

Fig. 2: Data analysis

(A) Schematic representation of the data analysis pipeline. In the image processing part, image data from SMLM experiments are localized and post-processed (for quality, drift, etc.). The resulting localization tables are added to a kinetochore database, which is then used as a backend for several manual analysis (visual selection and classification steps) and automated analysis steps (channel alignment and filtering). From the database, all measures can be extracted. Here, we used localization counts per cluster and protein cluster distances to determine protein stoichiometry using a protein standard calibration and POI-cnp1^{CENP-A} distances using Bayesian inference.

(B) Using *E. coli* ferritin FtnA as a counting standard to calibrate POI copy numbers. Reconstructed SMLM image of isolated mEos3.2-A69T-FtnA oligomers. In our exemplary sample image, all assembly intermediates (monomers, dimers, 8mers) as well as final 24mers and some aggregates can be seen (exemplary 8mers, 24mers and aggregates are highlighted with colored arrows). Scale bar 500 nm.

(C) Histograms of localization counts per selected 8mer (left) and 24mer (right) cluster. Using the mean (dashed lines) of 7.27 ± 2.72 for 8mers and 21.68 ± 10.28 for 24mers we determine a calibration factor of 0.9. N = 1458 (8mers) and N = 725 (24mers).

(D) POI numbers and robustness of the method. Localizations per POI cluster. POIs from the same subcomplex are shown in the same colors (COMA (green): fta2^{CENP-P}, fta7^{CENP-Q}; MIND (blue): mis12, nnf1^{PMF1}; NDC80c (red): spc25, ndc80^{HEC1}). The red dot indicates the mean, the green line indicates the median, the black box indicates the SE of the mean, and the whiskers indicates the STD. N = 57 for cnp20^{CENP-T}, 87 for fta2^{CENP-P}, 61 for fta7^{CENP-Q}, 86 for spc7^{KNL1}, 136 for mis12, 217 for nnf1^{PMF1}, 86 for spc25, 172 for ndc80^{HEC1}, 232 for dam1.

(E) Distributions of localizations per cnp1^{CENP-A} cluster are robust across different POI-3C measurements. The gray dotted line indicates the mean of all cnp1^{CENP-A} clusters for reference. N = 55 for cnp20^{CENP-T}-3C, 96 for fta2^{CENP-P}-3C, 68 for fta7^{CENP-Q}-3C, 239 for spc7^{KNL1}-3C, 197 for nnf1^{PMF1}-3C, 122 for mis12-3C, 68 for spc25-3C, 161 for ndc80^{HEC1}-3C, 239 for dam1-3C.

(F) Bayesian model to estimate inner-kinetochore distances. Schematic of our Bayesian model. To determine the real distance (marked in red) between cnp1^{CENP-A} and each POI from the measured centers of their respective clusters we assumed Gaussian measurement errors of uncertain size (dotted grey circles, right). To be able to disentangle the contribution of errors and real distance in the measured data, we took the position of the associated spindle pole into account, as the centroids of sad1, POI and cnp1^{CENP-A} clusters can be assumed to lie on a straight line (kinetochore microtubule (kMT) axis, left). The sad1 cluster closest to a

kinetochore is not necessarily the pole to which the kinetochore is attached to. Thus, we built a mixture model to take both possibilities into account. For each kinetochore pair, we thus obtain two options to check, marked by the green and orange triangle, right.

(G) The posterior density of cnp1^{CENP-A}-POI distances for each POI measured in this study was approximated using Hamiltonian Monte Carlo (see materials and methods). Number of centromeres used for distance measurement: N = 49 for cnp20^{CENP-T}, 82 for fta2^{CENP-P}, 58 for fta7^{CENP-Q}, 215 for spc7^{KNL1}, 161 for nnf1^{PMF1}, 102 for mis12, 51 for spc25, 135 for ndc80^{HEC1}, 155 for dam1. The code can be found in Supplementary File S1.

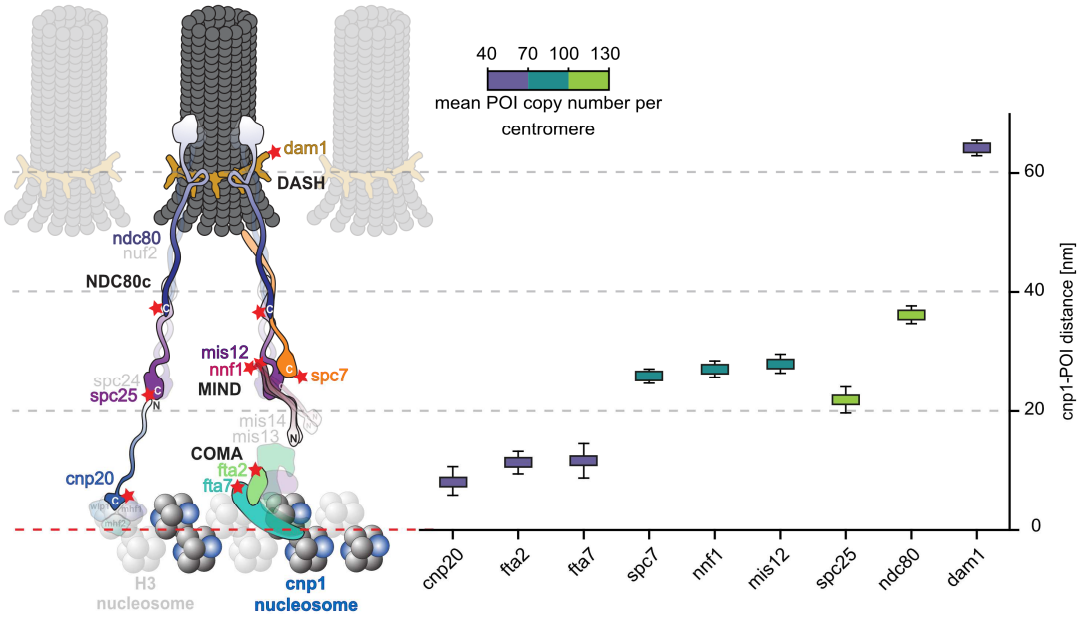

Fig. 3: POI-cnp1^{CENP-A} distances and protein stoichiometry within the kinetochore complex

Left Schematic of the regional *S. pombe* centromere with parts of the inner and outer KT. Whenever information was available, the shapes of POIs and subcomplexes are shown according to cryo-EM or x-ray crystallography data. Red stars mark the position of the C-terminal fluorescent protein marker mEos3.2-A69T. Structures drawn at 25% opacity were not investigated.

Right POI distances to the reference cnp1^{CENP-A} and POI copy numbers per centromeric region as measured in this study. The colored boxes mark the mean and the whiskers the standard deviation of the posterior probability density distribution for each cnp1^{CENP-A}-POI distance (Fig. 2 G, statistics in Table 1). The color of the box represents the mean POI copy number per cluster, as indicated by the scale bar (distributions of localization counts in Fig. 2 E, statistics in Table 2).

POI	mean distance [nm]	STD [nm]	N
cnp20^{CENP-T}	8.3	2.4	49
fta2^{CENP-P}	11.4	1.9	82
fta7^{CENP-Q}	11.7	2.9	58
spc7^{KNL1}	25.9	1.2	215
nnf1^{PMF1}	27.1	1.4	161
mis12	28.0	1.6	102
spc25	21.9	2.2	51
ndc80^{HEC1}	36.2	1.5	135
dam1	64.2	1.3	155

Table 1: Statistics of distance calculations

For each POI, the posterior mean distance, posterior standard deviation (STD) and the number N of KTs analyzed is listed. Full posterior distributions, approximated using Hamiltonian Monte Carlo (Materials & Methods), can be found in Fig. 2.

POI	mean count	STD	SE of mean	median	Mean POI copy numbers* (± SE)	FP tag	N
cnp1^{CENP-A}	46.8	28.0	0.8	40.0	ND	PamCherry1	1245
cnp20^{CENP-T}	55.0	32.5	4.3	47.0	61.1 ± 4.8	mEos3.2-A69T	57
fta2^{CENP-P}	49.6	27.9	3.0	43.0	55.1 ± 3.3	mEos3.2-A69T	87
fta7^{CENP-Q}	51.7	28.9	3.7	46.0	57.4 ± 4.1	mEos3.2-A69T	61
spc7^{KNL1}	85.9	48.4	3.0	76.0	95.4 ± 3.3	mEos3.2-A69T	259
nnf1^{PMF1}	83.3	47.2	3.2	70.0	92.6 ± 3.6	mEos3.2-A69T	217
mis12	65.8	33.1	2.8	57.5	73.1 ± 3.1	mEos3.2-A69T	136
spc25	107.2	52.2	5.6	49.5	119.1 ± 6.2	mEos3.2-A69T	86
ndc80^{HEC1}	96.5	51.2	3.9	88.0	107.2 ± 4.3	mEos3.2-A69T	172
dam1	57.3	33.1	2.2	49.5	63.7 ± 2.4	mEos3.2-A69T	232

Table 2: Statistics of POI localization counts per centromeric region

Distributions can be found in Fig. 2 E. *Mean POI copy numbers were derived from the mean localization counts of each POI using 0.9 as a calibration factor as determined by the FtnA protein standard (Materials & Methods). N number of centromeric regions analyzed.

References

Akamatsu, M., Y. Lin, J. Bewersdorf, and T.D. Pollard. 2017. Analysis of interphase node proteins in fission yeast by quantitative and superresolution fluorescence microscopy. *Molecular biology of the cell*. 28:3203-3214.

Allshire, R.C. 1995. Elements of chromosome structure and function in fission yeast. *Seminars in cell biology*. 6:55-64.

Aravamudhan, P., I. Felzer-Kim, K. Gurunathan, and A.P. Joglekar. 2014. Assembling the protein architecture of the budding yeast kinetochore-microtubule attachment using FRET. *Current Biology*. 24:1437-1446.

Balinovic, A., D. Albrecht, and U. Endesfelder. 2019. Spectrally red-shifted fluorescent fiducial markers for optimal drift correction in localization microscopy. *Journal of Physics D: Applied Physics*. 52:204002.

Bell, L., A. Seshia, D. Lando, E. Laue, M. Palayret, S.F. Lee, and D. Klenerman. 2014. A microfluidic device for the hydrodynamic immobilisation of living fission yeast cells for super-resolution imaging. *Sensors and actuators. B, Chemical*. 192:36-41.

Bestul, A.J., Z. Yu, J.R. Unruh, and S.L. Jaspersen. 2021. Redistribution of centrosomal proteins by centromeres and Polo kinase controls partial nuclear envelope breakdown in fission yeast. *Molecular biology of the cell*:mbc-E21.

Bindels, D.S., L. Haarbosch, L. Van Weeren, M. Postma, K.E. Wiese, M. Mastop, S. Aumonier, G. Gotthard, A. Royant, and M.A. Hink. 2017. mScarlet: a bright monomeric red fluorescent protein for cellular imaging. *Nature methods*. 14:53-56.

Black, B.E., L.E.T. Jansen, P.S. Maddox, D.R. Foltz, A.B. Desai, J.V. Shah, and D.W. Cleveland. 2007. Centromere identity maintained by nucleosomes assembled with histone H3 containing the CENP-A targeting domain. *Molecular cell*. 25:309-322.

Bock, L.J., C. Pagliuca, N. Kobayashi, R.A. Grove, Y. Oku, K. Shrestha, C. Alfieri, C. Golfieri, A. Oldani, and M. Dal Maschio. 2012. Cnn1 inhibits the interactions between the KMN complexes of the yeast kinetochore. *Nature cell biology*. 14:614-624.

Carpenter, B., A. Gelman, M.D. Hoffman, D. Lee, B. Goodrich, M. Betancourt, M. Brubaker, J. Guo, P. Li, and A. Riddell. 2017. Stan: A Probabilistic Programming Language. *Journal of Statistical Software*. 76:1 - 32.

Carroll, C.W., K.J. Milks, and A.F. Straight. 2010. Dual recognition of CENP-A nucleosomes is required for centromere assembly. *Journal of Cell Biology*. 189:1143-1155.

Chik, J.K., V. Moiseeva, P.K. Goel, B.A. Meinen, P. Koldewey, S. An, B.G. Mellone, L. Subramanian, and U.S. Cho. 2019. Structures of CENP-C cupin domains at regional centromeres reveal unique patterns of dimerization and recruitment functions for the inner pocket. *The Journal of biological chemistry*. 294:14119-14134.

Chikashige, Y., N. Kinoshita, Y. Nakaseko, T. Matsumoto, S. Murakami, O. Niwa, and M. Yanagida. 1989. Composite motifs and repeat symmetry in S. pombe centromeres: direct analysis by integration of NotI restriction sites. *Cell*. 57:739-751.

Cieslinski, K., Y.-L. Wu, L. Nechyporenko, S.J. Hoerner, D. Conti, and J. Ries. 2021. Nanoscale structural organization and stoichiometry of the budding yeast kinetochore. *BioRxiv*. 2021/469648.

Ciferri, C., S. Pasqualato, E. Screpanti, G. Varetti, S. Santaguida, G. Dos Reis, A. Maiolica, J. Polka, J.G. De Luca, and P. De Wulf. 2008. Implications for kinetochore-microtubule attachment from the structure of an engineered Ndc80 complex. *Cell*. 133:427-439.

Clarke, L. 1998. Centromeres: proteins, protein complexes, and repeated domains at centromeres of simple eukaryotes. *Current opinion in genetics developmental Neuroscience*. 8:212-218.

Coffman, V.C., P. Wu, M.R. Parthun, and J.-Q. Wu. 2011. CENP-A exceeds microtubule attachment sites in centromere clusters of both budding and fission yeast. *Journal of Cell Biology*. 195:563-572.

Curran, K.A., A.S. Karim, A. Gupta, and H.S. Alper. 2013. Use of expression-enhancing terminators in Saccharomyces cerevisiae to increase mRNA half-life and improve gene expression control for metabolic engineering applications. *Metab Eng*. 19:88-97.

D'Archivio, S., and B. Wickstead. 2017. Trypanosome outer kinetochore proteins suggest conservation of chromosome segregation machinery across eukaryotes. *The Journal of cell biology*. 216:379-391.

De Wulf, P., A.D. McAinsh, and P.K. Sorger. 2003. Hierarchical assembly of the budding yeast kinetochore from multiple subcomplexes. *Genes & development*. 17:2902-2921.

Dhatchinamoorthy, K., M. Shivaraju, J.J. Lange, B. Rubinstein, J.R. Unruh, B.D. Slaughter, and J.L. Gerton. 2017. Structural plasticity of the living kinetochore. *Journal of Cell Biology*. 216:3551-3570.

Dhatchinamoorthy, K., J.R. Unruh, J.J. Lange, M. Levy, B.D. Slaughter, and J.L. Gerton. 2019. The stoichiometry of the outer kinetochore is modulated by microtubule-proximal regulatory factors. *Journal of Cell Biology*. 218:2124-2135.

Dimitrova, Y.N., S. Jenni, R. Valverde, Y. Khin, and S.C. Harrison. 2016. Structure of the MIND complex defines a regulatory focus for yeast kinetochore assembly. *Cell*. 167:1014-1027.

Ding, R., K.L. McDonald, and J.R. McIntosh. 1993. Three-dimensional reconstruction and analysis of mitotic spindles from the yeast, Schizosaccharomyces pombe. *The Journal of cell biology*. 120:141-151.

Drinnenberg, I.A., S. Henikoff, and H.S. Malik. 2016. Evolutionary Turnover of Kinetochore Proteins: A Ship of Theseus? *Trends in cell biology*.

Drpic, D., A.C. Almeida, P. Aguiar, F. Renda, J. Damas, H.A. Lewin, D.M. Larkin, A. Khodjakov, and H. Maiato. 2018. Chromosome segregation is biased by kinetochore size. *Current Biology*. 28:1344-1356.

Dunleavy, E.M., G. Almouzni, and G.H. Karpen. 2011. H3. 3 is deposited at centromeres in S phase as a placeholder for newly assembled CENP-A in G1 phase. *Nucleus*. 2:146-157.

Edelstein, A., N. Amodaj, K. Hoover, R. Vale, and N. Stuurman. 2010. Computer control of microscopes using microManager. *Current protocols in molecular biology / edited by Frederick M. Ausubel ... [et al.]*. Chapter 14:Unit14 20.

Endesfelder, U., S. Malkusch, F. Fricke, and M. Heilemann. 2014. A simple method to estimate the average localization precision of a single-molecule localization microscopy experiment. *Histochemistry and cell biology*. 141:629-638.

Etheridge, T.J., R.L. Boulineau, A. Herbert, A.T. Watson, Y. Daigaku, J. Tucker, S. George, P. Jonsson, M. Palayret, D. Lando, E. Laue, M.A. Osborne, D. Klenerman, S.F. Lee, and A.M. Carr. 2014. Quantification of DNA-associated proteins inside eukaryotic cells using single-molecule localization microscopy. *Nucleic acids research*. 42:e146.

Etheridge, T.J., D. Villahermosa, E. Campillo-Funollet, A.D. Herbert, A. Irmisch, A.T. Watson, H.Q. Dang, M.A. Osborne, A.W. Oliver, and A.M. Carr. 2021. Live-cell single-molecule tracking highlights requirements for stable Smc5/6 chromatin association in vivo. *eLife*. 10:e68579.

Finan, K., A. Raulf, and M. Heilemann. 2015. A Set of Homo-oligomeric Standards Allows Accurate Protein Counting. *Angewandte Chemie International Edition*:n/a-n/a.

Giaever, G., A.M. Chu, L. Ni, C. Connelly, L. Riles, S. Véronneau, S. Dow, A. Lucau-Danila, K. Anderson, and B. André. 2002. Functional profiling of the Saccharomyces cerevisiae genome. *Nature*. 418:387-391.

Gonen, S., B. Akiyoshi, M.G. Iadanza, D. Shi, N. Duggan, S. Biggins, and T. Gonen. 2012. The structure of purified kinetochores reveals multiple microtubule-attachment sites. *Nature structural & molecular biology*. 19:925-929.

Griffiths, K., H. Masuda, S. Dhut, and T. Toda. 2008. Fission yeast dam1-A8 mutant is resistant to and rescued by an anti-microtubule agent. *Biochemical and biophysical research communications*. 368:670-676.
Guse, A., C.W. Carroll, B. Moree, C.J. Fuller, and A.F. Straight. 2011. In vitro centromere and kinetochore assembly on defined chromatin templates. *Nature*. 477:354-358.
Haase, J., P.K. Mishra, A. Stephens, R. Haggerty, C. Quammen, R.M. Taylor Ii, E. Yeh, M.A. Basrai, and K. Bloom. 2013. A 3D map of the yeast kinetochore reveals the presence of core and accessory centromere-specific histone. *Current Biology*. 23:1939-1944.
Hamilton, G.E., and T.N. Davis. 2020. Biochemical evidence for diverse strategies in the inner kinetochore. *Open biology*. 10:200284.
Hamilton, G.E., L.A. Helgeson, C.L. Noland, C.L. Asbury, Y.N. Dimitrova, and T.N. Davis. 2020. Reconstitution reveals two paths of force transmission through the kinetochore. *eLife*. 9.
Hara, M., M. Ariyoshi, E.I. Okumura, T. Hori, and T. Fukagawa. 2018. Multiple phosphorylations control recruitment of the KMN network onto kinetochores. *Nature cell biology*. 20:1378-1388.
Hayashi, A., D.Q. Ding, C. Tsutsumi, Y. Chikashige, H. Masuda, T. Haraguchi, and Y. Hiraoka. 2009. Localization of gene products using a chromosomally tagged GFP-fusion library in the fission yeast Schizosaccharomyces pombe. *Genes to cells : devoted to molecular & cellular mechanisms*. 14:217-225.
Hayles, J., V. Wood, L. Jeffery, K.L. Hoe, D.U. Kim, H.O. Park, S. Salas-Pino, C. Heichinger, and P. Nurse. 2013. A genome-wide resource of cell cycle and cell shape genes of fission yeast. *Open biology*. 3:130053.
Hinshaw, S.M., and S.C. Harrison. 2019a. The structure of the Ctf19c/CCAN from budding yeast. *eLife*. 8:e44239.
Hinshaw, S.M., and S.C. Harrison. 2019b. The structure of the Ctf19c/CCAN from budding yeast. *Elife*. 8.
Hinshaw, S.M., and S.C. Harrison. 2019c. The structure of the yeast Ctf3 complex. *eLife*. 8:e48215.
Hornung, P., P. Troc, F. Malvezzi, M. Maier, Z. Demianova, T. Zimniak, G. Litos, F. Lampert, A. Schleiffer, M. Brunner, K. Mechtler, F. Herzog, T.C. Marlovits, and S. Westermann. 2014. A cooperative mechanism drives budding yeast kinetochore assembly downstream of CENP-A. *The Journal of cell biology*. 206:509-524.
Jenni, S., and S.C. Harrison. 2018. Structure of the DASH/Dam1 complex shows its role at the yeast kinetochore-microtubule interface. *Science*. 360:552-558.
Joglekar, A.P., K. Bloom, and E.D. Salmon. 2009. In vivo protein architecture of the eukaryotic kinetochore with nanometer scale accuracy. *Current Biology*. 19:694-699.
Joglekar, A.P., D. Bouck, K. Finley, X. Liu, Y. Wan, J. Berman, X. He, E.D. Salmon, and K.S. Bloom. 2008. Molecular architecture of the kinetochore-microtubule attachment site is conserved between point and regional centromeres. *Journal of Cell Biology*. 181:587-594.
Joglekar, A.P., D.C. Bouck, J.N. Molk, K.S. Bloom, and E.D. Salmon. 2006. Molecular architecture of a kinetochore–microtubule attachment site. *Nature cell biology*. 8:581-585.
Johnston, K., A. Joglekar, T. Hori, A. Suzuki, T. Fukagawa, and E.D. Salmon. 2010. Vertebrate kinetochore protein architecture: protein copy number. *Journal of Cell Biology*. 189:937-943.
Jones, E., T. Oliphant, and P. Peterson. 2001. SciPy: Open Source Scientific Tools for Python.
Kim, D.-U., J. Hayles, D. Kim, V. Wood, H.-O. Park, M. Won, H.-S. Yoo, T. Duhig, M. Nam, G. Palmer, S. Han, L. Jeffery, S.-T. Baek, H. Lee, Y.S. Shim, M. Lee, L. Kim, K.-S. Heo, E.J. Noh, A.-R. Lee, Y.-J. Jang, K.-S. Chung, S.-J. Choi, J.-Y. Park, Y. Park, H.M. Kim, S.-K. Park, H.-J. Park, E.-J. Kang, H.B. Kim, H.-S. Kang, H.-M. Park, K. Kim, K. Song, K.B. Song, P. Nurse, and K.-L. Hoe. 2010. Analysis of a genome-wide set of gene deletions in the fission yeast Schizosaccharomyces pombe. *Nature biotechnology*. 28:617-623.

Kixmoeller, K., P.K. Allu, and B.E. Black. 2020. The centromere comes into focus: from CENP-A nucleosomes to kinetochore connections with the spindle. *Open biology*. 10:200051.
Kudalkar, E.M., E.A. Scarborough, N.T. Umbreit, A. Zelter, D.R. Gestaut, M. Riffle, R.S. Johnson, M.J. MacCoss, C.L. Asbury, and T.N. Davis. 2015. Regulation of outer kinetochore Ndc80 complex-based microtubule attachments by the central kinetochore Mis12/MIND complex. *Proceedings of the National Academy of Sciences*. 112:E5583-E5589.
Lando, D., U. Endesfelder, H. Berger, L. Subramanian, P.D. Dunne, J. McColl, D. Klenerman, A.M. Carr, M. Sauer, R.C. Allshire, M. Heilemann, and E.D. Laue. 2012. Quantitative single-molecule microscopy reveals that CENP-A(Cnp1) deposition occurs during G2 in fission yeast. *Open biology*. 2:120078.
Laplante, C., F. Huang, I.R. Tebbs, J. Bewersdorf, and T.D. Pollard. 2016. Molecular organization of cytokinesis nodes and contractile rings by super-resolution fluorescence microscopy of live fission yeast. *Proceedings of the National Academy of Sciences of the United States of America*. 113:E5876-E5885.
Lawrimore, J., K.S. Bloom, and E.D. Salmon. 2011. Point centromeres contain more than a single centromere-specific Cse4 (CENP-A) nucleosome. *Journal of Cell Biology*. 195:573-582.
Levenberg, B., and J.M. Buchanan. 1957. Biosynthesis of the purines: XII. Structure, enzymatic synthesis, and metabolism of 5-aminoimidazole ribotide. *Journal of Biological Chemistry*. 224:1005-1018.
Lukens, L.N., and J.M. Buchanan. 1959. Biosynthesis of the Purines: XXIV. The enzymatic synthesis of 5-amino-1-ribosyl-4-imidazolecarboxylic acid 5′-phosphate from 5-amino-1-ribosylimidazole 5′-phosphate and carbon dioxide. *Journal of Biological Chemistry*. 234:1799-1805.
Maclean, N. 1964. ELECTRON MICROSCOPY OF A FISSION YEAST, SCHIZOSACCHAROMYCES POMBE. 88:1459-1466.
Malkusch, S., and M. Heilemann. 2016. Extracting quantitative information from single-molecule super-resolution imaging data with LAMA - LocAlization Microscopy Analyzer. *Scientific reports*. 6:34486.
Maskell, D.P., X.-W. Hu, and M.R. Singleton. 2010. Molecular architecture and assembly of the yeast kinetochore MIND complex. *Journal of Cell Biology*. 190:823-834.
Matsuda, A., Y. Chikashige, D.-Q. Ding, C. Ohtsuki, C. Mori, H. Asakawa, H. Kimura, T. Haraguchi, and Y. Hiraoka. 2015. Highly condensed chromatins are formed adjacent to subtelomeric and decondensed silent chromatin in fission yeast. *Nature communications*. 6:1-12.
McDonald, N.A., A.L. Lind, S.E. Smith, R. Li, and K.L. Gould. 2017. Nanoscale architecture of the Schizosaccharomyces pombe contractile ring. *eLife*. 6:e28865.
McEwen, B.F., Y. Ding, and A.B. Heagle. 1998. Relevance of kinetochore size and microtubule-binding capacity for stable chromosome attachment during mitosis in PtK1 cells. *Chromosome Research*. 6:123-132.
McEwen, B.F., A.B. Heagle, G.O. Cassels, K.F. Buttle, and C.L. Rieder. 1997. Kinetochore fiber maturation in PtK1 cells and its implications for the mechanisms of chromosome congression and anaphase onset. *Journal of Cell Biology*. 137:1567-1580.
Meeks-Wagner, D., J.S. Wood, B. Garvik, and L.H. Hartwell. 1986. Isolation of two genes that affect mitotic chromosome transmission in S. cerevisiae. *Cell*. 44:53-63.
Meraldi, P., A.D. McAinsh, E. Rheinbay, and P.K. Sorger. 2006. Phylogenetic and structural analysis of centromeric DNA and kinetochore proteins. *Genome Biol*. 7:R23.
Migl, D., M. Kschonsak, C.P. Arthur, Y. Khin, S.C. Harrison, C. Ciferri, and Y.N. Dimitrova. 2020. Cryoelectron microscopy structure of a yeast centromeric nucleosome at 2.7 Å resolution. *Structure*. 28:363-370.
Musacchio, A., and A. Desai. 2017. A Molecular View of Kinetochore Assembly and Function. *Biology*. 6.

Ovesny, M., P. Krizek, J. Borkovec, Z. Svindrych, and G.M. Hagen. 2014. ThunderSTORM: a comprehensive ImageJ plug-in for PALM and STORM data analysis and super-resolution imaging. *Bioinformatics*. 30:2389-2390.

Pesenti, M.E., T. Raisch, D. Conti, K. Walstein, I. Hoffmann, D. Vogt, D. Prumbaum, I.R. Vetter, S. Raunser, and A. Musacchio. 2022. Structure of the human inner kinetochore CCAN complex and its significance for human centromere organization. *Mol Cell*. 82:2113-2131 e2118.

Petrovic, A., J. Keller, Y. Liu, K. Overlack, J. John, Y.N. Dimitrova, S. Jenni, S. Van Gerwen, P. Stege, and S. Wohlgemuth. 2016. Structure of the MIS12 complex and molecular basis of its interaction with CENP-C at human kinetochores. *Cell*. 167:1028-1040.

Petrovic, A., S. Mosalaganti, J. Keller, M. Mattiuzzo, K. Overlack, V. Krenn, A. De Antoni, S. Wohlgemuth, V. Cecatiello, and S. Pasqualato. 2014. Modular assembly of RWD domains on the Mis12 complex underlies outer kinetochore organization. *Molecular cell*. 53:591-605.

Petrovic, A., S. Pasqualato, P. Dube, V. Krenn, S. Santaguida, D. Cittaro, S. Monzani, L. Massimiliano, J. Keller, A. Tarricone, A. Maiolica, H. Stark, and A. Musacchio. 2010. The MIS12 complex is a protein interaction hub for outer kinetochore assembly. *The Journal of cell biology*. 190:835-852.

Pfau, S.J., and A. Amon. 2012. Chromosomal instability and aneuploidy in cancer: from yeast to man: 'Exploring aneuploidy: the significance of chromosomal imbalance'review series. *EMBO reports*. 13:515-527.

Przewloka, M.R., Z. Venkei, V.M. Bolanos-Garcia, J. Debski, M. Dadlez, and D.M. Glover. 2011. CENP-C is a structural platform for kinetochore assembly. *Current Biology*. 21:399-405.

Ribeiro, S.A., P. Vagnarelli, Y. Dong, T. Hori, B.F. McEwen, T. Fukagawa, C. Flors, and W.C. Earnshaw. 2010. A super-resolution map of the vertebrate kinetochore. *Proceedings of the National Academy of Sciences*. 107:10484-10489.

Rieder, C.L., E.A. Davison, L.C. Jensen, L. Cassimeris, and E.D. Salmon. 1986. Oscillatory movements of monooriented chromosomes and their position relative to the spindle pole result from the ejection properties of the aster and half-spindle. *Journal of Cell Biology*. 103:581-591.

Roscioli, E., T.E. Germanova, C.A. Smith, P.A. Embacher, M. Erent, A.I. Thompson, N.J. Burroughs, and A.D. McAinsh. 2020. Ensemble-level organization of human kinetochores and evidence for distinct tension and attachment sensors. *Cell reports*. 31:107535.

Roy, B., N. Varshney, V. Yadav, and K. Sanyal. 2013. The process of kinetochore assembly in yeasts. *FEMS microbiology letters*. 338:107-117.

Sanchez-Perez, I., S.J. Renwick, K. Crawley, I. Karig, V. Buck, J.C. Meadows, A. Franco-Sanchez, U. Fleig, T. Toda, and J.B.A. Millar. 2005. The DASH complex and Klp5/Klp6 kinesin coordinate bipolar chromosome attachment in fission yeast. *The EMBO journal*. 24:2931-2943.

Santaguida, S., and A. Amon. 2015. Short-and long-term effects of chromosome mis-segregation and aneuploidy. *Nat Rev Mol Cell Bio*. 16:473-485.

Schindelin, J., I. Arganda-Carreras, E. Frise, V. Kaynig, M. Longair, T. Pietzsch, S. Preibisch, C. Rueden, S. Saalfeld, B. Schmid, J.Y. Tinevez, D.J. White, V. Hartenstein, K. Eliceiri, P. Tomancak, and A. Cardona. 2012. Fiji: an open-source platform for biological-image analysis. *Nature methods*. 9:676-682.

Schittenhelm, R.B., F. Althoff, S. Heidmann, and C.F. Lehner. 2010. Detrimental incorporation of excess Cenp-A/Cid and Cenp-C into Drosophila centromeres is prevented by limiting amounts of the bridging factor Cal1. *Journal of cell science*. 123:3768-3779.

Schittenhelm, R.B., S. Heeger, F. Althoff, A. Walter, S. Heidmann, K. Mechtler, and C.F. Lehner. 2007. Spatial organization of a ubiquitous eukaryotic kinetochore protein network in Drosophila chromosomes. *Chromosoma*. 116:385-402.

Schleiffer, A., M. Maier, G. Litos, F. Lampert, P. Hornung, K. Mechtler, and S. Westermann. 2012. CENP-T proteins are conserved centromere receptors of the Ndc80 complex. *Nature cell biology*. 14:604-613.

Schubert, V., P. Neumann, A. Marques, S. Heckmann, J. Macas, A. Pedrosa-Harand, I. Schubert, T.-S. Jang, and A. Houben. 2020. Super-resolution microscopy reveals diversity of plant centromere architecture. *International journal of molecular sciences*. 21:3488.

Screpanti, E., A. De Antoni, G.M. Alushin, A. Petrovic, T. Melis, E. Nogales, and A. Musacchio. 2011. Direct binding of Cenp-C to the Mis12 complex joins the inner and outer kinetochore. *Current Biology*. 21:391-398.

Smith, C.A., A.D. McAinsh, and N.J. Burroughs. 2016. Human kinetochores are swivel joints that mediate microtubule attachments. *Elife*. 5.

Stan Development Team. 2019. CmdStanPy python package. Vol. 2021.

Stan Development Team. 2021. Stan Modeling Language Users Guide and Reference Manual.

Subach, F.V., G.H. Patterson, S. Manley, J.M. Gillette, J. Lippincott-Schwartz, and V.V. Verkhusha. 2009. Photoactivatable mCherry for high-resolution two-color fluorescence microscopy. *Nature methods*. 6:153-159.

Suzuki, A., B.L. Badger, and E.D. Salmon. 2015. A quantitative description of Ndc80 complex linkage to human kinetochores. *Nature communications*. 6:1-14.

Suzuki, A., B.L. Badger, X. Wan, J.G. DeLuca, and E.D. Salmon. 2014. The architecture of CCAN proteins creates a structural integrity to resist spindle forces and achieve proper Intrakinetochore stretch. *Developmental cell*. 30:717-730.

Suzuki, A., S.K. Long, and E.D. Salmon. 2018. An optimized method for 3D fluorescence co-localization applied to human kinetochore protein architecture. *eLife*. 7:e32418.

Tachiwana, H., W. Kagawa, T. Shiga, A. Osakabe, Y. Miya, K. Saito, Y. Hayashi-Takanaka, T. Oda, M. Sato, and S.-Y. Park. 2011. Crystal structure of the human centromeric nucleosome containing CENP-A. *Nature*. 476:232-235.

Tanaka, K., H.L. Chang, A. Kagami, and Y. Watanabe. 2009. CENP-C functions as a scaffold for effectors with essential kinetochore functions in mitosis and meiosis. *Developmental cell*. 17:334-343.

Tang, N.H., H. Takada, K.-S. Hsu, and T. Toda. 2013. The internal loop of fission yeast Ndc80 binds Alp7/TACC-Alp14/TOG and ensures proper chromosome attachment. *Molecular biology of the cell*. 24:1122-1133.

Toda, T., M. Yamamoto, and M. Yanagida. 1981. Sequential alterations in the nuclear chromatin region during mitosis of the fission yeast Schizosaccharomyces pombe: video fluorescence microscopy of synchronously growing wild-type and cold-sensitive cdc mutants by using a DNA-binding fluorescent probe. *Journal of Cell Science*. 52:271-287.

Tokunaga, M., N. Imamoto, and K. Sakata-Sogawa. 2008. Highly inclined thin illumination enables clear single-molecule imaging in cells. *Nature methods*. 5:159-161.

Tournier, S., Y. Gachet, V. Buck, J.S. Hyams, and J.B.A. Millar. 2004. Disruption of astral microtubule contact with the cell cortex activates a Bub1, Bub3, and Mad3-dependent checkpoint in fission yeast. *Molecular biology of the cell*. 15:3345-3356.

Tsien, R.Y. 1998. The green fluorescent protein. *Annual review of biochemistry*. 67:509-544.

Turkowyd, B., A. Balinovic, D. Virant, H.G.G. Carnero, F. Caldana, M. Endesfelder, D. Bourgeois, and U. Endesfelder. 2017. A General Mechanism of Photoconversion of Green-to-Red Fluorescent Proteins Based on Blue and Infrared Light Reduces Phototoxicity in Live-Cell Single-Molecule Imaging. *Angewandte Chemie*. 56:11634-11639.

Turkowyd, B., D. Virant, and U. Endesfelder. 2016. From single molecules to life: microscopy at the nanoscale. *Anal Bioanal Chem*. 408:6885-6911.

Valverde, R., J. Ingram, and S.C. Harrison. 2016. Conserved tetramer junction in the kinetochore Ndc80 complex. *Cell reports*. 17:1915-1922.

van de Linde, S., A. Loschberger, T. Klein, M. Heidbreder, S. Wolter, M. Heilemann, and M. Sauer. 2011. Direct stochastic optical reconstruction microscopy with standard fluorescent probes. *Nature protocols*. 6:991-1009.
van Hooff, J.J.E., E. Tromer, L.M. van Wijk, B. Snel, and G.J.P.L. Kops. 2017. Evolutionary dynamics of the kinetochore network in eukaryotes as revealed by comparative genomics. *EMBO reports*. 18:1559-1571.
Venkei, Z., M.R. Przewloka, Y. Ladak, S. Albadri, A. Sossick, G. Juhasz, B. Novák, and D.M. Glover. 2012. Spatiotemporal dynamics of Spc105 regulates the assembly of the Drosophila kinetochore. *Open biology*. 2:110032.
Virant, D., B. Traenkle, J. Maier, P.D. Kaiser, M. Bodenhofer, C. Schmees, I. Vojnovic, B. Pisak-Lukats, U. Endesfelder, and U. Rothbauer. 2018. A peptide tag-specific nanobody enables high-quality labeling for dSTORM imaging. *Nat Commun*. 9:930.
Virant, D., B. Turkowyd, A. Balinovic, and U. Endesfelder. 2017. Combining Primed Photoconversion and UV-Photoactivation for Aberration-Free, Live-Cell Compliant Multi-Color Single-Molecule Localization Microscopy Imaging. *Int J Mol Sci*. 18.
Vojnovic, I. 2016. Spatial and temporal organization of the kinetochore proteins sad1, cut12 and cnp1 in Schizosaccharomyces pombe studied by fluorescence single molecule methods at a nanometer resolution. *In* Chemistry. Vol. Master Thesis. Frankfurt University.
Vojnovic, I., J. Winkelmeier, and U. Endesfelder. 2019. Visualizing the inner life of microbes: practices of multi-color single-molecule localization microscopy in microbiology. *Biochem Soc Trans*. 47:1041-1065.
Walstein, K., A. Petrovic, D. Pan, B. Hagemeier, D. Vogt, I.R. Vetter, and A. Musacchio. 2021. Assembly principles and stoichiometry of a complete human kinetochore module. *Science Advances*. 7:eabg1037.
Wan, X., R.P. O'Quinn, H.L. Pierce, A.P. Joglekar, W.E. Gall, J.G. DeLuca, C.W. Carroll, S.-T. Liu, T.J. Yen, and B.F. McEwen. 2009. Protein architecture of the human kinetochore microtubule attachment site. *Cell*. 137:672-684.
Wang, S., J.R. Moffitt, G.T. Dempsey, X.S. Xie, and X. Zhuang. 2014. Characterization and development of photoactivatable fluorescent proteins for single-molecule–based superresolution imaging. *PNAS*. 111:8452-8457.
Wevrick, R., and H.F. Willard. 1989. Long-range organization of tandem arrays of alpha satellite DNA at the centromeres of human chromosomes: high-frequency array-length polymorphism and meiotic stability. *Proceedings of the National Academy of Sciences*. 86:9394-9398.
Winey, M., C.L. Mamay, E.T. O'toole, D.N. Mastronarde, T.H. Giddings Jr, K.L. McDonald, and J.R. McIntosh. 1995. Three-dimensional ultrastructural analysis of the Saccharomyces cerevisiae mitotic spindle. *The Journal of cell biology*. 129:1601-1615.
Winkelmeier, J. 2018. Cellular division of Schizosaccharomyces pombe studied by single molecule localization microscopy. *In* Biophysics. Vol. Master Thesis. Frankfurt University.
Wolter, S., A. Loschberger, T. Holm, S. Aufmkolk, M.C. Dabauvalle, S. van de Linde, and M. Sauer. 2012. rapidSTORM: accurate, fast open-source software for localization microscopy. *Nature methods*. 9:1040-1041.
Wynne, D.J., and H. Funabiki. 2016. Heterogenous architecture of vertebrate kinetochores revealed by 3D super-resolution fluorescence microscopy. *Mol Biol Cell mbc. E16-02-0130*.
Yan, K., J. Yang, Z. Zhang, S.H. McLaughlin, L. Chang, D. Fasci, A.E. Ehrenhofer-Murray, A.J.R. Heck, and D. Barford. 2019. Structure of the inner kinetochore CCAN complex assembled onto a centromeric nucleosome. *Nature*. 574:278-282.
Ye, A.A., S. Cane, and T.J. Maresca. 2016. Chromosome biorientation produces hundreds of piconewtons at a metazoan kinetochore. *Nature communications*. 7:13221.
Yuen, K.W., B. Montpetit, and P. Hieter. 2005. The kinetochore and cancer: what's the connection? *Current opinion in cell biology*. 17:576-582.

Zahedi, Y., M. Durand-Dubief, and K. Ekwall. 2020. High-Throughput Flow Cytometry Combined with Genetic Analysis Brings New Insights into the Understanding of Chromatin Regulation of Cellular Quiescence. *International journal of molecular sciences*. 21:9022.

Zielinska, A.P., E. Bellou, N. Sharma, A.-S. Frombach, K.B. Seres, J.R. Gruhn, M. Blayney, H. Eckel, R. Moltrecht, and K. Elder. 2019. Meiotic kinetochores fragment into multiple lobes upon cohesin loss in aging eggs. *Current Biology*. 29:3749-3765.

Zinkowski, R.P., J. Meyne, and B.R. Brinkley. 1991. The centromere-kinetochore complex: a repeat subunit model. *Journal of Cell Biology*. 113:1091-1110.

Supplementary Data

Unraveling the kinetochore nanostructure in *Schizosaccharomyces pombe* using multi-color SMLM imaging

David Virant[1,†], Ilijana Vojnovic[1,2,3,†], Jannik Winkelmeier[1,2,3,†], Marc Endesfelder[4], Bartosz Turkowyd[1,2,3], David Lando[5] and Ulrike Endesfelder[1,2,3*]

[1]Department of Systems and Synthetic Microbiology, Max Planck Institute for Terrestrial Microbiology and LOEWE Center for Synthetic Microbiology (SYNMIKRO), Marburg, Germany

[2]Department of Physics, Carnegie Mellon University, Pittsburgh, Pennsylvania, US

[3]Institute for Microbiology and Biotechnology, Rheinische-Friedrich-Wilhelms-Universität Bonn, Bonn, Germany

[4]Institute for Assyriology and Hittitology, Ludwig-Maximilians-Universität München, Germany

[5]Department of Biochemistry, University of Cambridge, Cambridge CB2 1EW, UK

[†]authors contributed equally

*corresponding author, email: endesfelder@uni-bonn.de

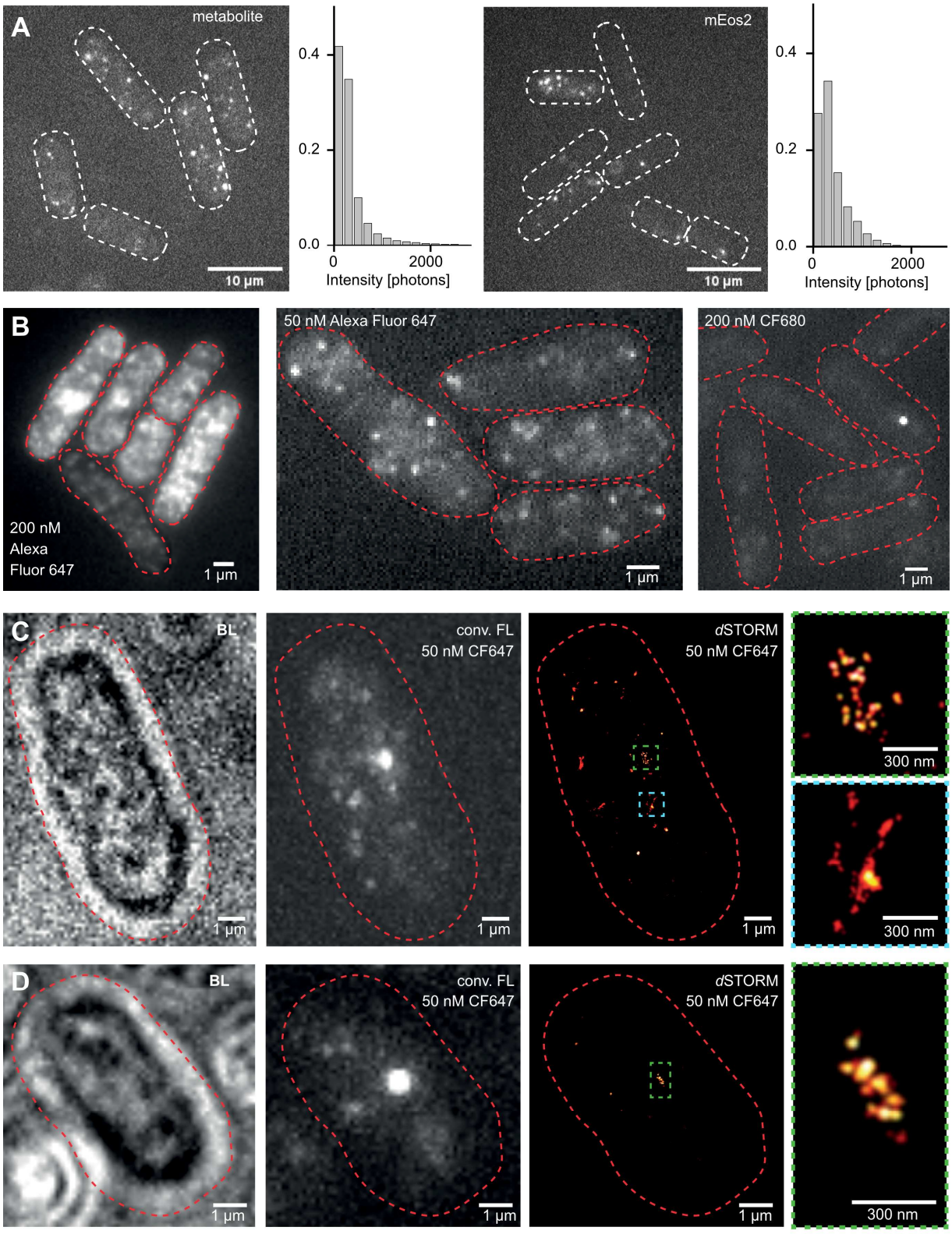

Figure S1. Developing the Labeling Strategy.

(A) Autofluorescence of metabolites overlaps with fluorescent protein signal intensity. Exemplary images from recorded movies of *S. pombe* cells containing either accumulated metabolites (due to a mutation in the ade6 gene, left) or expressing fluorescent proteins (cytosolic mEos2, right) at similar imaging conditions. Cell borders are shown as dashed lines. Scale bar 10 µm. Histograms of the intensities of individual localizations for both conditions. Localizations were filtered using a sigma of 70 - 200 nm. The metabolite signal strength overlaps with the fluorophore signal. Therefore, the autofluorescence noise cannot be reliably filtered from the fluorophore signal. Metabolite N = 35509, mEos2 N = 467680, bin size = 200 nm.

(B) Dye staining in *S. pombe* is heterogeneous and unreliable for low copy number targets. Staining of Halo-cnp1^{CENP-A} cells with the cyanine Alexa Fluor 647 200 nM (left), 50 nM (middle) shows a high degree of nonspecific labeling, even when using the blocking agents BSA and Image-IT (which reduce nonspecific interactions of the charged dye with the sample). Staining with 200 nM (right) of cyanine CF680 shows low labelling efficiency even after cell wall and membrane were partially digested with zymolyase and Triton-X100. We attribute the low efficiency to its large molecular weight (CF680 is about 2.3 times larger than Alexa Fluor 680 as it has masking groups to avoid nonspecific staining due to charges).

(C) Exemplary cell showing high unspecific staining of CF647-Halo-cnp1^{CENP-A} in brightlight (left), conventional fluorescence (middle) and SMLM imaging (right). Detailed views illustrating inset with the cnp1^{CENP-A} signal (green border) compared to some nonspecific signal (inset with blue border).

(D) Exemplary cell with low, nonspecific staining of CF647-Halo-cnp1^{CENP-A} at a high labeling efficiency.

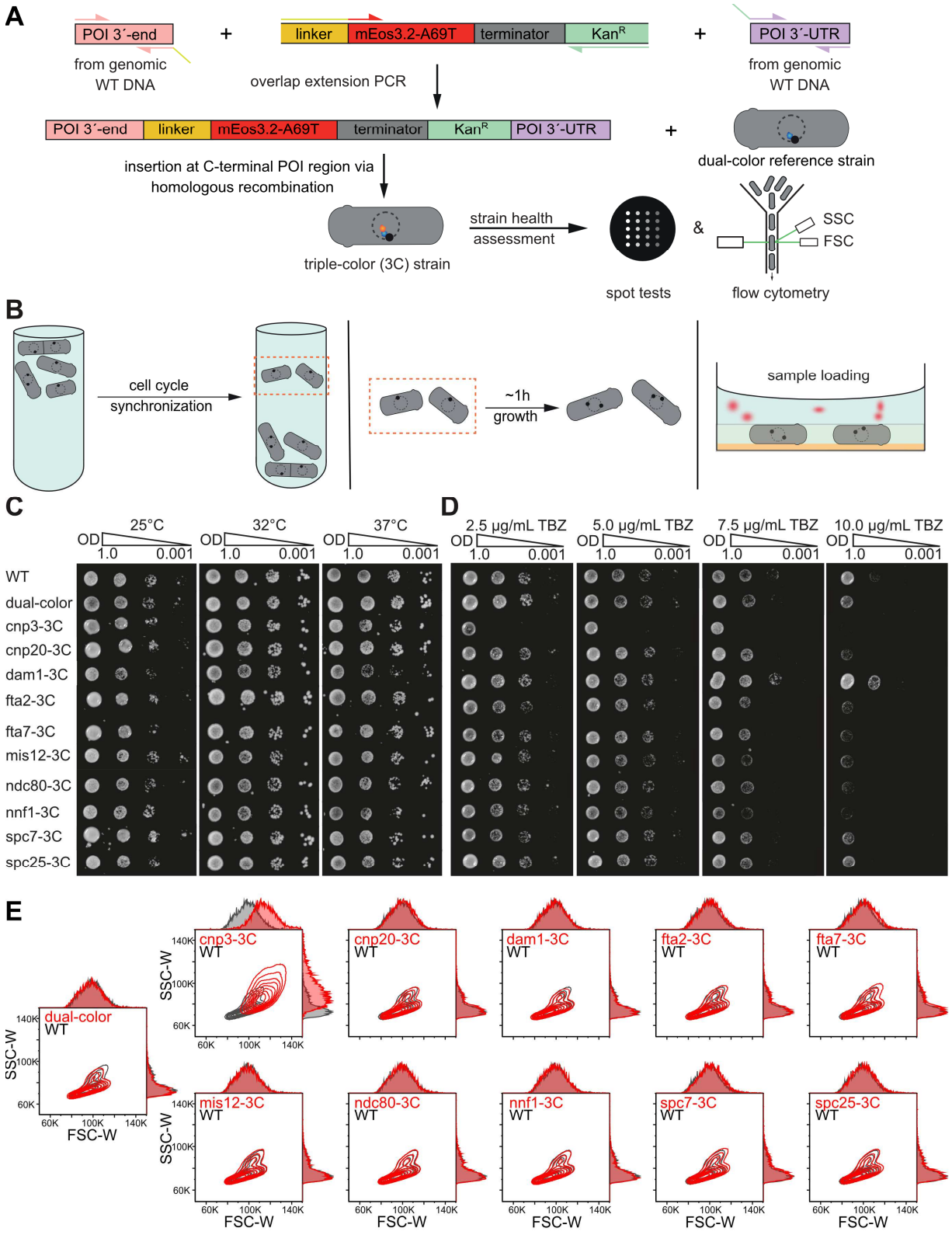

Figure S2. Cloning strategy, sample preparation and health assessment of 3C- strains.

(A) Cloning strategy. DNA fragments containing the POI 3'-end (pink), the FP-resistance cassette (yellow-red-grey-green) and the POI 3'- UTR (untranslated region, purple) were amplified with the corresponding primers with ~20 bp overlap to the future neighboring DNA fragments from either genomic WT DNA or a plasmid DNA. Pieces were then fused by overlap extension PCR and transformed into the dual-color reference strain (h+, leu1-32, ura4-D18, sad1:mScarlet-I:hphMX6, PAmCherry1:cnp1^{CENP-A}) using homologous recombination to create a triple-color strain library (Table S1).

(B) Sample preparation. Cell cultures were synchronized using lactose gradient centrifugation, which accumulates cells in early G2 phase in an upper band. The cells were then extracted from the gradient column, grown for another 1-1.5 h until mitosis and chemically fixed, washed and embedded in agarose gel with fiducial markers.

(C, D) Assessment of strain health & mitotic defects. Temperature (C) or thiabendazole (TBZ, D), which induces mitotic defects by microtubule depolymerization, sensitivities between the parental WT, the dual-color reference, and the individual triple-color (3C) strains were assessed by spot tests. Here, a tenfold dilution series of OD600 from 1.0 to 0.001 of overnight cultures was grown on either YES media plates at 25, 32 and 37°C for three days or YES media plates containing 2.5, 5.0, 7.5 and 10.0 µg/mL TBZ and incubation at 25°C for three days.

(E) Flow cytometry measurements to assess *S. pombe* strain health. FSC-W and SSC-W contour plots (each level within the contour plot consists of 10% measured cells) and their corresponding histograms of triple-color (POI-3C) strains and the dual-color template strain compared to a fission yeast wild-type (WT) strain. A defect in cell division usually results in increased cell length and higher FSC-W and SSC-W values, which we observed for cnp3^{CENP-C}-3C (top row, left column) but none of the other strains tested. N = 10.000 for each POI (see Materials & methods).

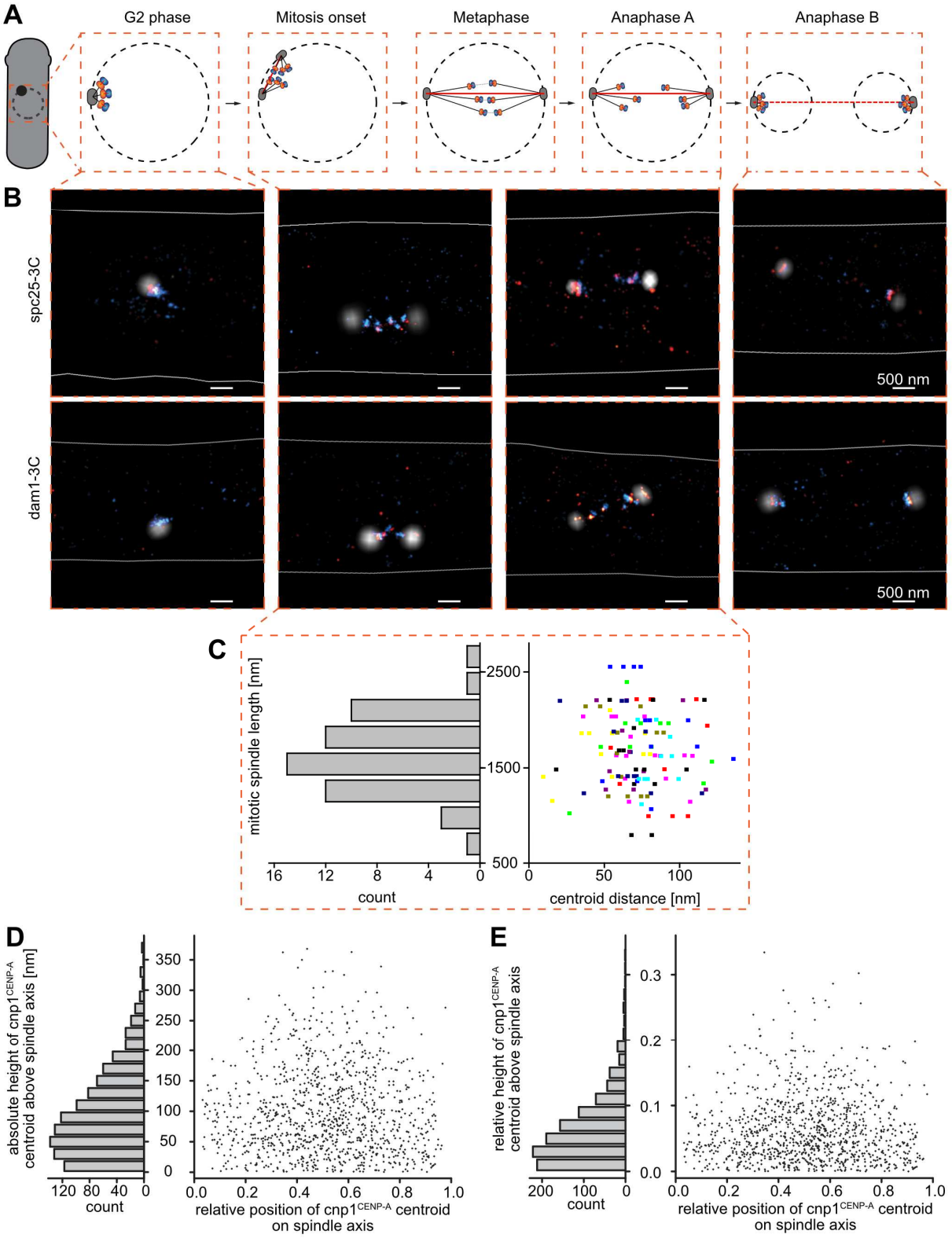

Figure S3. Centroid distance is independent of mitotic spindle length.

(A) Scheme of the *S. pombe* cell cycle (from left to right): A fission yeast cell in G2 phase is drawn with a nuclear envelope (NE; black dashed circle) and one spindle pole body (SPB, black). Insets show the nucleus changing over the cell cycle phases (G2, onset of mitosis, metaphase, Anaphase A and Anaphase B) with the kinetochore (orange) linking the centromere (blue) to the SPB via a bundle of kinetochore microtubules (black lines), while the spindle microtubules (red line) push the two SPBs further apart.

(B) Exemplary three-color SMLM images of spc25-3C (top row) and dam1-3C (bottom row) strains representing the cell cycle stages shown in (A). SPB (sad1-mScarlet-I) localizations are shown in white, kinetochores (POI-mEos3.2-A69T) in red, centromeres (PAmCherry1-cnp1^{CENP-A}) in blue, and the cell border (determined by the bright light image) is drawn as a white line. Scale bar 500 nm.

(C) Left: Histogram of an exemplary data set of mitotic spindle lengths (distance between the two SPBs during mitosis) for the POI dam1. **Right**: the distance between the centroids of individual kinetochore cluster pairs (POI and cnp1^{CENP-A}) plotted against the mitotic spindle length from the same cell. Data points of the same height and color are from the same mitotic spindle. All spindle lengths are shorter than the average nuclear diameter of 2-3 µm, thus excluding anaphase B cells. mitotic spindles N = 55, kinetochore cluster pairs N = 122, bin size = 280 nm.

(D, E) Angular offset of kMT and spindle axes. Plotted are relative position and height over the spindle axis (defined as sad1-sad1 centroid distance) for all measured cnp1^{CENP-A} centroids. Height of cnp1^{CENP-A} centroids is either plotted in absolute nanometer distances (D) to visualize that most kinetochores are in direct vicinity to the central bundle or normalized to the respective spindle length of the cells (E) to represent the angular distribution between the spindle and kMT axes. N = 1099, bin size = 20 nm.

Strain	Genotype	Source
SP176 (972)	wt h-	gift from Laue lab, Cambridge, UK
SP177/ wt h+	h+, ade6-210, leu1-32, ura4-D18	(Lando et al., 2012)
SP11/ DL70	h+, ade6-210, leu1-32, ura4-D18, PAmCherry1:cnp1	(Lando et al., 2012)
SP118	h-, sad1:mScarlet-I:hphMX6	this study
SP145	h+, leu1-32, ura4-D18, sad1:mScarlet-I:hphMX6, PAmCherry1:cnp1	this study
SP137	h+, leu1-32, ura4-D18, spc25:mEos3.2-A69T:kanMX6, sad1:mScarlet-I:hphMX6, PAmCherry1:cnp1	this study
SP141	h+, leu1-32, ura4-D18, mis12:mEos3.2-A69T:kanMX6, sad1:mScarlet-I:hphMX6, PAmCherry1:cnp1	this study
SP144	h+, leu1-32, ura4-D18, dam1:mEos3.2-A69T:kanMX6, sad1:mScarlet-I:hphMX6, PAmCherry1:cnp1	this study
SP146	h+, leu1-32, ura4-D18, fta2:mEos3.2-A69T:kanMX6, sad1:mScarlet-I:hphMX6, PAmCherry1:cnp1	this study
SP147	h+, leu1-32, ura4-D18, fta7:mEos3.2-A69T:kanMX6, sad1:mScarlet-I:hphMX6, PAmCherry1:cnp1	this study
SP150	h+, leu1-32, ura4-D18, cnp3:mEos3.2-A69T:kanMX6, sad1:mScarlet-I:hphMX6, PAmCherry1:cnp1	this study
SP152	h+, leu1-32, ura4-D18, ndc80:mEos3.2-A69T:kanMX6, sad1:mScarlet-I:hphMX6, PAmCherry1:cnp1	this study
SP153	h+, leu1-32, ura4-D18, nnf1:mEos3.2-A69T:kanMX6, sad1:mScarlet-I:hphMX6, PAmCherry1:cnp1	this study
SP154	h+, leu1-32, ura4-D18, spc7:mEos3.2-A69T:kanMX6, sad1:mScarlet-I:hphMX6, PAmCherry1:cnp1	this study

SP155	h+, leu1-32, ura4-D18, cnp20:mEos3.2-A69T:kanMX6, sad1:mScarlet-I:hphMX6, PAmCherry1:cnp1	this study
SP109	h+, ade6-210, leu1-32, ura4-D18, Halo:cnp1	(Vojnovic, 2016)
SP16	h+, ade6-210, leu1-32, ura4-D18, pREPnmt81-mEos2::Leu2	(Lando et al., 2012)
EC290	Rosetta DE3 pRSETa mEos3.2-A69T:FtnA	this study

Supplementary Table S1: *S. pombe* and *E. coli* strains used in this study

Primer name	**5'→3' SEQUENCE + overlap**
Ade6_F2	CTCATTAAGCTGAGCTGCCAAG
Ade6_R2	TGCATAGGCGACCATAGACAT
AGGSG_mEos3.2_F	gccggaggcagtggttct
Cnp3_F1	GGAAAGATCGAGGTCACAGT
Cnp3_F2	aatgctggtcgctatactgctgtcCAATACTAATAGTGTGTTATGGATTTCG
Cnp3_R1_AGGSG	GGGATTTTCCAAACGAACGAgccggaggcagtggt
Cnp3_R2	AAAGTCAAATCTAACGGTCGC
Cnp20_F1	TTCAACACTTGTGCTACCGGAAA
Cnp20_F2	aatgctggtcgctatactgctgtcTGCGTACTTCTCCTTTACATTCATC
Cnp20_R1_AGGSG	ACCTCCGGCAATTAAGAGAACCgccggaggcagtggt
Cnp20_R2	CGCTTGATTCGATACACTTACAAGT
Dam1-GFP F1	TGCCGAAAGCGCTGTAGAA
Dam1F2	aatgctggtcgctatactgctgtcATTTATTTAAGCAAGGGAGACTGGTTG
Dam1_R1_Overhang_ AGGSG_D2	AGAAACCTATTCCGCTTCCAGAgccggaggcagtggttct
Dam1R2	TAGCTTCTCCAATCTTCAATTTCCA
fta2_F1	CATGGACGCTCAATGTTTCT
fta2_F2	aatgctggtcgctatactgctgtcGAAGGATAAATTGATATTTTTAACATGGTT
fta2_R1_AGGSG	GGCATTATTTAAACCTCATTTGGGGgccggaggcagtggt
fta2_R2	AGTTCTTTTGGCAGAATGGG

Fta7_F1	TTCAGACTCCAACGATTTCTC
Fta7_F2	aatgctggtcgctatactgctgtcACATAGAAAAGCTAGAGCTTAAGAC
Fta7_R1_AGGSG	AGTCATCCAAACTTAAGATAAAGAATATCgccggaggcagtggt
Fta7_R2	GAGTTTAGGGTAGGGTAAGCA
KanR_cassette_R	Aatgctggtcgctatactgctgtc
Mis12_F1	TCTGCAGCATGCCGTTAAAAG
Mis12_F2	aatgctggtcgctatactgctgtcTACTAATCAACTAGCTAAAGTCTTGAGATG
Mis12_R1_AGGSG	CGGACATACTGACGAGCCTgccggaggcagtggt
Mis12_R2	TCTGACCCATTAACTCCAAATCTGT
Ndc80_F1	ACAACAGCTCAAACTTTCTTCG
Ndc80_F2	aatgctggtcgctatactgctgtcATTCTATTCATCGTATTGTGCTGTC
Ndc80_R1_AGGSG	ACCTATCTCGTTCGGAACTGgccggaggcagtggt
Ndc80_R2	ACGAACTGTTTTGGCTAAAAATTTG
Nnf1_F1	AAGCTTAATCAGGATCTGTTGG
Nnf1_F2	aatgctggtcgctatactgctgtcAAGAAGTAAATTTCTAATCAGTTGCA
Nnf1_R1_AGGSG	AACGAACAAGGAAATATAGAACGTgccggaggcagtggt
Nnf1_R2	CTCAAAAACATTCCAACGCAA
Spc7_F1	TTGAGCTATACCTGCGTTCGG
Spc7_F2	aatgctggtcgctatactgctgtcATATTAATGGGAATGATTAGCTATGCTGC
Spc7_R1_AGGSG	CTTGTCTTACTGTTTGGAACAAATACAGCgccggaggcagtggt
Spc7_R2	AAACCCGTAATGCGCTACAAAA

Spc25_F1	ATCAATCTTGCTGAAAGGGATTA
Spc25_F2	aatgctggtcgctatactgctgtcAGATCTTCTTCTTGTTTAACATAAACTT
Spc25_R1_AGGSG	TAGAAAGGATCTGTCTCAATTGATTgccggaggcagtggt
Spc25_R1_D2	TAGAAAGGATCTGTCTCAATTGATTgccggaggcagtggtATG
Spc25_R2	AACTGGTGGAATCCATGGT
mEos3.2_F_pRSET	ACGATAAGGATCGATGGGGATCCATGtctgccattaaaccgga
mEos3.2_R_FtnA	ggatgctccgctagccttgcgacgcgcattatcc
pRSET_F_preFtnA_68	aaggctagcggagcatcc
pRSET_R_blunt_68	GGATCCCCATCGATCCTTATCGT

Supplementary Table S2: List of primers used for constructing the 3C-library and the FtnA protein standard as listed in table S1

complex	components	expected ratios	measured ratios	weighted mean	STD
COMAc	fta2, fta7, mal2, mis17	1:1:1:1	1:1.0:NA:NA	56.0	28.2
MINDc	mis12, nnf1, mis13, mis14	1:1:1:1	1:1.3:NA:NA	85.1	43.1
NDC80c	ndc80, nuf2, spc24, spc25	1:1:1:1	1:NA:NA:1.1	111.2	51.7

Supplementary Table S3: Weighted mean of localization counts for POIs belonging to the same kinetochore subcomplex. N = 148 for COMAc, 353 for MINDc and 258 for NDC80c.

complexes	ratio	reference	host	method	cell cycle stage
cnp20^{CENP-T} : COMA	1 : 0.9	this study	*S. pombe*	SMLM imaging	Meta- to Anaphase A
	1: 2.0	(Cieslinski et al., 2021)	*S. cerevisiae*	SMLM imaging	Metaphase
MIND : spc7^{KNL1}	1 : 1.1	this study	*S. pombe*	SMLM imaging	Meta- to Anaphase A
	1 : 0.7	(Joglekar et al., 2008)	*S. pombe*	fluorescence ratio	G2 to Metaphase
	1 : 1.0	(Joglekar et al., 2008)	*S. pombe*	fluorescence ratio	Anaphase to Telophase
	1 : 0.7	(Lawrimore et al., 2011)	*S. pombe*	corrected from Joglekar et al. 2008	G2 to Metaphase
	1 : 1.3	(Joglekar et al., 2006)	*S. cerevisiae*	fluorescence ratio	Metaphase
	1 : 1.1	(Joglekar et al., 2006)	*S. cerevisiae*	fluorescence ratio	Anaphase
	1 : 1.0	(Lawrimore et al., 2011)	*S. cerevisiae*	fluorescence ratio	Anaphase
	1 : 0.7	(Dhatchinamoorthy et al., 2017)	*S. cerevisiae*	fluorescence ratio	Anaphase
	1 : 1.1	(Cieslinski et al., 2021)	*S. cerevisiae*	SMLM imaging	Metaphase
	1 : 0.8	(Johnston et al., 2010)	*Chicken DT40*	fluorescence ratio	Metaphase
	1 : 0.8	(Lawrimore et al., 2011)	*Chicken DT40*	fluorescence ratio	Metaphase
	1 : 0.8	(Emanuele et al., 2005)	*X. laevis*	Biochemical assay	unsynchronized
COMA : MIND	1 : 1.5	this study	*S. pombe*	SMLM imaging	Meta- to Anaphase A
	1 : 1.6	(Joglekar et al., 2008)	*S. pombe*	fluorescence ratio	G2 to Metaphase
	1 : 0.8	(Joglekar et al., 2008)	*S. pombe*	fluorescence ratio	Anaphase to Telophase
	1 : 1.6	(Lawrimore et al., 2011)	*S. pombe*	corrected from Joglekar et al. 2008	G2 to Metaphase
	1 : 2.2	(Joglekar et al., 2006)	*S. cerevisiae*	fluorescence ratio	Metaphase
	1 : 2.3	(Joglekar et al., 2006)	*S. cerevisiae*	fluorescence ratio	Anaphase

	1 : 2.3	(Lawrimore et al., 2011)	*S. cerevisiae*	fluorescence ratio	Anaphase
	1 : 2.3	(Dhatchinamoorthy et al., 2017)	*S. cerevisiae*	fluorescence ratio	Anaphase
	1 : 1.8	(Cieslinski et al., 2021)	*S. cerevisiae*	SMLM imaging	Metaphase

Supplementary Table S4: POI copy number ratios between different kinetochore subcomplexes

	Kinetochore subcomplex	**POI** (homolog in *S. cerevisiae*)	**distance [nm] ± STD** to *S.pombe* C-term spc7^{KNL1} (spc105), this study	**distance [nm] ± SEM** to *S. cerevisiae* C-term spc7^{KNL1} (spc105), Cieslinski et al.
cnp1^{CENP-A}		**cnp1^{CENP-A} (cse4)**	N-term: -25.9 ± 1.2	C-term: -16.9 ± 1.3
CCAN	**CBF3** (only in cerevisiae)	**N/A (cep3)**	/	-21.1 ± 1.7
		cnp3 (mif2)	/	-23.8 ± 2.0
	CENP-T/cnn1	**cnp20^{CENP-T} (cnn1)**	-17.6 ± 2.7	-20.1 ± 2.7
	COMA	**fta2^{CENP-P} (ctf19)**	-14.5 ± 2.2	-14.9 ± 1.7
		fta7^{CENP-Q} (okp1)	-14.2 ± 3.1	-13.4 ± 1.4
	CENP-N/Chl4	**mis15 (chl4)**	/	-23.5 ± 2.9
KMN	**KNL1/Spc105**	**spc7^{KNL1} (spc105)**	0	0
	MIND	**nnf1^{PMF1}**	1.2 ± 1.8	4.8 ± 2.6
		mis12 (mtw1)	2.1 ± 2	4.3 ± 0.6
		mis13 (dsn1)	/	3.1 ± 0.6

		mis14 (nsl1)	/	6.5 ± 1.5
	NDC80	**spc25**	-4 ± 2.5	-2.5 ± 0.8
		ndc80^{HEC1}	10.3 ± 1.9	13.6 ± 1.2
		nuf2	/	16.9 ± 1.5
Dam1/DASH	**Dam1/DASH**	**dam1**	38.3 ± 1.8	/
		ask1	/	44.3 ± 1.8

Supplementary Table S5: Comparison of protein cluster distances between our study in *S. pombe* and the study of Cieslinski et al. in *S. cerevisiae*. The studies used different reference proteins. Whereas our studies used N-terminal cnp1^{CENP-A} as the reference, Cieslinski et al used C-terminal spc7^{KNL1}. In the upper table, we thus converted our numbers and errors into the Cieslinski et al. reference frame by using our distance between C-terminal spc7^{KNL1} and N-terminal cnp1^{CENP-A}. From the literature, it is known that the intramolecular C- to N-terminal cnp1^{CENP-A} distance is about 3 - 5 nm (Migl et al., 2020; Sekulic et al., 2010; Tachiwana et al., 2011; Yan et al., 2019) which should be considered when comparing the numbers in the above table.

References

Cieslinski, K., Y.-L. Wu, L. Nechyporenko, S.J. Hoerner, D. Conti, and J. Ries. 2021. Nanoscale structural organization and stoichiometry of the budding yeast kinetochore. *BioRxiv*. 2021/469648.

Lando, D., U. Endesfelder, H. Berger, L. Subramanian, P.D. Dunne, J. McColl, D. Klenerman, A.M. Carr, M. Sauer, R.C. Allshire, M. Heilemann, and E.D. Laue. 2012. Quantitative single-molecule microscopy reveals that CENP-A(Cnp1) deposition occurs during G2 in fission yeast. *Open biology*. 2:120078.

Migl, D., M. Kschonsak, C.P. Arthur, Y. Khin, S.C. Harrison, C. Ciferri, and Y.N. Dimitrova. 2020. Cryoelectron microscopy structure of a yeast centromeric nucleosome at 2.7 Å resolution. *Structure*. 28:363-370.

Sekulic, N., E.A. Bassett, D.J. Rogers, and B.E. Black. 2010. The structure of (CENP-A–H4) 2 reveals physical features that mark centromeres. *Nature*. 467:347-351.

Tachiwana, H., W. Kagawa, T. Shiga, A. Osakabe, Y. Miya, K. Saito, Y. Hayashi-Takanaka, T. Oda, M. Sato, and S.-Y. Park. 2011. Crystal structure of the human centromeric nucleosome containing CENP-A. *Nature*. 476:232-235.

Vojnovic, I. 2016. Spatial and temporal organization of the kinetochore proteins sad1, cut12 and cnp1 in Schizosaccharomyces pombe studied by fluorescence single molecule methods at a nanometer resolution. *In* Chemistry. Vol. Master Thesis. Frankfurt University.

Yan, K., J. Yang, Z. Zhang, S.H. McLaughlin, L. Chang, D. Fasci, A.E. Ehrenhofer-Murray, A.J.R. Heck, and D. Barford. 2019. Structure of the inner kinetochore CCAN complex assembled onto a centromeric nucleosome. *Nature*. 574:278-282.

CHAPTER 3

Developing SExY for low abundant protein structures

This chapter is written in the style of a manuscript and was submitted as a research article in *Open Biology* in 2022 and is currently under peer review. For this publication, the initial project idea was proposed by Prof. Dr. Ulrike Endesfelder, Dr. Oliver D. Caspari and me and the experiments and analysis were conducted by Dr. Oliver D. Caspari, Mehmet Ali Hoskan and me. Prof. Dr. Ulrike Endesfelder and me designed the manuscript figures and tables and wrote the manuscript text with the input from all co-authors. The supplementary information of this work can be found in this chapter subsequently to the main publication.

In this publication, we present a novel imaging technique termed SExY, which combines ExM with PALM and achieves higher resolutions in fission yeast. By optimizing the protocol for fluorescent protein retention and isotropic expansion, low-abundant proteins such as KT proteins as well as multiple other nuclear targets could be visualized in greater detail.

Combining Single-molecule and Expansion microscopy in fission Yeast (SExY) to visualize protein structures at molecular detail

Ilijana Vojnovic[1,2,*,†], Oliver D. Caspari[1,**†], Mehmet Ali Hoşkan[1,***] and Ulrike Endesfelder[1,2,*, §]

[1] Department of Systems and Synthetic Microbiology, Max Planck Institute for Terrestrial Microbiology and LOEWE Center for Synthetic Microbiology (SYNMIKRO), Marburg, Germany

[2] Department of Physics, Carnegie Mellon University, Pittsburgh, Pennsylvania, US

* current address: Institut für Mikrobiologie und Biotechnologie, Rheinische Friedrich Wilhelms-Universität, Bonn, Germany

** current address: Institute Pasteur, Department of Microbiology, Paris, France

*** current address: University of Wisconsin-Madison, Department of Medical Microbiology & Immunology, Madison, Wisconsin, US

† authors contributed equally

§ corresponding author, email: endesfelder@uni-bonn.de

Keywords

Single-Molecule Localization Microscopy (SMLM), Photoactivated Localization Microscopy (PALM), Expansion Microscopy (ExM), *Schizosaccharomyces pombe (S. pombe)*, Protein Retention Yield, correlative ExM microscopy

Abstract

In this work, we have developed an expansion microscopy (ExM) protocol that combines ExM with photoactivated localization microscopy (ExPALM) for yeast cell imaging, and report a robust protocol for single molecule and expansion microscopy of fission yeast, short SExY.

Our optimized SExY protocol retains about 50% of the fluorescent protein (FP) signal, doubling the amount obtained compared to the original protein retention ExM (proExM) protocol. It allows for a fivefold, highly isotropic expansion of fission yeast cells, which we carefully controlled while optimizing protein yield. We demonstrate the SExY method on several exemplary molecular targets and explicitly introduce low-abundant protein targets, e.g., nuclear proteins such as cbp1 and mis16 and the centromere-specific histone protein cnp1.

The SExY protocol optimizations increasing protein yield could be beneficial for many studies, i.e. when targeting low abundance proteins or studies that rely on genetic labeling for various reasons, e.g. for proteins that cannot be easily targeted by extrinsic staining or in case artifacts introduced by unspecific staining interfere with data quality.

Introduction

The resolution of optical microscopy is constrained by the diffraction limit of light at about 200 nm [1]. However, most of molecular organization occurs in dimensions below this limit and therefore cannot be resolved by conventional light microscopic techniques. Super-resolution fluorescence microscopy (SRM) can be used to circumvent the diffraction limit by modulating the fluorescence of fluorescently labeled samples at a sub-diffraction level, thereby discriminating between them [2]. This is achieved either by precisely defined illumination patterns, e.g., in STED [3] and SIM [4] imaging, or by single-molecule localization microscopy (SMLM) methods, in which the fluorescence of individual, on- and off-blinking or on- and off-binding fluorophores is separated in time, e.g., in PALM [5], (d)STORM [6,7] or PAINT [8] techniques. More recently, expansion microscopy (ExM) techniques have been developed that physically expand the biological sample, increasing resolution by practically a factor of 3 - 20-fold as a result of inflating the structures [9–13]. In contrast to the "classical" SRM methods, where preparing a good sample mostly relies on choosing the right fluorophores (e.g. either photostable (SIM, STED), well-controlled photoswitching (SMLM) and being bright (all)) and optimizing for efficient and specific labeling (e.g. small labels for dense labeling, non-sticking labels for high specificity or genetic, covalent or high affinity labels for high efficiency) [2], ExM poses additional demands to the sample preparation due to the desired physical expansion: In ExM, the sample is anchored to a gel mesh and expanded upon incubation in aqueous media [9]. To achieve an isotropic expansion of the sample and thus a preservation of the underlying biological ultrastructure, all physical connections within the structure must be efficiently removed by e.g., cell wall removal [14–17] and protein digestion steps [10,18–21], and all target molecules must be properly linked to the gel mesh before expansion by e.g. anchoring [22–24] or linkage by fixation [22]. In this context, implementing ExM in organisms with rigid cell walls [14–17,25–27] or maintaining isotropic expansion within samples of heterogeneous "rigidity" [20,28–31] is a particular challenge. Recent work has shown that samples can show different macro- and micro-expansion factors, e.g., factors that vary within a gel or tissue or differ between different organelles or domains within organelles [20,28–31]. Finally, protocols are often not directly transferable between different samples. For example, an ExM method that preserved isolated centrioles from *Chlamydomonas reinhardtii* failed to isotopically expand chromatin in root tips of barley [28,32].

A second challenge in ExM is to retain the molecular information of the sample while breaking physical connections for expansion. The protein retention yield is typically measured by how many target molecules can still be detected via fluorescent markers in an expanded sample [23]. It is mainly affected by the protocol steps of protein digestion and gelation. Protein digestion involves homogenization of the sample by cleavage of the proteins' peptide chains

with proteinase K or collagenase type II, heat denaturation, or homogenizing agents such as SDS [9,10,18,19,21]. Gelation involves the generation of radicals during the polymerization chain reaction of monomers to form a polyacrylamide gel (PAA). Only recently, a radical-free gelation method using novel custom-synthesized monomers was developed [33]. Both, protein digestion and gelation, thus have potential to reduce the protein retention yield by degrading target sites for staining or by degrading genetically encoded markers.

Protocols combining ExM with SRM techniques to date have achieved an overall resolution of 1- 30 nm [34–37]. While a combination of ExM and SRM yields superior resolution, fluorophore choice and labeling strategy must suit both techniques, i. e. withstand and perform under the combined sample preparation and imaging protocols. To date, ExM was successfully combined with SIM [34], STED [35], dSTORM [36,37] and fluctuation-based technics [38,39]. These ExM-SRM protocols rely on extrinsic labeling techniques of the targets using labels with organic dyes, mainly immunofluorescence [34–39]. Furthermore, dSTORM uses ionic switching buffers needed for the on- and off-blinking of dyes. These buffers however shrink expanded gels from deionized water. Thus, ExSTORM relies on expansion in ionic buffers, which achieves only lower expansion of about threefold [36]. An alternative is Ex-SMLM [37]. Here, gels expanded in deionized water are embedded in an uncharged secondary gel. These double-layer gels achieve an about threefold increase and tolerate incubation in ionic switching buffers.

While current ExM-SRM protocols work well for abundant targets and larger (polymeric) structures in various samples, staining background signal from nonspecific adherent labels severely compromises imaging of sparse targets. Additionally, factors that hinder efficient extrinsic labeling such as e.g. a cell wall or a highly crowded and charged cytosol like in microbial organisms can complicate labeling [40] and can introduce artifacts [41]. To date, there are only a handful of publications on combined ExM and SRM strategies for microbiology, namely two studies using ExSIM of fungi [16] and bacteria [42], and one has combined ExM with SRRF imaging for viral SARS-Cov-2 particles [38].

In this work, we set out to establish a protocol for combined ExM and SMLM imaging in yeast. Here, our SMLM method of choice was PALM microscopy. In contrast to dSTORM, PALM microscopy makes use of genetic labeling using fluorescent proteins (FP) [2]. Thus, PALM samples intrinsically possess high labeling efficiency and specificity and does not rely on switching buffers which makes an implementation of ExPALM attractive for microbiological studies (at the price that current FPs offer lower photostability and photon yield compared to dyes). Nevertheless, as fluorescent proteins are affected and at least partially degraded by the ExM sample preparation protocols, so far, no protocols that combine ExM with PALM (ExPALM) exist.

Here, we combine PALM imaging with a proExM protocol [23] optimized for isotropy and protein retention for the fission yeast *S. pombe.* Using our optimized sample preparation protocols, we established an ExPALM protocol that preserves about 50% of the FP signal, doubling the retained amount in comparison when applying the protein retention ExM (proExM) protocol to the tested *S. pombe* cell samples. Our optimized protocol achieves a fivefold, highly isotropic expansion of fission yeast cells which we tested for several molecular targets. Taken together, this protocol is the first demonstration of combined Single-molecule and Expansion Microscopy of Yeast (SExY microscopy).

Materials and methods

Strain construction

C-terminal tagging of cbp1 with mEos2 [43] and sad1 with mScarlet-I [44] was adapted from [45]. First, two intermediate plasmids were created. For creating cbp1-mEos2, a pBluescript II SK+ plasmid containing the *Saccharomyces cerevisiae* ADH1 terminator, a kanamycin resistance gene and the mEos2 gene was constructed using primers with 20 bp overlap sequences (primers 9-14, table S3) [45]. Similarly, for creating sad1-mScarlet-I, a pFA6-mScarlet-I-ADH1-hphMX6 plasmid was constructed amplifying mScarlet-I from pFA6a-mScarlet-I-hphNT1 [46] (primers 24-25) and pFA6-ADH1-hphMX6 (primers 15-16) from pFA6-hphMX6 [47]. DNA fragments were combined by Gibson Assembly (New England Biolabs, cat. #E5510S), transformed into competent DH5α cells, streaked onto LB Amp^R plates and incubated overnight at 37°C. Single colonies were picked, grown in LB Amp^R cultures for 2 h at 37°C and plasmids were extracted (ZymoPure II Plasmid Midiprep kit, Zymo Research, cat. #D4200S) and checked by sequencing (Eurofins Genomics Germany GmbH). In a second step, 200-600 bp DNA fragments up- and downstream of the respective insertion site were amplified from isolated genomic DNA from h^- *S. pombe* cells with 20 bp overlaps to the flanking genes using primers 1-4 for cbp1 and 17,19 & 22-23 for sad1. The DNA fragments were combined with the corresponding FP-ADH1-antibiotic resistance fragment using overlap-extension PCR [48] for sad1-mScarlet-I or SLiCE [49] for cbp1-mEos2. 10 µl of the PCR mix were transformed into either competent *h^+ ade6-210 leu1-32 ura4-D18 mEos2:cnp1 or h- WT strain* utilizing the Frozen-EZ Yeast Transformation II Kit (Zymo Research, cat. #T2001). Cells were streaked onto YES agar plates, incubated overnight at 32°C, replica plated onto either YES Kan^R or YES Hyg^R agar plates and grown at 32°C for another two days. Successful genomic integration was checked by colony-PCR and DNA sequencing (Eurofins Genomics Germany GmbH).

For N-terminal tagging of mis16, DNA fragments up- and downstream of the insertion site where generated using primers 5-8. The DNA fragments were combined with mEos2-mis16

using SLiCE [49]. 10 µl of the PCR mix were transformed into either competent *h⁺ ade6-M210 leu1-32 ura4-D18 ura4nm41:mis16* cells utilizing the Frozen-EZ Yeast Transformation II Kit (Zymo Research, cat. #T2001). Cells were streaked out onto YES agar plates containing 1 g/L 5-Fluoroorotic Acid and 50 mg/mL uracil and grown at 32°C for two days. Successful genomic integration was checked by colony-PCR and DNA sequencing (Eurofins Genomics Germany GmbH).

Protease Enzyme Activity Assay

The colorimetric assay to measure possible protease activities of the different enzymes was adapted from [50,51]. In short, casein (Sigma-Aldrich, cat. #C7078-500G) was digested to release tyrosine. After stopping the digestion with tricholoroacetic acid (Sigma-Aldrich, cat. # T0699-100ML), released tyrosine was measured by absorption at 660 nm using Folin & Ciocalteu's Phenol reagent (Sigma-Aldrich, cat. # F9252-100ML). Enzymes were tested at their respective optimal working temperature and digestion buffer for 10 min. Concentration ranges were 0.2-1.0 U/mL for proteinase K, 0.2-1.0, 10 U/mL and 50 U/mL for Zymolyase and β-glucoronidase and 0.02-0.1 U/mL for lysing enzyme. Controls with 20 mM of the protease inhibitor phenylmethylsulfonylfluorid (PMSF, ThermoFisher Scientific, cat. #36978) were conducted for proteinase K and lysing enzyme and a standard curve of free L-tyrosine (Sigma-Aldrich, cat. # T3754-50G) was measured.

***S. pombe* cell culture**

S. pombe strains were grown on YES or EMM -leu agar plates at 32°C for two days. Single colonies were picked and inoculated overnight in YES or EMM -leu medium at 25°C. Overnight cultures were diluted to OD_{600} 0.05 for YES and OD_{600} 0.1 for EMM -leu cultures and grown at 25°C to 0.5-0.8. For imaging non-expanded cells expressing cytosolic mEos2, the EMM-leu overnight cultures were diluted to OD_{600} 0.2 in EMM containing 5 µM thiamine to repress mEos2 expression and were grown for 3 h at 25°C.

Sample preparation using the SExY protocol

The SExY protocol was adapted from the proExM method [23] and optimized for PALM and expansion microscopy in fission yeast. The ideal cell density for sample preparation was determined to be 6 OD/mL for POI strains and 12 OD/mL for SP16 expressing cytosolic mEos2 which was added to all samples for reference and drift correction. The appropriate volumes were transferred to fresh Erlenmeyer flasks and fixed with 3.2% paraformaldehyde (Sigma-Aldrich, cat. #F8775-4X25ML) and 0.1% glutaraldehyde (Sigma-Aldrich, cat. #G5882-50ML) at 25°C for 10 min. The cells were harvested by centrifugation (358 g, 2 min, RT), resuspended in 1 mL 1x PBS and washed twice in 1 mL 1x PBS for 5 min. The cells were washed twice with 200 µL 1x S-c/P5.8 (1.2 M D-Sorbitol (Sigma-Aldrich, cat. #S1876-500G) in citrate/phosphate

buffer (Sigma-Aldrich, cat. #C0759-1KG and cat. #S7907-500G), pH 5.8) for 10 min each. The pellet after centrifugation was resuspended in 1 mL per 6 OD/mL Lallzyme MMX mix (100 mg/mL Lallzyme MMX (Lallemand, cat. #ElO11-2240-15), 1.2 M D-Sorbitol in citrate/phosphate buffer, pH 5.8) and incubated at 30°C for 2 h for cell wall digestion. Subsequently, the cells were washed twice in 1 mL 1x S-PBS (1.2 M D-Sorbitol in 1x PBS, pH 7.4). To anchor the amine groups of the proteins to the PAA gel mesh, the cell pellets were resuspended in 200 µL per 6 OD/mL AcX solution (0.1 mg/ml Acryloyl X (Invitrogen, cat. #A20770), 1% (v/v) DMSO (Carl Roth, cat. # A994.1) in 1x S-PBS). Each POI strain was mixed with SP16 in a 1:2 ratio and incubated at 25°C overnight. The next day, the sample was washed twice with 500 µL 1x S-PBS for 15 min. Round coverslips were cleaned in 1 M KOH for 30 min and rinsed with MilliQ. Air-dried coverslips were incubated with 100 µL poly-L-lysine (Sigma-Aldrich, cat. # P8920) for 20 min at room temperature (RT) and then assembled into custom made imaging gel cassettes made of polyoxymethylene (POM). Since a previous study found that an initial incubation of the monomer solution with the sample without the catalysator yielded higher expansion factors [31], the cell pellets were resuspended in half of the 1.06 x Monomer solution (8.625% (w/w) Sodium Acrylate (Sigma-Aldrich, cat. # 408220-25G), 2.5% (w/w) 37:1 Acrylamide:Bisacrylamide (Sigma-Aldrich, cat. # A6050-100ML), 0.15% (w/w) N,N'-Methylenebisacrylamide (Sigma-Aldrich, cat. #M1533-25ML), 2 M NaCl (Sigma-Aldrich, cat. #S3014-500G) in 1x PBS) together with 0.2% TEMED (Research Products Int, cat. #T18000-0.05) and 0.05% of freshly prepared L-glutathione (Carl Roth, cat. #6832.3). This pre-gelation mix was pipetted onto the coverslip in the imaging gel cassette and incubated for 10 min at 37°C in the dark. Gelation was initiated by addition of 0.2% APS (Carl Roth, cat. #9178.3) and the rest of the 1.06x Monomer solution to the pre-gelation mix and thoroughly mixed by vigorous pipetting. The gel cassettes were placed into a humid environment using petri dishes with wet paper towels wrapped in aluminum foil and incubated at 37°C for 1 h. The gels were then incubated in 2 mL digestion buffer (50 mM Tris (Carl Roth, cat. #AE15.2) pH 7.5, 1 mM EDTA (Sigma-Aldrich, cat. #EDS-100G), 0.2% Triton X-100 (Sigma-Aldrich, cat. #T8787-50ML), 1 M NaCl) with 3 U/mL effective proteinase K (ThermoFisher, cat. #EO0491) at 37°C for 30 min in the aluminum foil wrapped mini petri dishes (Sarstedt, cat. #82.1135.500). Thereafter, gels were washed with MilliQ water, transferred to petri dishes, wrapped in aluminum foil and fully expanded in 100 mL MilliQ for 4 h at RT, exchanging MilliQ every hour. Ibidi 8-well glass bottom slides (Ibidi, cat. #80807), which were previously cleaned with 1 M KOH (Sima-Aldrich, cat. #221473-2.5KG-M) for 30 min and washed twice with MilliQ, were incubated with poly-L-lysine for 20 min and air dried. The expanded gel was cut using a scalpel, transferred into an Ibidi well, excess water was removed and the gel was incubated for 10 min. After that, the gel was secured in place by embedding it in 2% agarose (Carl Roth, cat.

#3810.3) and allowing the agarose to dry for 10 min. The gel was submerged in 300 µL MilliQ and then imaged.

Tests of various sample preparation steps while optimizing the protocol

Cell wall digestion: To lyse the cell wall, the chemically fixed and washed cells were treated with various enzymes and tested for a homogenous macroscale expansion via fluorescence microscopy. The utilized enzymes and conditions for cell wall digestion can be found in supplementary table S1.

Permeabilization: For permeabilizing the cell membrane, the fixed and in 1xPBS washed cells were resuspended in 200 µL 1xPBS containing 0.1% Triton X-100 and incubated at 37°C for 30 minutes. Afterwards the cell wall was digested and the initial pro-ExM protocol for fission yeast was continued.

Protein digestion by heat denaturation: The initial pro-ExM protocol adapted for fission yeast was performed until the gelation step, where 0.05% glutathione were added to the gelation as described above. Afterwards, the gel was submerged into 2 mL of the 50 mM Tris.HCl buffer at pH 8.0 and incubated at 65°C for 15 min. Then the gel was incubated in the renaturing buffer (35 mM KCl_2, 1 mM $MgCl_2$, 1 mM DTT, 30% glycerol, 50 mM Tris.HCl, pH 8.0) at RT for 30 min.

Protein digestion by homogenization with SDS and heat denaturation: The sample was prepared the same way as for the heat denaturation until protein digestion. The gel was then submerged in 2 mL freshly prepared SDS solution (200 mM SDS, 200 mM NaCl, 50 mM Tris HCl, pH 8.0) and incubated at 37°C for 30 min with a subsequent incubation at 65°C for 15 min. After washing the gel with deionized water, it was fully submerged in renaturing buffer and incubated at RT for 30 min.

Gelation including glutathione: To determine the effect of glutathione, 0-0.5% freshly prepared glutathione was added to the pre-gelation mix and incubated with the sample for 10 min at 37°C in the dark. After initiation of the gelation, samples were taken for fluorescence intensity measurement, and the rest of the sample was digested and expanded as described above. The gel rigidity of the expanded gels was determined visually and haptically.

Microscope setup

For all imaging experiments, a custom build setup based on an automated Nikon Ti Eclipse microscopy body with suitable dichroic and emission filters (ET dapi/Fitc/cy3 dichroic, ZT405/488/561rpc rejection filter, ET525/50 for GFP and the green form of mEos2 or ET610/75 for mScarlet-I and the red photoconverted form of mEos2, all AHF Analysentechnik, Germany) and a CFI Apo TIRF 100× oil objective (NA 1.49, Nikon) was used. A perfect focus system

(Nikon, Germany) was utilized for z-axis control, except for ExPALM imaging, where the sample was imaged at 10-80 µm depth. All lasers (405 nm OBIS, 488 nm Sapphire LP and 561 nm OBIS, Coherent Inc. USA) were modulated by an acousto-optical tunable filter (AOTF) from Gooch and Housego, USA. Fluorescence detection was performed by an emCCD camera (iXON Ultra 888, Andor, UK) at a pixel size of 129 nm. Image acquisition was controlled by a customized version of µManager [52].

Fluorescence imaging of GFP-nup132

Expanded and non-expanded GFP-nup132 cells were identified using a 488 nm laser (21 $W*cm^{-2}$ at the sample level). A fluorescence video with an exposure time of 100 ms and 50 frames was acquired using 81 $W*cm^{-2}$ at the sample level.

Fluorescence imaging and analysis of sad1-mScarlet-I

While optimizing the ExPALM protocol, a sample was taken after every step of the protocol and placed on a cleaned and poly-L-lysine coated Ibidi 8-well glass bottom slide. After 15 minutes of settling time, the sample was either washed twice (1x PBS for fixation/ permeabilization steps or 1x S-PBS for cell wall digestion/anchoring steps) or prevented from drying/shrinking by adding 1-2 drops of MilliQ in gelation/expansion steps. Only cells in mitosis with two sad1-mScarlet-I spots were imaged. A video of ten imaging frames of the sad1-mScarlet-I fluorescence was taken with an exposure time of 100 ms and in epi-illumination using a 561 nm laser. Laser intensities as measured at the sample level were 3 $W*cm^{-2}$ (live-anchoring) and 6 $W*cm^{-2}$ (gelation-protein digestion). The integrated intensity of the fluorescent spots and a close-by background area were measured in a 14x22 pixel ROI in the first three imaging frames using ImageJ [53]. The final intensity measure was obtained by calculating the mean of the three frames for both ROIs and subtracting the background ROI from the fluorescence signal ROI.

PALM imaging and analysis of expanded cells

Expanded cbp1-mEos2 and mis16-mEos2 cells were identified in the gel by their fluorescence in epi-illumination using the 488 nm laser (21 $W*cm^{-2}$ at the sample level) and PALM videos were acquired with an exposure time of 60-80 ms for 3000-5000 frames photoconverting and imaging mEos2 by continuous illumination of 405 nm laser (3-12 $W*cm^{-2}$ at the sample level) and 561 nm laser (1.2 $kW*cm^{-2}$ at the sample level). For imaging the DNA, the DNA was stained after mEos2 read-out using 100 nM TO-PRO™-3 Iodide (Invitrogen, cat. # T3605) which was added to the imaging well on the microscope stage and incubated for 30 minutes. A fluorescence video with an exposure time of 100 ms and 50 frames was acquired using the 561 nm laser (0.5 $kW*cm^{-2}$ at the sample level). Expanded mEos2-cnp1/sad1-mScarlet-I cells where identified by mScarlet-I fluorescence using the 561 nm laser. A fluorescence movie with

an exposure time of 100 ms and 50 frames was acquired using the 561 laser (0.5 kW*cm^{-2} at the sample level). Remaining mScarlet-I fluorescence was photobleached (1.2 kW*cm^{-2} at the sample level, 561 nm laser) and the mEos2 signal and the TO-PRO™-3 Iodide DNA stain were imaged as described above.

All samples contained cells expressing cytosolic mEos2, which served as marker for drift correction. Each field of view contained at least one cell expressing cytosolic mEos2 and was corrected by cross correlation using a custom script (Python 3.7). Frames with unreliable drift correction, which typically occurred at the end of PALM videos at low localization densities, were discarded.

All images were reconstructed in Rapidstorm 3.2 with a pixel size of 10 nm [54]. Localization precision was determined using the NeNA method [55] and calculated in the open-source software Lama [56]. For image representation, all images were blurred by a Gaussian using their NeNA value as the sigma value. PALM images were overlaid with corresponding fluorescence images of sad1-mScarlet-I and DNA in ImageJ 1.52p.

PALM imaging and analysis of non-expanded cells

Cells expressing cytosolic mEos2 were fixed with 3.2% paraformaldehyde (Sigma-Aldrich, cat. #F8775-4X25ML) and 0.1% glutaraldehyde (Sigma-Aldrich, cat. #G5882-50ML) and embedded in 0.5% agarose gels in an Ibidi 8-well glass bottom slide together with a 1:500 dilution of sonicated FluoSpheres carboxylate-modified, 0.2 µm, dark red (660/680) (Molecular probes, cat. #F8807). PALM videos were acquired with an exposure time of 60 ms for 3000-5000 frames photoconverting and imaging mEos2 by pulsed illumination of 405 nm laser (3-12 W*cm^{-2} at the sample level) and 561 nm laser (1.2 kW*cm^{-2} at the sample level).

Each field of view was corrected by fiducial drift correction using a custom script (Python 3.7). All images were reconstructed in Rapidstorm 3.2 with a pixel size of 10 nm [54]. Localization precision was determined using the NeNA method [55] and calculated in the open-source software Lama [56]. For image representation, all images were tracked in Rapidstorm 3.2 with an allowed blinking interval of 5 frames and a sigma set to the NeNA value. After filtering out all trajectories with 3 steps and less, a PALM image was reconstructed in Rapidstorm 3.2 and blurred by a Gaussian using the NeNA value as sigma value.

Determination of expansion factor

The expansion factor was measured by the cell width and the nuclear size of expanded and non-expanded cells. For the cell width, the mean and standard error of cells in reconstructed PALM images of fixed and expanded cells expressing cytosolic mEos2 were measured. For measuring the nuclear expansion factor, the mean and standard error of the nuclear diameter

were determined in fluorescence images of expanded and non-expanded GFP-nup132 cells were taken. Cells with non-spherical nuclei were excluded from the analysis. The expansion factor was calculated by dividing the expanded cell width or nuclear size with the non-expanded cell width or nuclear size.

Assessment of microscale isotropy of individual expanded cells by evaluating the distribution of cytosolic mEos2 molecules

Nearest neighbor distances between cytosolic mEos2 localizations in expanded cells were compared to cytosolic mEos2 localizations in non-expanded cells in R, v3.6.1 (https://www.r-project.org/), using RStudio, 2022.07.2+576 (https://www.rstudio.com/) and the spatstat package [57]. To be able to compare the distances, first, point densities (number of points per cell area) were evaluated for all cells. Next, for a given expanded cell, areas of the 30 non-expanded cells were enlarged *in silico* until point densities matched. Then, the average nearest neighbor distances were calculated. Finally, the mean (μ) across non-expanded cells was subtracted from the value of the expanded cell (x_i), and normalized to the standard deviation (σ) of the distribution of non-expanded cells: $(x_i - \mu)/\sigma$. A two-sided student's t-test was performed.

Results and discussion

In this work, we established a sample preparation and imaging protocol which combines the super-resolution technique PALM with a proExM protocol optimized for isotropy and protein retention for the fission yeast *S. pombe,* which we named Single-molecule and Expansion microscopy in fission Yeast (SExY). Figure 1a shows our final ExM preparation protocol which consists of six steps, namely chemical fixation of the cells and subsequent cell wall digestion, protein anchoring and gelation of the polyacrylamide gel, which is then followed by protein digestion and the final expansion step. In Figure 1b, two exemplary *S. pombe* cells are shown, one at normal size and one expanded by the final SExY protocol to an about 5-fold size. Both cytosolically express the FP mEos2 whose positions were super-resolved by PALM imaging. While cytosolic, free diffusive mEos2 molecules are generally distributed throughout the cell, SExY also clearly resolves their (expected) non-random, small-scale substructured distribution, e.g., small omitted regions of round vesicles and a maximum of FPs near the nucleus.

Essential aspects of the SExY protocol are, first, an isotropic and satisfactory expansion, both at the macro- and microscale, and second, a high protein retention yield to preserve protein yield, i.e. the FP signal for PALM readout. Importantly, neither was the case when using the original proExM protocol on *S. pombe* cells. For verifying the isotropic expansion of the cells, we measured the cell width of cells expressing cytosolic mEos2 as seen in PALM images

(Figure 1 c, left). For verifying the isotropic expansion of organelles, we measured the nuclear diameter of cells in interphase that expressing GFP-tagged nuclear pore protein Nup132 (Figure 1 c, right). Non-expanded cells yielded a cell width of 2.4 µm ± 0.19 µm and a nuclear diameter of 2.36 µm ± 0.34 µm, cells expanded with the SExY protocol showed a cell width of 11.8 µm ± 1.8 µm and a nuclear diameter of 11.6 µm ± 1.4 µm. This resulted in a macroscale expansion factor of 4.9 (standard error (s.e.) 0.2, standard deviation (s.d.) 0.8) as measured by the cell width and a factor of 4.9 (s.e. 0.2, s.d. 0.9) for the nuclear diameter. Notably, the achieved expansion is higher than in current protocols that combine ExM with dSTORM and achieve an about threefold expansion [36,37]. To assess isotropic expansion on the microscale, we examined the cell boundaries of cells expressing cytosolic mEos2 which were expanded using either the initial proExM protocol (adding the step of using Lallzyme MMX for cell wall digestion) or the optimized SExY protocol. When applying the original protocol, we found a substantial fraction of mEos2 molecules located outside the main cell area within the polyacrylamide mesh network, apparently pulled outward due to heterogeneous expansion and resulting in "fuzzy" cell boundaries. In contrast, cell boundaries were clearly defined when the SExY protocol was applied (Figure 1d), indicating a more defined and homogeneous microscale expansion. Furthermore, statistical testing for changes in cytosolic mEos2 FP distribution upon expansion did not show any changes (Supplementary Figure 1). While prior to optimization of the protocol, individual expanded cells show a relatively high variation in cytosolic mEos2 distribution relative to non-expanded cells (up to 1.88 s. d.), indicating non-isotropic expansion, post-optimization all expanded cells lie well within the range expected for isotropic expansion (up to 0.5 s.d. in relation to the mean of non-expanded cells).

To measure the protein retention yield, we quantified the fluorescent signal retained from the spindle pole protein sad1 tagged with mScarlet-I from cells during anaphase B in mitosis. For our initial proExM protocol, we found that only 22% (s.e. 2.0%, s.d. 12.4%) of the fluorescence signal was retained when compared to fixed cells (Figure 1e). However, using the SExY protocol, about 46% (s.e. 3.1%, s.d. 21.8%) of the sad1-mScarlet-I signal was preserved, doubling the retained amount.

Altogether, these quality measures indicate that the SExY protocol is a promising approach to map protein structures in fission yeast. To achieve this, we have optimized the cell wall digestion, gelation and protein digestion steps in the development of the final SExY protocol. We report on these optimizations and discuss their rationale in detail in the following sections.

Efficient and complete cell wall digestion of fission yeast

We tested various cell wall removal enzymes commonly used in fission yeast studies [58–60] and visualized expanded *S. pombe* cells that cytosolically expressed mEos2. We found that zymolyase, zymolyase in combination with lysing enzyme, snail enzyme, and lyticase caused

partial expansion of yeast cells visible by “hour-glass” like shapes failing to expand the septum or earlier cytokinesis sites (Figure 2 a). Lallzyme MMX, chitinase, and β-glucoronidase completely expanded *S. pombe* cells and showed comparable mEos2 signal to the non-expanded cells (Figure 1 b, Supplementary Table S1).

The fact that we were able to fully expand fission yeast cells using a chitinase for cell wall digestion may indicate that chitin is present at the septum. The fission yeast septum consists of a primary septum composed predominantly of β-(1,3)-glucan and a flanking secondary septum composed of α(1,3)-glucan and branched β(1,6)-glucan [61,62]. Chitin synthase genes (chs1, chs2) are present, but their function is still controversial [63,64]. On the one hand, chs2 has been shown to be localized to the growing septal edges in vegetative *S. pombe* cells, yet chs2 possesses several mutations at sites critical for chitin synthesis [64–66]. We decided not to further investigate the "hourglass-like phenotypes” and the potential localization of chitin at the septum and instead proceeded to the next steps of protein digestion and gelation to be optimized, using Lallzyme MMX as our standard for cell wall digestion, as it was the cheapest and most reliable alternative among the three enzymes that resulted in complete expansion in our hands. In a recent study, *S. pombe* was successfully expanded using zymolyase for cell wall removal [67]. We speculate that this may be explained by the generally harsher conditions of this protocol, e.g., an additional fixation step with ice-cold acetone and replacement of proteinase K digestion with SDS treatment, which may be at the expense of protein retention yield, but this was not specified.

Increasing the protein retention yield

To evaluate how much fluorescent signal of the fluorescent proteins is retained after each step of sample preparation, we measured the fluorescent spot intensity of the mScarlet-I-tagged spindle pole protein sad1, whose structure and protein copy numbers is well-defined during anaphase B in mitosis [68]. For our initial protocol, following the proExM protocol with an added step for cell wall digestion using Lallzyme MMX, only 22% (s.e. 2.0%, s.d. 12.4%) of the signal was retained compared to chemical fixed samples (Figure 1e). This overall loss of fluorescent protein signal was mainly caused by three processing steps: A decrease of 18% (s.e. 2.8%, s.d. 29.6%) after permeabilization with 0.1 % Triton X-100, a decrease of another 22% (s.e. 2.5%, s.d.23.9%) after cell wall digestion using Lallzyme MMX compared to the previous step in the protocol and a decrease of another 46% (s.e. 2.0%, s.d. 12.4%) after protein digestion (Supplementary Figure S2). We therefore targeted these three steps for optimization of the protocol.

In a first optimization, we excluded a separate permeabilization step using Triton X-100 as we hypothesized that the cell membrane is sufficiently disintegrated combining the steps of fixation with 3.2% para-formaldehyde and 0.1% glutaraldehyde and of protein digestion in a buffer

containing Triton X-100. Cells expanded with a protocol excluding this step indeed expanded normally (examples in Figure 1). Furthermore, we tested proteinase K as well as the different enzymes for cell wall removal for their proteinase activity in a colorimetric assay measuring tyrosine release in casein digestion (Figure 2b and Supplementary Figure S3). For proteinase K, we found that the proteinase activity for 1 U/mL of our stock was reduced to only 64% for freshly bought proteinase K and lower for older stocks. A control with protease inhibitor phenylmethylsulfonylfluorid (PMSF) showed no residual proteinase activity. Therefore, for all further experiments, we determined the effective proteinase K activity using the colorimetric assay and adjusted the used concentrations accordingly. Among the cell wall removal enzymes, only the lysing enzyme and Lallzyme MMX showed proteinase activity, whereas zymolyase and β-glucoronidase showed no activity at 1 U/mL and even at higher concentrations of 50 U/mL. Compared to proteinase K at a 10-fold higher concentration, lysing enzyme at a concentration of 0.1 U/mL showed rather strong activity. For Lallzyme MMX we detected a (low) proteinase activity at 10 mg/ml. Importantly, we found no significant decrease in fluorescence intensity of sad1-mScarlet-I after the exclusion of a separate permeabilization step with Triton X-100 (Supplementary Figure S2b). We thus speculate that Lallzyme MMX without the detergent step at this early stage of the protocol might be hindered to freely access the cell, in particular the nucleus, and thus does not show visible proteinase activity on sad1-mScarlet-I fluorescence. When adjusting the proteinase K concentration for protein digestion (see below), we nevertheless could measure an effect when blocking the proteinase activity of Lallzyme MMX by PMSF. In general, different proteinase K activities in different labs could be one cause for inhomogeneous expansions [20,28–31].

On the basis of excluding a separate permeabilization step and using 10 mg/ml of Lallzyme MMX for cell wall digestion, we then optimized protein digestion and tested different methods that have been reported in the ExM literature: protein digestion using proteinase K [9], heat denaturation [10] and denaturation using SDS [19]. Homogenization by heat denaturation or treatment with SDS resulted in expanded fission yeast cells, but no or very low fluorescent signal for sad1-mScarlet-I or cytosolically expressed mEos2 was subsequently detected (data not shown). Using the proteinase K concentration from the proExM protocol, we were able to expand and image fluorescently-labeled fission yeast, albeit with severe signal loss. As sufficient sample homogenization is critical for isotropic expansion, we tested different proteinase K concentrations to determine the minimal needed concentration of use. We found that the lowest effective concentration that allowed isotropic expansion on both, the macro- and the microscale of the sample was 3 U/mL (controlled for efficiency by the activity assay). Lower concentrations of proteinase K or a cell wall digest of Lallzyme MMX in the presence of the proteinase inhibitor PMSF followed by 3 U/mL proteinase K during protein digestion resulted in heterogeneous samples with a symptomatically increasing fraction of non-

expanded cells cumulating at the bottom of the gel, only semi-expanded (two- to threefold expansion) or non-isotropic expanded cells, and only partially expanded gels (data not shown). For the final SExY protocol, we thus use the protease activity of 3 U/mL proteinase K combined with the protease activity of Lallzyme MMX which represents the minimum protein digestion level for homogeneous expansion of fission yeast to maintain a robust ExM protocol while retaining the maximum possible fluorescence signal.

In a final optimization, we then focused on the gelation step of the protocol as the free radicals that emerge during the gelation of the PAA gel have been shown to reduce the protein retention yield as well [23,33]. While we were not able to detect this loss in the initial protocol, we could detect the negative effect of the gelation process on protein retention after having optimized the other protocol steps (Figure 2c). To minimize the loss, we tested whether a presumably milder gelation by adding the antioxidant glutathione (GSH), an efficient radical scavenger, would yield a higher retention yield, since glutathione can accept a radical at its sulfur moiety by hydrogen atom transfer (GS·), adding a hydrogen at the former radical site of proteins [69,70]. To test this hypothesis, we measured the fluorescence intensity of sad1-mScarlet-I after PAA gelation for different glutathione concentrations and found a fluorescence increase of about 27% (s.e. 12.8%, s.d. 85%) when adding 0.05% glutathione (Figure 2c). At higher glutathione concentrations, no further increase in fluorescence spot intensity but a decrease in PAA gel rigidity was observed until gelation was completely abolished at concentrations of 0.4% glutathione and higher (Figure 2c). Presumably, the lower PAA gel rigidity stems from overall shorter PAA chains in the gel mesh, e.g. by glutathione reacting with growing PAA radical chains and thus terminating the chains early or by glutathione radicals (GS·) forming glutathione disulfide (GSSG), decreasing the overall radical concentration. In the final SExY protocol, we thus use 0.05% glutathione during gelation.

Finally, during this work, we tested several commonly used FPs for their fluorescence retention in ExM sample preparation as it is a known problem that chromophores often do not withstand treatments in correlative imaging protocols, e.g. when combining fluorescence microscopy with electron microscopy [71]. For conventional fluorophores, we tested GFP and mCherry, commonly used FPs of different origin from jellyfish and coral, in a dual-color strain expressing two nuclear pore protein fusions [72]. While GFP-Nup132 was clearly visible, we could not detect mCherry-Nup131 in the expanded cells (Figure 3d). Interestingly, we then found that mScarlet-I, a synthetic FP constructed by rational design based on several red FPs but with a high sequence identity of 86% to mCherry, survives the protocol and we could obtain images of expanded cells with mScarlet-I labeled spindle pole protein sad1 (Figure 3 e, f). Due to mScarlet-I's superior brightness and red color (allowing to image deeper into the samples than when using GFP), we decided to use it for the characterization of protein retention (Figure 2)

[73]. For PALM imaging, mainly FPs from Anthozoan corals, either DsRed-type like PAmCherry or Kaede-type like the Eos/Dendra/Maple FP family, are used [40]. We tested photoactivatable PAmCherry which showed no residual fluorescence already after fixation (data not shown). From previous studies it is known that PAmCherry photoactivation is substantially reduced for fixation protocols including glutaraldehyde [74]. Within the ExM protocol, a comparably high glutaraldehyde concentration is used. We thus hypothesize that PAmCherry was fully quenched by glutaraldehyde when fixing the samples. In contrast, the green-to-red photoconvertible FP mEos2 survives the ExM protocol just fine. We therefore tagged different low and high abundant proteins with different cellular localizations with mEos2 to validate our imaging sensitivity and FP survival during SExY imaging. Using mEos2, we could successfully super-resolve proteins in expanded cells such as the nuclear DNA binding protein cbp1 (Figure 3b) [75] and the nuclear protein mis16 (Figure 3c) [76] as well as rather low abundant proteins such as the centromere-specific histone protein cnp1 (Figure 3 e, f), which is only present in several tens to a few hundred copies per cell [41,77]. Using TO-PRO-3 Iodide, we co-visualized DNA (Figure 3 c, e).

On a small technical note, we also explored different drift correction strategies for PALM imaging of expanded gels. Drift correction of PALM data is commonly needed, as the recording of a PALM movie can take up to several minutes in which the sample can physically drift. This drift is often corrected by adding fiducial markers to the sample, e.g. fluorescent polystyrene beads or gold nanoparticles [78]. For expanded gels, we found that fiducial markers (even when covalently linking them to the gel mesh by amine groups) to a large extend either ended up at the bottom of the expanded gel and in case of polystyrene beads, high amounts of individual dyes leached out into the gel and resulted in cells coated by fuzzy background signal (data not shown). Thus, we decided to use cross-correlation drift correction [79], which was previously also used in ExSTORM and Ex-SMLM [36,37]. While cross-correlation approaches work well for large statistics, thus directly on samples with high abundant proteins such as e.g. microtubules (as imaged in the ExSTORM and Ex-SMLM works), the correction of low abundant protein signal fails due to insufficient statistics. Therefore, we mixed all samples with cells that cytosolically expressed mEos2 at high amounts and used the latter as markers for cross-correlation.

Conclusions

With the combination of ExM with PALM (ExPALM) we close a gap in available super-resolution and ExM correlative protocols. We report the homogenous expansion of fission yeast *S. pombe* cells to a fivefold expanded size while retaining about 50% of FP signal by several optimization steps of the original proExM protocol. The final protocol, which we termed SExY (“Single-molecule and Expansion Microscopy of Yeast”) is robust and reproducible, and

extends the ExM toolbox by a correlative protocol for ExPALM imaging in microbiology. SExY explicitly excludes a separate permeabilization step with a detergent, uses Lallzyme MMX for digestion of the cell wall as an alternative to pricier enzymes and/or lysing components that only show heterogenous or partial expansion, i.e. most striking “hour-glass” shaped phenotypes, includes a fine-tuned protein digest using proteinase K at a controlled effective potency of 3 U/ml and a gentler PAA gelation by adding 0.05% glutathione. We suppose that the improved microscale isotropy in expansion as seen in SExY (Figure 1d) stems from the dual effect of optimized homogenous protein digestion and overall shorter PAA chains due to the milder gelation.

SMLM imaging has high demands for labeling specificity and efficiency. SExY as a correlative PALM imaging technique is especially suitable for low abundant proteins as it does not rely on indirect target labelling via organic dyes using immunofluorescence and covalent bioconjugation methods (which are prone to unspecific staining due to the charge and molecular crowding in microbes [41]) and is optimized for a high protein retention yield retaining 50% of the FP signal. Cells expanded by the SExY protocol show a high five-fold expansion compared to Ex-SMLM and ExSTORM that both report only a three-fold expansion, which can be attributed to the needed photoswitching buffers. Thus, for some research, using SExY as an ExPALM method might diminish the need for additional expansion steps of the sample in iterative ExM protocols.

Possible future optimizations should be to implement a non-radical, highly defined lattice-like gel into the method as e.g. recently introduced by the Tetragel [33,80]. This might lower loss of FP signal during gelation. Second, the range of suitable FPs should be extended. As the selection of FPs suitable for high quality PALM imaging is rather small [2,40], we believe that engineering optimized FP variants for correlative ExM approaches based on current FPs might be an effective strategy. Engineering FPs that are not further affected by ExM protocol steps, e.g. that are less sensitive to a specific protein digestion method, offers high advantage [81]. This strategy has been shown successful for other correlative methods, e.g. in the development of mEos4 FPs. Here, nucleophilic amino acid residues that crosslink with aldehydes were replaced so that mEos4 variants tolerate osmium (OsO_4) fixation – a treatment needed for electron microscopy [82].

Overall, the new correlative protocol is valuable for all yeast researchers who wish to combine ExM imaging with super-resolution imaging. In particular, we believe that the optimizations in protein retention yield, encompassing retention yield for fluorescent proteins, will also be of interest to a larger audience in microbial cell biology research and will extend to even more distant research areas if their interest involves studying low abundance proteins or for any

reason relies on genetic labeling, e.g. when proteins are not readily accessible by extrinsic staining.

Author contributions

I.V, O.C. and U.E. designed the research; I.V., O.C. and M.A.H. conducted all experiments and analyzed the data; I.V. and U.E. designed manuscript figures and tables and wrote the manuscript with input from all authors.

Funding

This work was supported by funds from the Max Planck Society, the SYNMIKRO Post-Doc short-term fellowship to O.C. and start-up funds at Carnegie Mellon University.

Acknowledgements

We would like to thank Dr. David Lando, Dr. David Virant and Prof. Dr. Haruhiko Asakawa for sharing their strains for this study.

Competing interests

Authors declare no competing interests.

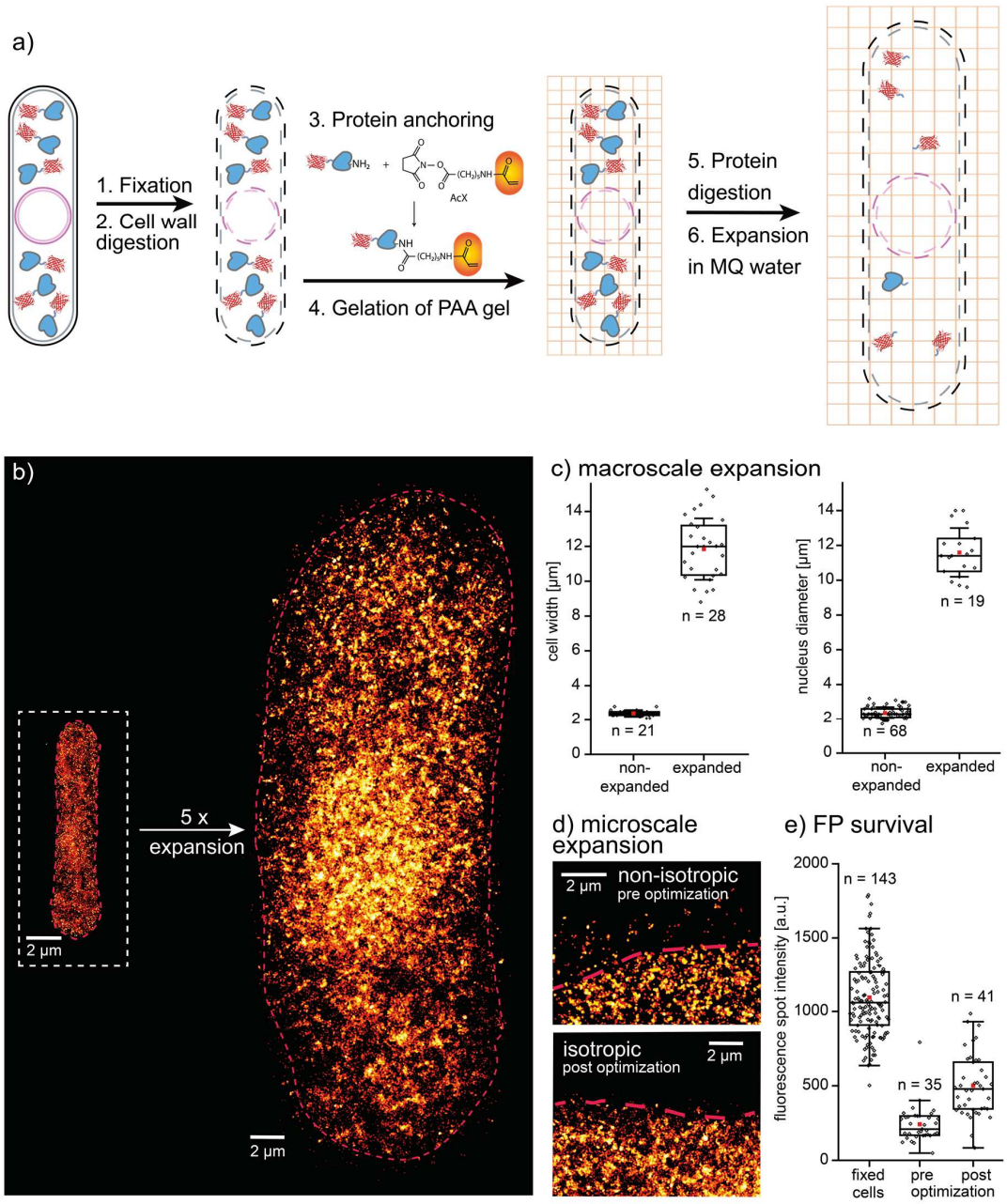

Figure 1: Principle and performance of the SExY method.

a) Principle of SExY sample preparation, a correlative ExPALM protocol for expanding yeast. Shown are cell wall (black), cell membrane (grey), inner and outer nuclear membrane (magenta), target protein (blue), FP marker (red) and the PAA gel mesh (orange). The acrylate group of the protein anchoring agent AcX is highlighted in orange. b) Fission yeast cells expand ~ 5-fold using the SExY protocol, c) SExY provides a macroscale isotropic expansion as determined by two different samples, measuring i) cell widths and ii) nuclear diameter (Nup132) of non-expanded and expanded cells. The expansion factor was determined to be

4.9 (s.e. 0.2, s.d. 0.8) (cell width) and 4.9 (s.e. 0.2, s.d. 0.9) (nuclear diameter), respectively. d) Additionally, the isotropic microscale expansion of the SExY protocol was probed investigating cell borders. Here, cells expanded with the SExY protocol show no mEos2 localizations being pulled outside of the cell area and hence an isotropic expansion on the microscale. e) SExY retains 46% (s.e. 3.1%, s.d. 21.8%) of FP signal retention whereas the original proExM protocol retained 22% (s.e. 2.0%, s.d. 12.4%).

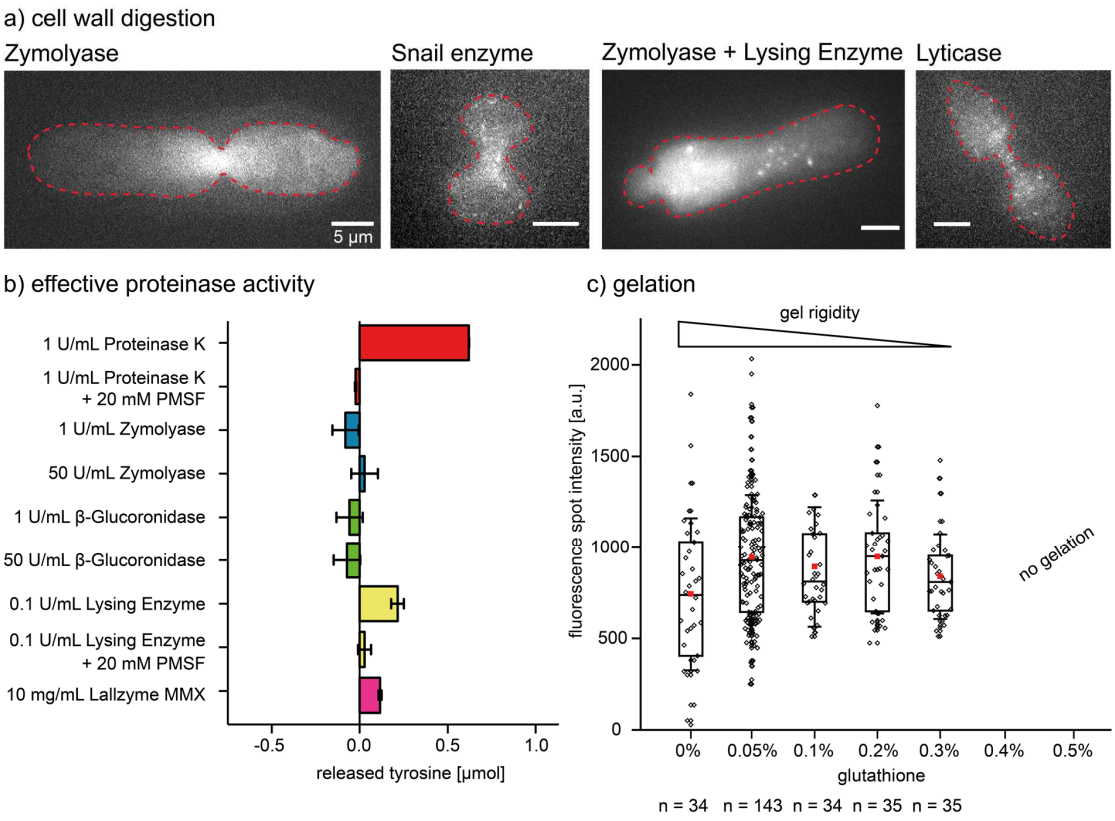

Figure 2: Protocol optimizations for SExY

a) Examples of incomplete cell wall digestion using zymolyase, snail enzyme, a combination of zymolyase and lysing enzyme and lyticase. All tested conditions lead to a partial and non-isotropic expansion constrained by remaining cell wall. b) The proteinase activity of proteinase K (red) in comparison to different cell wall digesting enzymes measured by the release of tyrosine during casein digestion. Zymolyase (blue), β-glucoronidase (green), lysing enzyme (yellow) and Lallzyme MMX (magenta). Adding proteinase inhibitor PMSF successfully suppressed tyrosine release. c) sad1-mScarlet-I signal shows an increase of 27% (s.e. 12.8%, s.d. 85%) in FP retention when adding 0.05% glutathione during gelation. Gel rigidity decreases with increasing glutathione concentration. Thus, no gel formation at 0.4% and higher was achieved.

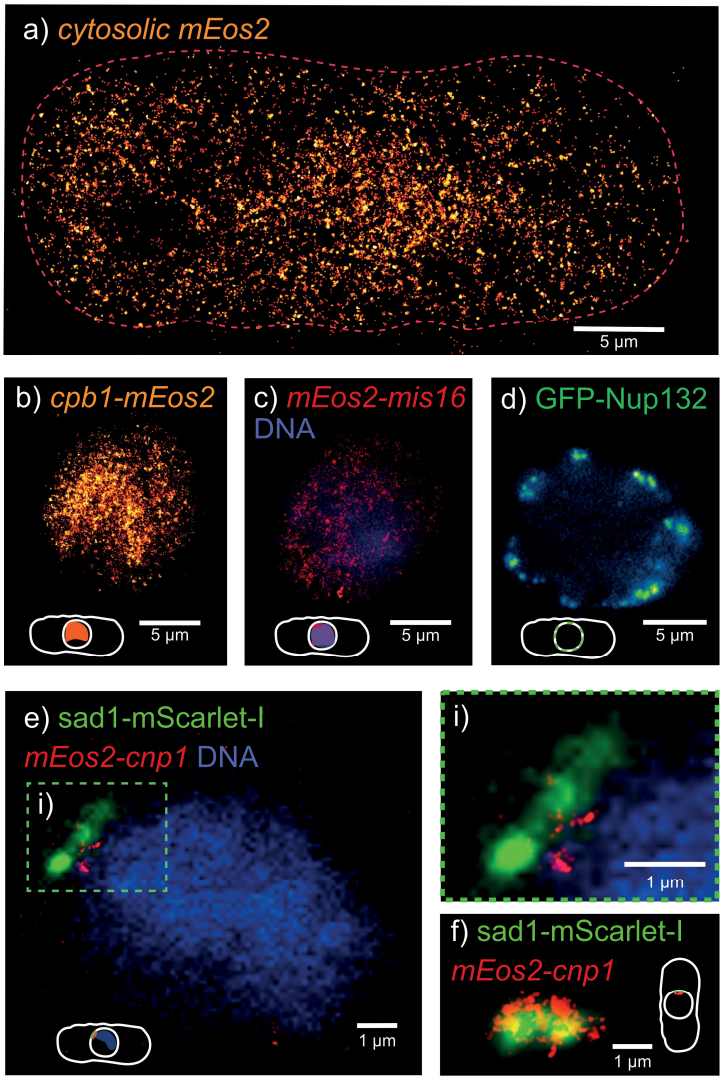

Figure 3: Examples of SExY microscopy

SExY imaging of high (a-c) and low (d-f) abundant proteins in fission yeast. Super-resolved targets are marked in italic, targets imaged by conventional epifluorescence in regular script. a) mEos2 expressed in the cytosol, b) nuclear DNA binding protein cbp1, c) nuclear protein mis16 and DNA (TO-PRO™-3 Iodide), d) nuclear pore protein Nup132, e-f) centromeric histone protein cnp1 relative to the spindle pole body protein sad1; combined with visualizing DNA (TO-PRO™-3 Iodide) (e, inset i)).

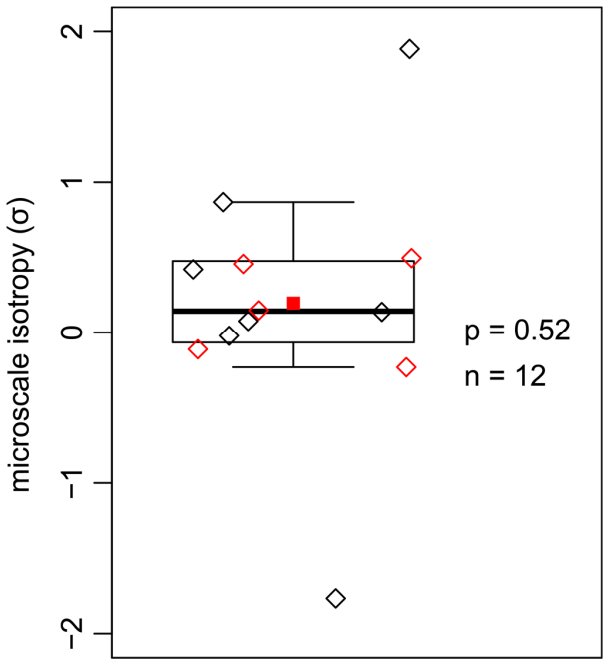

Supplementary Figure S1: Microscale isotropy of expanded cells measured by the distribution of cytosolic mEos2 FP

Microscale isotropy is measured by calculating the average nearest neighbor distance between mEos2 localizations of each individual expanded cell, normalized to the standard deviation (σ) of the distribution of average nearest neighbor distances of cytosolic mEos2 molecules of 30 non-expanded cells (details in Materials & Methods). The distribution of expanded cells is centered near 0, i.e. equivalent to non-expanded cells, suggesting there is no systematic distortion introduced by the expansion. When using the protocol prior to optimization (black diamonds), individual cells show high variance values (extremes: -1.77 and 1.88 σ) which indicates inhomogeneous expansion of those cells. By contrast, post-optimization (red diamonds), all expanded cells lie in the range -0.2 to 0.5 σ, and thus well within one standard deviation of the mean. Thus, within the limits of these low number statistics, we find no evidence for deviation from isotropic expansion when using the optimized SExY protocol.

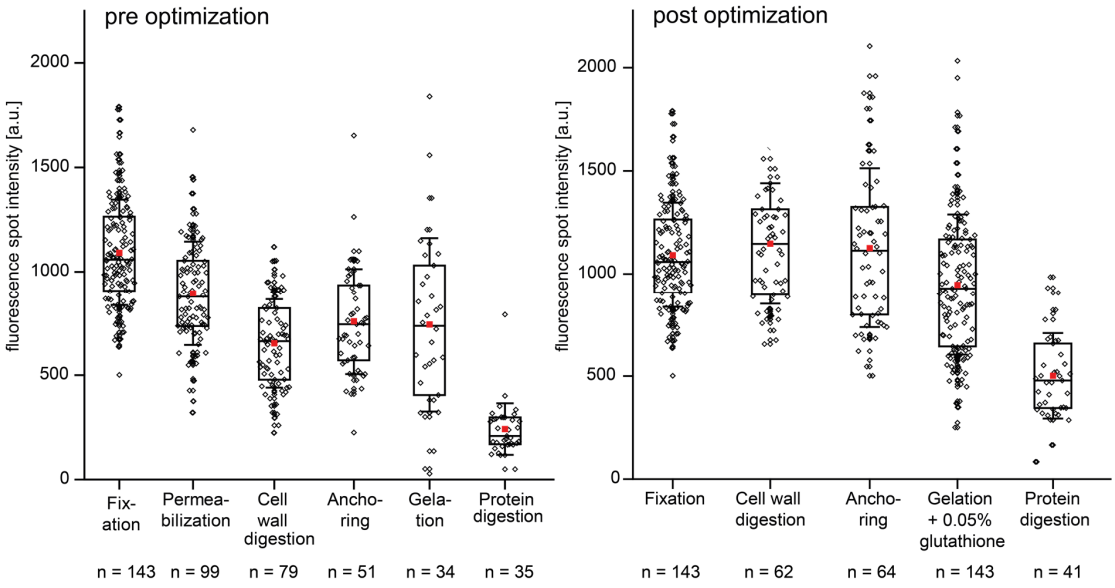

Supplementary Figure S2: Fluorescence signal retention

Fluorescence spot intensities of the spindle pole body protein sad1 fused to mScarlet-I were measured in Anaphase B for every protocol step pre- and post-optimization. Crucial for FP signal retention were the omission of a permeabilization step, a milder gelation using 0.05% glutathione and the use of proteinase K in protein digestion at a proteinase activity of 3 U/mL. Importantly, the effective proteinase K activity was controlled by an activity assay prior to use.

This supplementary figure provides an overview of the individual steps in the protocols. Some of the data can also be seen in Figures 1e and 2c and are presented again for completeness and clarity. This includes the data shown for the fixation step. They are shown in Figure 1e and are plotted twice here, before and after optimization. The data after protein digestion are also identical in Figure 1e. The data after gelation at 0% and 0.05% glutathione are also shown in Figure 2c.

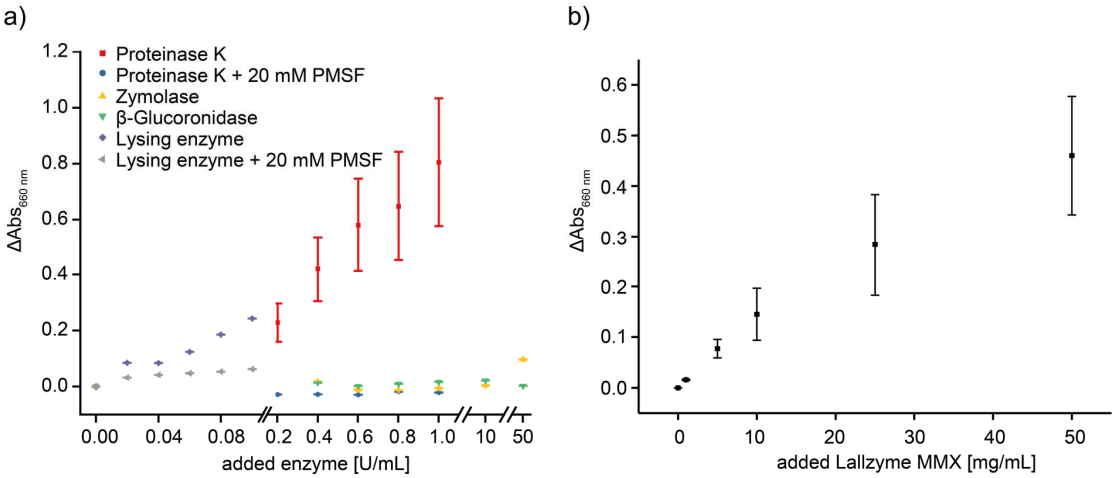

Supplementary Figure S3: Protease activity determination

Protease activity was measured using the enzymatic release of tyrosine during casein digestion, visualized by Folin & Ciocalteu's Phenol reagent absorbance at 660 nm. a) Proteinase K (red), proteinase K + PMSF (blue), zymolyase (yellow), β-glucoronidase (green), lysing enzyme (light purple) and lysing enzyme + PMSF (dark purple). b) Protease activity for Lallzyme MMX.

Enzyme	Conditions	Partial expansion	Full expansion
Lallzyme MMX	100 mg/mL in S-c/P5.8, pH 5.8, 30°C, 2 h	no	yes
Zymolase 20T	5 mg/ml Zymolyase 20T, 10 mM β-mercaptoethanol (Sigma-Aldrich, cat. # M6250-100ML) in S-PBS, 37°C	yes	no
β-Glucoronidase	≥ 1 kU/ml (Sigma-Aldrich, cat. # G2133-50KU) in S-c/P 4.8, pH 4.8, 37°C	no	yes
Snail hepatopancreatic extract	1 mg/ml snail extract, 10 mM β-mercaptoethanol in S-c/P pH 5.8, 25°C or 30°C	yes	no
Chitinase	0.5 mg/ml = 0.1 U/ml Chitinase (Sigma-Aldrich, cat. # C6137-25UN), 1 M NaCl in 50 mM PBS, pH 6, 37°C	no	yes
Zymolyase + Lysing Enzyme	5 mg/ml = 100 U/ml Zymolyase 20T, 1 mg/ml Lysing Enzymes (Sigma-Aldrich, cat. # L1412-5G) from Trichoderma harzianum, 10 mM β-mercaptoethanol in S-KP	yes	no
Lyticase	100 U/ml (Sigma-Aldrich, cat. # L2524-200KU) in S-PBS, 25°C or 30°C	yes	no

Supplementary Table S1: Overview of conditions and resulting expansion of all tested cell wall digestion enzymes.

Strain	Genotype	Origin
SP176	WT *h⁻*	Gift from Dr. David Lando, Prof. Laue group, Cambridge, UK
SP148	*h⁺ ade6-210 leu1-32 ura4-D18 mEos2:cnp1 sad1:mScarlet-I :hphMX6*	Created by Ilijana Vojnovic, this work
SP31	*h⁻ cbp1:mEos2:kanMX6*	Created by David Virant
SP15	*h⁺ ade6-210 leu1-32 ura4-D18 mis16:mEos2*	Gift from Dr. David Lando, Prof. Laue group, Cambridge, UK
SP16	*h⁺ ade6-210 leu1-32 ura4-D18 pREPnmt81-mEos2::Leu2*	[77]
SP17	*h⁺ ade6-210 leu1-32 ura4-D18 pREPnmt81-PAmcherry1::Leu2*	[77]
HA1618	*h^{90} ade6-216 ura4-D18 leu1-32 nup131::ura4⁺ nup132::GFP-nup132⁺ lys1⁺::mCherry-nup131⁺*	[72]

Supplementary Table S2: List of strains created or used in this study.

No	Primer name	Primer sequence (5' → 3')
1	cbp1_F1	atcaaattgcttcgcagtacatgg
2	cbp1_R1	aatcgcactaccactgcctccggcggtgcttctcaaacgagaaagattc
3	cbp1_F2	aatgctggtcgctatactgctgtctgtctgtattcgttgtgcatatttgac
4	cbp1_R2	gctcgtatagcgattttgcgtt
5	mis16_F1	agttcaactgatcgccgtgt
6	mis16_R1	aatcgcactaccactgcctccggcctccagatccctaggagaaacct
7	mis16_F2	aatgctggtcgctatactgctgtcagttggccatagaaaaaaacccaaa
8	mis16_R2	tcgcagacttgcaaaatgaacaa
9	1F mEos2	cgaattcctgcagcccgccggaggcagtggtagtgcgattaagccagacatg
10	1R mEos2	ttatcgtctggcattgtcaggc
11	2F KanR	gacaatgccagacgataaggcgcgccagatctacttcta
12	2R KanR	agaactagtggatcccccgacagcagtatagcgaccagc
13	R1 pBSKII	aatgctggtcgctatactgctgtc
14	F2 pBSKII	gccggaggcagtggtagtgcgatt
15	pFA6_F_mScarlet_ovh	gtggtatggatgaattgtacaagtagggcgcgccagatctacttcta
16	pFA6_R_mScarlet_ovh	gcttcgcctttagaaaccataccactgcctccggctca
17	sad1_transformation_F	gagacgaccatctgcattcatacc
18	sad1_transformation_R	acactaatattcgcgacgtgtttcc
19	sad1_R1_mScarlet	agatgaatcttgacccgtattctctg
20	mScarlet_F_sad1_ovh	cagagaatacgggtcaagattcatctgccggaggcagtggtatggtttctaaaggcgaagcc
21	Hyg_cass_sad1_R	gaattcgagctcgtttaaactgga
22	sad1_F2_hygB_ovh	tccagtttaaacgagctcgaattcagacctacaaaatgtaagatataaa
23	sad1_R2_mScarlet	acatgtagttcgaagtaattc
24	mScarlet1_F_blunt	atggtttctaaaggcgaagc
25	mScarlet1_R_blunt	ctacttgtacaattcatccataccac
26	ADH1F#2 stop	tagtagggcgcgccagatctactt
27	ADH1R#2 overhang	gggacgaggcaagctaaacagatctatattaccctgttatccctagcgga
28	MX6 F#2 no overhang	agatctgtttagcttgcctcg
29	pFA6a MX6 R	ttgtccataccactgcctccggctcacctaaatcgtatgtgtatgataca

Supplementary Table S3: List of primers used in this study.

References

[1] Abbe E. 1873 Beiträge zur Theorie des Mikroskops und der mikroskopischen Wahrnehmung. *Archiv f. mikrosk. Anatomie* **9**, 413–468. (http://dx.doi.org/10.1007/BF02956173).

[2] Turkowyd B, Virant D, Endesfelder U. 2016 From single molecules to life: microscopy at the nanoscale. *Analytical and bioanalytical chemistry* **408**, 6885–6911. (http://dx.doi.org/10.1007/s00216-016-9781-8).

[3] Klar TA, Hell SW. 1999 Subdiffraction resolution in far-field fluorescence microscopy. *Optics letters* **24**, 954–956. (http://dx.doi.org/10.1364/ol.24.000954).

[4] Gustafsson MG. 2000 Surpassing the lateral resolution limit by a factor of two using structured illumination microscopy. *Journal of microscopy* **198**, 82–87. (http://dx.doi.org/10.1046/j.1365-2818.2000.00710.x).

[5] Betzig E, Patterson GH, Sougrat R, Lindwasser OW, Olenych S, Bonifacino JS, Davidson MW, Lippincott-Schwartz J, Hess HF. 2006 Imaging intracellular fluorescent proteins at nanometer resolution. *Science (New York, N.Y.)* **313**, 1642–1645. (http://dx.doi.org/10.1126/science.1127344).

[6] Heilemann M, van de Linde S, Schüttpelz M, Kasper R, Seefeldt B, Mukherjee A, Tinnefeld P, Sauer M. 2008 Subdiffraction-resolution fluorescence imaging with conventional fluorescent probes. *Angewandte Chemie (International ed. in English)* **47**, 6172–6176. (http://dx.doi.org/10.1002/anie.200802376).

[7] Rust MJ, Bates M, Zhuang X. 2006 Sub-diffraction-limit imaging by stochastic optical reconstruction microscopy (STORM). *Nature methods* **3**, 793–795. (http://dx.doi.org/10.1038/nmeth929).

[8] Sharonov A, Hochstrasser RM. 2006 Wide-field subdiffraction imaging by accumulated binding of diffusing probes. *Proceedings of the National Academy of Sciences of the United States of America* **103**, 18911–18916. (http://dx.doi.org/10.1073/pnas.0609643104).

[9] Chen F, Tillberg PW, Boyden ES. 2015 Optical imaging. Expansion microscopy. *Science (New York, N.Y.)* **347**, 543–548. (http://dx.doi.org/10.1126/science.1260088).

[10] Ku T, Swaney J, Park J-Y, Albanese A, Murray E, Cho JH, Park Y-G, Mangena V, Chen J, Chung K. 2016 Multiplexed and scalable super-resolution imaging of three-dimensional protein localization in size-adjustable tissues. *Nature biotechnology* **34**, 973–981. (http://dx.doi.org/10.1038/nbt.3641).

[11] Chang J-B *et al.* 2017 Iterative expansion microscopy. *Nature methods* **14**, 593–599. (http://dx.doi.org/10.1038/nmeth.4261).

[12] Truckenbrodt S, Maidorn M, Crzan D, Wildhagen H, Kabatas S, Rizzoli SO. 2018 X10 expansion microscopy enables 25-nm resolution on conventional microscopes. *EMBO reports* **19**. (http://dx.doi.org/10.15252/embr.201845836).

[13] Cheng S, Zhao Y. 2019 Nanoscale imaging of E. coli cells by expansion microscopy. *Discoveries (Craiova, Romania)* **7**, e98. (http://dx.doi.org/10.15190/d.2019.11).

[14] Chen L, Yao L, Zhang L, Fei Y, Mi L, Ma J. 2021 Applications of Super Resolution Expansion Microscopy in Yeast. *Front. Phys.* **9**. (http://dx.doi.org/10.3389/fphy.2021.650353).

[15] Kunz TC, Rühling M, Moldovan A, Paprotka K, Kozjak-Pavlovic V, Rudel T, Fraunholz M. 2021 The Expandables: Cracking the Staphylococcal Cell Wall for Expansion Microscopy. *Frontiers in cellular and infection microbiology* **11**, 644750. (http://dx.doi.org/10.3389/fcimb.2021.644750).

[16] Götz R, Panzer S, Trinks N, Eilts J, Wagener J, Turrà D, Di Pietro A, Sauer M, Terpitz U. 2020 Expansion Microscopy for Cell Biology Analysis in Fungi. *Frontiers in microbiology* **11**, 574. (http://dx.doi.org/10.3389/fmicb.2020.00574).

[17] Trinks N, Reinhard S, Drobny M, Heilig L, Löffler J, Sauer M, Terpitz U. 2021 Subdiffraction-resolution fluorescence imaging of immunological synapse formation between NK cells and A.

fumigatus by expansion microscopy. *Communications biology* **4**, 1151. (http://dx.doi.org/10.1038/s42003-021-02669-y).
[18] Drelich L, Aboulouard S, Franck J, Salzet M, Fournier I, Wisztorski M. 2021 Toward High Spatially Resolved Proteomics Using Expansion Microscopy. *Analytical chemistry* **93**, 12195–12203. (http://dx.doi.org/10.1021/acs.analchem.0c05372).
[19] M'Saad O, Bewersdorf J. 2020 Light microscopy of proteins in their ultrastructural context. *Nature communications* **11**, 3850. (http://dx.doi.org/10.1038/s41467-020-17523-8).
[20] Campbell LA, Pannoni KE, Savory NA, Lal D, Farris S. 2021 Protein-retention expansion microscopy for visualizing subcellular organelles in fixed brain tissue. *Journal of neuroscience methods* **361**, 109285. (http://dx.doi.org/10.1016/j.jneumeth.2021.109285).
[21] Yu C-CJ *et al.* 2020 Expansion microscopy of C. elegans. *eLife* **9**. (http://dx.doi.org/10.7554/eLife.46249).
[22] Chozinski TJ, Halpern AR, Okawa H, Kim H-J, Tremel GJ, Wong ROL, Vaughan JC. 2016 Expansion microscopy with conventional antibodies and fluorescent proteins. *Nature methods* **13**, 485–488. (http://dx.doi.org/10.1038/nmeth.3833).
[23] Tillberg PW *et al.* 2016 Protein-retention expansion microscopy of cells and tissues labeled using standard fluorescent proteins and antibodies. *Nature biotechnology* **34**, 987–992. (http://dx.doi.org/10.1038/nbt.3625).
[24] Damstra HG, Mohar B, Eddison M, Akhmanova A, Kapitein LC, Tillberg PW. 2021 *Visualizing cellular and tissue ultrastructure using Ten-fold Robust Expansion Microscopy (TREx)*.
[25] Lim Y, Shiver AL, Khariton M, Lane KM, Ng KM, Bray SR, Qin J, Huang KC, Wang B. 2019 Mechanically resolved imaging of bacteria using expansion microscopy. *PLoS biology* **17**, e3000268. (http://dx.doi.org/10.1371/journal.pbio.3000268).
[26] Fan Y, Lim Y, Wyss LS, Park S, Xu C, Fu H, Fei J, Hong Y, Wang B. 2021 Mechanical expansion microscopy. *Methods in cell biology* **161**, 125–146. (http://dx.doi.org/10.1016/bs.mcb.2020.04.013).
[27] Kao P, Nodine MD. 2021 Application of expansion microscopy on developing Arabidopsis seeds. *Methods in cell biology* **161**, 181–195. (http://dx.doi.org/10.1016/bs.mcb.2020.06.004).
[28] Kubalová I, Schmidt Černohorská M, Huranová M, Weisshart K, Houben A, Schubert V. 2020 Prospects and limitations of expansion microscopy in chromatin ultrastructure determination. *Chromosome research : an international journal on the molecular, supramolecular and evolutionary aspects of chromosome biology* **28**, 355–368. (http://dx.doi.org/10.1007/s10577-020-09637-y).
[29] Büttner M, Lagerholm CB, Waithe D, Galiani S, Schliebs W, Erdmann R, Eggeling C, Reglinski K. 2021 Challenges of Using Expansion Microscopy for Super-resolved Imaging of Cellular Organelles. *Chembiochem : a European journal of chemical biology* **22**, 686–693. (http://dx.doi.org/10.1002/cbic.202000571).
[30] Zhu C *et al.* 2021 Measurement of expansion factor and distortion for expansion microscopy using isolated renal glomeruli as landmarks. *Journal of biophotonics* **14**, e202100001. (http://dx.doi.org/10.1002/jbio.202100001).
[31] Pernal SP *et al.* 2020 Nanoscale imaging using differential expansion microscopy. *Histochemistry and cell biology* **153**, 469–480. (http://dx.doi.org/10.1007/s00418-020-01869-7).
[32] Gambarotto D *et al.* 2019 Imaging cellular ultrastructures using expansion microscopy (U-ExM). *Nature methods* **16**, 71–74. (http://dx.doi.org/10.1038/s41592-018-0238-1).
[33] Gao R, Yu C-CJ, Gao L, Piatkevich KD, Neve RL, Munro JB, Upadhyayula S, Boyden ES. 2021 A highly homogeneous polymer composed of tetrahedron-like monomers for high-isotropy expansion microscopy. *Nature nanotechnology* **16**, 698–707. (http://dx.doi.org/10.1038/s41565-021-00875-7).

[34] Halpern AR, Alas GCM, Chozinski TJ, Paredez AR, Vaughan JC. 2017 Hybrid Structured Illumination Expansion Microscopy Reveals Microbial Cytoskeleton Organization. *ACS nano* **11**, 12677–12686. (http://dx.doi.org/10.1021/acsnano.7b07200).
[35] Li R, Chen X, Lin Z, Wang Y, Sun Y. 2018 Expansion enhanced nanoscopy. *Nanoscale* **10**, 17552–17556. (http://dx.doi.org/10.1039/C8NR04267E).
[36] Xu H *et al.* 2019 Molecular organization of mammalian meiotic chromosome axis revealed by expansion STORM microscopy. *Proceedings of the National Academy of Sciences of the United States of America* **116**, 18423–18428. (http://dx.doi.org/10.1073/pnas.1902440116).
[37] Zwettler FU, Reinhard S, Gambarotto D, Bell TDM, Hamel V, Guichard P, Sauer M. 2020 Molecular resolution imaging by post-labeling expansion single-molecule localization microscopy (Ex-SMLM). *Nature communications* **11**, 3388. (http://dx.doi.org/10.1038/s41467-020-17086-8).
[38] Shaib AH *et al.* 2022 *Expansion microscopy at one nanometer resolution*.
[39] Wang B, Yao L, Jing Y, Fei Y, Bai Q, Mi L, Ma J. 2020 Multicomposite super-resolution microscopy: Enhanced Airyscan resolution with radial fluctuation and sample expansions. *Journal of biophotonics* **13**, e2419. (http://dx.doi.org/10.1002/jbio.201960211).
[40] Vojnovic I, Winkelmeier J, Endesfelder U. 2019 Visualizing the inner life of microbes: practices of multi-color single-molecule localization microscopy in microbiology. *Biochemical Society transactions* **47**, 1041–1065. (http://dx.doi.org/10.1042/BST20180399).
[41] Virant D, Vojnovic I, Winkelmeier J, Endesfelder M, Turkowyd B, Lando D, Endesfelder U. 2021 *Unraveling the kinetochore nanostructure in Schizosaccharomyces pombe using multi-color single-molecule localization microscopy*.
[42] Götz R, Kunz TC, Fink J, Solger F, Schlegel J, Seibel J, Kozjak-Pavlovic V, Rudel T, Sauer M. 2020 Nanoscale imaging of bacterial infections by sphingolipid expansion microscopy. *Nature communications* **11**, 6173. (http://dx.doi.org/10.1038/s41467-020-19897-1).
[43] McKinney SA, Murphy CS, Hazelwood KL, Davidson MW, Looger LL. 2009 A bright and photostable photoconvertible fluorescent protein. *Nature methods* **6**, 131–133. (http://dx.doi.org/10.1038/nmeth.1296).
[44] Bindels DS *et al.* 2017 mScarlet: a bright monomeric red fluorescent protein for cellular imaging. *Nature methods* **14**, 53–56. (http://dx.doi.org/10.1038/nmeth.4074).
[45] Hayashi A, Ding D-Q, Da-Qiao D, Tsutsumi C, Chikashige Y, Masuda H, Haraguchi T, Hiraoka Y. 2009 Localization of gene products using a chromosomally tagged GFP-fusion library in the fission yeast Schizosaccharomyces pombe. *Genes to cells : devoted to molecular & cellular mechanisms* **14**, 217–225. (http://dx.doi.org/10.1111/j.1365-2443.2008.01264.x).
[46] Abella M, Andruck L, Malengo G, Skruzny M. 2021 Actin-generated force applied during endocytosis measured by Sla2-based FRET tension sensors. *Developmental cell* **56**, 2419-2426.e4. (http://dx.doi.org/10.1016/j.devcel.2021.08.007).
[47] Hentges P, van Driessche B, Tafforeau L, Vandenhaute J, Carr AM. 2005 Three novel antibiotic marker cassettes for gene disruption and marker switching in Schizosaccharomyces pombe. *Yeast (Chichester, England)* **22**, 1013–1019. (http://dx.doi.org/10.1002/yea.1291).
[48] Bryksin AV, Matsumura I. 2010 Overlap extension PCR cloning: a simple and reliable way to create recombinant plasmids. *BioTechniques* **48**, 463–465. (http://dx.doi.org/10.2144/000113418).
[49] Zhang Y, Werling U, Edelmann W. 2012 SLiCE: a novel bacterial cell extract-based DNA cloning method. *Nucleic acids research* **40**, e55. (http://dx.doi.org/10.1093/nar/gkr1288).
[50] Cupp-Enyard C. 2008 Sigma's Non-specific Protease Activity Assay - Casein as a Substrate. *Journal of visualized experiments : JoVE*. (http://dx.doi.org/10.3791/899).

[51] Lowry O, Rosebrough N, Farr AL, Randall R. 1951 PROTEIN MEASUREMENT WITH THE FOLIN PHENOL REAGENT. *Journal of Biological Chemistry* **193**, 265–275. (http://dx.doi.org/10.1016/S0021-9258(19)52451-6).
[52] Edelstein A, Amodaj N, Hoover K, Vale R, Stuurman N. 2010 Computer control of microscopes using μManager. *Current protocols in molecular biology* **Chapter 14**, Unit14.20. (http://dx.doi.org/10.1002/0471142727.mb1420s92).
[53] Schindelin J *et al.* 2012 Fiji: an open-source platform for biological-image analysis. *Nature methods* **9**, 676–682. (http://dx.doi.org/10.1038/nmeth.2019).
[54] Wolter S, Löschberger A, Holm T, Aufmkolk S, Dabauvalle M-C, van de Linde S, Sauer M. 2012 rapidSTORM: accurate, fast open-source software for localization microscopy. *Nature methods* **9**, 1040–1041. (http://dx.doi.org/10.1038/nmeth.2224).
[55] Endesfelder U, Malkusch S, Fricke F, Heilemann M. 2014 A simple method to estimate the average localization precision of a single-molecule localization microscopy experiment. *Histochemistry and cell biology* **141**, 629–638. (http://dx.doi.org/10.1007/s00418-014-1192-3).
[56] Malkusch S, Heilemann M. 2016 Extracting quantitative information from single-molecule super-resolution imaging data with LAMA - LocAlization Microscopy Analyzer. *Scientific reports* **6**, 34486. (http://dx.doi.org/10.1038/srep34486).
[57] Baddeley A, Rubak E, Turner R. 2016 *Spatial point patterns*. *Methodology and applications with R.* Chapman & Hall/CRC Interdisciplinary statistics series. Boca Raton, Florida: CRC Press.
[58] Flor-Parra I, Zhurinsky J, Bernal M, Gallardo P, Daga RR. 2014 A Lallzyme MMX-based rapid method for fission yeast protoplast preparation. *Yeast* **31**, 61–66. (http://dx.doi.org/10.1002/yea.2994).
[59] Forsburg SL, Rhind N. 2006 Basic methods for fission yeast. *Yeast* **23**, 173–183. (http://dx.doi.org/10.1002/yea.1347).
[60] Požgajová M, Navratilova A, Trakovicka A. 2017 Determination of the efficient enzyme concentration for lytic digestion of vegetative cells but not spores in Schizosaccharomyces pombe. *Acta fytotechn zootechn* **20**, 20–22. (http://dx.doi.org/10.15414/afz.2017.20.01.20-22).
[61] Pérez P, Cortés JCG, Cansado J, Ribas JC. 2018 Fission yeast cell wall biosynthesis and cell integrity signalling. *Cell surface (Amsterdam, Netherlands)* **4**, 1–9. (http://dx.doi.org/10.1016/j.tcsw.2018.10.001).
[62] García Cortés JC, Ramos M, Osumi M, Pérez P, Ribas JC. 2016 The Cell Biology of Fission Yeast Septation. *Microbiology and molecular biology reviews : MMBR* **80**, 779–791. (http://dx.doi.org/10.1128/MMBR.00013-16).
[63] Bowen AR, Chen-Wu JL, Momany M, Young R, Szaniszlo PJ, Robbins PW. 1992 Classification of fungal chitin synthases. *Proceedings of the National Academy of Sciences of the United States of America* **89**, 519–523. (http://dx.doi.org/10.1073/pnas.89.2.519).
[64] Ding DQ, Tomita Y, Yamamoto A, Chikashige Y, Haraguchi T, Hiraoka Y. 2000 Large-scale screening of intracellular protein localization in living fission yeast cells by the use of a GFP-fusion genomic DNA library. *Genes to cells : devoted to molecular & cellular mechanisms* **5**, 169–190. (http://dx.doi.org/10.1046/j.1365-2443.2000.00317.x).
[65] Matsuo Y, Tanaka K, Nakagawa T, Matsuda H, Kawamukai M. 2004 Genetic analysis of chs1+ and chs2+ encoding chitin synthases from Schizosaccharomyces pombe. *Bioscience, biotechnology, and biochemistry* **68**, 1489–1499. (http://dx.doi.org/10.1271/bbb.68.1489).
[66] Martín-García R, Durán A, Valdivieso M-H. 2003 In Schizosaccharomyces pombe chs2p has no chitin synthase activity but is related to septum formation. *FEBS Letters* **549**, 176–180. (http://dx.doi.org/10.1016/S0014-5793(03)00812-3).

[67] Hinterndorfer K, Laporte MH, Mikus F, Petrozzi LT, Bourgoint C, Prouteau M, Dey G, Loewith R, Guichard P, Hamel V. 2022 *Ultrastructure Expansion Microscopy reveals the nanoscale cellular architecture of budding and fission yeast*.
[68] Bestul AJ, Yu Z, Unruh JR, Jaspersen SL. 2017 Molecular model of fission yeast centrosome assembly determined by superresolution imaging. *The Journal of cell biology* **216**, 2409–2424. (http://dx.doi.org/10.1083/jcb.201701041).
[69] Osburn S, Berden G, Oomens J, Gulyuz K, Polfer NC, O'Hair RAJ, Ryzhov V. 2013 Structure and Reactivity of the Glutathione Radical Cation: Radical Rearrangement from the Cysteine Sulfur to the Glutamic Acid α-Carbon Atom. *ChemPlusChem* **78**, 970–978. (http://dx.doi.org/10.1002/cplu.201300057).
[70] Ramis R, Casasnovas R, Ortega-Castro J, Frau J, Álvarez-Idaboy JR, Mora-Diez N. 2019 Modelling the repair of carbon-centred protein radicals by the antioxidants glutathione and Trolox. *New J. Chem.* **43**, 2085–2097. (http://dx.doi.org/10.1039/C8NJ05544K).
[71] Watanabe S, Punge A, Hollopeter G, Willig KI, Hobson RJ, Davis MW, Hell SW, Jorgensen EM. 2011 Protein localization in electron micrographs using fluorescence nanoscopy. *Nature methods* **8**, 80–84. (http://dx.doi.org/10.1038/nmeth.1537).
[72] Asakawa H *et al.* 2019 Asymmetrical localization of Nup107-160 subcomplex components within the nuclear pore complex in fission yeast. *PLoS genetics* **15**, e1008061. (http://dx.doi.org/10.1371/journal.pgen.1008061).
[73] Hagan I, Yanagida M. 1995 The product of the spindle formation gene sad1+ associates with the fission yeast spindle pole body and is essential for viability. *The Journal of cell biology* **129**, 1033–1047. (http://dx.doi.org/10.1083/jcb.129.4.1033).
[74] Endesfelder U, Finan K, Holden SJ, Cook PR, Kapanidis AN, Heilemann M. 2013 Multiscale spatial organization of RNA polymerase in Escherichia coli. *Biophysical journal* **105**, 172–181. (http://dx.doi.org/10.1016/j.bpj.2013.05.048).
[75] Baum M, Clarke L. 2000 Fission yeast homologs of human CENP-B have redundant functions affecting cell growth and chromosome segregation. *Molecular and cellular biology* **20**, 2852–2864. (http://dx.doi.org/10.1128/MCB.20.8.2852-2864.2000).
[76] Hayashi T, Fujita Y, Iwasaki O, Adachi Y, Takahashi K, Yanagida M. 2004 Mis16 and Mis18 are required for CENP-A loading and histone deacetylation at centromeres. *Cell* **118**, 715–729. (http://dx.doi.org/10.1016/j.cell.2004.09.002).
[77] Lando D *et al.* 2012 Quantitative single-molecule microscopy reveals that CENP-A(Cnp1) deposition occurs during G2 in fission yeast. *Open biology* **2**, 120078. (http://dx.doi.org/10.1098/rsob.120078).
[78] Balinovic A, Albrecht D, Endesfelder U. 2019 Spectrally red-shifted fluorescent fiducial markers for optimal drift correction in localization microscopy. *J. Phys. D: Appl. Phys.* **52**, 204002. (http://dx.doi.org/10.1088/1361-6463/ab0862).
[79] Mlodzianoski MJ, Schreiner JM, Callahan SP, Smolková K, Dlasková A, Santorová J, Ježek P, Bewersdorf J. 2011 Sample drift correction in 3D fluorescence photoactivation localization microscopy. *Optics express* **19**, 15009–15019. (http://dx.doi.org/10.1364/OE.19.015009).
[80] Lee H, Yu C-C, Boyden ES, Zhuang X, Kosuri P. 2021 Tetra-gel enables superior accuracy in combined super-resolution imaging and expansion microscopy. *Scientific reports* **11**, 16944. (http://dx.doi.org/10.1038/s41598-021-96258-y).
[81] Campbell BC, Paez-Segala MG, Looger LL, Petsko GA, Liu CF. 2022 Chemically stable fluorescent proteins for advanced microscopy. *Nature methods*. (http://dx.doi.org/10.1038/s41592-022-01660-7).

[82] Kopek BG *et al.* 2017 Diverse protocols for correlative super-resolution fluorescence imaging and electron microscopy of chemically fixed samples. *Nature protocols* **12**, 916–946. (http://dx.doi.org/10.1038/nprot.2017.017).

CHAPTER 4

Discussion & Outlook

4.1 Investigating the kinetochore nanostructure using multi-color SMLM

The KT is a multi-protein complex of over fifty different proteins and plays a vital role in cell division as it is a part of the spindle apparatus and serves as a linker tethering the SPB bound kMT to the centromere in chromosomes. Any incorrect segregation of chromatids during mitosis or meiosis irreversibly leads to aneuploidy or cell death [61]. Therefore, it is vital to investigate the KT structure, function, attachment and regulation. So far, most of the KT proteins and their interaction partners have been identified using biochemical pull-down assays and individual partial or complete KT subcomplex structures were resolved *in vitro* by EM or X-ray crystallography. Nevertheless, the full KT complex could not be resolved at high-resolution due to its complexity and flexibility.

4.1.1 Triangulation strategy & suitable reference proteins

Therefore, the goal of this thesis was to build a map of the human-like regional KT complex in fission yeast *in vivo* at a nanometer resolution using multi-color SMLM during its most stretched form in mitotic meta- to anaphase A for the first time. To undertake this task, a reliable quantitative multi-color SMLM approach had to be established for fission yeast, that includes but is not limited to the determination of individual KT protein stoichiometries as well as intra-KT distances. For this we decided to triangulate the position of several KT-POIs a time in relation to two reference proteins. By selecting one reference protein at the centromere, which serves as the KT assembly platform, and one at the SPB, which nucleates the kMT needed to generate the force to separate sister-chromatids, this approach allows for on one hand an intrinsic counting and strain health standard and on the other hand identification of the correct cell cycle stage due to the presence and distance of two SPBs during mitosis as well as precisely focus on the mitotic spindle plane. Furthermore, this triangulation tactic allows for an enhanced accuracy of distance calculations since we expect that all three proteins fall on one axis, which allows for a direct estimation of the size of the measurement errors from the deviation of the axis using Bayesian inference. We estimated that suitable reference proteins should be highly abundant and present throughout the cell cycle with no regulatory function. As Lando *et al.* previously showed that cnp1$^{\text{CENP-A}}$ fulfils these criteria and could successfully conduct single-color PALM experiments, we decided to use cnp1$^{\text{CENP-A}}$ as the centromeric reference protein [36]. After

preliminary genetic tagging of several SPB proteins with an enzyme tag, we evaluated possible effects of the tag on the biological function by measuring the cell length, which is a measure for a delayed mitosis and decided on sad1$^{SUN1/2}$, an inner nuclear membrane anchor of the SPB, as a reliable SPB reference protein [192].

4.1.2 Fluorescence background issues in fission yeast

As single-molecule sensitive experiments require highly optimized sample preparation and imaging schemes (see chapter 1.2.2) [193], this is further complicated by introducing a) more targets, which require compatible fluorophore combinations, and b) microorganisms as imaging hosts, which are densely crowded and possess complex cell walls, which may reduce extrinsic labeling efficiency or specificity using organic dyes (see chapter 1.2.3) [194]. To design a multi-color SMLM strategy for fission yeast as a host, we first determined which color channels are suitable for single-molecule sensitivity. Here, we detected a high degree of autofluorescence, which lead to the omission of the green and blue color channels reducing the available fluorophore combinations to red and far red color channels. Additionally, we found that fission yeast strains containing ade6-M210 and ade6-M216 selection markers that disrupt the adenine biosynthesis pathway and accumulate a bright red precursor [195, 196] used for easy screening of colonies on agar plates, introduce a high background in the red color channel where single presursor molecules were detected to be as bright as the green-to-red photoconvertable FP mEos2 (see figure S1 A in chapter 2). This makes a differentiation between background and real signal impossible. Hence, we 'cured' our fission yeast strains by transforming the wildtype adenine gene and selecting for white colonies on YES agar plates with a low amount of adenine and subsequent sequencing. This way, we were still able to utilize the red color channel for fluorophore detection.

4.1.3 Evaluation of multi-color SMLM approaches

Generally, target proteins can be labeled extrinsically using organic dyes conjugated to enzyme and peptide tags or anti- and nanobodies via immunofluorescence or alternatively intrinsically using FPs, which are integrated into or next to the genetic locus of the POI. While organic dyes are brighter thus yield a higher signal-to-noise ratio, which itself yields a higher localization precision, they also require dye specific switching buffers to induce blinking, which reduces possible dye combinations [197]. Additionally, organic dyes are at risk to unspecifically and heterogeneously stain the sample and thus introduce higher background signal, leading to false positive clusters, which is especially critical for low abundant proteins such as KT proteins. Nevertheless, we tested and evaluated different commonly used organic dyes by staining both reference proteins, which were genetically tagged to an enzyme tag (SNAP- [198] or HaloTag [199]). Here we found that the highly charged Alexa Fluor 647 introduced high unspecific labeling even after meticulous protocol optimizations masking possible charges and adding multiple washing steps using various buffers in fixed fission yeast cells (see figure S1, B) in chapter 2). On the other hand CF680, which bears masked charges, showed low labeling efficiencies albeit the unspecific staining was significantly reduced compared to Alexa Fluor 647, which may be attributed to its larger molecular size (see figure S1 B) in chapter 2). However, even with partial removal of the fission yeast cell wall using Zymolase, CF680 labeling efficiency was not significantly increased, which may be due to the high molecular crowing of the cytosol. Even though staining of Halo-cnp1^{CENP-A} with CF647 produced the best labeling efficiency and

specificity of all tested dyes, it still introduced several false positive clusters with roughly the same size as legitimate KT clusters (see figure S1, C and D) in chapter 2). Therefore, our final labeling approach relied exclusively on FPs, as they do not require any switching buffers and have a 1:1 POI to FP labeling ratio. However, it was shown that some FPs such as mEos2 are known to aggregate at locally high concentrations [200], which is the case for the dense KT structure and should thus be avoided. In case of certain mEos2 tagged KT proteins, we detected elongated fission yeast cells compared to the wildtype that might indicate a delayed mitosis due to the tags interference with the function of the KT proteins. Ultimately, we chose a dual-color orthogonal PALM imaging approach, where the green-to-red photoconvertable FP mEos3.2-A69T [201] is first fully read-out by primed conversion photoactivated localization microscopy (PC-PALM) using 488 and 730 nm laser light with a subsequent full read-out of the photoactivatable FP PAmCherry [202] by ultra-violet photoactivated localization microscopy (UV-PALM) using 405 nm laser light [203]. Here, it is noteworthy to point out that the preceding PC-PALM of mEos3.2-A69T was shown to not pre-activate nor extensively bleach PAmCherry. Since both FPs emit in the red color channel, we also selected the bright and monomeric conventional FP mScarlet-I [204] as the third fluorophore of choice, which emits in the same channel, creating a chromatic aberration free imaging scheme. Thus, the final imaging strategy is as follows: First mitotic cells are identified by two SPBs and the spindle plane is focus by visualizing the SPB reference protein sad1$^{SUN1/2}$ labeled with mScarlet-I, a snapshot is acquired and residual mScarlet-I signal is bleached by prolonged 561 nm laser light exposure. Subsequently, the KT-POI labeled with mEos3.2-A69T is fully read-out by PC-PALM after which a short bleaching step with 488 nm laser light is performed to eliminate any residual mEos3.2-A69T. Finally, the centromeric reference protein cnp1^{CENP-A} labeled with PAmCherry is also fully read-out using UV-PALM.

4.1.4 Protein functionality and mitotic delay of 3C-strain library

Therefore, we generated a triple-color (3C) strain library consisting of about 26 3C-strains, of which ten strains were successfully imaged and analysed to date. Since introducing three genetic fluorescent tags to vital proteins in the division process might affect the cell physiology and/or reduce the protein functionality, we conducted spot tests examining possible temperature sensitivities or KT-MT deficiencies introduced by thiabendazole (TBZ), which is a MT depolymerizing drug used to detect mitotic defects [139] (see figure S2 C and D in chapter 2). Additionally, we tested all strains for an altered phenotype and compared them to the wildtype via flow cytometry (see figure S2 E in chapter 2). Except for the cnp3^{CENP-C} 3C-strain and the dam1 3C-strain all strains did not deviate from the wildtype phenotype, temperature or TBZ growth behaviour. The cnp3^{CENP-C} 3C-strain showed both a larger cell size and an increased sensitivity to TBZ. This might be caused by the hindered interaction of the C-terminus of cnp3^{CENP-C} with the CATD domain at the N-terminus of cnp1^{CENP-A}, which in case of the cnp3^{CENP-C} 3C-strain are both labeled by two 2-3 nm large FPs [38, 205, 206]. Moreover, the single color cnp3^{CENP-C}-mEos3.2-A69T strain, which possesses a native cnp1^{CENP-A}, did not show a modified phenotype, which supports this assumption (data not shown). Nevertheless, the cnp3^{CENP-C} 3C-strain was excluded from further analysis. However, since the N-terminus of cnp3^{CENP-C} was shown to interact with the mis12^{MIS12}/nnf1^{PMF1} head domain of the MIND complex [97, 98], alternative cnp3^{CENP-C} 3C-strains should insert the FP tag internally. In contrast to that, the dam1 3C-strain showed a slightly higher tolerance to higher TBZ concentrations compared to the wildtype. A similar effect was documented in two independent studies, where TBZ tolerance increased when the C-terminus of dam1 was truncated (dam1-127) [207] or mutations were added

to the C-terminus (H126R and E149G) [208]. This might indicate that the FP tagged to the dam1 C-terminus might increase the KT-kMT attachment. Since the dam1 3C-strain only showed a slight TBZ tolerance yet no change in phenotype, it was included into further analysis.

4.1.5 Protocol optimization, data analysis and controls

Moreover, fission yeast rapidly divides with a generation time of 2-4 h [1] depending on the growth media and temperature, of which the whole mitosis only lasts about 30 min [209, 210]. Since meta-anaphase A are the only cell cycle stages in which single centromeres can be resolved with SMLM, more fission yeast cells were caught in mitosis using a lactose gradient based cell synchronization, where smaller cells were isolated from longer cells, grown until mitosis and then chemically fixed (see figure S2 B in chapter 2). All acquired movies were localized, drift-corrected and channel aligned using fiducial markers, quality filtered, cluster and KT selected and the annotated data finally stored in a SQL database in several rounds of manual selection and automated analysis (for a detailed description of the data analysis see figure 2 A in chapter 2 and the Materials & Methods section in chapter 2). As first measures we extracted the cnp1$^{\text{CENP-A}}$-POI distances and POI and cnp1$^{\text{CENP-A}}$ copy numbers and stoichiometries. In short, we evaluated multiple methods to determine cnp1$^{\text{CENP-A}}$-POI distances, and ultimately used Bayesian inference and deduced the posterior probability distribution of individual cnp1$^{\text{CENP-A}}$-POI distances using the probabilistic programming language Stan. To account for over- and under-counting caused by e.g. blinking and thus multiple detections of the same fluorophore or no detected fluorescence caused by incorrect FP folding, respectively, the localizations per POI cluster were calibrated utilizing the bacterial ferritin FtnA counting standard, which forms distinct 8mers and 24mers [211, 212] (see figure 2 B and C in chapter 2). Since cnp1$^{\text{CENP-A}}$ is tagged in every 3C-strain, it additionally functions as an intrinsic counting reproducibility control between different imaging days as well as another KT functionality expression control between different 3C-strains (see figure 2 E in chapter 2). This intrinsic counting standard showed about 50 cnp1$^{\text{CENP-A}}$ copies per centrosome with no significant differences between the ten imaged 3C-strains.

4.1.6 KT distances and stoichiometries

The cnp1$^{\text{CENP-A}}$-POI distances, POI stoichiometries and ratios can be found in tables 1, 2, S3 and S4 and graphically illustrated in figure 3 in chapter 2.

Starting with the inner KT, we investigated fta2$^{\text{CENP-P}}$ and fta7$^{\text{CENP-Q}}$ of the COMA complex and found that our data agrees with the 1:1:1:1 stoichiometry of single components of the heterotetrameric COMA complex previously shown in cryo-EM data of isolated budding yeast COMA complexes [213]. From the same study, the distances between the N-terminus of cnp1$^{\text{CENP-A}}$ and the C- termini of fta2$^{\text{CENP-P}}$ or fta7$^{\text{CENP-Q}}$ were calculated to be 9.7 and 10.7 nm, respectively, which nicely coincides with our data.

We also measured cnp20$^{\text{CENP-T}}$ as another important inner KT protein, which is part of the CENP-TWSX complex. Here, we found that the cnp20$^{\text{CENP-T}}$ C-terminus is in proximity to the aforementioned COMA complex. Additionally, we determined the ratio of inner KT subcomplexes and found that the ratio of cnp20$^{\text{CENP-T}}$ to COMA complex in fission yeast is 1:0.9, which deviates from the 1:2.0 ratio measured in another multi-color SMLM approach recently conducted in budding yeast [214]. This might be caused by the fact that in contrast to the outer KT the inner KT is less conserved [82–84]. Since cnp1$^{\text{CENP-A}}$ is a rapidly evolving KT landmark protein on top of which the inner KT assembles,

it might be the driving force for inner KT adaptation [85–87]. It was shown that different organisms favour and rely on different inner KT pathways based on cnp20$^{\text{CENP-T}}$, cnp3$^{\text{CENP-C}}$ and/or the COMA complex [88–92]. Budding yeast e.g. is believed to primarily rely on the COMA complex as a tether to the outer KT with cnp3$^{\text{CENP-C}}$ serving as a backup pathway [111, 120] as two COMA proteins and cnp3$^{\text{CENP-C}}$ are essential, while budding yeast cells carrying a deletion of cnp20$^{\text{CENP-T}}$ remain viable [107–109, 121–123]. On the flipside, while the preferred inner KT pathway in fission yeast is not known yet [120], our copy number data and the fact that the whole COMA complex and cnp20$^{\text{CENP-T}}$ are essential [101, 109, 129, 130], while cnp3$^{\text{CENP-C}}$ is not [101, 103, 108], suggest that fission yeast relies on the COMA complex and cnp20$^{\text{CENP-T}}$ in equal measures.

To investigate the outer KT we selected mis12$^{\text{MIS12}}$ and nnf1$^{\text{PMF1}}$ of the MIND complex, spc7$^{\text{KNL1}}$ of the KNL1 complex, spc25$^{\text{SPC25}}$ and ndc80$^{\text{NDC80}}$ of the NDC80c and dam1 of the DASH complex. Our measurements place the C-termini of mis12$^{\text{MIS12}}$ and nnf1$^{\text{PMF1}}$ close to each other, which is congruent with other work utilizing conventional fluorescence microscopy [215], FRET [216] or EM [131]. In contrast to that we detected the spc7$^{\text{KNL1}}$ C-terminus close to the C-termini of mis12$^{\text{MIS12}}$ and nnf1$^{\text{PMF1}}$, which is in agreement with EM studies [131, 217]. While comparing our copy numbers of these three KT proteins, we calculated a 1:1.3 ratio within the MIND complex, which deviates from the expected 1:1:1:1 ratio [132, 218]. However, this might be due to unexpectedly low copy numbers measured for mis12$^{\text{MIS12}}$, as a the 1:1.0 ratio of nnf1$^{\text{PMF1}}$ to spc7$^{\text{KNL1}}$ is in agreement with previous *in vitro* measurements [131, 132]. Since the mis12$^{\text{MIS12}}$-3C-strain did not show any phenotypical changes or mitotic delays, this outlayer remains a mystery and needs further investigation by additional imaging of the remaining MIND components mis13$^{\text{DSN1}}$ and mis14$^{\text{NSL1}}$.

Next, we studied spc25$^{\text{SPC25}}$ and ndc80$^{\text{NDC80}}$ of the heterotetrameric NDC80c. The calculated ndc80$^{\text{NDC80}}$ to spc25$^{\text{SPC25}}$ ratio derived from the protein copy numbers was 1:1.1, which is in agreement with crystal structures with an expected 1:1:1:1 ratio of all four components of the NDC80c heterotetramer [134, 135]. The cnp1$^{\text{CENP-A}}$-spc25$^{\text{SPC25}}$ distance is shorter than our measured cnp1$^{\text{CENP-A}}$-MIND distances, which might be caused by an overlap of the MIND and NDC80c C-termini and yield a more stable interaction. This hypothesis is supported by the detection of several overlapping contact sites between the MIND and NDC80c complex registered in cross-linking data [219].

Finally, we measured dam1 of the DASH complex. Although the C-terminus of dam1 was shown to interact with the globular HEC1 domain of ndc80$^{\text{NDC80}}$ in budding yeast [216, 220], our distances of the C-termini of dam1 and ndc80$^{\text{NDC80}}$ suggest a shorter distance closer to the loop region of ndc80$^{\text{NDC80}}$. This might be due to the shorter amino acid sequence of fission yeast dam1 with 155 aa in comparison to budding yeast dam1 with 343 aa [142]. To further confirm this hypothesis, ndc80$^{\text{NDC80}}$ could be tagged internally in its loop region, as well as at the head domain. While generally inner KT proteins were shown to be less abundant than proteins of the outer KT, dam1 copy numbers in fission and budding yeast deviate from each other. Here, dam1 in budding yeast is an essential protein [109] and appears in larger numbers than its fission yeast homologue [221], which is unessential [222] and could be found at the same protein copy number levels as the inner KT [221].

4.1.7 Outlook

While extracting cnp1$^{\text{CENP-A}}$-POI distances and POI copy numbers is a first step to understand the KT structure in fission yeast, other measures, such as cluster shapes and densities, which can be easily extracted from the aforementioned KT database, could shed more light into the organization of

individual KT proteins. With the addition of the remaining 3C-strains to the library and subsequent imaging, it should be possible to in time create a map of the complete native fission yeast KT complex. With the map of the native KT structure at hand, the impact of key mutations within the KT subcomplexes, effects of over-expression and deletion strains as well as impacts of environmental changes can be investigated in the future and compared to the native structure.

However, certain technical aspects and controls could be improved. As the acquisition of one imaging sequence is relatively long, this project could benefit from an high-throughput automatized image acquisition. For this, stage and focus control, region of interest (ROI) selection, calibrated laser feedback-loops to tightly control the FP photophysics, as well as scripts for repeating imaging routines for different ROIs have to be implemented first. Since the FtnA counting standard was expressed in *E. coli*, isolated and then imaged via single-molecule surfaces, this *in vitro* correction factor might deviate from the *in vivo* and *in situ* correction factor. Therefore, it would be beneficial to express the FtnA-FP oligos directly in our host either in the cytosol (*in vivo*) or in the nucleus (*in situ*). To do so, the expression needs to be tightly regulated, which can be achieved via a special expression system recently established in fission yeast [223]. Furthermore, the cnp3$^{\text{CENP-C}}$ triple-color strain showed a sensitivity to TBZ and longer cell lengths compared to the wildtype, yet the single-color strain did not. This is indicative for interferences in the proteins functionality caused by the proximity of the FP tags of cnp1$^{\text{CENP-A}}$ and cnp3$^{\text{CENP-C}}$. Therefore, it would be helpful to select another outer KT protein as one of the reference proteins instead of cnp1$^{\text{CENP-A}}$ at the centromere to map cnp3$^{\text{CENP-C}}$ correctly in the future.

It was previously shown that an over-expression of certain KT proteins or complexes, lead to a stoichiometry imbalance of KT proteins and was hypothesized to cause severe chromosome missegregation caused by absorption of available binding partners, needed for a stable KT structure (this is nicely summarized in the following reviews [224, 225]). Therefore, investigating the KT structure and composition under missregulation of single KT proteins or subcomplexes is vital to understand aneuploidy or cancer. Interestingly, preliminary single-color PALM experiments of mEos2-cnp1$^{\text{CENP-A}}$ in a Δwee1 background resulted in small fission yeast cells and severely elevated cnp1$^{\text{CENP-A}}$ copy numbers compared to the native wee1 strain (data not shown). Wee1 is a protein kinase that negatively regulates the mitotic entry through inhibition of the Cdc2/cyclin B kinase complex [226]. Deletion of wee1 thus leads to smaller fission yeast cells with a shorter G2 and prolonged G1 phase[227]. However, it is not known why the cnp1$^{\text{CENP-A}}$ copy numbers are elevated, as cnp1$^{\text{CENP-A}}$ deposition is usually restricted to G2 phase [36]. Thus, it would be desirable to investigate other KT protein copy numbers in a Δwee1 background strain as well as in a strain over-expressing wee1. Here, investigating cnp20$^{\text{CENP-T}}$ could be beneficial, as it is considered to be a cnp1$^{\text{CENP-A}}$ independent KT protein [119].

To investigate which inner KT pathway is the primary and which the backup pathway in fission yeast, several deletions and truncations can be introduced to the existing 3C-strains. For instance a change in POI copy numbers of COMA and cnp20$^{\text{CENP-T}}$ 3C-strains in a Δcnp3$^{\text{CENP-C}}$ background could hint to which pathway is preferred, while cnp1$^{\text{CENP-A}}$ would serve as a copy number read-out control and give an estimate for how the KT assembly platform changes. Furthermore, it was shown that the N-terminus of mis17$^{\text{CENP-U}}$ in the COMA complex in budding yeast interacts with the mis12$^{\text{MIS12}}$/nnf1$^{\text{PMF1}}$ head domain of the MIND complex [98]. Deleting the N-terminus of mis17$^{\text{CENP-U}}$ in a Δcnp3$^{\text{CENP-C}}$ background strain, would presumably only leave cnp20$^{\text{CENP-T}}$ as the main inner KT pathway. Since cnp20$^{\text{CENP-T}}$ was shown to interact via its N-terminus either directly [112, 115–118] or indirectly via the MIND complex [112–114] with NDC80c, it would be interesting to compare cnp20$^{\text{CENP-T}}$, MIND

and NDC80c copy numbers to investigate if the direct or indirect cnp20$^{\text{CENP-T}}$ pathway is preferred.

Finally, it was shown in *in vitro* EM data that the DASH complex in budding yeast assembles in one to two rings around the single kMT with an inner and outer diameter of 39 nm and 56 nm, respectively [142]. However, no ring-like structure could be found *in vivo* yet. Even with our SMLM experiments we could not resolve a ring-like structure for dam1, this could be attributed to on one hand three overlapping DASH complexes in our detected clusters and lateral localization precisions of about 20 nm. To overcome this issue, combining our SMLM approach with ExM, which is a recently developed imaging technique that increases the resolution by physical expansion of the sample, would be beneficial (more details in chapters 1.2.4, 3 and 4.2).

4.2 Development and establishment of SExY

While SMLM techniques yield imaging resolutions of about 20 nm, this resolution might not be sufficient for certain research questions. One such question is e.g. the presence of multiple ring-like structures of the DASH complex (part of the outer KT) around the kMT. While one or two rings were detected *in vitro* at high resolutions using EM and X-ray crystallography, none could be visualized *in vivo* using conventional fluorescence microscopy or SMLM [142, 143]. To improve the resolution of SMLM, we established a novel imaging technique called SExY in fission yeast, which combines PALM with ExM. In ExM the sample is linked to a swellable gel mesh, which physically expands upon incubation with deionized water or specific buffers and thus increases the resolution by the corresponding *in vivo* EF [153] (see figure 1.4). Therefore, pairing ExM with PALM yields improved resolutions to the single-digit nanometer regime. However, critical aspects are on the one hand an isotropic expansion of the whole sample and on the other hand a satisfactory protein retention yield, for which we optimized. In our final SExY protocol we achieved a 5-fold expansion of fission yeast cells with superior isotropy and twice the amount of retained fluorescence signal compared to the original protein retention expansion microscopy (proExM) protocol [172] (see figure 1 b-e in chapter 3).

4.2.1 Cell wall digestion of fission yeast

To remove the cell wall, we first tested different common cell wall removal enzymes for fission yeast and visualized the expanded cells expressing mEos2 in the cytosol. We found that while Zymolyase, Zymolyase in combination with Lysing enzyme, Snail enzyme and Lyticase yielded a partial hourglass-like expansion of fission yeast with the septum or former cytokinesis sites being left unexpanded, Lallzyme MMX, Chitinase and β-Glucoronidase expanded fission yeast fully (see figure 2 a and table S1 in chapter 3). The fission yeast septum forms a primary septum consisting of mainly β-(1,3)-glucan and a flanking secondary septum layer consisting of α(1,3)-glucan and branched β(1,6)-glucan at mid cell [228, 229]. While chitin synthase genes (chs1 and chs2) were detected in fission yeast, the function of particularly chs2 is still controversial [230, 231]. On one hand fission yeast chs2 was shown to localize to the growing septum edges in vegetative cells, and on the other hand chs2 was shown to have several mutations in locations crucial for chitin synthesis [230, 232, 233]. Additionally, chs1 is required in spore formulation as Δchs1 strains showed a sporulation phenotype [234]. The fact that we were able to evenly expand fission yeast using a Chitinase during cell wall digestion might indicate that some chitin is indeed present at the septum. At the same time as

we established SExY in fission yeast, another research group established a conventional 4x U-ExM protocol [185] for fission and budding yeast solely based on organic dyes [235]. Interestingly, they were able to expand fission yeast evenly by using Zymolyase in the cell wall removal step. However, this might be due to an additional subsequent fixation step using ice-cold acetone, which we believe might be enough to remove residual cell wall parts. Nevertheless, we decided to use Lallzyme MMX for the cell wall digestion step as it is the cheapest and most reliable alternative out of the three enzymes resulting in a complete expansion and does not need additional fixation steps [236].

4.2.2 Increasing the protein retention yield

To evaluate how much FP is retained after our initial proExM protocol containing a cell wall digestion step using Lallzyme MMX, we tagged the spindle pole protein sad1$^{SUN1/2}$ with the conventional FP mScarlet-I and read-out the fluorescent spot intensity of single sad1$^{SUN1/2}$ spots during mitosis after every step in the protocol. Here, we found that the protein retension yield after this initial ExM protocol was only 23% (see figure 1 e in chapter 3). We also found a decrease in fluorescence spot intensity for sad1$^{SUN1/2}$-mScarlet-I of 17% after permeabilization with Triton X-100 and another decrease of 22% after cell wall digestion using Lallzyme MMX compared to the signal detected after fixation with 3.2% para-formaldehyde and 0.1% glutaraldehyde (see figure S2 in chapter 3). Due to this we excluded a separate permeabilization step using Triton X-100 as we hypothesized that the cell membrane is sufficiently disintegrated during the fixation step with para-formaldehyde and the protein digestion step with the protein digestion buffer additionally containing 0.2% Triton X-100. Furthermore, we assumed that Lallzyme MMX might possess a proteinase activity, which we along with other cell wall digestion enzymes investigated by the colorimetric determination of released tyrosine during casein digestion [237, 238] and compared it to proteinase K (see figures 2 b and S3 in chapter 3). Released tyrosine binds to the Folin & Ciocalteu's Phenol reagent, which alters the solution from a yellow to blue color and thus shifts its absorption peak. Interestingly, we found that the proteinase activity for 1 U/mL of our freshly bought proteinase K stock is significantly reduced and only 64% of the expected 1 µmol of released tyrosine were detected. As a control, we also determined the protease activity of proteinase K in presence of the protease inhibitor phenylmethylsulfonylfluorid (PMSF). In this case we could not detect any proteinase activity, ruling out any errors in the protease activity assay. Due to our reduced proteinase K activity, we assumed that the previously reported impaired isotropy of ExM could be a result of varying effective proteinase K activities in different labs. We suggest checking its activity regularly as it might also degrade over time with multiple freezing and thawing cycles. From the tested cell wall enzymes only Lysing enzyme and Lallzyme MMX showed a significant proteinase activity, while Zymolyase and β-glucoronidase at 1 U/mL and even at higher concentrations of 50 U/mL did not. Lysing enzyme at a concentration of 0.1 U/mL exhibited a strong proteinase activity compared to proteinase K at a 10-fold higher concentration, which could again be inhibited in presence of PMSF. Although we detected a minor proteinase activity for Lallzyme at 10 mg/mL, which is the end concentration used in our cell wall digestion step, we continued its use as we assumed that we could reduce some of the pricier proteinase K in the protein digestion step. As we found no significant decrease in fluorescence spot intensity of sad1$^{SUN1/2}$-mScarlet-I after exclusion of a separate permeabilization step and the cell wall digestion using Lallzyme MMX, we assume that the proteinase activity in Lallzyme MMX might mainly digest proteins in the outer cell layers and not in the nucleus where sad1$^{SUN1/2}$ is localized (see figure S2 in chapter 2).

Protein digestion optimization

While homogenization using heat denaturation or treatment with sodium dodecyl sulfate (SDS) did result in expanded gels containing fission yeast cells, no fluorescence signal for sad1$^{SUN1/2}$-mScarlet-I or the green or red chromophore form of cytosolically expressed mEos2 could be detected (data not shown). However, we were able to expand fission yeast upon protein digestion with proteinase K. For this, we optimized the proteinase K concentration and found that the lowest possible effective concentration yielding an isotropic expansion of the gel and sample was 3 U/mL. Lower concentrations of proteinase K or a cell wall digestion of Lallzyme in presence of the proteinase inhibitor PMSF in combination with 3 U/mL proteinase K in the protein digestion step resulted in only partially expanded gels (data not shown). Therefore, we concluded that the protease activity of 3 U/mL proteinase K together with the detected protease activity in Lallzyme MMX are needed for a homogeneous expansion of fission yeast whilst retaining the maximum possible FP amount.

Gelation optimization

Since free radicals during the gelation of the PAA gel can reduce the protein retention yield, we attempted to introduce a milder gelation by adding the well-studied antioxidant glutathione (GSH), which serves as a highly efficient free radical scavenger. The added GSH can 'rescue' proteins by hydrogen-atom transfer (HAT), which places the radical on the sulphur moiety of the glutathione (GS·) and adds a hydrogen at the former radical site of the protein [239, 240]. Due to this, we tested the fluorescence spot intensity of sad1$^{SUN1/2}$-mScarlet-I after PAA gelation at different GSH concentrations, which we prepared fresh on the day of use. We found an increase of 26% in the gelation step with an addition of 0.05% GSH to the 10 min incubation step pre-gelation of tetramethylethylenediamine (TEMED), which serves as the gelation catalyst, and half the monomer solution (see figure 2 c in chapter 3). Thereafter, the remaining monomer solution and the radical starter ammonium persulfate (APS) were added and thoroughly mixed with the rest for gelation mix. Interestingly, no increase in fluorescence spot intensity could be detected for higher GSH concentrations and the PAA gel rigidity decreased with higher GSH concentrations until no gelation occurred for 0.4% GSH and higher (see figure 2 c). For an easier handing of the PAA gel, we decided to use 0.05% glutathione onward. We believe the lower PAA gel rigidity could stem from GSH additionally reacting with growing PAA radical chains and thus terminating them or two GSH radicals (GS·) reacting with each other and forming GSH disulphide (GSSG), which results in a decrease of available radicals. Both scenarios would lead to shorter PAA chains in the gel mesh. To summarize, we hypothesize that the improved microscale isotropy in our optimized SExY protocol stems from the dual effect of a more homogeneous protein digestion and a milder gelation with shorter PAA chains (see figure 1 d in chapter 3) and showed that our optimization attempts doubled the retained fluorescence signal.

4.2.3 Validation of critical factors for SExY

We verified an even expansion of the cytosol and the nucleus after treatment with the optimized SExY protocol by measuring the cell width of a fission yeast strain expressing the photoconvertible FP mEos2 [241] in the cytosol and the nuclear diameter by visualizing the nuclear pore protein Nup132 of non-expanded and expanded cells (see figure 1 b, c in chapter 3). For measurement of the nuclear diameter, we included only perfectly round nuclei in interphase, as the shape of the nucleus changes during the cell cycle. The ratio between expanded and non-expanded cells resulted in a similar macroscale EF of

4.92 for the cell width and 4.91 for the nuclear diameter, which shows an even macroscale expansion of different organells and stands in contrast to current methods combining expansion microscopy with SMLM that only yield a 3x expansion factor [188, 189]. Furthermore, we compared the cell boarders of cytosolically expressing mEos2 cells pre- and post-protocol optimizations and found less mEos2 strands linked to the PAA gel mesh outside of our cells post optimizations (see figure 1 d in chapter 3). We also analysed the distribution of mEos2 clusters within the cytosol pre- and post-optimization compared to non-expanded cells and found that, in contrast to post-optimization, pre-optimization cells show a relatively high variation from non-expanded cells. We attribute these findings to a more homogeneous microscale expansion resulting from an altered gelation step and the determination of the effective protease activity of proteinase K in the protein digestion step. For our initial proExM protocol, for which we only added the cell wall digestion using Lallzyme MMX for fission yeast, we found that the fluorescent signal retained from the spindle pole protein sad1$^{SUN1/2}$ tagged with mScarlet-I in mitosis after this initial expansion protocol was only 23% compared to the fluorescence signal of fixed sad1$^{SUN1/2}$-mScarlet-I (see figure 1 e in chapter 3). However, after our optimizations we found that 46% of our sad1$^{SUN1/2}$-mScarlet-I signal was retained.

4.2.4 Critical aspects for correlative ExM and PALM

To combine PALM with our optimized ExM protocol, we first tested different commonly used FPs in PALM and found that the photoactivatable FP PAmCherry expressed in the cytosol showed no fluorescence activation after fixation with paraformaldehyde and glutaraldehyde (data not shown), which is in accordance with previous findings claiming a reduction in PAmCherry activation after fixation with low concentrations of glutaraldehyde [242]. Fortunately, the green-to-red photoconvertible FP mEos2 survived the ExM treatment(see figures 1 b, figure 2 a and figure 3 a-c, e-f in chapter 3). Since PAmCherry was derived from mCherry it is not surprising that we also detected a severe fluorescence loss after fixation of nuclear pores tagged with mCherry (data not shown) [202]. Due to this, we tagged different high and low abundant proteins with mEos2 to validate our imaging sensitivity and FP survival during SExY imaging. We successfully imaged high abundant proteins such as cytosolically expressed mEos2, the DNA binding protein cbp1^{CENP-B} and the cnp1^{CENP-A} loading kinetochore protein mis16 as well as low abundant proteins such as the kinetochore protein cnp1^{CENP-A}, which is only present in several tens to a few hundred copies per cell [15, 36] at higher resolution using SExY (see figure 3 a-c, e-f in chapter 3). Additionally, we visualized DNA as a highly abundant target and the spindle pole protein sad1$^{SUN1/2}$ as well as the nuclear pore protein Nup132 as low abundant targets at lower resolution using conventional fluorescence microscopy (see figure 3 c-f in chapter 3). The recording of a PALM movie can take up to several minutes in which the sample can physically drift on the imaging stage. To correct for this drift, the detected signal itself is used for a cross-correlation drift correction [243], which was previously also used in ExSTORM and Ex-SMLM [188, 189]. While cross-correlation stably corrects the drift of high abundant proteins such as e.g. microtubules, the correction of low abundant proteins is insufficient. Therefore, we simultaneously imaged the sample with several cytosolically expressing mEos2 cells as markers for cross-correlation in the same plane, which allowed for a reliable drift correction. With the combination of ExM with PALM (expansion photoactivated localization microscopy (ExPALM)) we closed the gap of available SRM and ExM combinations and broadened the toolbox of the ExM field for microbiology (SExY). On top of that SExY also has a higher EF (~5x) compared to Ex-SMLM and ExSTORM (~3x), which in some cases might diminish the need for additional expansions of the sample by iterative ExM approaches.

4.2.5 Outlook

One way to further improve ExPALM and SExY would be the implementation of a non-radical gelation, as it was shown, that more fluorescence signal could be retained compared to the conventional radical polymerization of PAA gels [161]. However, the monomer building blocks needed are custom synthesized and hard to come by, which could exacerbate the implementation and continued use of a non-radical gelation.

Furthermore, other mEos-like FPs such as e.g. Dendra2 or Maple could be tested for survival of the ExPALM or SExY protocol as well as new proteinase- or heat-resistant photoconvertable FPs could be designed to expand the palette of available photoswitchable FPs suitable for ExPALM or SExY protocols [244, 245].

Since PAmCherry, which was used to label the centromeric reference protein in our 3C-strain library, did not survive the SExY protocol using glutaraldehyde in the fixation step, we will not be able to measure cnp1$^{\text{CENP-A}}$-POI distances with our initial multi-color PALM scheme, which will limit further studies to a single target imaged at super-resolution until other suitable FPs have been designed.

As this technique was initially designed to investigate the KT nanostructure at higher resolutions, it would be interesting to expand the DASH complex and examine, if the complex forms one or two rings around the kMT *in vivo* as it was shown to do *in vitro*. While our multi-color SMLM approach could not resolve a ring-like structure of the DASH complex, as previously mentioned, the extracted copy numbers suggest around 60 dam1 molecules per centrosome, which attributes to 20 dam1 molecules per microtubule. From crystallography data it was previously shown that 17 DASH complexes form a ring around one kMT [142]. With the use of SExY this ring-like structure might be visualized for *in vivo* the first time.

SExY could also potentially resolve the thick MT bundle in mitosis, which consists of kMTs and antiparallel microtubule fibers connecting the opposite SPBs, and give us insights into how many kMTs attach to a single centromere. As we on one hand could not resolve this thick MT bundle using PALM alone (see figure 4.1), yet on the other hand it was shown, that the resolution in EM is sufficient to resolve this bundle, we believe that SExY is the optimal technique to answer this question, as it combines a single digit resolution with the specific, high-contrast read-out of the fluorescent label.

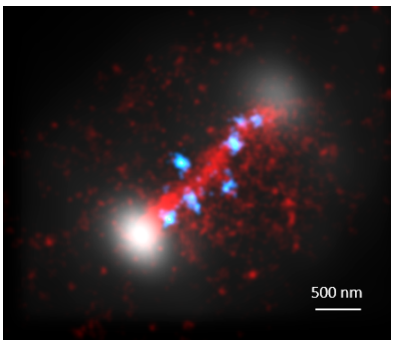

Figure 4.1: SMLM is unable to resolve single kMTs within the MT bundle present during mitosis in fission yeast. The spindle pole protein sad1 is depicted in grey, cnp1$^{\text{CENP-A}}$ in blue and the MT subunit α-tubulin (atb2) in red. Scale bar 500 nm. Image recorded by Jannik Winkelmeier.

Appendix

APPENDIX A

Other published work

A.1 Novel tool development for SMLM imaging of dense structures

This chapter is written in the style of a manuscript and was published as a research article in *Nature Communications* in 2018. I contributed to this work by designing and executing some of the cloning work and analysing some of the acquired data.

In this publication, we establish and benchmark a novel nanobody for SMLM labeling of dense multi-protein structures. We also show its applicability to track diffusing proteins using single-particle tracking photoactivated localization microscopy (sptPALM).

nature COMMUNICATIONS

ARTICLE

DOI: 10.1038/s41467-018-03191-2 OPEN

A peptide tag-specific nanobody enables high-quality labeling for dSTORM imaging

David Virant[1], Bjoern Traenkle[2], Julia Maier[2], Philipp D. Kaiser[3], Mona Bodenhöfer[3], Christian Schmees[3], Ilijana Vojnovic[1], Borbála Pisak-Lukáts[1], Ulrike Endesfelder[1] & Ulrich Rothbauer[2,3]

Dense fluorophore labeling without compromising the biological target is crucial for genuine super-resolution microscopy. Here we introduce a broadly applicable labeling strategy for fixed and living cells utilizing a short peptide tag-specific nanobody (BC2-tag/bivBC2-Nb). BC2-tagging of ectopically introduced or endogenous proteins does not interfere with the examined structures and bivBC2-Nb staining results in a close-grained fluorophore labeling with minimal linkage errors. This allowed us to perform high-quality dSTORM imaging of various targets in mammalian and yeast cells. We expect that this versatile strategy will render many more demanding cellular targets amenable to dSTORM imaging.

[1] Department of Systems and Synthetic Microbiology, Max Planck Institute for Terrestrial Microbiology and LOEWE Center for Synthetic Microbiology (SYNMIKRO), Karl-von-Frisch Strasse 16, Marburg 35043, Germany. [2] Pharmaceutical Biotechnology, Eberhard Karls University Tuebingen, Markwiesenstrasse 55, Reutlingen 72770, Germany. [3] Natural and Medical Sciences Institute at the University of Tuebingen, Markwiesenstrasse 55, Reutlingen 72770, Germany. These authors contributed equally: David Virant, Bjoern Traenkle, Ulrike Endesfelder and Ulrich Rothbauer. Correspondence and requests for materials should be addressed to U.E. (email: ulrike.endesfelder@synmikro.mpi-marburg.mpg.de) or to U.R. (email: ulrich.rothbauer@uni-tuebingen.de)

Fluorescence-based super-resolution microscopy (SRM) is becoming increasingly applied in cell biology. Single-molecule localization microscopy (SMLM) techniques, such as (direct) stochastic optical reconstruction microscopy ((d) STORM) provide outstanding spatial resolutions and have enabled unprecedented insights into the organization of subcellular components[1–3]. However, the quality and value of SMLM imaging can be limited due to poor photon emission or detection efficiency, low fluorophore labeling densities, linkage errors or steric hindrances[4–6]. Most current SMLM labeling approaches employ antibodies or recombinant proteins either fused to photoactivatable fluorescent proteins (FPs) or fluorogen-labeling enzymes, such as the Halo-, CLIP-, or SNAP-tag[7–10]. While conventional antibodies introduce significant linkage errors by displacing the fluorophore from the target, large protein/enzyme tags can affect expression, cellular localization, folding and/or function of the respective fusion protein[11–13]. Although small peptide tags, such as FLAG-, HA-, or Myc-tag[14–16] are available, those epitopes often have to be arranged in multiple arrays to recruit medium-affine binding antibodies[17] and thus do not provide dense labeling sufficient for high-quality SRM.

Instead of using antibodies, a 15-amino-acid peptide-tag can be visualized by high-affinity fluorescently labeled monomeric streptavidin[18], which, however, can be affected by the binding of endogenously biotinylated proteins. Alternatively, reversibly on- and off-binding labels in point accumulation for imaging of nanoscale topography (PAINT) microscopy allow for a continuous and therefore ultra-high density readout as they are not limited by a predefined fluorophore tagging pattern[19]. Yet, this approach can only be used for distinguishable structures like membranes or DNA combined with illumination-confined arrangements, such as in surface-near or lightsheet illuminations[20]. The visualization of other structures by PAINT approaches relies on a specific labeling commonly achieved by DNA-PAINT[21, 22].

As a promising substitute for conventional antibodies, small-sized nanobodies (antibody fragments derived from heavy-chain-only camelid antibodies) coupled to organic dyes were recently introduced for SRM. Nanobodies targeting native proteins, such as components of the nuclear pore complex, tubulin, or vimentin were described for dSTORM imaging[23–25]. Despite their capability to directly probe endogenous antigens, the de novo generation of gene-specific nanobodies and their validation for SRM imaging purposes is cumbersome and time-consuming[26, 27], which is reflected by the fact that only a very limited number of SRM-compatible nanobodies are available by now[25]. Due to their applicability for nanoscopy of widely used FP-fusions, GFP-, and RFP-nanobodies became very popular tools for SMLM[28, 29]. However, this strategy relies on the correct expression of FP-fusions and does not cope with problems arising from mislocalization or dysfunction[12, 13, 30]. Thus, nanobodies directed against short and inert tags might prove advantageous for SRM.

Here we introduce a versatile labeling and detection strategy comprised the short and inert BC2 peptide-tag (PDRKAAVSHWQQ) and a corresponding high-affinity bivalent nanobody (bivBC2-Nb) for high-quality dSTORM imaging. We demonstrate the benefits of our approach for close-grained fluorophore labeling with minimal linkage error of various ectopically introduced and endogenous targets in fixed and living cells.

Results

Development of a dSTORM suitable BC2-tag/bivBC2-Nb system. As originally described, we first labeled the BC2-Nb at accessible lysine residues by N-hydroxysuccinimide (NHS) ester fluorophores, such as Alexa Fluor 647 (AF647)[31]. While BC2-$Nb_{AF647\ (NHS)}$ is sufficient for wide-field microscopy (Fig. 1a, left panel, Supplementary Fig. 1a, b), dSTORM imaging of BC2-tagged proteins revealed a rather low-staining efficiency resulting in inferior structural labeling coverage (Fig. 1b, left panel). Thus, we analyzed the binding properties of a bivalent format of the BC2-Nb (bivBC2-Nb) (Fig. 1a, right panel). We assessed its binding kinetics by biolayer interferometry (BLI) and observed a considerably reduced dissociation rate compared to monovalent BC2-Nb (Supplementary Fig. 1c). Notably, this decrease in dissociation rate is not caused by simultaneous binding of the bivBC2-Nb to two BC2 epitopes as confirmed by a BLI assay using a tandem-BC2-tag of two consecutively linked BC2 epitopes (BC2-BC2-tag) (Supplementary Fig. 1d).

Nevertheless, antigen labeling using the bivBC2-Nb conjugated to NHS-ester fluorophores (bivBC2-$Nb_{AF647\ (NHS)}$) did not yield the expected visual improvement of staining specificity (Fig. 1a, right panel). Considering the crystal structure[31], we designed a site-directed, enzymatic coupling strategy, which should not affect the paratope and binding properties of bivBC2-Nb. Using the Sortase A system, we linked peptides conjugated to a single-AF647 fluorophore in a defined 1:1 ratio to the C-terminus of bivBC2-Nb (bivBC2-$Nb_{AF647\ (sort)}$)[32, 33]. This approach significantly improved the staining specificity by a factor of two compared to bivBC2-$Nb_{AF647\ (NHS)}$ (Fig. 1a, right panel, Fig. 1c and Supplementary Fig. 1a, b, e). An exemplary dSTORM image of a HeLa cell transiently expressing $vimentin_{BC2T}$ and stained with the bivBC2-$Nb_{AF647\ (sort)}$ illustrates the remarkable quality of the BC2-tag/bivBC2-Nb labeling strategy (Fig. 1b, right panel). For a better understanding bivBC2-$Nb_{AF647\ (sort)}$ is referred to bivBC2-Nb_{AF647} in the following.

Since the BC2-Nb was originally developed against β-catenin[34], we assessed the influence of the background staining of endogenous β-catenin on the labeling quality. To distinguish background due to general unspecific staining from additional β-catenin staining, we compared HeLa cells (not expressing any GFP epitope) stained with a GFP-targeting nanobody (GFP-Nb_{AF647}) to HeLa cells stained with bivBC2-Nb_{AF647}. Further, we performed bivBC2-Nb_{AF647} staining in HeLa cells transiently expressing the non-structural, autophagosomal marker protein LC3B fused to the BC2-tag ($_{BC2T}$LC3B), which is - in the absence of autophagy- homogeneously distributed throughout the cytoplasm. By analyzing the dSTORM data using DBSCAN clustering[35], we measured a slightly increased level of 1.7 (±0.3 S.D.) nanobodies per square micrometer for bivBC2-Nb_{AF647} compared to the unspecific background staining of 0.61 (±0.03 S.D.) GFP-Nb_{AF647} per μm^2. However, this level is considerably lower compared to 7.2 (±1.3 S.D.) bivBC2-Nb_{AF647} per μm^2 which we obtained for the staining of $_{BC2T}$LC3B expressing cells (Fig. 1d, Supplementary Fig. 2a). We then compared signal intensities derived from bivBC2-Nb_{AF647}-stained HeLa cells, which were either left untreated or incubated with CHIR99021 (CHIR) to accumulate endogenous β-catenin[34]. While immunolabeling with a β-catenin-specific antibody showed a strong enrichment in CHIR-treated cells (Supplementary Fig. 2b), dSTORM imaging revealed only a minor increase of bivBC2-Nb_{AF647} localizations (Supplementary Fig. 2c, left panel). Moreover, in CHIR-treated HeLa cells transiently expressing $vimentin_{BC2T}$, the nanobody signal was almost exclusively detectable at vimentin fibers (Supplementary Fig. 2c, right panel). Overall, bivBC2-Nb_{AF647} staining resulted in 36 (±2 S.D.) localizations per μm^2 for untreated HeLa cells, 133 (±5 S.D.) localizations per μm^2 for CHIR-treated HeLa cells, 2493 (±285 S.D.) localizations per μm^2 for HeLa-$vimentin_{BC2T}$ cells and 2490 (±456 S.D.) localizations per μm^2 for CHIR-treated HeLa-$vimentin_{BC2T}$ cells (Supplementary Fig. 2d). From this we conclude that even if present at high

levels, the BC2-epitope of β-catenin has a negligible impact on staining of ectopically introduced antigens.

For a stoichiometric quantification of the labeling quality of the BC2-tag/bivBC2-Nb detection system, we utilized the *Escherichia coli* protein ferritin (FtnA) recently described as a homo-oligomeric protein standard of 24 subunits[36]. We expressed BC2-tagged, as well as SNAP-tagged FtnA-24mers in U2OS cells and performed dSTORM imaging on cell lysates immobilized on coverslips[36]. By measuring single-AF647 blinking events, we obtained the parameters of the corresponding log-normal distribution ($\mu = 5.68$, $\sigma = 0.4$), which describes the probability distribution of single-molecule fluorescence intensities (Supplementary Fig. 3a). We then measured the fluorescence intensities of immobilized FtnA oligomers labeled with the BC2-tag/bivBC2-Nb or SNAP-tag system. We compared these distributions to the expected fluorescence intensity distributions of fully labeled FtnA-24mers, calculated from the single-molecule fluorescence intensity distribution and the degree of labeling of each component (Methods section). As a result, the BC2-tag/bivBC2-Nb FtnA-oligomer staining revealed a completeness of labeling of

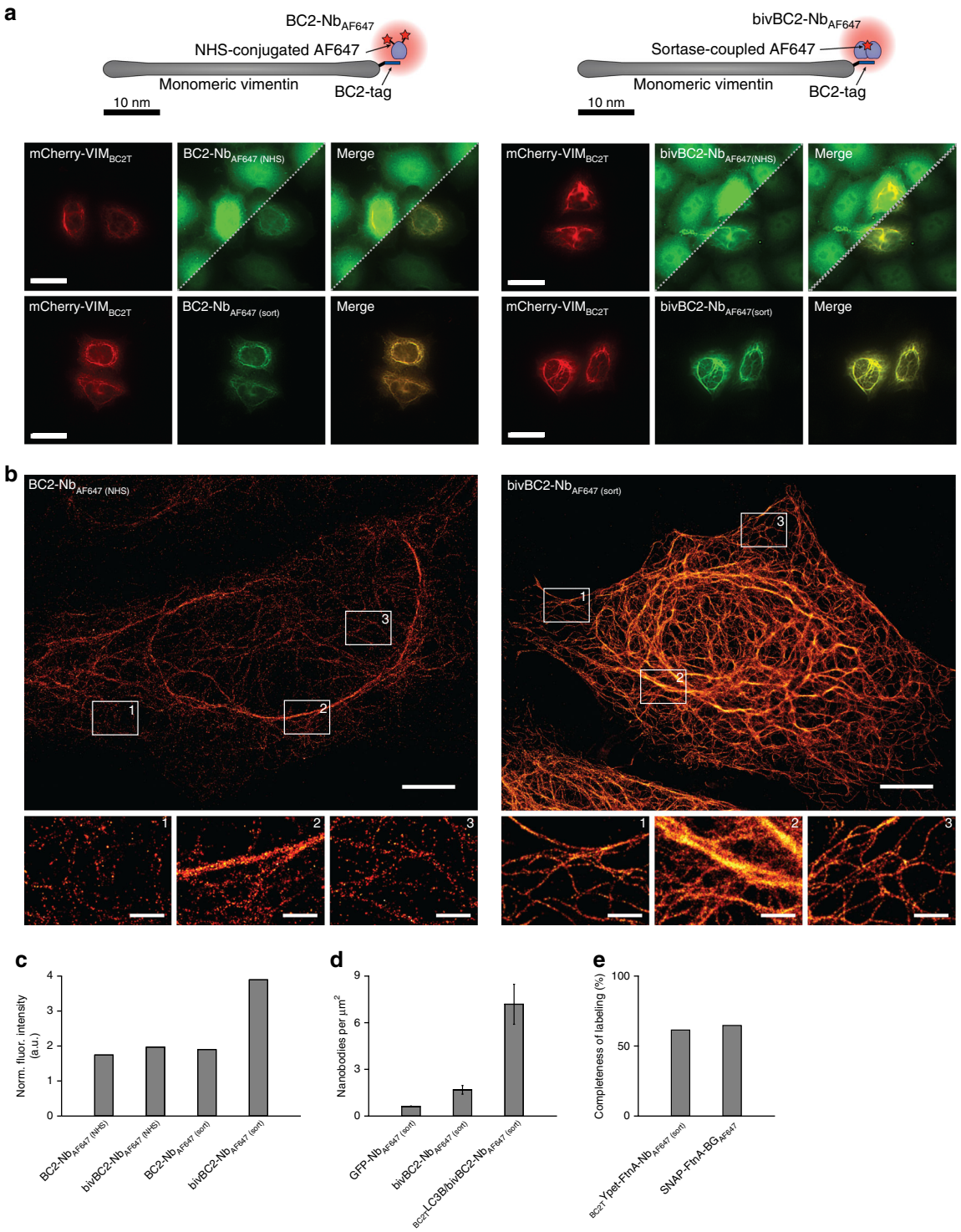

61.4% which competes with the covalent SNAP-tag FtnA-staining efficiency of 64.7% (Fig. 1e, Supplementary Fig. 3b) and outcompetes photoactivation/photoconversion efficiencies of fluorescent proteins[37]. Notably, our observation of a rather low efficiency of about 65% for the SNAP-tag labeling is in agreement with reported assessments[36, 38], and conference presentations by K. Yserentant (2017).

Comparison of different labeling strategies for SMLM. As genetic tagging of structural proteins like vimentin often impairs their structure and function[39, 40], we evaluated the influence of the short BC2-tag on vimentin structure formation and compared the BC2-tag/bivBC2-Nb detection system with established strategies focusing on image quality and apparent organization of the vimentin network. We performed SMLM on native vimentin in comparison to vimentin fused to photoactivatable mCherry (PAmCherry-vimentin), eGFP (GFP-vimentin), or the BC2-tag (Fig. 2a, b). For our studies, we transiently expressed the corresponding proteins for 24 h in HeLa cells followed by chemical fixation of the cells. Native vimentin was visualized with the recently described vimentin-specific nanobody bivVB6-Nb_{AF647}[25, 41], while PAmCherry-vimentin was mapped directly. The other constructs were labeled with the nanobodies GFP-Nb_{AF647} or bivBC2-Nb_{AF647}, respectively. Image analysis of the vimentin network visualized by the different labeling strategies revealed considerable phenotypic differences (Fig. 2b, c; images of all cells quantitatively analyzed Supplementary Fig. 4a–d; analysis routine Supplementary Fig. 4e and Methods section). 94% of native vimentin fibers labeled with the bivVB6-Nb_{AF647} showed widths lower than 150 nm. In contrast, cells with incorporated PAmCherry-vimentin were smaller and showed a high percentage (20%) of thick vimentin bundles above 150 nm width, while in GFP-vimentin expressing cells more than 96% of all detectable vimentin fibers had widths below 75 nm (Fig. 2c). Compared to the N-terminally labeled counterparts, cells expressing vimentin-PAmCherry displayed a highly similar phenotype whereas cells expressing vimentin C-terminally fused to GFP (vimentin-GFP) showed an even more severely fragmented vimentin network (Supplementary Fig. 5). Obviously, both type and position of the FP affects the formation of the vimentin network and induce altered cellular phenotypes. The various observed morphological alterations are likely caused by several mislocalization and self-oligomerization artifacts induced by the different FP moieties derived either from jelly fish (GFP) or red corals (DsRed)[40, 42]. Notably, no phenotypic changes or significant differences in the abundance of fiber widths were detected between native and BC2-tagged vimentin (96% of all fibers below 150 nm, 4% above 150 nm; Fig. 2b, c and Methods section).

We then assessed the SMLM image quality achievable by the different labeling approaches. The quality is dependent on two main factors; (i) the optical resolution dictated by the precision with which fluorescent spots can be localized, and (ii) the structural resolution determined by the labeling density (coverage) and the physical distance between fluorophore and target (linkage error). We assessed these parameters for each analyzed fiber individually. The localization precision was calculated by a Nearest Neighbor based Analysis (NeNA)[43], the labeling density was determined by the lengthwise fluorescent signal coverage along each fiber, and the linkage error by quantifying the apparent width of fibers of the smallest fiber category. For further comparison, we calculated the Fourier Image REsolution (FIRE) values[44] (see Supplementary Note 1). Since the readout of all three nanobody labeling strategies relies on the same bright fluorophore (AF647), NeNA yielded the same optical resolution statistics with a mean NeNA localization precision of about 9–12 nm. The fluorescent-protein PAmCherry has a lower photon yield and achieves an average NeNA value of 17 nm (Supplementary Fig. 6). The structural resolution as assessed by the different labeling coverage statistics revealed significant differences (Fig. 2c, Supplementary Fig. 6 and Methods section). For PAmCherry-vimentin, we observed the lowest coverage among all labeling strategies for thin fibers, and a maximum coverage of ~75% for thick fibers, which is likely due to inefficient chromophore formation and photoactivation. The low coverage of ~50% for the GFP-Nb is more likely explained by a steric hindrance in incorporating GFP-tagged molecules into the native vimentin network, which is in line with our observation of only thin fibers. The highest labeling coverage was observed for bivBC2-Nb with a coverage of ~80% for fibers below 75 nm width, and nearly full coverage of fibers exceeding a width of 150 nm. For thin fibers it exceeds the coverage obtained with the bivVB6-Nb for native vimentin, which might be due to a reduced accessibility of the native epitope within assembled vimentin filaments. To assess the impact of the size of the labeling probe on the structural resolution, we compared our bivBC2-Nb-based approach with conventional, monoclonal antibody staining (Supplementary Fig. 7a). Antibody labeling resulted in nearly complete coverage of thin vimentin fibers (>75 nm) (Supplementary Fig. 7b), and the AF647-based readout resulted in the same localization precision and optical

Fig. 1 Comparison and characterization of BC2-nanobody (BC2-Nb) formats for wide-field and dSTORM imaging. **a** Schematic illustration of the BC2-Nb dye-conjugation strategies. Monovalent and bivalent BC2-Nbs were either conjugated with Alexa Fluor 647 (AF647) via N-hydroxysuccinimide (NHS) ester (left panel) or linked to AF647 by enzymatic sortase coupling (right panel). Wide-field imaging of chemically fixed HeLa cells expressing mCherry-$vimentin_{BC2T}$ (mCherry-VIM_{BC2T}) stained with modified BC2-Nbs. Monovalent versions of the BC2-Nbs (NHS- and sortase-coupled) are depicted on the left panel, corresponding bivBC2-Nbs are displayed on the right side. Stainings with NHS-conjugated nanobodies are shown in two different image contrasts, the upper half in the same brightness and contrast as the sortase-coupled nanobodies; in the lower half with an adjusted contrast. Scale bars, 25 µm. **b** Representative dSTORM images of chemically fixed HeLa cells expressing $vimentin_{BC2T}$, stained with the monomeric NHS-conjugated BC2-$Nb_{AF647\ (NHS)}$ (left) and the sortase-coupled bivBC2-$Nb_{AF647\ (sort)}$ (right). Scale bars, images 5 µm, insets 1 µm. Image reconstruction details are given in Methods section. **c** Assessment of staining quality in wide-field fluorescence imaging. Labeling of the different nanobody formats was quantified by calculating the ratio of the signal intensity of mCherry-VIM_{BC2T} expressing cells to non-transfected cells (background), (BC2-$Nb_{AF647\ (NHS)}$: $n = 115$; bivBC2-$Nb_{AF647\ (NHS)}$: $n = 134$; BC2-$Nb_{AF647\ (sort)}$: $n = 150$; bivBC2-$Nb_{AF647\ (sort)}$: $n = 195$) (Methods section, Supplementary Fig. 1). **d** Assessment of bivBC2-Nb_{AF647} staining of endogenous β-catenin. Bar chart summarizes measured nanobody per μm^2 values for untransfected chemically fixed HeLa cells stained with GFP-Nb_{AF647} or bivBC2-Nb_{AF647} in comparison to chemically fixed HeLa cells transiently expressing $_{BC2T}$LC3B stained with bivBC2-Nb_{AF647}, errors given as standard deviation (S.D.), $N = 3$ cells for each condition (Methods section, Supplementary Fig. 2). **e** Quantification of completeness of labeling for the bivBC2-Nb and SNAP-tag labeling systems using FtnA-oligomers of 24 subunits. Bar chart summarizes median values of FtnA-24mer fluorescence intensities as percentage of theoretical maxima (Methods section, Supplementary Fig. 3)

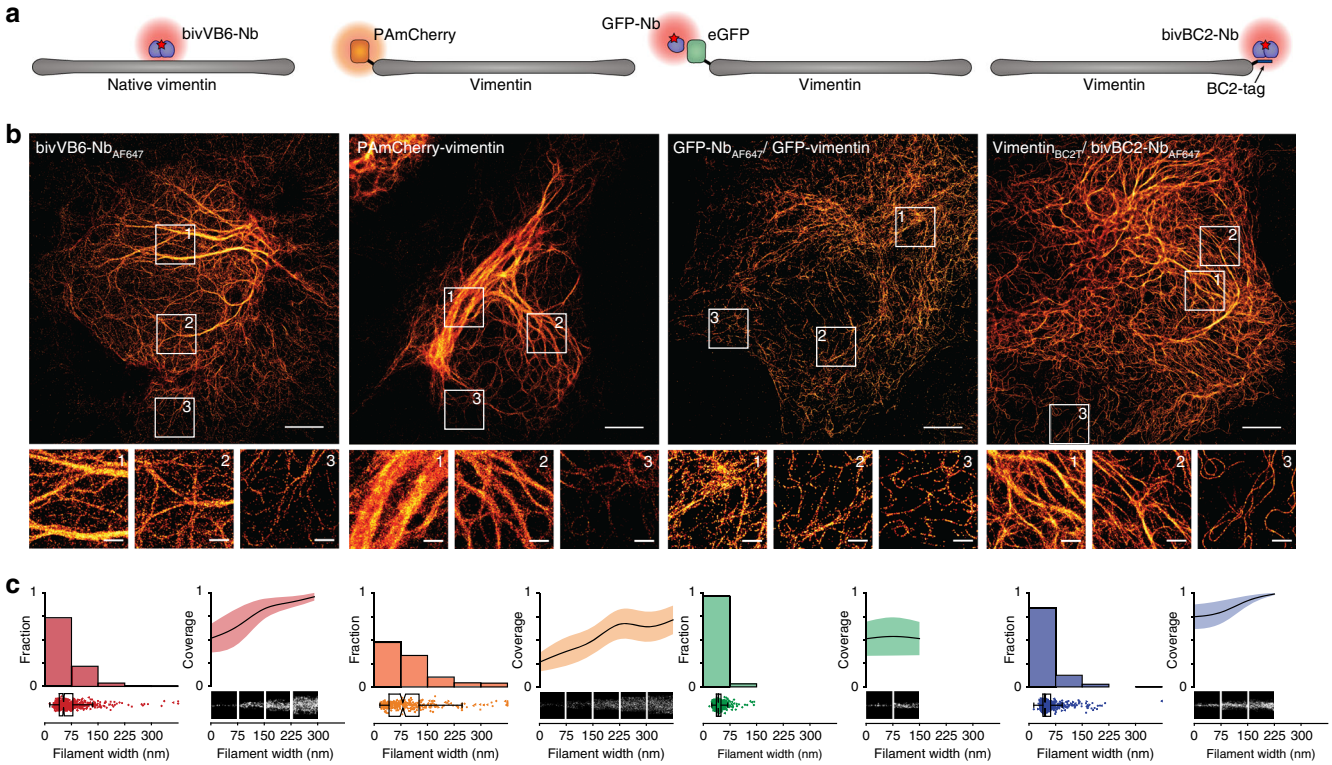

Fig. 2 Super-resolution imaging and analysis of differently labeled vimentin constructs. **a** Schematic illustration of labeling strategies used for comparative SRM imaging of native or ectopically expressed vimentin. **b** Representative PALM/dSTORM images of chemically fixed Hela cells expressing the corresponding constructs outlined in **a** or native vimentin (left panel). Insets show magnifications of representative vimentin filaments of varying thickness (1—thick, 2—medium, 3—thin, peripheral). Scale bars, 5 µm in main images, 1 µm in insets. **c** Filament widths as histograms (left) with a bin size of 75 nm (*x*-axis) plotted against relative fraction (*y*-axis). Full data are represented underneath the histograms as box + scatter plots with the same *x*-axis. The box marks the three quartiles and the whiskers mark 95% of all the data. The average lengthwise fluorophore coverage was calculated for each bin and plotted (right) as mean filament width (black line) and standard deviation (colored area) against relative fraction covered by fluorophores (*y*-axis). Width and lengthwise fluorophore coverage were analyzed for a total of 676 (bivVB6-Nb$_{AF647}$), 295 (PAmCherry), 724 (GFP-Nb$_{AF647}$), and 620 (bivBC2-Nb$_{AF647}$) filaments, $N = 5$ cells for each condition, cells, and selected filaments are shown in Supplementary Fig. 4. Image reconstruction details are given in Methods section

resolution statistics (Supplementary Fig. 7c). Despite the high-labeling coverage, the antibody-mediated displacement of the fluorophore led to an increased linkage error. Accordingly, we measured an average width of ~55 nm for thin vimentin fibers probed with the antibody, whereas a smaller apparent width of ~40 nm was observed with bivBC2-Nb (Supplementary Fig. 7c).

Detection of various cellular targets with the bivBC2-Nb. Next we analyzed whether the BC2-tag/bivBC2-Nb detection system is transferable to other structural proteins. To test whether orientation of the BC2-tag affects the incorporation of the recombinant protein into endogenous structures, we transiently expressed cDNAs of mouse *TUBA1B*, human *LMNB1*, or *ACTB* either comprising the BC2-tag on the N- or the C-terminus in different cell lines followed by detection with bivBC2-Nb$_{AF647}$. As exemplarily shown for tubulin alpha-1B, C-terminal addition of the BC2-tag yielded more distinct microtubule structures compared to the N-terminally tagged version (Supplementary Fig. 8). For lamin B1, we observed no differences regarding the tag position whereas ectopically expressed β-actin is only incorporated into the actin cytoskeleton when the BC2-tag is located at the N-terminus, which is in accordance to previously tested tagging approaches[45]. dSTORM imaging of HeLa cells expressing either lamin$_{BC2T}$ or $_{BC2T}$actin, as well as U2OS cells transiently expressing tubulin$_{BC2T}$ revealed that BC2-tagged proteins are efficiently incorporated in the corresponding structures and could be imaged at high-resolution reaching localization precisions of 9–12 nm as previously shown for vimentin$_{BC2T}$ (Fig. 3a–c, Supplementary Fig. 9). As individual microtubules have a defined diameter of 25 nm these structures serve as an experimental benchmark for SRM[24, 28, 46]. Simulations on nanobody labeling of microtubules using a maximal probe displacement of 5 nm and a localization precision cutoff of 10 nm have yielded an apparent fiber width of about 40 nm[24], which is in perfect agreement to our measured fiber width of 38.2 ± 9.2 nm (Supplementary Fig. 9a). Moreover, a detailed analysis of individual actin fibers comprising transiently expressed $_{BC2T}$actin showed comparable labeling densities as previously obtained for vimentin$_{BC2T}$ (Supplementary Fig. 9b-d).

Additionally, we used our approach to visualize non-structural proteins, namely the autophagosomal marker protein LC3B and the extracellular membrane marker GFP-GPI[47, 48]. To monitor induction of autophagy, we co-expressed $_{BC2T}$LC3B and GFP-LC3B in HeLa or A549 cells followed by incubation with DMSO or rapamycin to induce autophagosome formation. Wide-field imaging of chemically fixed cells, stained with bivBC2-Nb$_{AF647}$, showed a clear co-localization of GFP and nanobody signals at defined spots in rapamycin-treated cells, indicating correct localization of BC2-tagged LC3B at autophagosomes[47, 49]

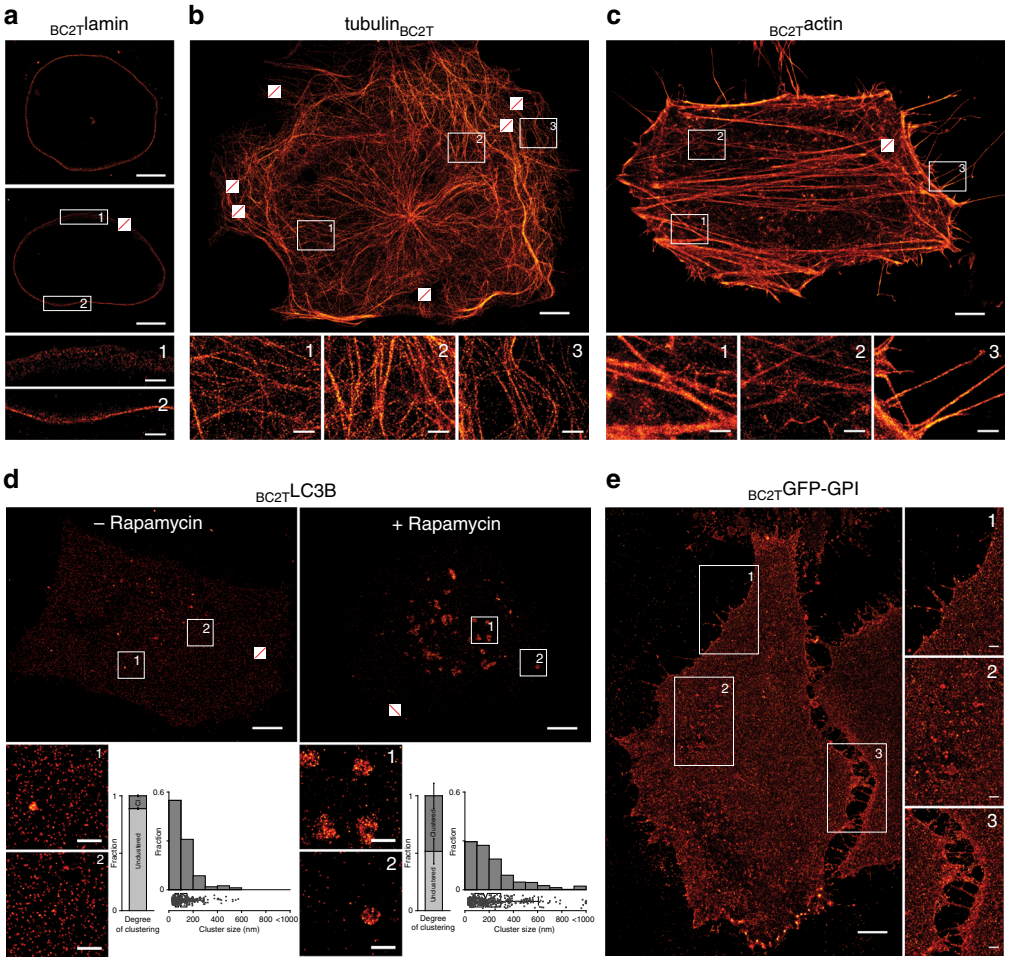

Fig. 3 Super-resolution imaging of transiently expressed BC2-tagged proteins in chemically fixed cells. Representative dSTORM images of a **a** HeLa cell expressing $_{BC2T}$lamin, **b** U2OS cell expressing tubulin$_{BC2T}$ (filament width statistics in Supplementary Fig. 9a), **c** HeLa cell expressing $_{BC2T}$actin (coverage statistics in Supplementary Fig. 9b), **d** HeLa cells expressing $_{BC2T}$LC3B either left untreated or treated with rapamycin. Bar charts represent the degree of clustering, given as a relative fraction of cluster points versus noise points, errors given as standard deviation (S.D.). Histograms represent cluster diameters as determined by DBSCAN analysis with a bin size of 100 nm (*x*-axis) plotted against relative fraction (*y*-axis). Full data are represented underneath the histograms as box + scatter plots with the same *x*-axis. The box marks the three quartiles and the whiskers mark 95% of all the data. Total number of clusters $n = 342$ in non-treated cells, $n = 405$ in treated cells, $N = 3$ cells for untreated cells and $N = 4$ cells for rapamycin-treated cells (Supplementary Fig. 11), and **e** HeLa cells expressing $_{BC2T}$GFP-GPI. All cells were stained with bivBC2-Nb$_{AF647}$ (Methods section). Scale bars, images 5 µm, insets 1 µm. Crossed out rectangles mark the position of fiducial markers used for drift correction. Image reconstruction details are given in Methods section

(Supplementary Fig. 10a). Further, dSTORM imaging and subsequent DBSCAN cluster analysis of newly formed autophagosomes in $_{BC2T}$LC3B expressing cells after incubation with rapamycin revealed diameters of ~0.3–1.0 µm for these foci (Fig. 3d, Supplementary Fig. 11, Methods section), which is in accordance to previous findings[50, 51]. For BC2-tagged GFP-GPI ($_{BC2T}$GFP-GPI), we observed a clear co-localization of the nanobody and the GFP signal at the plasma membrane in chemically fixed HeLa cells (Supplementary Fig. 10b). Notably, with dSTORM, we detected a defined spatial organization of $_{BC2T}$GFP-GPI, e.g., the formation of small clusters and enrichment of $_{BC2T}$GFP-GPI molecules at cell–cell contacts, compared to a diffraction-limited, homogenous distribution observable by wide-field microscopy (Fig. 3e, Supplementary Fig. 10b).

Visualization of endogenous proteins with the bivBC2-Nb. To utilize the BC2-tag as an endogenous marker under native promotor expression, we first replaced the gene coding for the nuclear DNA-binding protein cbp1 at its endogenous loci in the fission yeast *Schizosaccharomyces pombe (S. pombe)* by a C-terminally BC2-tagged version (cbp1$_{BC2T}$). Cells expressing cbp1$_{BC2T}$ show growth rates comparable to wild type (wt) and exhibit no morphological changes (Supplementary Fig. 12a, b). As *S. pombe* possesses a thick cell wall and a highly packed cellular environment, any immunofluorescence-based SRM approach suffers from high-unspecific background and low-staining quality. Notably, by staining endogenously expressed cbp1$_{BC2T}$ utilizing the bivBC2-Nb$_{AF647}$ we were now able to visualize an endogenous nuclear protein in *S. pombe* by dSTORM imaging (Supplementary Fig. 12a). Second, we stably introduced the coding sequence of the BC2-tag under the native β-actin promotor at the 5′-end of the first exon of endogenous β-actin in HeLa and A549 cells using the CRISPR/Cas9 technology. After monoclonal selection of cells exhibiting a heterozygous integration of $_{BC2T}$actin (HeLa-$_{BC2T}$ACTB; A549-$_{BC2T}$ACTB, Methods section) we treated both cell lines with transforming growth

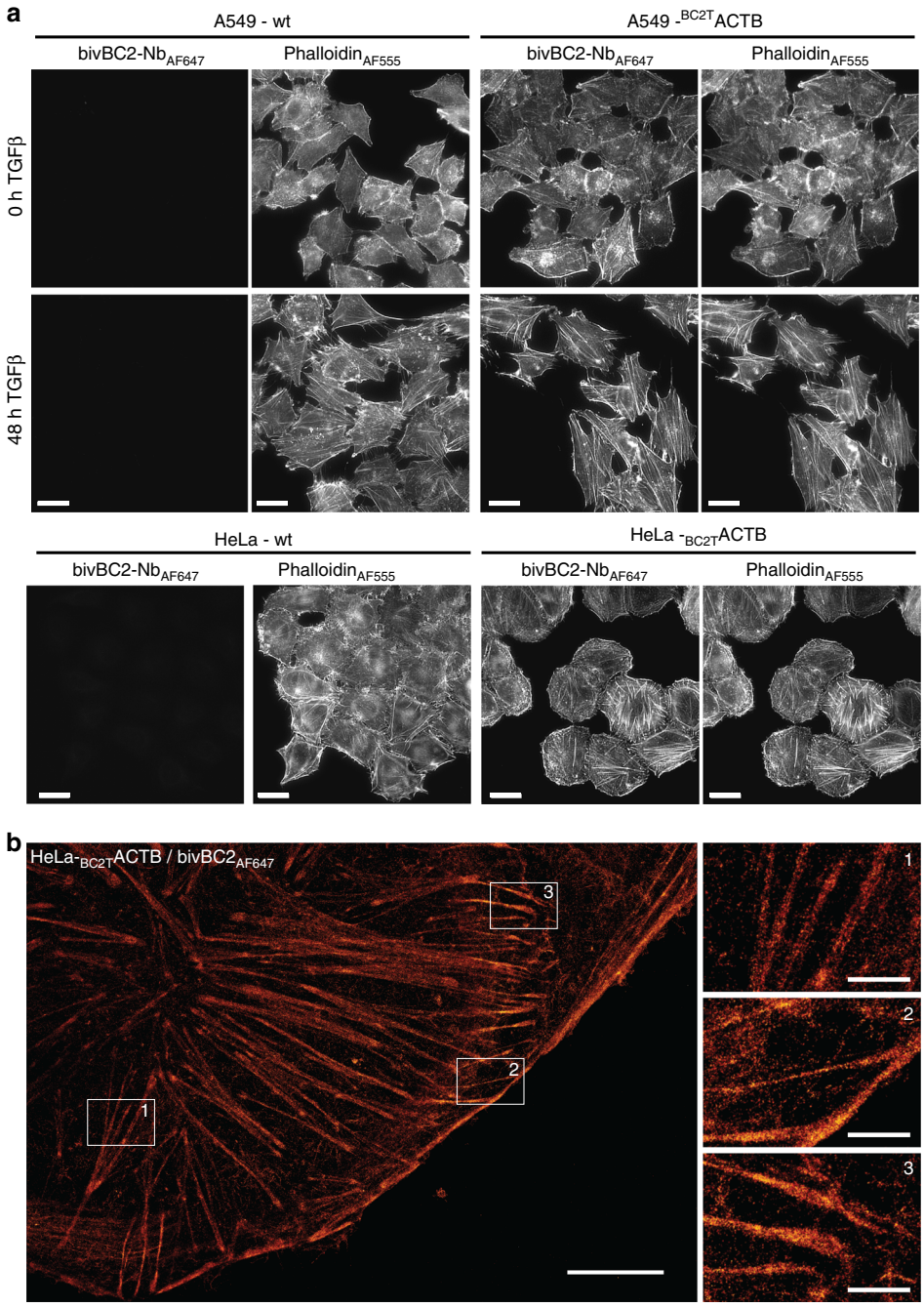

Fig. 4 Visualization of endogenously expressed BC2-tagged actin labeled with bivBC2-Nb_{AF647}. **a** Wide-field images of chemically fixed wild-type A549 and HeLa (-wt; left panel), as well as chemically fixed A549-$_{BC2T}$ACTB and HeLa-$_{BC2T}$ACTB cells (right panel). Cells were either left untreated (0 h) or stimulated for 48 h with TGFβ (5 ng ml^{-1}) followed by staining with $phalloidin_{AF555}$ and bivBC2-Nb_{AF647}. Scale bars, 25 µm. **b** dSTORM image of a representative HeLa-$_{BC2T}$ACTB cell. Scale bars, image 5 µm, insets 1 µm. Image reconstruction details are given in Methods section. Imaging sequence taken from raw data acquisition can be found in Supplementary Movie 5, assessment of AF647 photophysics under dSTORM imaging conditions can be found in Supplementary Fig. 15

factor β (TGFβ) and monitored the induction of actin stress fibers by co-staining with bivBC2-Nb_{AF647} and $phalloidin_{AF555}$. As expected, we detected the formation of stress fibers only in A549 wt and A549-$_{BC2T}$ACTB cells, which are described to respond to TGFβ[52] (Fig. 4a). dSTORM imaging further allowed a detailed insight into the non-disturbed actin network (Fig. 4b). These findings indicate that BC2-tagging of endogenous proteins is a viable approach for SRM studies to visualize cellular targets at endogenous levels and with minimal functional interference.

bivBC2-Nb visualizes its target proteins in living cells. To realize the advantages of the BC2-tag/bivBC2-Nb system also for live-cell applications, we first performed time-lapse imaging of HeLa cells transiently expressing $_{BC2T}$GFP-GPI. After addition of bivBC2-Nb_{AF647} to the imaging medium, we observed a fast recruitment of the nanobody to its membrane-located antigen (Supplementary Fig. 13a), with a saturation of the nanobody signal within 20–30 min (Supplementary Fig. 13b). Single-particle tracking dSTORM imaging further allowed us to trace the highly

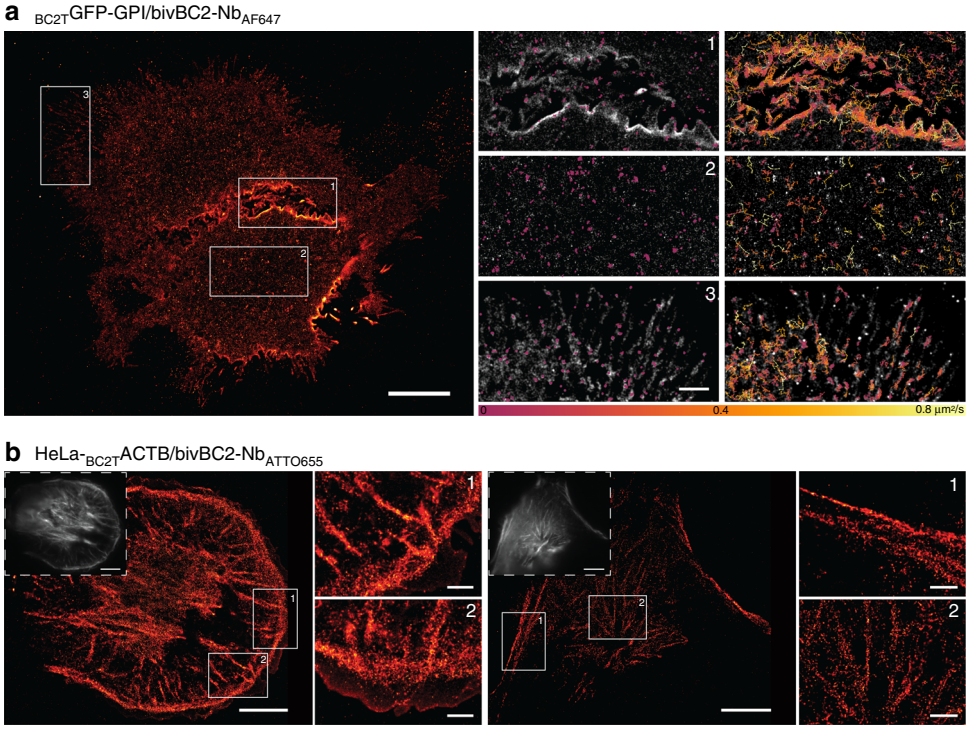

Fig. 5 Super-resolution imaging and single-particle tracking in live HeLa cells. **a** dSTORM image of live $_{BC2T}$GFP-GPI expressing HeLa cells stained with bivBC2-Nb$_{AF647}$ and insets in gray scale overlaid with single-particle trajectories of immobile (diffusion coefficient below 0.02 µm^2 s^{-1}, left) and mobile (diffusion coefficient above 0.02 µm^2 s^{-1}, right). Color scale of diffusion coefficients is given under insets. Scale bars 10 µm in images, 2 µm in insets. Supplementary Movies 1–4 show the recorded live $_{BC2T}$GFP-GPI dynamics of the whole cell and the corresponding insets. **b** Live-cell dSTORM images of two HeLa-$_{BC2T}$ACTB cells stained with bivBC2-Nb$_{ATTO655}$. Wide-field fluorescence images in upper left corners. Scale bars in 10 µm, 2 µm in insets. Image reconstruction details are given in Methods section. Imaging sequence taken from raw data acquisition can be found in Supplementary Movie 6, assessment of ATTO655 photophysics under live cell dSTORM imaging conditions can be found in Supplementary Fig. 15

dynamic movements of thousands of $_{BC2T}$GFP-GPI molecules along the plasma membrane in high spatial and temporal resolution, e.g., the increased dynamics at cell-to-cell contact areas (Fig. 5a, Supplementary Movies 1–4). Second, for bivBC2-Nb staining of intracellular targets in living cells, we adapted a lipid-based protein transfection protocol[53, 54] and introduced bivBC2-Nb conjugated to different dyes into our cell lines HeLa-$_{BC2T}$ACTB and A549-$_{BC2T}$ACTB. Within 2 h, we observed cellular uptake of nanobody and its accumulation at the actin cytoskeleton irrespective of the attached fluorophore (Supplementary Fig. 14a). Prolonged time-lapse imaging of live HeLa-$_{BC2T}$ACTB cells for 5 h revealed a stable staining of the cytoskeleton (Supplementary Fig. 14b). Finally, we performed live-cell dSTORM imaging replacing AF647 with the fluorophore ATTO655 which is currently one of the few organic dyes exhibiting sufficient photoswitching under physiological intracellular conditions[8]. Two hours after nanobody transduction, dSTORM imaging of the bivBC2-Nb$_{ATTO655}$ staining revealed the intracellular actin network of HeLa-$_{BC2T}$ACTB cells (Fig. 5b) with sub-diffraction details as previously seen for chemically fixed HeLa-$_{BC2T}$ACTB cells (Fig. 4b). We further documented the photophysical differences in performance of the ATTO655 fluorophore, which is outcompeted by AF647 both in blinking statistics and brightness (Supplementary Fig. 15, Supplementary Movies 5 and 6). In summary, these data demonstrate that the bivBC2-Nb is functional within living cells where it retains its outstanding binding capacities allowing for live-cell dSTORM imaging. Other recently reported protein transduction approaches offer numerous alternatives to introduce the bivBC2-Nb in various cell types for live-cell imaging of BC2-tagged proteins[41, 55–61].

Discussion

In this study, we developed and extensively characterized a broadly applicable and transferable labeling strategy based on a structurally minimal tag in combination with the first peptide-specific nanobody suitable for SRM. In contrast to the widely established GFP/GFP-Nb system[28, 62] for dSTORM imaging of fusion proteins comprising a large fluorescent moiety, the short and inert BC2-tag allows an efficient and dense incorporation of ectopically and endogenously expressed proteins into higher-ordered cellular structures in mammalian and yeast cells. In particular, it does not interfere with the native organization of structural proteins, such as vimentin, lamin, actin, and tubulin known to be easily compromised by large protein tags. We demonstrated that all tested BC2-tagged proteins are efficiently detected with a high affinity, bivalent nanobody format, robustly labeled in a one-to-one nanobody to fluorophore ratio exhibiting a high-labeling efficiency competing with covalent detection systems. Together, this enables high-labeling coverage with minimal linkage error and thus allows for genuine SRM studies of physiologically undisturbed cellular structures. Moreover, the bivBC2-Nb is functional in living cells where it retains its binding capacity and labels its target structures over extended time periods, which renders the BC2-tag/bivBC2-Nb labeling system into a versatile tool for SRM imaging of fixed and living cells.

Methods

Expression constructs. All primer sequences used for cloning are listed in a Supplementary Table 1. The expression construct coding for vimentin N-terminally fused to eGFP (GFP-vimentin) was previously described[41]. For generation of a photoactivatable (PA) mCherry (PAmCherry) fusion construct of vimentin (PAmCherry-vimentin) the coding sequence of PAmCherry was PCR-amplified from the pBAD/HisB-PAmCherry1 vector using the following primer set: PAmCherry-F and PAmCherry-R. The PCR product was purified, digested with the restriction enzymes AgeI and BglII and ligated in the AgeI/BglII sites of a vector coding for mCherry-vimentin thereby replacing mCherry with PAmCherry. An expression construct coding for vimentin with a C-terminal BC2-tag (vimentin$_{BC2T}$) was generated by the replacement of the mCherry sequence from a mCherry-Vimentin-BC2T (mCherry-vimentin$_{BC2T}$) fusion construct previously described[31]. Thus, vimentin$_{BC2T}$ cDNA was PCR-amplified using the primer VIM-BC2T-for and ligated into NheI and BamHI restriction sites of the template construct. Constructs coding for vimentin C-terminally fused to PAmCherry (vimentin-PAmCherry) and vimentin C-terminally fused to eGFP (vimentin-GFP) were generated by Gibson assembly of the three following fragments: fragment 1- pEGFP-N1 vector backbone digested with NheI and BsrGI, fragment 2- vimentin amplified from vimentin$_{BC2T}$ with the primer set VIM-for and VIM-rev, fragment 3- PAmCherry amplified from PAmCherry-vimentin or eGFP amplified from GFP-vimentin using the primer set PAmCherry/eGFP-for and PAmCherry/eGFP-rev. Fragments were assembled using the Gibson-Assembly Master Mix (New England Biolabs, cat. #E2611) according to the manufacturer's protocol. An expression construct coding for BC2-tagged β-actin ($_{BC2T}$actin) was generated by the combination of two PCR fragments derived from an eGFP-actin construct previously described in ref. [62]. The first PCR fragment was generated using primer BC2TActb(1)-for and BC2TActb(1)-rev. The second PCR fragment was generated using primer BC2TActb(2)-for and BC2TActb(2)-rev. Both DNA fragments were purified and ligated by compatible sticky ends generated by BssHII and SexAI restriction enzymes. To generate a BC2-tagged laminB1 ($_{BC2T}$lamin) expression construct the lamin B1 cDNA was PCR-amplified from a GFP-Lamin B1 DNA template[62] by PCR using primer BC2TLamin-for and BC2TLamin-rev and cloned into XhoI and NheI restriction sites of pEGFP-N1 vector thus introducing the BC2-tag sequence. The expression construct coding for C-terminally BC2-tagged lamin (lamin$_{BC2T}$) was generated by the replacement of the vimentin cDNA of the above described vimentin$_{BC2T}$ by lamin cDNA PCR-amplified from GFP-Lamin B1 using the primer laminBC2T-for and laminBC2T-rev. DNA fragments were purified and ligated by compatible sticky ends generated by NheI and BssHII restriction enzymes. The expression construct coding for C-terminally BC2-tagged tubulin (tubulin$_{BC2T}$) was generated by substituting vimentin cDNA of the above described vimentin$_{BC2T}$ with the tubulin cDNA PCR-amplified from pPAmCherry-tubulin (addgene 31930) with primers tubulinBC2T-for and tubulinBC2T-rev using restriction enzymes NheI and BssHII.

The expression construct coding for N-terminally BC2-tagged tubulin ($_{BC2T}$tubulin) was generated by substituting actin cDNA of the above described $_{BC2T}$actin with the tubulin cDNA PCR-amplified from pPAmCherry-tubulin (addgene 31930) with primers BC2Ttubulin-for and BC2Ttubulin-rev using restriction enzymes BssHII and BamHI. Mammalian expression construct coding for GFP-LC3B fusion protein, was generated by insertion of LC3B cDNA into BglII and EcoRI restriction sites of pEGFP-C1 expression vector. The expression construct coding for N-terminally BC2-tagged LC3B ($_{BC2T}$LC3B) was generated by substituting actin cDNA of the above described $_{BC2T}$actin with the LC3B cDNA PCR-amplified from GFP-LC3B using primers BC2TLC3B-for and BC2TLC3B-rev using restriction enzymes BssHII and BamHI. BC2T-tagged GFP-GPI construct for mammalian expression was generated by insertion of synthetic DNA fragment with an ORF coding for signal peptide of human CD59 (aa 1–25), BC2-Tag, eGFP and amino acids 92–128 of huCD59, which contains the GPI attachment site at aa 102 into BglII and NotI restriction sites of pEGFP-N2 vector DNA. Plasmids coding for Ypet-FtnA and SNAP-FtnA were purchased from addgene (cat. #98280 and 98282). To generate the expression construct coding for $_{BC2T}$Ypet-FtnA, BC2T was inserted to the N-terminus of Ypet-FtnA by PCR amplification of the complete Ypet-FtnA plasmid using BC2TYpet-for and BC2TYpet-rev. Subsequent recircularization of the amplified plasmid was performed using BssHII restriction sites.

All generated expression constructs were confirmed by sequencing and SDS-PAGE followed by western blot analysis using antibodies directed against eGFP (ChromoTek, cat. #3H9, dilution 1:1000), mCherry (ChromoTek, cat. #6G6, dilution 1:4000) or a BC2-Nb coupled to Alexa Fluor 647 (Thermo Fisher Scientific, cat. #A20006) (BC2-Nb$_{AF647}$, dilution 1:200) as previously described[31].

Bacterial expression vectors coding for the GFP-nanobody (GFP-Nb), the BC2-nanobody (BC2-Nb), and the bivalent BC2 nanobody (bivBC2-Nb) were provided by ChromoTek with a corresponding material transfer agreement. The bacterial expression construct of the bivalent VB6 nanobody (bivVB6-Nb) was previously described[41]. For all three constructs the original tag was replaced by a Sortase-tag (GSLPETG) upon PCR amplification of the full plasmid using the forward primer SorTag-Ins_for and SorTag-Ins_rev and subsequent recircularization using terminal AgeI restriction sites. The resulting expression constructs were confirmed by sequencing and bacterial expression followed by SDS-PAGE and immunoblot analysis using a C-terminal anti-His antibody (ThermoFisher Scientific, cat. #R930-25, dilution 1:1000). An expression vector coding for SortaseΔ59 (pET28a-SrtAdelta59) was a gift from Hidde Ploegh (Addgene plasmid #51138)[63].

Recombinant protein production and nanobody labeling. GFP-Nb, bivVB6-Nb, BC2-Nb, and bivBC2-Nb all comprising a C-terminal Sortase-tag were expressed and purified as previously described[41, 64] and stored at −80 °C or immediately used for labeling. SortaseΔ59 was expressed and purified as described[63]. Alexa Fluor 647 (AF647)-coupled peptide H-Gly-Gly-Gly-Doa-Lys-NH_2 (sortase substrate) was purchased from Intavis AG. Chemical dye conjugation of BC2-Nb or bivBC2-Nb was carried out as described previously[31]. Briefly, purified nanobody was labeled with the N-hydroxysuccinimide (NHS) ester activated AF647 (ThermoFisher Scientific, cat. #A20006) according to manufacturer's guidelines. After coupling, unbound dye was removed by separation on Zeba Spin Desalting Columns (ThermoFisher Scientific, cat. #89890). For analysis, 0.1 µg of nanobodies were subjected to SDS-PAGE and analyzed on a Typhoon Trio (GE-Healthcare, excitation 633 nm, emission filter settings 670 nm BP 30) and subsequent Coomassie staining.

Degree of labeling (DOL, dye-to-protein ratio) was determined by absorption spectroscopy according to the instructions provided by ThermoFisher Scientific (stated for cat. #A20173). For BC2-Nb and bivBC2-Nb NHS-conjugated nanobodies DOLs of 1.8 ± 0.5 and 2.1 ± 0.7 were determined.

Sortase coupling of nanobodies was performed as previously described[33]. Briefly, 25 µM nanobody, 75 µM dye-labeled peptide dissolved in sortase buffer (50 mM Tris, pH 7.5, and 150 mM NaCl) and 100 µM sortase were mixed in coupling buffer (50 mM Tris, pH 7.5, 150 mM NaCl, and 10 mM $CaCl_2$) and incubated for 5 h at 25 °C. Uncoupled nanobody and sortase were depleted using Ni-NTA resin (Biorad, cat. #1560131). Unbound dye was removed using Zeba Spin Desalting Columns (ThermoFisher Scientific, cat. #89890). The dye-labeled protein fraction was analyzed by SDS-PAGE followed by fluorescent scanning on a Typhoon Trio (GE-Healthcare, excitation 633 nm, emission filter settings 670 nm BP 30) and subsequent Coomassie staining. For all sortase-coupled nanobodies DOLs of 0.7 ± 0.15 were determined.

Bio-layer interferometry (BLI). The dissociation constants of BC2-Nb and bivBC2-Nb were determined on BLItz system (Pall ForteBio). Synthetic BC2 and BC2-BC2 (with $(GGGGS)_2$ linker) peptides with an N-terminal biotin-DoA-DoA-linker (Intavis AG) were immobilized on Streptavidin (SA) dip and read biosensors (Pall ForteBio, cat. #18-5020) using a concentration of 50 µM. For kinetic measurements of BC2- or bivBC2-Nbs three concentrations (120 nM, 240 nM, and 480 nM) of the Nbs in diluent buffer (1× PBS, 0.1% (w/V) BSA (Carl Roth, cat. #8076), 0.1 % (w/V) Triton X-100 (Sigma-Aldrich, cat. #T8787)) were used. Each measurement was done in duplicates with an association time of 180 s followed by 240 s dissociation in diluent buffer. Kinetic constants were determined using BLItz software (BLItz Pro 1.2, Pall ForteBio) according to global fitting of data sets.

Cell culture and transfection. The HeLa Kyoto cell line (Cellosaurus no. CVCL_1922) was obtained from S. Narumiya (Kyoto University, Japan), and the A549, U2OS and COS-7 cell lines were obtained from ATCC (CCL-185, HTB-96, CRL-1651). All cell lines were tested negative for mycoplasma using the PCR mycoplasma kit Venor GeM Classic (Minerva Biolabs, cat. #11-1025) and the Taq DNA Polymerase (Minerva Biolabs, cat. #53-0100). Since this study does not include cell line specific analysis, all cell lines were used without additional authentication. HeLa Kyoto, U2OS and COS-7 cells were cultured in DMEM +GlutaMAX (Life Technologies, cat. #31966-021) supplemented with 10% FCS (Life Technologies, cat. #10270-106) and 1 unit ml^{-1} pen/strep (Life Technologies, cat. #15140-122). A549 cells were cultured in DMEM/F-12 (1:1) (Life Technologies, cat. #21331-020) supplemented with 10% FCS (Life Technologies, cat. 10270-106), 1 unit ml^{-1} pen/strep (Life Technologies, cat. #15140-122) and 2 mM L-glutamine (Life Technologies, cat. #25030-024). Cells were trypsinized for passaging and cultivated at 37 °C in a humidified chamber with a 5% CO_2 atmosphere. Transient transfection of HeLa Kyoto, U2OS, and COS-7 cells with Lipofectamine 2000 (ThermoFisher Scientific, cat. #11668019) and transfection of A549 cells with Lipofectamine LTX (ThermoFisher Scientific, cat. #15338100) was carried out according to manufactures instruction.

***S. pombe* strain construction**. The cloning strategy for BC2-tagging of the *CBP1* gene at the C-terminus was adapted from[65]. The *Saccharomyces cerevisiae* ADH1 terminator and kanamycin resistance gene were amplified from the PAW8 plasmid[66] using the following primer pair F_KanR_BC2 and R_KanR. ~250 bp sequences up- and down-stream of the *cbp1* gene were amplified from purified *S. pombe* DNA, with the primer pairs F1_cbp1, cbp1_BC2_R1, and F2_cbp1, R2_cbp1. Primers were designed to generate PCR products with overlapping regions of at least 20 bp. DNA fragments were assembled with overlap-extension PCR[67], using melting temperatures of the overlapping regions as the annealing temperature. All PCRs were performed with Q5 High-Fidelity DNA polymerase (New England Biolabs, cat. #M0491L). Volume of 10 µl of the PCR product was transformed into wild-type *S.pombe* using the Frozen-EZ Yeast Transformation II Kit (Zymo Research, cat. #T2001), plated onto YES agar plates and incubated overnight at 30 °C, then replica plated onto 200 µg ml^{-1} G418 (Thermo Fisher

Scientific,) YES agar plates and incubated at 30 °C until single colonies were visible. Genomic integration was confirmed by colony PCR and DNA sequencing (Eurofins).

***S. pombe* cell culture**. *S.pombe* was grown in YES medium (5 g yeast extract, 30 g glucose, 225 mg of each l-adenine, histidine, leucine, uracil, lysine hydrochloride in 1 l of Milli-Q water) at 30 °C overnight, then inoculated into fresh YES to a starting OD_{600} of 0.1, grown to an OD600 of 0.4 and collected by centrifugation. Pellets were washed once with PEM buffer (100 mM Pipes, 1 mM EGTA, 1 mM $MgSO_4$, pH 6.9), then fixed for 15 min in 3.7% paraformaldehyde (PFA, Sigma-Aldrich, cat. #F8775) in PEM, washed 3 × 10 min with PEM containing 100 mM NH_4Cl to quench the fixation, then permeabilized with a 1:1 mixture of methanol and acetone at −20 °C for 10 min. Fixed and permeabilized cells were then washed 3 × with PEMBAL buffer (PEM + 1% BSA, 0.1% NaN_3, 100 mM lysine hydrochloride) and incubated in PEMBAL overnight. Before staining, cells were blocked with Image-iT FX signal enhancer (ThermoFisher Scientific, cat. #I36933) for 1 h, then stained for 48 h at 4 °C in PEMBAL containing ~0.5 µg ml^{-1} of bivBC2–Nb_{AF647} and 0.1% Triton X-100 (Sigma-Aldrich, cat. #T8787). Finally, cells were washed 2× with PEM containing 0.1% Tween-20 (Sigma-Aldrich, cat. #P7949), post-fixed with 4% PFA (Sigma-Aldrich, F8775) and 0.25% (w/V) glutaraldehyde (Sigma-Aldrich, cat. #G5882) in PEM for 10 min, then washed 2× with PEM and immobilized on poly-L-lysine coated Ibidi 8-well glass bottom slides (Ibidi GmbH, cat. #80826), previously cleaned with a 2% solution of Hellmanex III (Helma Analytics).

CRISPR/Cas9D10A expression vector construct and HDR template. Paired sgRNAs were designed for the *ACTB* (actin beta, *Homo sapiens*; PubMed Gene ID: 60) target gene locus using an online CRISPR gRNA design tool[68, 69] and synthesized as Ultramer DNA Oligonucleotides (Integrated DNA Technologies), *ACTB*_sgRNA and *ACTB*_HDR (Supplementary Table 1).

Next, paired sgRNAs were cloned according to a previously described procedure into a plasmid harboring Cas9D10A and a puromycin resistance cassette[70]. Briefly, the sgRNA fragment were PCR amplified using sgRNA_fw and sgRNA_rev primer thereby adding 3′ and 5′ domains homologous to plasmid encoded hU6 promotor and gRNA scaffold sequences, respectively. The 148 bp PCR amplicon was gel-purified and ligated at a 3:1 ratio to the 415 bp fragment generated by BbsI digest of the pDonor_U6 plasmid (a gift from Andrea Ventura, Addgene plasmid #69312)[70] using the NEBuilder Cloning Kit (New England Biolabs, cat. #E5520S). After treatment with Exonuclease RecBCD (New England Biolabs, cat. # M0345L) the column purified DNA plasmid was digested over night at 37 °C with BbsI. The linearized plasmid was then ligated into the BbsI-digested and dephosphorylated pSpCas9n(BB)-2A-Puro plasmid (a gift from Feng Zhang, Addgene plasmid #62987)[71] using T4 DNA ligase (NEB). Single-clone derived DNA plasmids were purified using QIAGEN Plasmid Midi Kit (Qiagen, cat. #12145) and verified by sequencing. The homology directed repair (HDR) template ACTB_HDR was synthesized as Ultramer DNA Oligonucleotides (IDT). HDR templates encoded for the HDR insert carrying the intended BC2-tag knock-in mutation flanked by left and right homology arms (each 50 bp) homologous to the *ACTB* target gene locus.

Generation of BC2-tag knock-in cell lines. 1 × 10^6 Hela Kyoto and A549 cells, respectively, were co-transfected at 50% confluency with 6.5 µg *ACTB*_HDR template oligonucleotide and 5.5 µg cloned Cas9N_Puro_*ACTB*_sgRNA expression vector construct or pEGFP plasmid (to control for transfection efficiency), respectively. For transfection of Hela cells Lipofectamine 2000 (ThermoFisher Scientific, cat. #11668019) and for A549 cells Lipofectamine LTX reagent (Thermo Fisher Scientific, cat. #15338100) was used. After 24 h, cells were trypsinized and re-plated in culture medium containing 1 µg ml^{-1} puromycin dihydrochloride (Sigma-Aldrich, cat. #P8833). Forty-eight hours later mock-transfected control cells were completely killed by the antibiotic. Puromycin-resistant cell pools were expanded for 1 week and subsequently used for detection of CRISPR/Cas9D10A-induced BC2-tag knock-in by immunofluorescence staining using the bivBC2-Nb_{AF647} and genomic PCR. Monoclonal knock-in cell lines were derived from cell pools showing successful BC2-tag knock-in by limiting dilution.

Genomic PCR of BC2-tag knock-in cells. Genomic DNA was isolated from puromycin-resistant cells using the QIAamp DNA Mini Kit (Qiagen, cat. #12125) according to manufacturer's instructions. Quantity 500 ng of purified genomic DNA was used for PCR amplification of the integrated BC2-tag sequence from the *ACTB* target gene locus using the primer ACTB_fw and BC2_rev. PCR products were separated on 1.5% agarose gels and visualized using ethidium bromide staining.

Immunofluorescence staining for wide-field microscopy. For immunofluorescence staining ~1.5 × 10^4 HeLa Kyoto, U2OS cells, COS-7, or A549 cells per well of an 8-well µ-slide (Ibidi GmbH, cat. #80826) were plated. Next day, cells were transfected with plasmids coding for GFP-vimentin, mCherry-$vimentin_{BC2T}$, PAmCherry-vimentin, vimentin-GFP, vimentin-PAmCherry, $vimentin_{BC2T}$, $_{BC2T}$actin, $_{BC2T}$lamin, $lamin_{BC2T}$, $_{BC2T}$tubulin, $tubulin_{BC2T}$, GFP-LC3B, $_{BC2T}$LC3B, $_{BC2T}$GFP-GPI, and Ypet-FtnA or $_{BC2T}$Ypet-FtnA.

Twenty-four hours after transfection or in case of U2OS cells expressing $_{BC2T}$tubulin, $tubulin_{BC2T}$, Ypet-FtnA, or $_{BC2T}$Ypet-FtnA cells 72 h after transfection, cells were washed twice with PBS and fixed with 3.7% w/V paraformaldehyde (PFA) in PBS for 10 min at RT. Fixed cells were washed three times with PBS and permeabilized with a 1:1 mixture of methanol/acetone for 5 min at −20 °C. After three washing steps with PBS, cells were blocked with Image-iT FX signal enhancer (Thermo Fisher Scientific, cat. #I36933) for 30 min. Subsequently cells were washed with and stored in PBS until staining. For nanobody staining, GFP-Nb_{AF647}, BC2-$Nb_{AF647\ (NHS)}$, BC2-$Nb_{AF647\ (sort)}$, bivBC2-$Nb_{AF647\ (NHS)}$, bivBC2-$Nb_{AF647\ (sort)}$, or bivVB6-Nb_{AF647} was added with a final concentration of ~50 ng ml^{-1} in 5% BSA in TBS-T (0.05% (w/V) Tween) and incubated overnight at 4 °C. Unbound nanobodies were removed by three additional washing steps with TBS-T. Images were acquired with a MetaXpress Micro XL system (Molecular Devices) and ×40 magnification.

For staining of endogenous β-catenin, ~5000 HeLa Kyoto cells per well were seeded in a µclear 96-well plate (Greiner Bio One, cat. #655090). Cells were either transfected with an expression plasmid coding for $vimentin_{BC2T}$ or left untransfected. Twenty-four hours after transfection cells were further left untreated or continuously cultured in the presence of 10 µM CHIR99021 for 16 h. Subsequently, cells were washed twice with PBS and fixed with 3.7% w/V paraformaldehyde (PFA) in PBS for 10 min at RT. After three washing steps with PBS, cells were permeabilized and blocked with 0.1% Triton X-100 in 5% BSA in TBS-T for 30 min. For detection of endogenous β-catenin, cells were incubated with an anti-β-catenin antibody (BD Biosciences, cat. #610154, dilution 1:200) followed by detection with an Alexa Fluor 488 labeled anti-mouse-antibody (Invitrogen, cat. #A10680, dilution 1:1000).

Generation of $_{BC2T}$Ypet-FtnA and SNAP-FtnA lysates. Cell lysates comprising BC2-tagged FtnA oligomers were generated from transiently $_{BC2T}$Ypet-FtnA transfected U2OS cells and immobilized on Poly-L-lysine-coated 8-well µ-slides (Sigma-Aldrich cat. # P4707; Ibidi, cat. # 80826)[36].

Staining of $_{BC2T}$Ypet-FtnA and SNAP-FtnA lysates. Wells of an 8-well µ-slide (Ibidi, cat. #80826) containing lysates of $_{BC2T}$Ypet-FtnA and SNAP-FtnA expressing U2OS cells were blocked with 10% BSA in PBS for 30 min, then with Image-iT FX signal enhancer (ThermoFisher Scientific, cat. #I36933) for an additional 60 min. Nanobodies were diluted to ~0.5 µg ml^{-1} in staining (PBS, 10% BSA, 0.1% (V/V) Triton X-100 (Sigma-Aldrich, cat. #T8787)). SNAP-Surface Alexa Fluor 647 (New England Biolabs, cat. #S9136S) was diluted to 0.1 µM in the same solution. Volume of 200 µl of the staining solution was added to each well and stained for 6 h at room temperature. After staining, wells were washed three times for 15 min with PBS containing 0.1% Tween-20. The nanobody staining was post-fixed with 4% PFA and 0.25% glutaraldehyde in PBS for 5 min to make the binding permanent. In the case of SNAP, the binding is already covalent. Wells were then washed an additional three times for 15 min with PBS and imaged overlaid with 300 µl of PBS.

Protein transduction. HeLa$_{_BC2T}$ACTB, or A549$_{_BC2T}$ACTB were plated at ~5000 cells per well of a µclear 96-well plates (Greiner Bio One, cat. #655090) and cultivated at standard conditions. Next day, Nbs were transduced using Pro-DeliverIN (OZ Biosciences, cat. #PI10250) according to manufacturer's protocol. Per well of a 96-well plate 0.25 µl of Pro-DeliverIN was mixed with 0.75 µg Nb and incubated for 15 min at RT. Volume of 20 µl Opti-MEM (ThermoFisher Scientific, cat. #31985062) was added to the mixture and immediately transferred to the cell culture medium in the well. After 2 h, medium was replaced by imaging medium DMEM^{gfp}-2 (Evrogen, cat. #MC102) supplemented with 10% FCS, 2 mM L-glutamine and cells were imaged.

Live-cell staining and imaging. HeLa Kyoto transiently expressing $_{BC2T}$GFP-GPI, HeLa-$_{BC2T}$ACTB, or A549-$_{BC2T}$ACTB cells were plated at ~5000 cells per well of a µclear 96-well plate (Greiner Bio One, cat. #655090) and cultivated at standard conditions. Next day, time-lapse imaging was performed in a humidified chamber (37 °C, 5% CO_2) of a MetaXpress Micro XL system (Molecular Devices) at ×40 magnification. For live-cell staining of $_{BC2T}$GFP-GPI, culture medium was replaced without washing by live-cell visualization medium DMEM^{gfp}-2 (Evrogen, cat. #MC102) supplemented with 10% FCS, 2 mM L-glutamine and 1 µg ml^{-1} bivBC2-Nb_{AF647}. Time-lapse imaging with 4–5 min intervals was started immediately upon medium replacement. For live-cell staining of HeLa-$_{BC2T}$ACTB and A549-$_{BC2T}$ACTB upon protein transduction of nanobodies, cells were washed once with and placed in DMEM^{gfp}-2 medium 2 h after addition of transduction mix (see "protein transduction" section above) and imaged in hourly intervals.

Quantification of staining intensities. HeLa Kyoto cells were plated at ~5000 cells per well of a µclear 96-well plates (Greiner Bio One, cat. #655090) and transfected with expression plasmid for mCherry-VIM_{BC2T}. Next day, cells were fixed and stained with the same concentration (1 µg ml^{-1}) of monovalent or bivalent BC2-Nbs conjugated to AF647 either by NHS conjugation or via sortase coupling. To assess staining q uality of the different nanobody formats we calculated the ratio of the staining intensity in mCherry-VIM_{BC2T} expressing cells and in non-transfected cells (background). Staining intensities were determined using a

custom-written cell identification algorithm (MetaXpress, Custom module editor). In brief, transfected cells were identified based on cell size parameters and a threshold setting for mCherry fluorescence intensity above local background. Background fluorescence was defined as the average fluorescence of the remaining image area precluding mCherry-VIM$_{BC2T}$ expressing cells. For statistical significance the average fluorescence intensity of a large number of transfected cells was determined (BC2-Nb$_{AF647\ (NHS)}$: $n = 115$; bivBC2-Nb$_{AF647\ (NHS)}$: $n = 134$; BC2-Nb$_{AF647\ (sort)}$: $n = 150$; bivBC2-Nb$_{AF647\ (sort)}$: $n = 195$).

Immunofluorescence staining for dSTORM imaging. To achieve the higher labeling density required for dSTORM imaging the staining protocol was slightly modified. Cells were prepared the same way as described up to the storage step in PBS. After storage, cells were blocked with 10% (w/V) BSA (Carl Roth, cat. #8076) in PBS for 30 min, then additionally with Image-iT FX signal enhancer (ThermoFisher Scientific, cat. #I36933) for 60 min. Antibodies and nanobodies were diluted to ~0.5 µg ml^{-1} in staining/permeabilization solution (PBS, 10% BSA, 0.1% (V/V) Triton X-100 (Sigma-Aldrich, cat. #T8787)). Conventional immunostaining was done at 4 °C for 24 h with the primary antibody (V9, mouse monoclonal, Sigma-Aldrich, cat. #347M-1)[72] followed by two washes with PBS, and then stained at 4 °C for 24 h with the secondary antibody (donkey-anti-mouse AF647, ThermoFisher Scientific, cat. #A-31571). For staining with nanobodies, cells were incubated at 4 °C for 48 h. Unbound Nbs were removed by two washes with PBS-T (0.1% w/V Tween-20 (Sigma-Aldrich, cat. #P7949)) and samples were post-fixed with 4% PFA (Sigma-Aldrich, cat. #F8775) and 0.25% (w/V) glutaraldehyde (Sigma-Aldrich, cat. #G5882) in PBS for 5 min to make the binding permanent. Finally, cells were washed twice with PBS to remove fixation solution and stored in PBS with 0.1% (w/V) sodium azide (Carl Roth, cat. #4221) until imaging.

dSTORM imaging and post-processing. A 1:5000 dilution of fluorescent beads (FluoSpheres 715/755, ThermoFisher Scientific, cat. #F8799) was sonicated to break up clumps of beads. Volume of ~5 µl of the beads were added to the sample and allowed to settle and adhere for 15 min, to serve as fiducial markers for drift correction. Images were recorded on a customized Nikon Ti-Eclipse inverted microscope, equipped with a CFI Apochromat TIRF ×100 objective with a numerical aperture of 1.49 (Nikon) and an iXON ULTRA 888 EMCCD camera (Andor). AF647 was imaged in 100 mM MEA (Sigma-Aldrich, cat. #M6500-25G) with a glucose oxidase (Sigma-Aldrich, cat. #G2133, C100) oxygen scavenger system[73]. The sample was illuminated with an OBIS LX 637 nm laser (Coherent) which was filtered through a ZET 640/10 bandpass, modulated by an Acousto-Optic Tunable Filter (Gooch & Housego, TF525-250-6-3-GH18) and focused by a ZET405/488/561/640 m dichroic mirror (Chroma) onto the back focal plane of the objective resulting in a final intensity of 2–4 kW cm^{-2} in the sample. The readout was collected by blocking the laser light by the bandpass ZET405/488/561/640 and passing through a 689/23 nm single-band bandpass filter (All filters AHF Analysentechnik AG). For each dSTORM image reconstruction, 10,000–20,000 imaging frames with an exposure time of 70 ms were recorded at a pixel size of 129 nm. The camera, microscope and AOTF were controlled by µManager software[74] on a PC workstation. Single-molecule localizations were extracted from the movies with the open-source software Rapidstorm 3.2.[75] Drift correction was performed by custom written Python 2.7 algorithms that extract and correct for fluorescent bead tracks. NeNA as described in ref. [43] was done with the open-source software Lama[76] on a section of the image that contained no fiducial markers. Localizations appearing within the radius of the NeNA value on several frames were grouped into one localization using the Kalman tracking filter in Rapidstorm 3.2. Final images were reconstructed at a pixel size of 10 nm. For visualization, a Gaussian blur filter was applied in the ImageJ software using NeNA as the sigma value. dSTORM imaging in yeast cells was performed in PEM buffer containing 10 mM MEA (Sigma-Aldrich, M6500) and 1 mM methyl viologen dichloride hydrate (MV) (Sigma-Aldrich, cat. #856177).

PALM imaging and post-processing. For imaging of PAmCherry-vimentin, the sample was illuminated with an OBIS LX 561 laser (Coherent), filtered through a ZET 561/10 clean-up filter (AHD Analysentechnik, Germany) at an intensity of 800 W cm^{-2} and an OBIS LX 405 laser (Coherent) at intensites of ~25–5000 mW cm^{-2}. The readout was collected through a 610/75 bandpass filter (AHF Analysentechnik, Germany). Twenty thousand imaging frames were recorded at an exposure time of 70 ms. The number of PAmCherry molecules activated each frame was kept at a steady rate by increasing 405 laser intensity until all of the PAmCherry was readout. All other microscope parameters and image post-processing remained the same as for dSTORM imaging.

Super-resolution analysis of endogenous β-catenin staining. To evaluate the effect of endogenous β-catenin staining on dSTORM imaging of low-abundance non-structural proteins, non-transfected HeLa and $_{BC2T}$LC3B expressing HeLa cells were fixed and stained with bivBC2-Nb$_{AF647}$ or GFP-Nb$_{AF647}$ for 48 h, imaged and post-processed as described in the "Immunofluorescence staining for dSTORM imaging" and "dSTORM imaging and post-processing" sections".

Analysis was performed on non-transfected HeLa cells stained with bivBC2-Nb$_{AF647}$ or GFP-Nb$_{AF647}$, in comparison to $_{BC2T}$LC3B-expressing cells stained with bivBC2-Nb$_{AF647}$. The GFP-Nb$_{AF647}$ staining served as a baseline of non-specific nanobody binding. Three 15 × 15 µm ROIs for each condition were analyzed with DBSCAN (DBSCAN parameters: $\varepsilon = 40$ nm; MinPts = 6)[35] to identify single nanobodies. The density of nanobodies per µm^2 was calculated for each ROI and the means of each condition plotted as bar charts with S.D. as the error.

To evaluate the effect of endogenous β–catenin staining when imaging abundant structural proteins, non-treated and CHIR99021-treated non-transfected and vimentin$_{BC2T}$ expressing HeLa cells were stained with bivBC2-Nb$_{AF647}$ and imaged as described in the "Immunofluorescence staining for dSTORM imaging" and "dSTORM imaging and post-processing" sections. Localization counts for three cells per condition were obtained with the RapidSTORM software[75] and cell areas were measured in Fiji[77]. Localizations per µm^2 were calculated and the means of each condition plotted as bar charts with S.D. as the error.

Imaging of $_{BC2T}$Ypet-FtnA and SNAP-FtnA lysates. A 488 nm Sapphire laser (Coherent Inc., Santa Clara, California USA) was used to excite the Ypet and the readout was collected through a 525/50 single bandpass filter (AHF Analysentechnik AG). Otherwise, the microscope setup was the same as described in the dSTORM paragraph above. The red laser intensity was reduced to ~0.4 kW cm^{-2}, to avoid pixel saturation when imaging stained FtnA oligomers while still allowing for the detection of single-AF647 molecule blinking events. In the case of $_{BC2T}$Ypet-FtnA, fluorescent spots were identified by their Ypet signal. Since the SNAP-tagged FtnA oligomers lacked the Ypet signal, they were excited with very low 640 nm laser (>0.01 W cm^{-2}) and chosen within 2 s to avoid photobleaching. Both were then imaged for 200 frames with an exposure time of 50 ms.

$_{BC2T}$Ypet-FtnA and SNAP-FtnA analysis. The fluorescence microscopy movies were analyzed with a custom ImageJ script in the open access software Fiji[77]. AF647 single-molecule blinking events were identified in the last 100 frames of the movies. Molecules that blinked at least twice in the last 100 frames were selected in different quadrants of the imaged area. A round ROI with a diameter of 10 pixels was drawn around each molecule and the intensity trace of the ROI for all 200 frames was extracted. The integrated intensity value was plotted over time using the software OriginPro (Origin Lab Corp.). Only blinking events with a clear jump in the integrated intensity values co-inciding with a visual blink in the movie were measured. Intensity of blinking events was measured by calculating the difference between baseline and peak intensity of the event (Supplementary Fig. 3a). A total of $N = 157$ blinking events were measured. The single-molecule integrated intensity values were binned with a bin size of 100 AD counts, plotted as a relative frequency histogram and fitted with the log-normal distribution function in OriginPro (Origin Lab Corp.):

$$f(x) = \frac{1}{x\sigma\sqrt{2\pi}} e^{-\frac{(\ln x - \mu)^2}{2\sigma^2}}$$

as described in ref. [78] yielding $\mu = 5.68$ and $\sigma = 0.4$ (Supplementary Fig. 3a). FtnA-oligomer spots were analyzed in a similar manner, with the integrated intensity value of the diameter of 10 pixels ROI of the second frame used for further analysis. A total of 130 $_{BC2T}$Ypet-FtnA spots and 89 SNAP-FtnA spots were analyzed. The integrated intensity data was binned with a bin size of 1000 AD counts and plotted as relative frequency histograms (Supplementary Fig. 3b). Approximating the labeling of FtnA oligomers with AF647 molecules with a binomial distribution, with the degree of labeling (0.7 ± 0.15 in case of the bivBC2-Nb$_{AF647}$ nanobody and 0.95 ± 0.05 in case of the AF647-BG) representing the p and the number of FtnA molecules in an oligomer representing the n parameter, we could calculate the probability for the occurrence of each labeling state (e.g., 24, 23, 22… AF647 per oligomer). Data sets assuming full labeling were simulated by calculating the linear combination of calibration distributions following the binomial mixture of visual oligomeric states due to the degree of labeling by recursively convolving the single-fluorophore log-normal distribution ($\mu = 5.68$, $\sigma = 0.4$) using a MatLab (MathWorks, Natick, MA-US)-based tool, as published and described in ref. [78]. To evaluate the completeness of labeling with the bivBC2-Nb$_{AF647}$ nanobody and the SNAP-tag, we then compared the medians of the simulated fully labeled scenario data sets with our measured distributions.

Image analysis of dSTORM images. A custom ImageJ script was used to measure the widths and coverages of vimentin, actin, and tubulin fibers on reconstructed non-blurred images. The segmented line tool in ImageJ was used to manually draw lines along vimentin filaments and line thickness was adjusted to fit the filament. Each image was divided into 10 × 10 µm sections and 15 random filaments were measured in each section. Line selections were straightened using the straighten tool and an intensity profile was plotted for each filament. To determine filament width, the intensity profile was fitted with a Gaussian curve and the resulting sigma value was multiplied with 2.35 to obtain the full width at half maximum (FWHM). To determine lengthwise coverage the image was converted into a binary image and the fraction of covered area of the middle 3 pixels was calculated. To reduce measurement error, line selections were wobbled by 0.5 pixels in four directions and values from all 5 measurements were averaged. To estimate image resolution, custom written Python 2.7 (Python Software Foundation) and Fiji[77] algorithms utilizing code from the Lama software[76] and GDSC SMLM ImageJ plugin (http://

www.sussex.ac.uk/gdsc/intranet/microscopy/imagej/gdsc_plugins) were used. NeNA localization precision[43] and Fourier Image Resolution (FIRE)[44] were calculated for all analyzed regions. To calculate FIRE, localization files were split into two by alternating frames ("random split" option unchecked). The threshold was set to Fixed 1/7 and the Fourier image scale was set to a constant 16 for all analyzed regions. Other parameters were left as default (auto image scale = 2048, sampling factor = 1). The results were plotted using the software OriginPro (Origin Lab Corp.).

LC3B clustering analysis. Imaging and post-processing of $_{BC2T}$LC3B cells was done as described in the "dSTORM imaging and post-processing" section. The obtained localization files were loaded into the MatLab-based software PALMsiever[79]. Density-based clustering analysis was performed with the density-based spatial clustering of applications with noise (DBSCAN) algorithm (DBSCAN parameters: $\varepsilon = 50$ nm; MinPts = 40)[35]. Three cells were analyzed for the untreated conditions and four cells for the rapamycin-treated conditions. To compare the degree of clustering, the ratio of non-clustered to clustered localizations was calculated for each cell. Points assigned as core and border points by DBSCAN were considered as clustered, while noise points were considered as non-clustered. Cluster size was calculated with a custom-written Python 2.7 script, measuring the average distance of cluster points from the cluster center of mass. Degree of clustering results were plotted as stacked bar charts, using S.D. as the error and the cluster sizes were plotted as histograms with a bin size of 100 nm, as well as individual data points and box + whisker plots, the ends of the box marking the 1st and 3rd quartiles, notch marking the median and whiskers encompassing 95% of the data in OriginPro (Origin Lab Corp.).

Live cell dSTORM imaging. HeLa Kyoto transiently expressing $_{BC2T}$GFP-GPI and HeLa-$_{BC2T}$ACTB were seeded in 8-well Ibidi µ-slides to an approximate density of 7500–15,000 cells per well, cultivated for 24 h at standard conditions then sealed in falcon tubes containing equilibrated culture medium. Upon arrival, cells were placed in an incubator for 3 h to recover and re-equilibrate. Meanwhile, 3 µl of Pro-DeliverIN was mixed with 9 µg of nanobody and incubated at RT for 15 min. After incubation, 60 µl of Opti-MEM were added to the mix and transferred into culture wells containing 300 µl of culturing medium. Cells were incubated for 2 h in the incubator, then washed two times with pre-equilibrated imaging medium DMEMgfp-2 without FCS. Volume of 300 µl of pre-equilibrated imaging medium without FCS, supplemented with the appropriate STORM buffer components were added to the wells. Well slide lids were sealed with parafilm and imaged on a custom built piezo-electric heating stage at 37 °C.

For imaging of $_{BC2T}$GFP-GPI, cells were stained with the bivBC2-Nb$_{AF647}$ and the imaging medium without FCS was supplemented with filter sterilized Tris-Hydrochloride to a final concentration of 100 mM and 10 mM MEA. The microscope setup remained as before. To record single-molecule tracks, 640 nm laser intensity was reduced to 1–2 W cm^{-2} and 20,000 imaging frames were recorded with an exposure time of 40 ms. For imaging of $_{BC2T}$ACTB, cells were stained with the bivBC2-Nb$_{ATTO655}$ and the imaging medium without FCS was supplemented with 50 µM ascorbic acid. ATTO655 was excited with 2-4 W cm^{-2} of 640 nm laser and 20,000 imaging frames were recorded with an exposure time of 50 ms. $_{BC2T}$ACTB images were processed as described in the "dSTORM imaging and post-processing" section.

Live cell image processing and analysis. Single-$_{BC2T}$GFP-GPI particles were tracked with the help of customized tracking software written in C++ and visualized by customized software written in C++, to filter for trajectories of at least 5 steps and group single-molecule localizations or trajectories by their apparent diffusion coefficient (as calculated by MSD analysis). Only trajectories with 5 or more steps were used for analysis and visualization. Single-particle trajectories were grouped into immobile (diffusion coefficient <0.02 µm^2 s^{-1}) and mobile particles (diffusion coefficient >0.02 µm^2 s^{-1}) and overlaid on top of a super resolution image reconstructed in Rapidstorm 3.2[75].

General statistical analysis of vimentin, actin, and tubulin. All labeling methods were repeated at least twice and imaged on at least two different days using the same setup and imaging parameters. Five cells from each labeling method were chosen based on the quality of drift correction. Cells were divided into 10 × 10 µm quadrants and 15 filaments in each quadrant were randomly chosen for analysis by at least two different people. All measured values were plotted as individual data points and box + whisker plots, the ends of the box indicating the first and third quartiles and the notch indicating the median. The whiskers encompass 95% of all the data. To confirm that the results of the different labeling methods differ significantly, vimentin filament widths were divided into a thin (0–75 nm), medium (75–150 nm), and thick (150 nm and above) category on which we performed a χ^2-test of homogeneity. The total number of measured filaments was high enough to ensure adequate test power (n-values for all conditions given in Supplementary Fig. 4). χ^2-values confirmed that the filament phenotypes for the labeling methods do differ at a 0.001 level of significance. To confirm that the ratio of fiber thicknesses does not significantly differ between bivVB6-Nb$_{AF647}$ and bivBC2-Nb$_{AF647}$, a χ^2 homogeneity test was performed on the categories 0–150 nm width and 150 nm and above, yielding a 0.001 level of significance. To test for correlation between FIRE, NeNA and coverage values, linear regression was performed pairwise on FIRE/NeNA, FIRE/coverage, and NeNA/coverage for all labeling methods. For FIRE/NeNA pairs, the slope of the linear correlation fits for bivVB6-Nb$_{AF647}$, GFP-Nb$_{AF647}$, and bivBC2-Nb$_{AF647}$ was significantly different from 0 at a 0.05 level of significance, while in the case of PAmCherry it was not. Correlating FIRE and NeNA to coverage, the slope of the linear fit was never significantly different from 0 at a 0.05 level of significance.

Data availability. The data that support the findings of this study are available from the corresponding authors upon reasonable request.

Received: 29 June 2017 Accepted: 26 January 2018
Published online: 02 March 2018

References

1. Betzig, E. et al. Imaging intracellular fluorescent proteins at nanometer resolution. *Science* **313**, 1642–1645 (2006).
2. Hess, S. T., Girirajan, T. P. & Mason, M. D. Ultra-high resolution imaging by fluorescence photoactivation localization microscopy. *Biophys. J.* **91**, 4258–4272 (2006).
3. Rust, M. J., Bates, M. & Zhuang, X. Sub-diffraction-limit imaging by stochastic optical reconstruction microscopy (STORM). *Nat. Methods* **3**, 793–796 (2006).
4. Thompson, R. E., Larson, D. R. & Webb, W. W. Precise nanometer localization analysis for individual fluorescent probes. *Biophys. J.* **82**, 2775–2783 (2002).
5. Fernández-Suárez, M. & Ting, A. Y. Fluorescent probes for super-resolution imaging in living cells. *Nat. Rev. Mol. Cell Biol.* **9**, 929–943 (2008).
6. Deschout, H. et al. Precisely and accurately localizing single emitters in fluorescence microscopy. *Nat. Methods* **11**, 253–266 (2014).
7. Fornasiero, E. F. & Opazo, F. Super-resolution imaging for cell biologists: concepts, applications, current challenges and developments. *Bioessay.: News Rev. Mol., Cell. Dev. Biol.* **37**, 436–451 (2015).
8. Turkowyd, B., Virant, D. & Endesfelder, U. From single molecules to life: microscopy at the nanoscale. *Anal. Bioanal. Chem.* **408**, 6885–6911 (2016).
9. Grimm, J. B. et al. A general method to fine-tune fluorophores for live-cell and in vivo imaging. *Nat. Methods* **14**, 987–994 (2017).
10. Li, C., Tebo, A. G. & Gautier, A. Fluorogenic labeling strategies for biological imaging. *Int. J. Mol. Sci.* **18**, 1473 (2017).
11. Hosein, R. E., Williams, S. A., Haye, K. & Gavin, R. H. Expression of GFP-actin leads to failure of nuclear elongation and cytokinesis in *Tetrahymena thermophila*. *J. Eukaryot. Microbiol.* **50**, 403–408 (2003).
12. Snapp, E. L. Fluorescent proteins: a cell biologist's user guide. *Trends Cell Biol.* **19**, 649–655 (2009).
13. Stadler, C. et al. Immunofluorescence and fluorescent-protein tagging show high correlation for protein localization in mammalian cells. *Nat. Methods* **10**, 315–323 (2013).
14. Hopp, T. P. et al. A short polypeptide marker sequence useful for recombinant protein identification and purification. *Nat. Biotechnol.* **6**, 1204–1210 (1988).
15. Wilson, I. A. et al. The structure of an antigenic determinant in a protein. *Cell* **37**, 767–778 (1984).
16. Evan, G. I., Lewis, G. K., Ramsay, G. & Bishop, J. M. Isolation of monoclonal antibodies specific for human c-myc proto-oncogene product. *Mol. Cell Biol.* **5**, 3610–3616 (1985).
17. Viswanathan, S. et al. High-performance probes for light and electron microscopy. *Nat. Methods* **12**, 568–576 (2015).
18. Chamma, I. et al. Mapping the dynamics and nanoscale organization of synaptic adhesion proteins using monomeric streptavidin. *Nat. Commun.* **7**, 10773 (2016).
19. Sharonov, A. & Hochstrasser, R. M. Wide-field subdiffraction imaging by accumulated binding of diffusing probes. *Proc. Natl Acad. Sci. USA* **103**, 18911–18916 (2006).
20. Legant, W. R. et al. High-density three-dimensional localization microscopy across large volumes. *Nat. Methods* **13**, 359–365 (2016).
21. Agasti, S. S. et al. DNA-barcoded labeling probes for highly multiplexed Exchange-PAINT imaging. *Chem. Sci.* **8**, 3080–3091 (2017).
22. Schnitzbauer, J., Strauss, M. T., Schlichthaerle, T., Schueder, F. & Jungmann, R. Super-resolution microscopy with DNA-PAINT. *Nat. Protoc.* **12**, 1198 (2017).
23. Pleiner, T. et al. Nanobodies: site-specific labeling for super-resolution imaging, rapid epitope-mapping and native protein complex isolation. *Elife* **4**, e11349 (2015).
24. Mikhaylova, M. et al. Resolving bundled microtubules using anti-tubulin nanobodies. *Nat. Commun.* **6**, 7933 (2015).

25. Traenkle, B. & Rothbauer, U. Under the microscope: single-domain antibodies for live-cell imaging and super-resolution microscopy. *Front. Immunol.* **8**, 1030 (2017).
26. Fridy, P. C. et al. A robust pipeline for rapid production of versatile nanobody repertoires. *Nat. Methods* **11**, 1253–1260 (2014).
27. Moutel, S. et al. NaLi-H1: a universal synthetic library of humanized nanobodies providing highly functional antibodies and intrabodies. *Elife* **5**, e16228 (2016).
28. Ries, J., Kaplan, C., Platonova, E., Eghlidi, H. & Ewers, H. A simple, versatile method for GFP-based super-resolution microscopy via nanobodies. *Nat. Methods* **9**, 582–584 (2012).
29. Tang, A.-H. et al. A trans-synaptic nanocolumn aligns neurotransmitter release to receptors. *Nature* **536**, 210–214 (2016).
30. Margolin, W. The price of tags in protein localization studies. *J. Bacteriol.* **194**, 6369–6371 (2012).
31. Braun, M. B. et al. Peptides in headlock–a novel high-affinity and versatile peptide-binding nanobody for proteomics and microscopy. *Sci. Rep.* **6**, 19211 (2016).
32. Popp, M. W. L. & Ploegh, H. L. Making and breaking peptide bonds: protein engineering using sortase. *Angew. Chem. Int. Ed.* **50**, 5024–5032 (2011).
33. Massa, S. et al. Sortase A-mediated site-specific labeling of camelid single-domain antibody-fragments: a versatile strategy for multiple molecular imaging modalities. *Contrast Media Mol. Imaging* **11**, 328–339 (2016).
34. Traenkle, B. et al. Monitoring interactions and dynamics of endogenous beta-catenin with intracellular nanobodies in living cells. *Mol. Cell Proteom.* **14**, 707–723 (2015).
35. Endesfelder, U. et al. Multiscale spatial organization of RNA polymerase in *Escherichia coli*. *Biophys. J.* **105**, 172–181 (2013).
36. Finan, K., Raulf, A. & Heilemann, M. A set of homo-oligomeric standards allows accurate protein counting. *Angew. Chem. Int. Ed.* **54**, 12049–12052 (2015).
37. Durisic, N., Laparra-Cuervo, L., Sandoval-Alvarez, A., Borbely, J. S. & Lakadamyali, M. Single-molecule evaluation of fluorescent protein photoactivation efficiency using an in vivo nanotemplate. *Nat. Methods* **11**, 156–162 (2014).
38. Szymborska, A. et al. Nuclear pore scaffold structure analyzed by super-resolution microscopy and particle averaging. *Science* **341**, 655–658 (2013).
39. Mendez, M. G., Kojima, S. & Goldman, R. D. Vimentin induces changes in cell shape, motility, and adhesion during the epithelial to mesenchymal transition. *FASEB J.* **24**, 1838–1851 (2010).
40. Wang, S., Moffitt, J. R., Dempsey, G. T., Xie, X. S. & Zhuang, X. Characterization and development of photoactivatable fluorescent proteins for single-molecule–based superresolution imaging. *Proc. Natl. Acad. Sci. USA* **111**, 8452–8457 (2014).
41. Maier, J., Traenkle, B. & Rothbauer, U. Real-time analysis of epithelial-mesenchymal transition using fluorescent single-domain antibodies. *Sci. Rep.* **5**, 13402 (2015).
42. Cranfill, P. J. et al. Quantitative assessment of fluorescent proteins. *Nat. Methods* **13**, 557 (2016).
43. Endesfelder, U., Malkusch, S., Fricke, F. & Heilemann, M. A simple method to estimate the average localization precision of a single-molecule localization microscopy experiment. *Histochem. Cell Biol.* **141**, 629–638 (2014).
44. Nieuwenhuizen, R. P. et al. Measuring image resolution in optical nanoscopy. *Nat. Methods* **10**, 557–562 (2013).
45. Brault, V., Sauder, U., Reedy, M. C., Aebi, U. & Schoenenberger, C.-A. Differential epitope tagging of actin in transformed *Drosophila* produces distinct effects on myofibril assembly and function of the indirect flight muscle. *Mol. Biol. Cell* **10**, 135–149 (1999).
46. Vale, R. D. The molecular motor toolbox for intracellular transport. *Cell* **112**, 467–480 (2003).
47. Hansen, T. E. & Johansen, T. Following autophagy step by step. *BMC.Biol.* **9**, 39 (2011).
48. Legler, D. F. et al. Differential insertion of GPI-anchored GFPs into lipid rafts of live cells. *FASEB J.* **19**, 73–75 (2005).
49. Yang, Z. & Klionsky, D. J. Mammalian autophagy: core molecular machinery and signaling regulation. *Curr. Opin. Cell Biol.* **22**, 124–131 (2010).
50. Mizushima, N., Ohsumi, Y. & Yoshimori, T. Autophagosome formation in mammalian cells. *Cell Struct. Funct.* **27**, 421–429 (2002).
51. Jin, M. & Klionsky, D. J. Regulation of autophagy: modulation of the size and number of autophagosomes. *FEBS Lett.* **588**, 2457–2463 (2014).
52. Tirino, V. et al. TGF-β1 exposure induces epithelial to mesenchymal transition both in CSCs and non-CSCs of the A549 cell line, leading to an increase of migration ability in the CD133+A549 cell fraction. *Cell Death Dis.* **4**, e620 (2013).
53. Róna, G. et al. Dynamics of re-constitution of the human nuclear proteome after cell division is regulated by NLS-adjacent phosphorylation. *Cell Cycle* **13**, 3551–3564 (2014).
54. Oba, M. & Tanaka, M. Intracellular internalization mechanism of protein transfection reagents. *Biol. Pharm. Bull.* **35**, 1064–1068 (2012).
55. Avignolo, C. et al. Internalization via Antennapedia protein transduction domain of an scFv antibody toward c-Myc protein. *FASEB J.* **22**, 1237–1245 (2008).
56. Marschall, A. L., Frenzel, A., Schirrmann, T., Schungel, M. & Dubel, S. Targeting antibodies to the cytoplasm. *MAbs* **3**, 3–16 (2011).
57. Sharei, A. et al. A vector-free microfluidic platform for intracellular delivery. *Proc. Natl. Acad. Sci. USA* **110**, 2082–2087 (2013).
58. Aigrain, L., Sustarsic, M., Crawford, R., Plochowietz, A. & Kapanidis, A. N. Internalization and observation of fluorescent biomolecules in living microorganisms via electroporation. *J. Vis. Exp.* **96**, 52208 (2015).
59. Hennig, S. et al. Instant live-cell super-resolution imaging of cellular structures by nanoinjection of fluorescent probes. *Nano Lett.* **15**, 1374–1381 (2015).
60. Teng, K. W. et al. Labeling proteins inside living cells using external fluorophores for microscopy. *Elife* **5**, e20378 (2016).
61. Roder, R. et al. Intracellular delivery of nanobodies for imaging of target proteins in live cells. *Pharm. Res.* **34**, 161–174 (2017).
62. Rothbauer, U. et al. Targeting and tracing antigens in live cells with fluorescent nanobodies. *Nat. Methods* **3**, 887–889 (2006).
63. Guimaraes, C. P. et al. Site-specific C-terminal and internal loop labeling of proteins using sortase-mediated reactions. *Nat. Protoc.* **8**, 1787–1799 (2013).
64. Rothbauer, U. et al. A versatile nanotrap for biochemical and functional studies with fluorescent fusion proteins. *Mol. Cell Proteom.* **7**, 282–289 (2008).
65. Hayashi, A. et al. Localization of gene products using a chromosomally tagged GFP-fusion library in the fission yeast *Schizosaccharomyces pombe*. *Genes Cells* **14**, 217–225 (2009).
66. Watson, A. T., Garcia, V., Bone, N., Carr, A. M. & Armstrong, J. Gene tagging and gene replacement using recombinase-mediated cassette exchange in *Schizosaccharomyces pombe*. *Gene* **407**, 63–74 (2008).
67. Bryksin, A. V. & Matsumura, I. Overlap extension PCR cloning: a simple and reliable way to create recombinant plasmids. *Biotechniques* **48**, 463–465 (2010).
68. Labun, K., Montague, T. G., Gagnon, J. A., Thyme, S. B. & Valen, E. CHOPCHOPv2: a web tool for the next generation of CRISPR genome engineering. *Nucleic Acids Res.* **44**, W272–W276 (2016).
69. Montague, T. G., Cruz, J. M., Gagnon, J. A., Church, G. M. & Valen, E. CHOPCHOP: a CRISPR/Cas9 and TALEN web tool for genome editing. *Nucleic Acids Res.* **42**, W401–W407 (2014).
70. Vidigal, J. A. & Ventura, A. Rapid and efficient one-step generation of paired gRNA CRISPR-Cas9 libraries. *Nat. Commun.* **6**, 8083 (2015).
71. Ran, F. A. et al. Genome engineering using the CRISPR-Cas9 system. *Nat. Protoc.* **8**, 2281–2308 (2013).
72. Nahidiazar, L., Agronskaia, A. V., Broertjes, J., van den Broek, B. & Jalink, K. Optimizing imaging conditions for demanding multi-color super resolution localization microscopy. *PLoS ONE* **11**, e0158884 (2016).
73. Van De Linde, S. et al. Direct stochastic optical reconstruction microscopy with standard fluorescent probes. *Nat. Protoc.* **6**, 991–1009 (2011).
74. Edelstein, A. D. et al. Advanced methods of microscope control using μManager software. *J. Biol. Methods* **1**, e10 (2014).
75. Carlini, L., Holden, S. J., Douglass, K. M. & Manley, S. Correction of a depth-dependent lateral distortion in 3D super-resolution imaging. *PLoS ONE* **10**, e0142949 (2015).
76. Malkusch, S. & Heilemann, M. Extracting quantitative information from single-molecule super-resolution imaging data with LAMA–LocAlization MicroscopyAnalyzer. *Sci. Rep.* **6**, 34486 (2016).
77. Schindelin, J. et al. Fiji: an open-source platform for biological-image analysis. *Nat. Methods* **9**, 676–682 (2012).
78. Zanacchi, F. C. et al. A DNA origami platform for quantifying protein copy number in super-resolution. *Nat. Methods* **14**, 789–792 (2017).
79. Pengo, T., Holden, S. J. & Manley, S. PALMsiever: a tool to turn raw data into results for single-molecule localization microscopy. *Bioinformatics* **31**, 797–798 (2014).

Acknowledgements

The authors thank Christian Linke-Winnebeck and Benjamin Ruf (both ChromoTek GmbH) for technical support in nanobody production and labeling, Yana Parfyonova for cloning of the $_{BC2T}$GFP-GPI construct and performing corresponding live cell studies, Maruša Kustec for help with general statistical tests, Urban Završnik for help with Python programming language scripting, Alex Herbert for help with his GDSC SMLM FIRE ImageJ Plugin and Knut Drescher for kindly providing his mammalian cell culture equipment. D.V., I.V., B.P.-L., and U.E. acknowledge funding by the Max Planck Society, SYNMIKRO and the Fonds der Chemischen Industrie. U.R., B.T., and J.M. gratefully acknowledge the Ministry of Science, Research and Arts of Baden-Württemberg (V.1.4.-H3-1403-74) for financial support.

Author contributions

U.E. and U.R. conceived the study. D.V., B.T., J.M., P.D.K., M.B., C.S., I.V., B.P.-L., U.E., and U.R. performed all experiments, U.E. and U.R. wrote the manuscript with the input from all authors.

Additional information

Supplementary Information accompanies this paper at https://doi.org/10.1038/s41467-018-03191-2.

Competing interests: U.R. is shareholder of the company ChromoTek GmbH. All other authors declare no competing financial interests.

Reprints and permission information is available online at http://npg.nature.com/reprintsandpermissions/

Publisher's note: Springer Nature remains neutral with regard to jurisdictional claims in published maps and institutional affiliations.

Supplementary Information

A peptide tag-specific nanobody enables high-quality labeling for dSTORM imaging

Virant et al.,

Supplementary Note 1

As an additional, independent measure, we applied Fourier-Ring Correlation (FRC)[1]. The Fourier Image Resolution (FIRE) value is determined by the highest spatial frequencies which still positively correlate with each other above a chosen threshold. Thus, in the case of highly blinking dyes like AF647, the FIRE value mainly correlates with the optical resolution. Only when using a blinking correction factor or in the case of seldom-blinking fluorophores like PAmCherry it also takes the structural resolution into account[1]. Since all nanobodies were coupled to AF647, their stainings yielded highly similar FIRE values of 40 to 50 nm. These values correlate with the 9 to 12 nm NeNA localization precisions, which also mainly rely on the optical properties of the fluorophore (**Supplementary Fig. 6**). Notably, the labeling coverages of the individual fibers do not correlate with their NeNA and FIRE values which illustrates why the optical resolution should not be mistaken as an overall resolution. In the case of PAmCherry, a relatively seldom-blinking fluorophore, blinking events have a much smaller impact on the calculation of the FIRE value. Consequently, FIRE values for PAmCherry are closer to the actual overall resolution as the structural resolution is taken into account. As PAmCherry has low coverages of 35% for the thinnest fibers and up to 75% for the thickest fibers, the high FIRE values of 120 nm clearly illustrates that the limiting factor for the overall resolution is not the optical resolution (NeNA 17 nm) but rather the low coverage (**Supplementary Fig. 6**). The contribution of the linkage error to overall resolution is shown by comparing the sizes of the thinnest filaments stained with either nanobodies or conventional antibodies (**Supplementary Fig. 7**). The differences cannot be differentiated using the FIRE value since both approaches use AF647 as the readout (**Supplementary Fig. 7**). The bias in FIRE values is also visible in the structural analysis of $_{BC2T}$actin filaments (**Supplementary Fig. 9b**).

Supplementary Table 1

Primer sequences

primer name	Sequence (5´- 3´)
PAmCherry-F	ATATATACCGGTGCCACCATGGTGAGCAAGGGCGAGG
PAmCherry-R	ATATATAGATCTGCTTGTACAGCTCGTCCATGCC
VIM-BC2T-for	ATATATGCTAGCGCCACCATGTCCACCAGGTCCGTGTCCTCGTCC
VIM-BC2T-rev	GATCCGGTGGATCCCGGGCCC
VIM-for	AGTGAACCGTCAGATCCGCTA
VIM-rev	TCCACCTAAGCTTGAGCTCGAGATCTGTTCAAGGTCATCGTGATGCT
PAmCherry/eGFP-for	TCGAGCTCAAGCTTAGGTGGAGGAGGTTCTGTGAGCAAGGGCGAGGA
PAmCherry/eGFP-rev	ATCTAGAGTCGCGGCCGCTTACTTGTACAGCTCGTCCATGC
BC2TActb(1)-for	AAGCGCGCTGTTAGTCACTGGCAGCAAGATGATGATATCGCCGCGCT
BC2TActb(1)-rev	GACTTTCCACACCTGGTTGCTGA
BC2TActb(2)-for	TCAGCAACCAGGTGTGGAAAGTC
BC2TActb(2)-rev*	CGGCGCGCTTTCTGTCTGGCATGGTGGCGACCGGTAGC
BC2TLamin-for	GGACTCGAGATGCCAGACAGAAAGGCGGCTGTTAGTCACTGGCAGCAAGCGACTGCGACC CCCGT
BC2TLamin-rev	GGAGCTAGCATTACATAATTGCACAGCTTCTATTGGAT
laminBC2T-for	AAAGCTAGCGCCACCATGGCGACTGCGACC
laminBC2T-rev*	AAAGCGCGCTTGCGATCAGGCATAATTGCACAGCTTCTA
tubulinBC2T-for	AAAGCTAGCGCTACCGGTCGCCACCATGCGTGAGTGCATCTCCAT
tubulinBC2T-rev*	AAAGCGCGCTTGCGATCAGGGTATTCCTCTCCTTCTTCCTCACCCTC
BC2Ttubulin-for*	AATGCGCGCCGTGAGCCATTGGCAGCAGCGTGAGTGCATCTCCATCC
BC2Ttubulin-rev	ATTGGATCCCTAGTATTCCTCTCCTTCTTCCTCA
BC2TLC3B-for*	GTAGCGCGCCGTGAGCCATTGGCAGCAGCCGTCGGAGAAGACCTTCAA
BC2TLC3B-rev	GGTGGATCCTTACACTGACAATTTCATCCCGA
BC2TYpet-for*	AAAGCGCGCTTGCGATCAGGCATGGTGGCGACCGGTG
BC2TYpet-rev*	AAAGCGCGCCGTCTCTCATTGGCAGCAGGTGAGCAAAGGCGAAGAGCTG
SorTag Ins_for	TTACCGGTCACCACCATCACCATCACTAAG
SorTag Ins_rev	TTACCGGTTTCCGGCAGGCTACCTGAGGAGACGGTGACCTGG
F_KanR_BC2	AAGGCCGCAGTTTCACATTGGCAACAATAAGGCGCGCCAGATCTACTT
R_KanR	GACAGCAGTATAGCGACCAGC
F1_cbp1	ATCAAATTGCTTCGCAGTACATGG
cbp1_BC2_R1	CAATGTGAAACTGCGGCCTTTCTGTCAGGGGTGCTTCTCAAACGAGAAAGATTC
F2_cbp1	AATGCTGGTCGCTATACTGCTGTCTGTCTGTATTCGTTGTGCATATTTGAC
R2_cbp1	GCTCGTATAGCGATTTTGCGTT
ACTB_sgRNA	CTTGTGGAAAGGACGAAACACCCGAGAATAGCCGGGCGCGCTGTTTGGGTCTTCGAGAAG ACCTCACCGCCGTTGTCGACGACGAGCGGTTTTAGAGCTAGAAATAGC
ACTB_HDR	GAAGTGGCCAGGGCGGGGGCGACCTCGGCTCACAGCGCGCCCGGCTATTCTCGCAACTC ACCATGCCTGATCGGAAGGCCGCCGTGAGCCATTGGCAGCAGGATGATGATATCGCCGCG CTCGTCGTCGACAACGGGTCCGGCATGTGCAAGGCCGGCTTCGCGGGCGACGATGCCCCC CC
sgRNA_fw	TTTCTTGGCTTTATATATCTTGTGGAAAGGACGAAAC
sgRNA_rev primer	GACTAGCCTTATTTTAACTTGCTATTTCTAGCTCTAAAAC
ACTB_fw	GGGGCTGGGAATTGGCGCTAATTG
BC2_rev	TGCTGCCAATGGCTCACGGCG

* to facilitate cloning, primer sequence encodes an amino acid substitution A>R at position 5 of BC2-tag. This substitution does not affect binding properties of BC2-Nb as shown previously.[2]

Supplementary Figures

Supplementary Figure 1

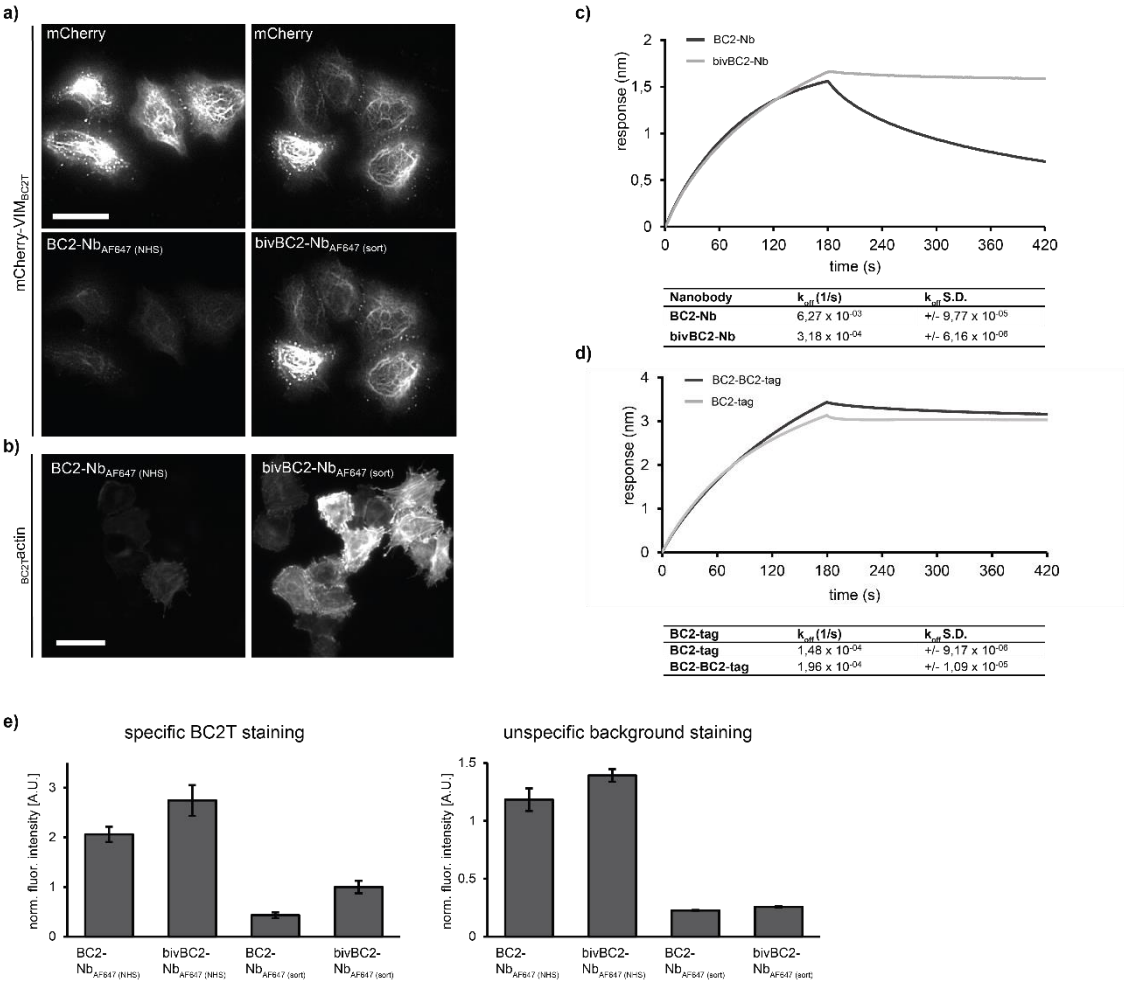

Nanobody	k_{off} (1/s)	k_{off} S.D.
BC2-Nb	6,27 x 10^{-03}	+/- 9,77 x 10^{-05}
bivBC2-Nb	3,18 x 10^{-04}	+/- 6,16 x 10^{-06}

BC2-tag	k_{off} (1/s)	k_{off} S.D.
BC2-tag	1,48 x 10^{-04}	+/- 9,17 x 10^{-06}
BC2-BC2-tag	1,96 x 10^{-04}	+/- 1,09 x 10^{-05}

Characterization of binding properties and labeling intensities of monovalent vs. bivalent BC2-Nb. (**a**) Comparison of labeling intensities of mono- and bivalent BC2 nanobodies either labeled via NHS conjugation to Alexa Fluor 647 (BC2-Nb$_{AF647\ (NHS)}$) or sortase-mediated coupling (bivBC2-Nb$_{AF647\ (sort)}$). HeLa cells transiently expressing a C-terminally BC2-tagged mCherry-vimentin construct (mCherry-VIM$_{BC2T}$, upper row) were fixed and stained with either BC2-Nb$_{AF647\ (NHS)}$ (lower row, left panel) or bivBC2-Nb$_{AF647\ (sort)}$ (lower row, right panel). Scale bar, 50 µm. (**b**) Comparison of labeling intensities of BC2-Nb$_{AF647\ (NHS)}$ and bivBC2-Nb$_{AF647\ (sort)}$ on BC2-tagged actin ($_{BC2T}$actin). HeLa cells transiently expressing $_{BC2T}$actin were fixed and stained with either BC2-Nb$_{AF647\ (NHS)}$ (left panel) or bivBC2-Nb$_{AF647\ (sort)}$ (right panel). Scale bar, 50 µm. (**c**) Determination of nanobody binding kinetics by bio-layer interferometry. Exemplary sensograms of BC2-Nb (240 nM) and bivBC2-Nb (120 nM) are shown. The table summarizes

the dissociation rate (k_{off}) and standard deviation (S.D.) of BC2-Nb and bivBC2-Nb derived from the analysis of three concentrations (120 nM, 240 nM, 480 nM). (**d**) Determination of bivBC2-$Nb_{AF647\ (sort)}$ binding kinetics on mono or tandem BC2-tag (BC2-BC2-tag). Exemplary sensograms of bivBC2-$Nb_{AF647\ (sort)}$ (120 nM) are shown. The table summarizes the dissociation rate (k_{off}) and standard deviation (S.D.) of bivBC2-$Nb_{AF647\ (sort)}$ derived from the analysis of three concentrations (120 nM, 240nM, 480nM). (**e**) Assessment of staining quality. Labeling of the different nanobody formats was quantified by measuring the signal intensity of mCherry-VIM_{BC2T} expressing cells (left) and non-transfected cells (background, right), (BC2-$Nb_{AF647\ (NHS)}$: n=115; bivBC2-$Nb_{AF647\ (NHS)}$: n=134; BC2-$Nb_{AF647\ (sort)}$: n=150; bivBC2-$Nb_{AF647\ (NHS)}$: n=195). Calculated ratio is shown in **Fig 1c**.

Supplementary Figure 2

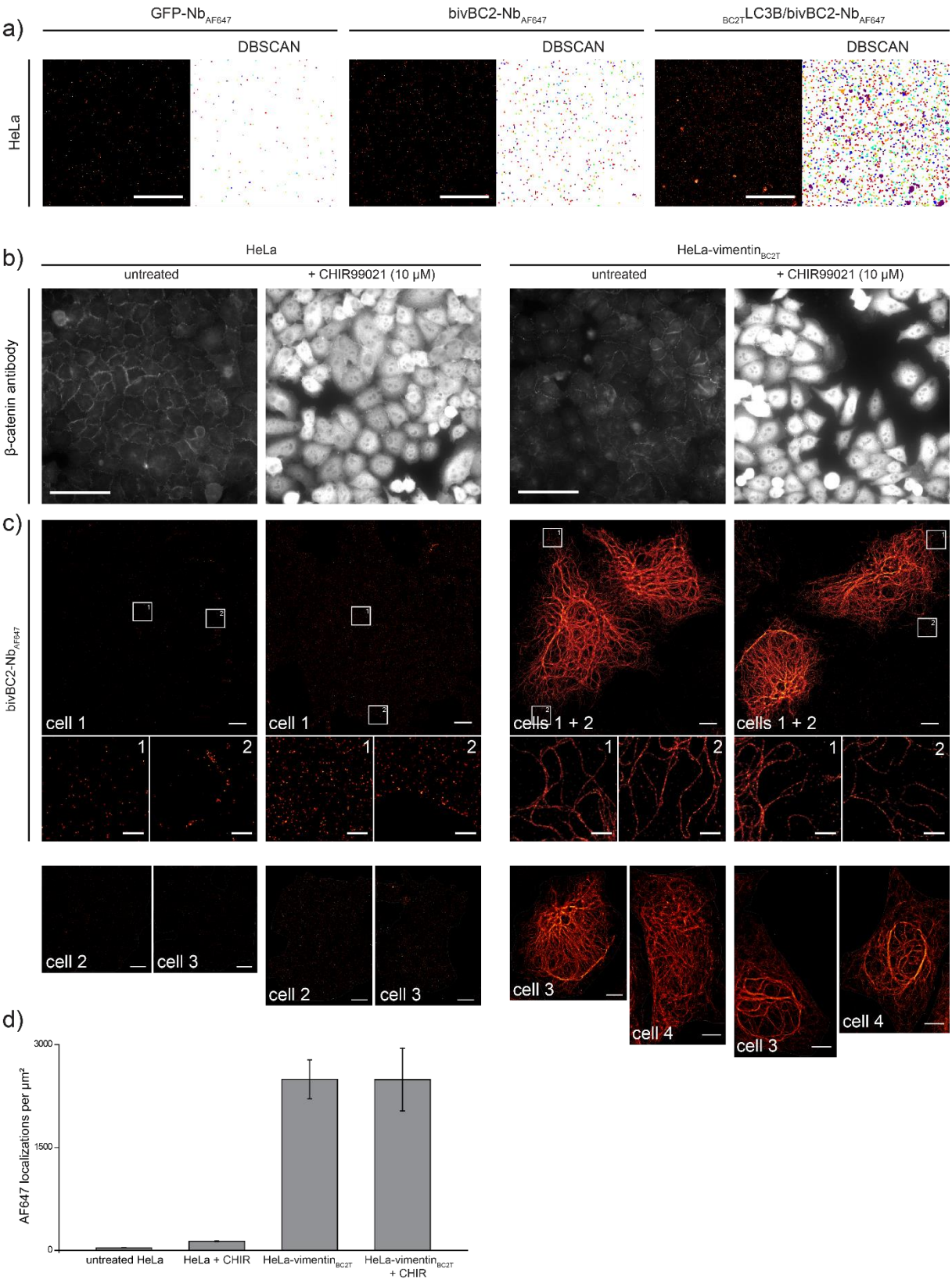

Assessment of bivBC2-Nb$_{AF647}$ staining of endogenous β-catenin (**a**) dSTORM images and corresponding DBSCAN plots, showing only clustered localizations of untransfected

chemically fixed HeLa cells stained with GFP-Nb_{AF647} and bivBC2-Nb_{AF647} , as well chemically fixed HeLa cells transiently expressing $_{BC2T}$LC3B stained with bivBC2-Nb_{AF647} . Scale bars 5 µm. N = 3 cells for each condition. Bar chart summarizing all three conditions is shown in **Fig. 1c**. (**b**) Untransfected HeLa cells (left panel) or HeLa cells expressing C-terminally BC2-tagged vimentin (vimentin$_{BC2T}$) were left untreated or incubated with CHIR99021. Cells were chemically fixed and stained with a conventional anti-β-catenin antibody. Scale bar, 100 µm. (**c**) dSTORM images of cells as described in (**b**) stained with bivBC2-Nb_{AF647}. Scale bars in images 5 µm and 1 µm in insets. Additional dSTORM images used in localization counting analysis (lower panel). (**d**) Localization counts per μm^2 plotted as bar charts for all four conditions. Errors are given as standard deviation (S.D.). Image reconstruction details are given in the **Methods** section.

Supplementary Figure 3

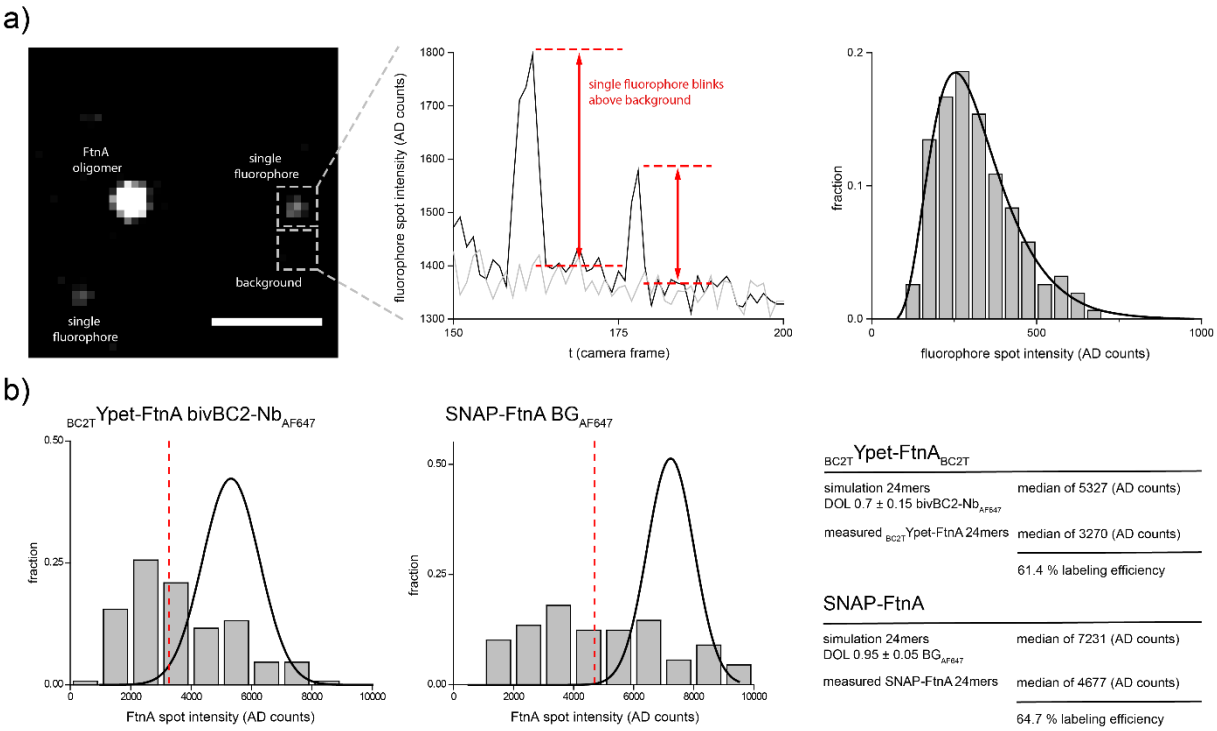

Quantification of completeness of labeling of FtnA oligomers tagged with the BC2- or SNAP-tag. (**a**) Wide-field fluorescence image of a $_{BC2T}$YPET-FtnA oligomer stained with the bivBC2-Nb$_{AF647}$ and single AF647 molecules bound to the slide surface (dashed line). Scale bar 1 µm. Single AF647 molecule intensity trace plotted in integrated intensity AD counts (y axis) over time in frame number (x axis). Blinking events are visible as clear jumps in fluorescence over the background (marker with red arrows and dashed lines). Right panel shows distribution of AF647 single molecule intensities plotted as a relative fraction histogram of integrated intensities with a bin size of 100 AD counts, fitted with a log-normal distribution function. (**b**) Distribution of bivBC2-Nb$_{AF647}$ and AF647-BG stained $_{BC2T}$Ypet-FtnA and SNAP-FtnA spot intensities (in the red channel) plotted as relative fraction histograms of integrated intensity AD counts with a bin size of 1000 AD counts is shown. Red lines represent the median value of both populations and the black curves represent the intensity distribution of simulated theoretical staining maximum. Table summarizes median values of simulations and measured distributions of FtnA oligomers which yields the completeness of labeling for both labeling systems. Corresponding summarizing bar chart is shown in **Fig. 1c**.

Supplementary Figure 4

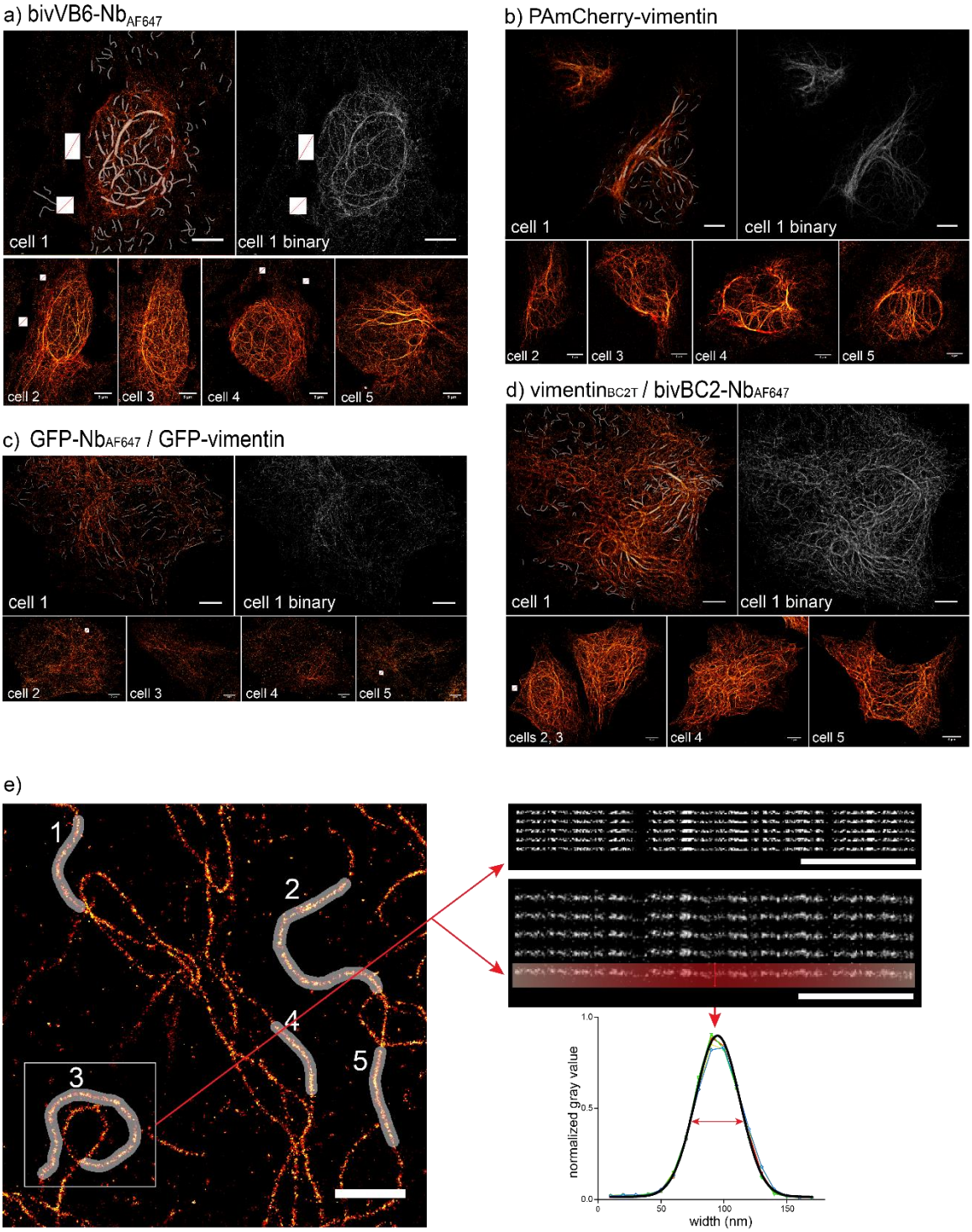

Analysis of PALM/dSTORM images of vimentin filaments in chemically fixed HeLa cells. (**a**) dSTORM images of five cells with native vimentin labeled with bivVB6-Nb$_{AF647}$. (**b**) dSTORM images of five cells expressing GFP-vimentin labeled with GFP-Nb$_{AF647}$. (**c**) dSTORM images of five cells expressing vimentin$_{BC2T}$ labeled with bivBC2-Nb$_{AF647}$. (**d**) PALM images of five cells expressing PAmCherry-vimentin. Scale bars, 5 µm.

Cells were analyzed with a custom-written ImageJ script. Each image was divided into 10 µm x 10 µm sections and 15 filaments per section were analyzed. First images include overlays for all analyzed filaments. All images are calculated corresponding to their individual experimental spatial resolution using the NeNA value. A binary version of each image was used to calculate filament coverages. The workflow is summarized in (**e**); first, lines were drawn along filaments. To minimize the selection and pixilation error, selections were shifted by 0.5 pixels (5 nm) in all directions to obtain five measures in total for each filament by straightening all selections. The middle 3 pixels filaments were taken from the binary image to calculate lengthwise coverage. The coverage of each filament was obtained from averaging the five measurements. To determine the filament width, lengthwise intensity profiles of the five filament selections were fitted with Gaussian curves. The average full width at half maximum (FWHM) of the five selections yields the average filament width. Width and lengthwise fluorophore coverage were analyzed for a total of 676 (bivVB6-Nb_{AF647}), 295 (PAmCherry), 724 (GFP-Nb_{AF647}) and 620 (bivBC2-Nb_{AF647}) filaments as shown in **Fig. 2**. Scale bars, 1 µm. Image reconstruction details are given in the **Methods** section

Supplementary Figure 5

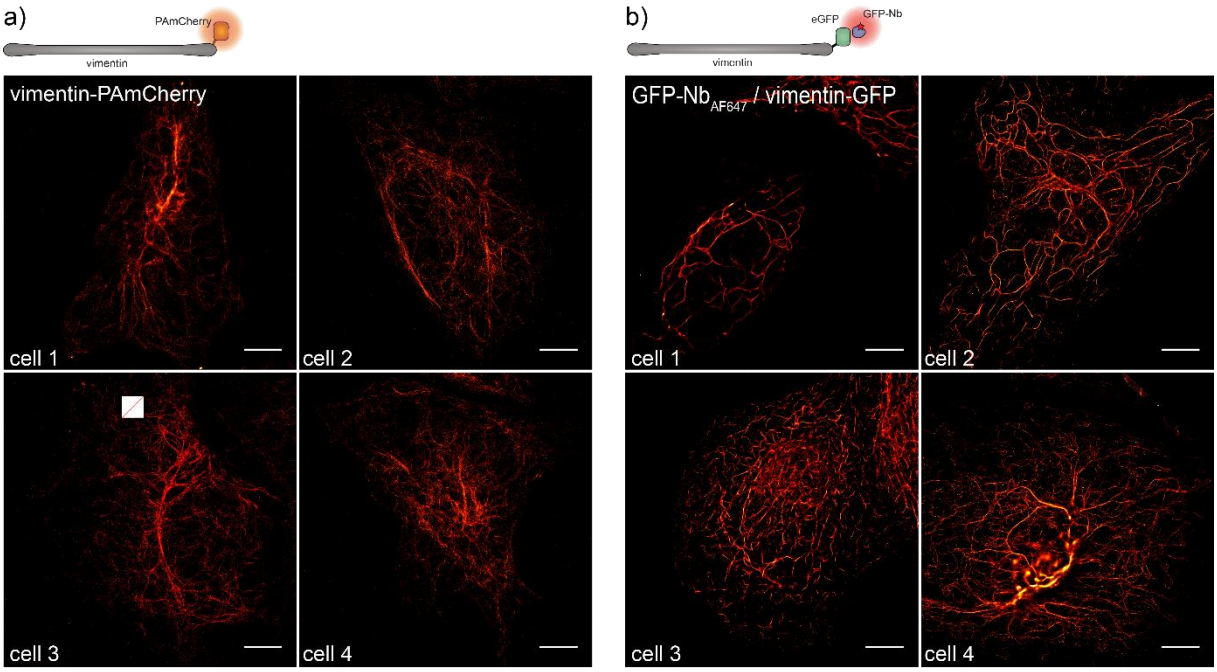

Representative PALM images of chemically fixed HeLa cells transiently expressing (**a**) vimentin C-terminally tagged with photoactivatable mCherry (vimentin-PAmCherry) and (**b**) dSTORM images of chemically fixed HeLa cells transiently expressing vimentin C-terminally with eGFP followed by staining with GFP-Nb_{AF647} are shown. While vimentin-PAmCherry expressing cells are small and show thick vimentin bundles and few thin filaments (cell 1 - 4), vimentin-GFP expressing cells display different phenotypes, from only a few thick filaments (cell 1), networks of uniform medium-thick filaments (cell 2), fragmented filaments (cell 3) and very few cells that appear physiological (cell 4). Scale bars, 5 µm. Image reconstruction details are given in the **Methods** section.

Supplementary Figure 6

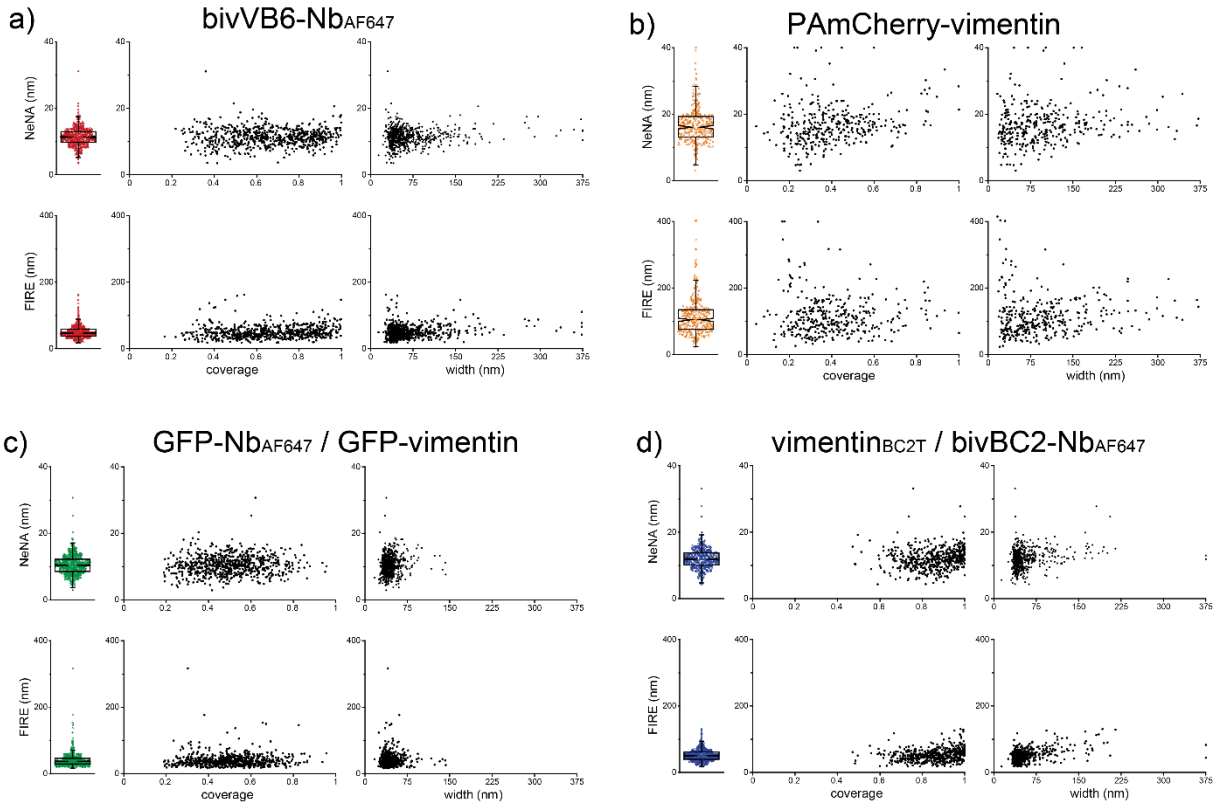

Plots of NeNA and FIRE image resolution analysis for PALM/dSTORM images. Graphs are shown for (**a**) native vimentin labeled with bivVB6-Nb_{AF647}, (**b**) GFP-vimentin labeled with GFP-Nb_{AF647} (**c**) $vimentin_{BC2T}$ labeled with bivBC2-Nb_{AF647} (**d**) PAmCherry-vimentin. Scatter + box plots (the box marks the 3 quartiles and the whiskers mark 95% of all the data) of all calculated NeNA (upper) and FIRE (lower) values as individual filament measurements. Individual NeNA and FIRE values were also plotted against filament coverage (middle, in fraction) and filament width (left, in nm) for each condition. The total number of filament ROIs was 636 (NeNA bivVB6$_{AF647}$), 644 (FIRE bivVB6$_{AF647}$), 347 (NeNA PAmCherry), 353 (FIRE pPAmCherry), 714 (NeNA bivVB6$_{AF647}$), 682 (FIRE bivVB6$_{AF647}$), 514 (NeNA bivBC2-Nb_{AF647}) and 519 (FIRE bivBC2-Nb_{AF647}). Numbers differ slightly from the total n of chosen ROIs as for some ROIs no NeNA or FIRE value could be calculated.

Supplementary Figure 7

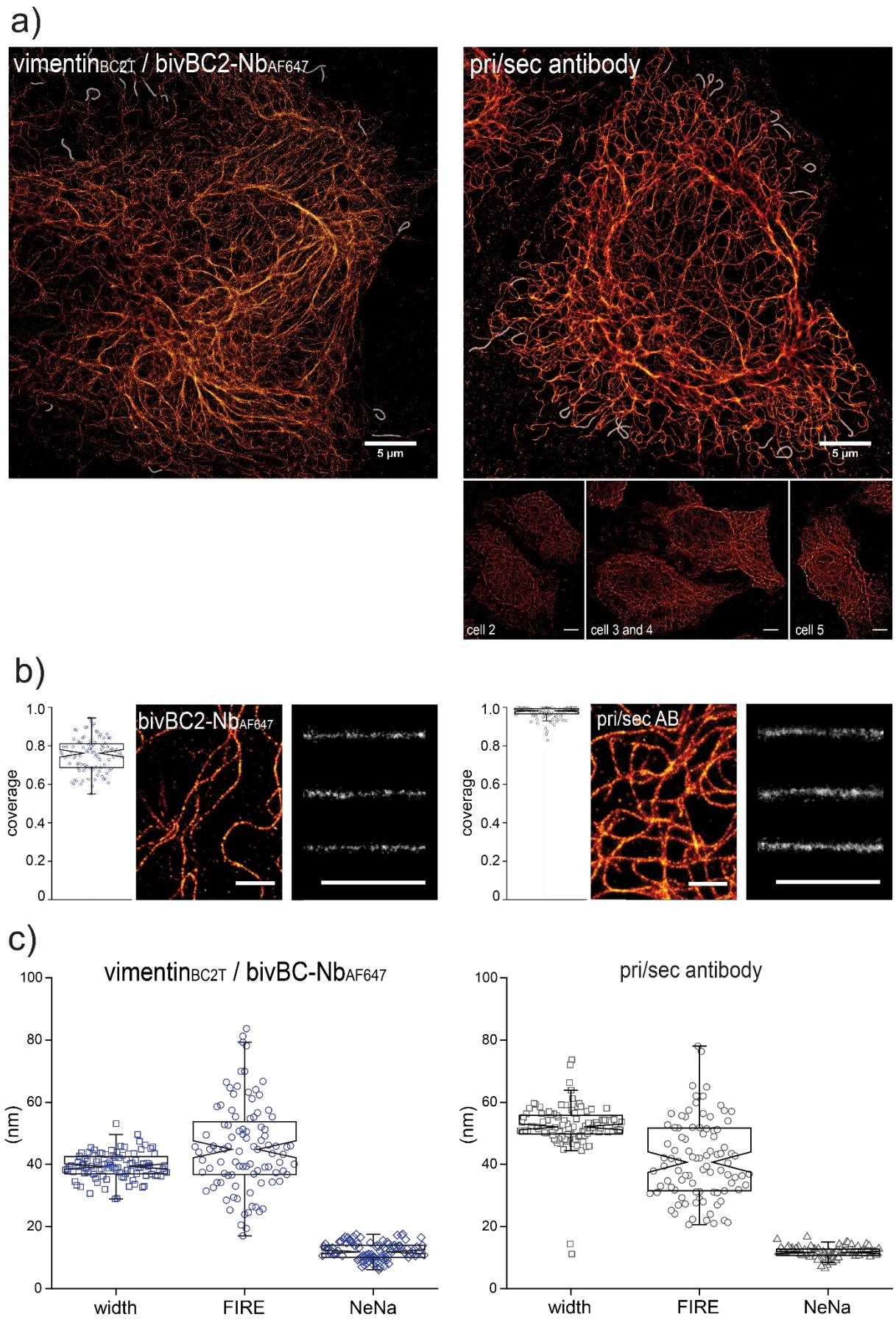

bivBC2-Nb labeling of BC2-tagged vimentin compared to conventional antibody labeling of native vimentin. (**a**) Representative dSTORM images of chemically fixed HeLa cells expressing $vimentin_{BC2T}$ stained with $bivBC2\text{-}Nb_{AF647}$ or chemically fixed HeLa cells where native vimentin was stained with a conventional primary antibody followed by staining with a secondary antibody coupled to AF647. Scale bars, 5 µm. 100 peripheral (single) filaments were analyzed per labeling strategy. (**b**) Coverage analyses of affinity tags. Scatter + box plots (the box marks the 3 quartiles and the whiskers mark 95% of all the data.) of thin filament coverages for $bivBC2\text{-}Nb_{AF647}$ and pri/sec antibody staining plotted as individual filament statistics of fluorophore covered fractions and representative peripheral filaments, before analysis and straightened. Scale bars, 1 µm. 100 filaments were analyzed per method. (**c**) Scatter + box plots (descriptive statistics same as (**b**) of thin filament widths, FIRE values and NeNA values for all conditions. Image reconstruction details are given in the **Methods** section.

Supplementary Figure 8

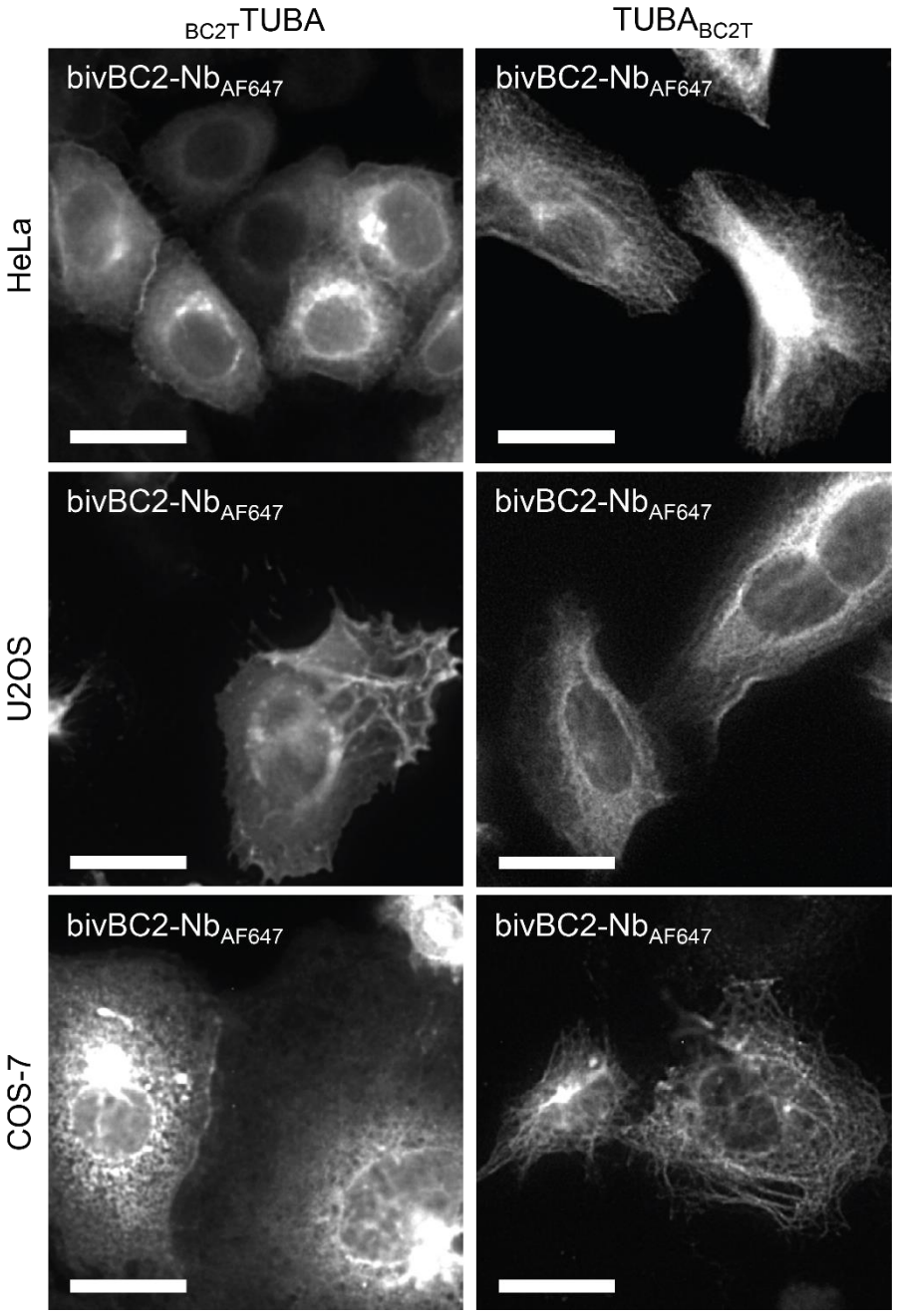

Visualization of N- or C-terminally BC2-tagged tubulin-alpha-1B chain (*TUBA*) in human cells. Immunofluorescence images of chemically fixed HeLa, U2OS and COS-7 cells transiently expressing N- or C-terminally BC2-tagged tubulin ($_{BC2T}$TUBA, TUBA$_{BC2T}$). Cells were stained with the bivBC2-Nb$_{AF647}$. Scale bars, 25 µM.

Supplementary Figure 9

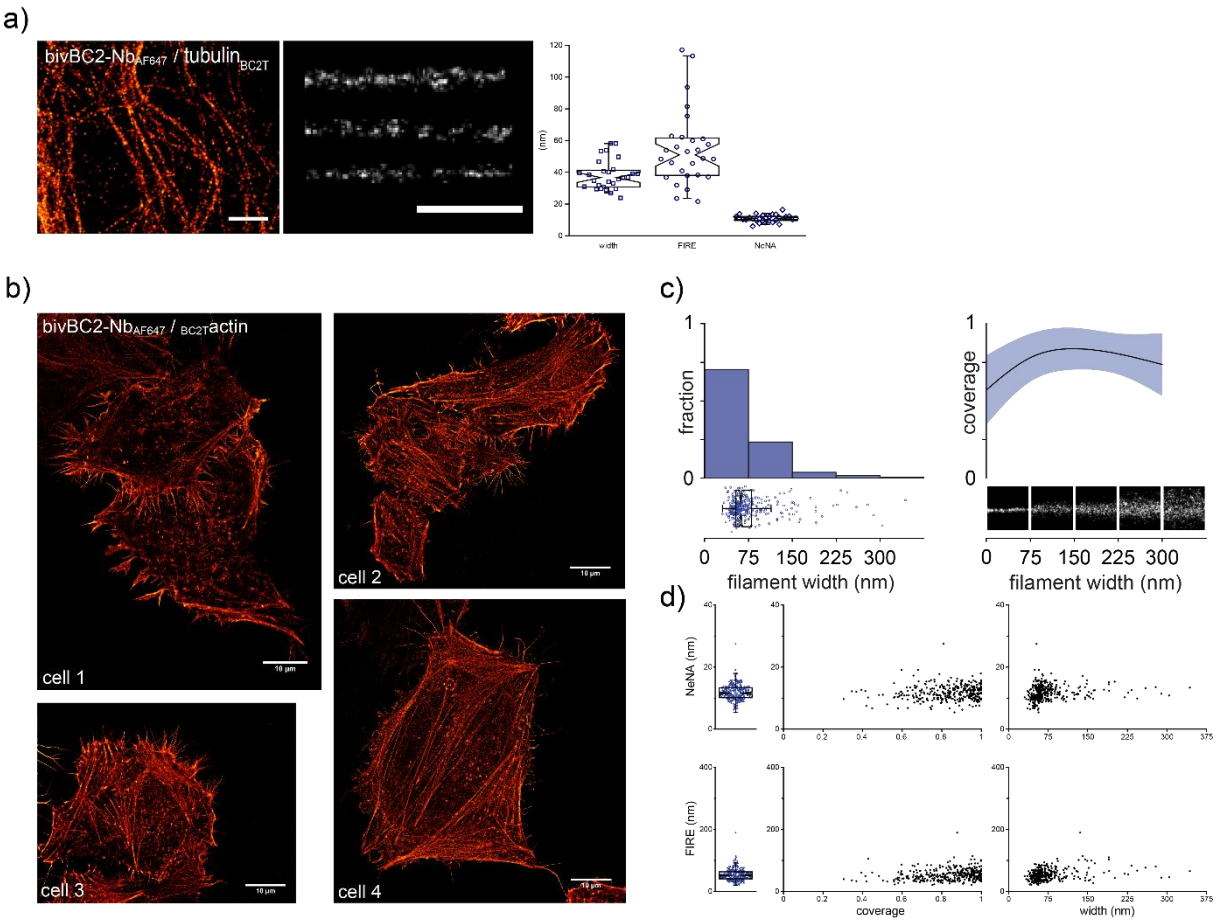

Image resolution measures for tubulin and actin visualized by tubulin$_{BC2T}$ or $_{BC2T}$actin respectively. (**a**) Tubulin fibers of an exemplary HeLa cell expressing tubulin$_{BC2T}$ are straightened like for vimentin in **Supplementary Fig. 4** and **6** and analyzed for filament width yielding a FWHM of 38.2 ± 9.2 nm. (n = 29 fibers). (**b**) dSTORM images of five chemically fixed cells expressing $_{BC2T}$actin labeled with bivBC2-Nb$_{AF647}$. Scale bars, 10 µm. (**c**) Actin filament widths as histograms (left) with a bin size of 75 nm (x axis) plotted against relative fraction (y axis). Full data is represented underneath the histograms as box + scatter plots with the same x axis. The box marks the 3 quartiles and the whiskers mark 95% of all the data. The average lengthwise fluorophore coverage was calculated for each bin and plotted (right) as mean filament width (black line) and standard deviation (colored area) against relative fraction covered by fluorophores (y axis). A total of 351 filaments were analyzed for width and lengthwise fluorophore coverage. (**d**) Scatter + box plots of all calculated NeNA (upper) and FIRE (lower) as individual filament measurements. Individual NeNA and FIRE values were

also plotted against filament coverage (middle, in fraction) and filament width (left, in nm). (Sample size same as in (**c**)). Image reconstruction details are given in the **Methods** section.

Supplementary Figure 10

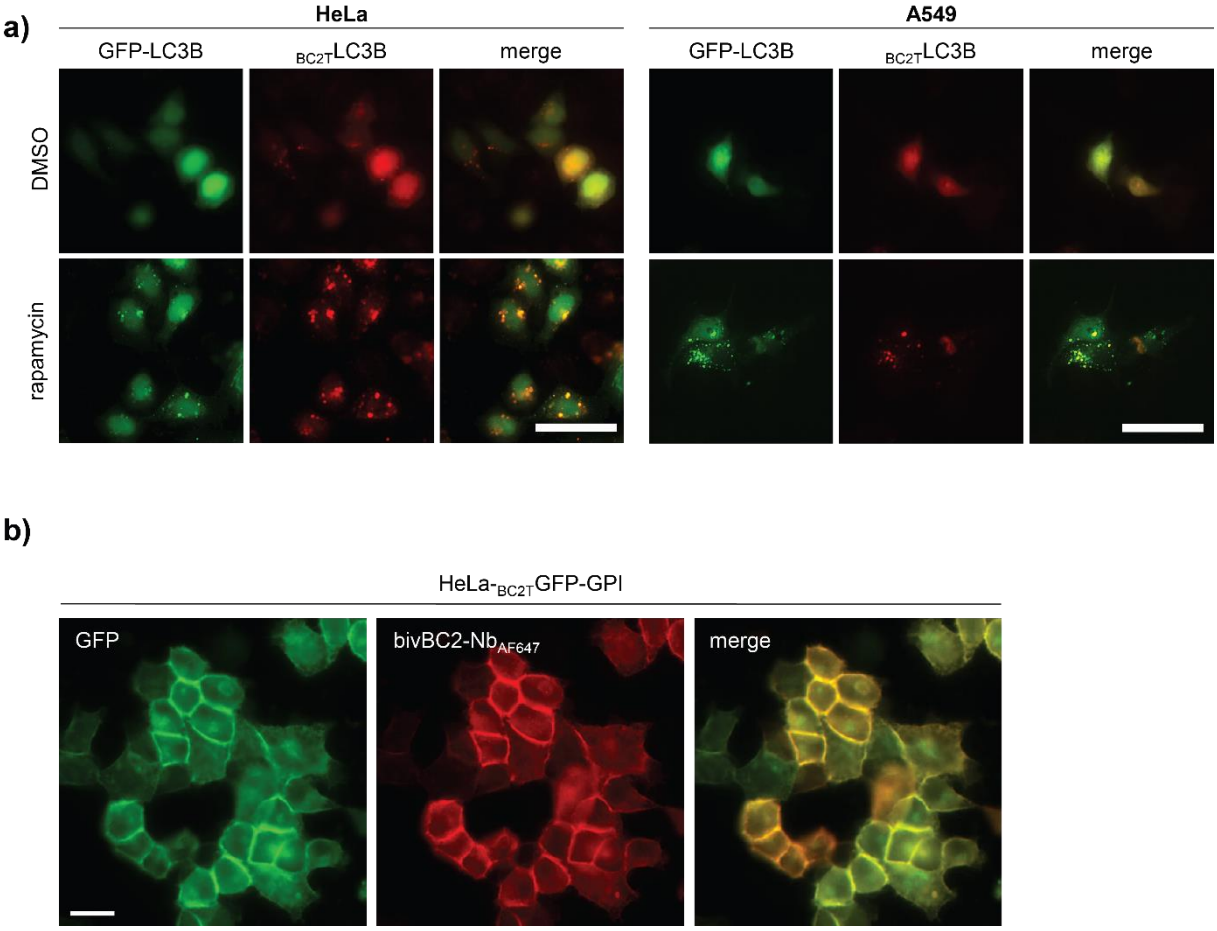

Detection of non-structural proteins with the BC2-tag/bivBC2-Nb system. (**a**) HeLa cells or A549 cells transiently coexpressing GFP-LC3B and $_{BC2T}$LC3B were incubated with 0.5 µM rapamycin to induce autophagy or control treated with 0.1 % DMSO. Shown are images of chemically fixed cells displaying the co-localizing GFP- and bivBC2-Nb$_{AF647}$ signal after 20 h incubation with rapamycin. (**b**) HeLa cells expressing $_{BC2T}$GFP-GPI were chemically fixed and stained with the bivBC2-Nb$_{AF647}$. Shown are representative images displaying co-localizing GFP- and bivBC2-Nb$_{AF647}$ signals at the plasma membrane. Scale bars, 25 µm.

Supplementary Figure 11

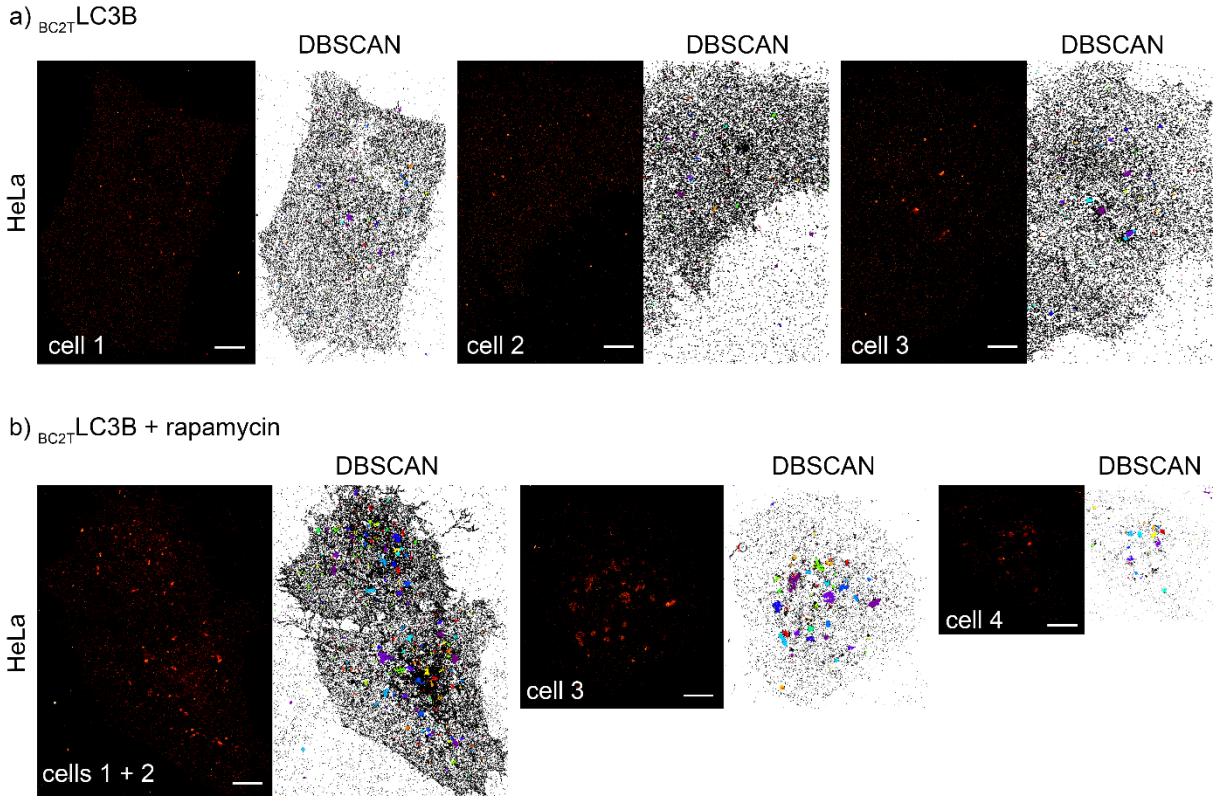

dSTORM images (left) and corresponding DBSCAN plots (right) of all the chemically fixed HeLa cells transiently expressing $_{BC2T}$LC3B that were used for analysis shown in **Fig. 3d**. (**a**) non-treated cells, n = 120 clusters for cell 1, 76 clusters for cell 2 and 146 clusters for cell 3. (**b**) cells treated with rapamycin, n = 203 clusters for cell 1, 74 for cell 2, 85 for cell 2 and 43 for cell 4. Image reconstruction details are given in the **Methods** section. Summarizing bar charts are shown in **Fig. 3d**.

Supplementary Figure 12

a)

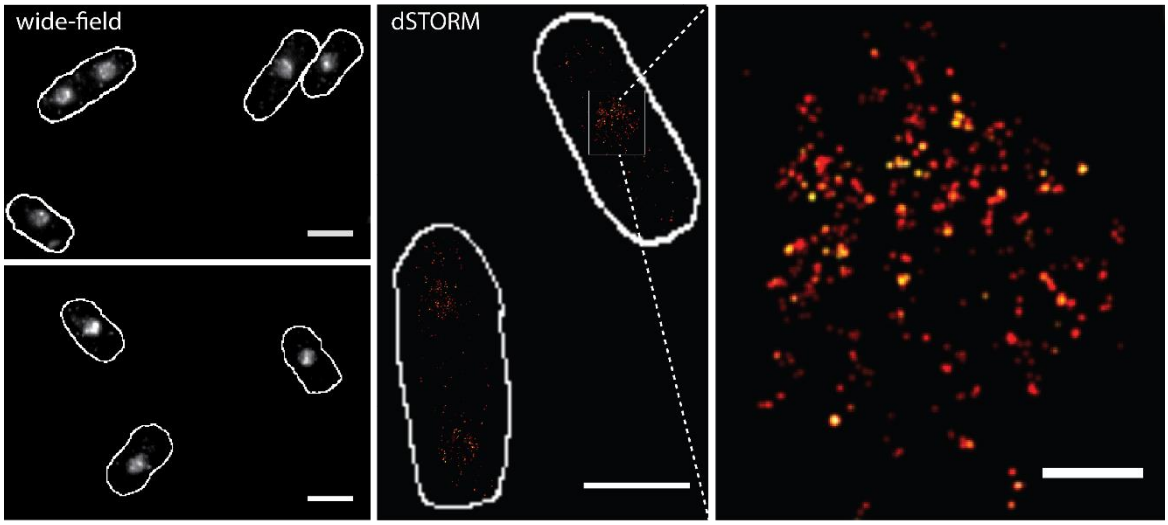

b)

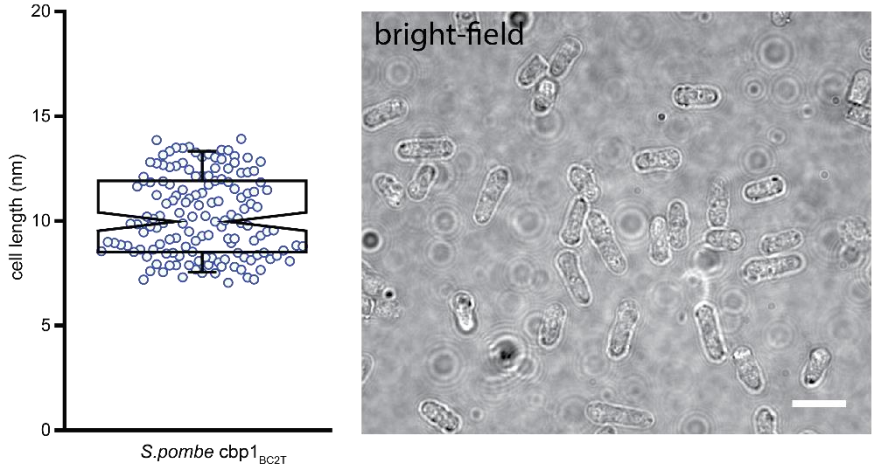

Labeling of the endogenously tagged DNA-binding protein cbp1 in *S. pombe.* (**a**) Shown are exemplary wide-field images of C-terminally tagged cbp1 ($cbp1_{BC2T}$) in chemically fixed *S. pombe* cells, scale bar, 10 µm (left panel). The nuclear $cbp1_{BC2T}$ was then imaged by dSTORM to resolve the distribution of individual proteins within the nucleus, scale bar, 5 µm (inset, scale bar, 0.5 µm). (**b**) The *S. pombe* strain encoding $cbp1_{BC2T}$ at the endogenous locus does not show any growth defects when analyzing the cell length distribution, n = 100 cells, nor abnormalities in the phenotype. Scale bar, 10 µm. Image reconstruction details are given in the **Methods** section.

Supplementary Figure 13

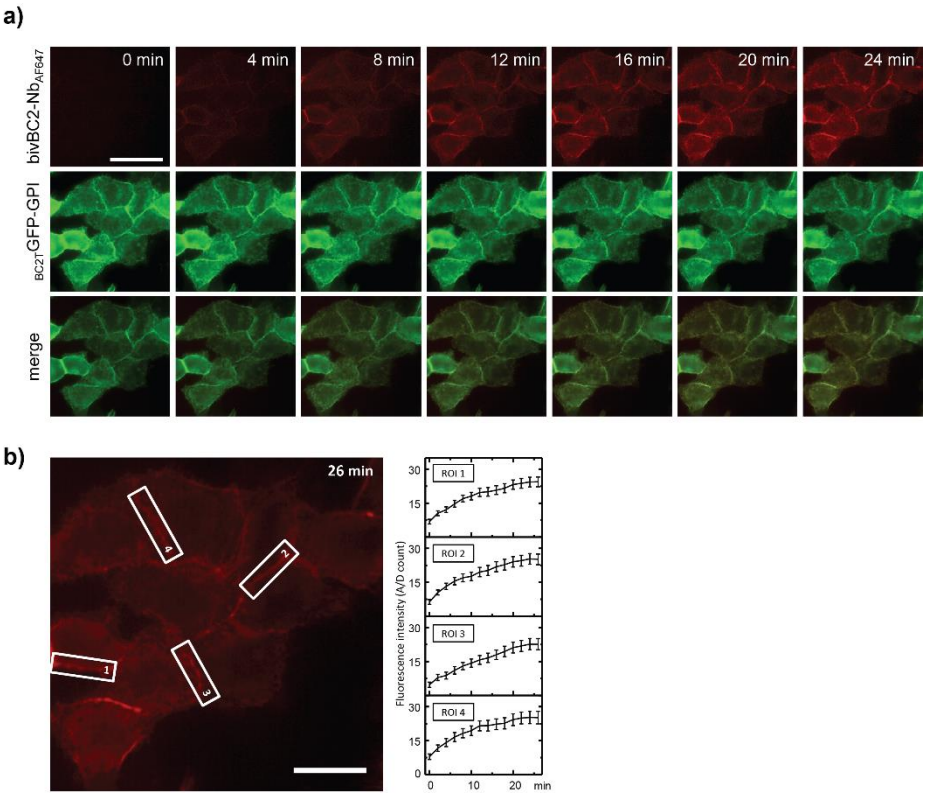

Imaging of BC2-tagged membrane protein in living cells. (**a**) HeLa cells expressing $_{BC2T}$GFP-GPI were subjected to live cell imaging 72 h after transfection. Shown are images displaying the nanobody signal (upper row) and GFP-signal (mid-row) derived from time lapse acquisition starting with the addition of bivBC2-Nb$_{AF647}$. Scale bar, 50 µm. (**b**) The fluorescence staining process was assessed by quantifying the fluorescence intensity increase over time for four different regions of interest (ROI 1 - 4, left) of cellular contact zones. Plotted (right) are the mean intensity values of each ROI and s.e.m. error bars. Scale bar 25 µm.

Supplementary Figure 14

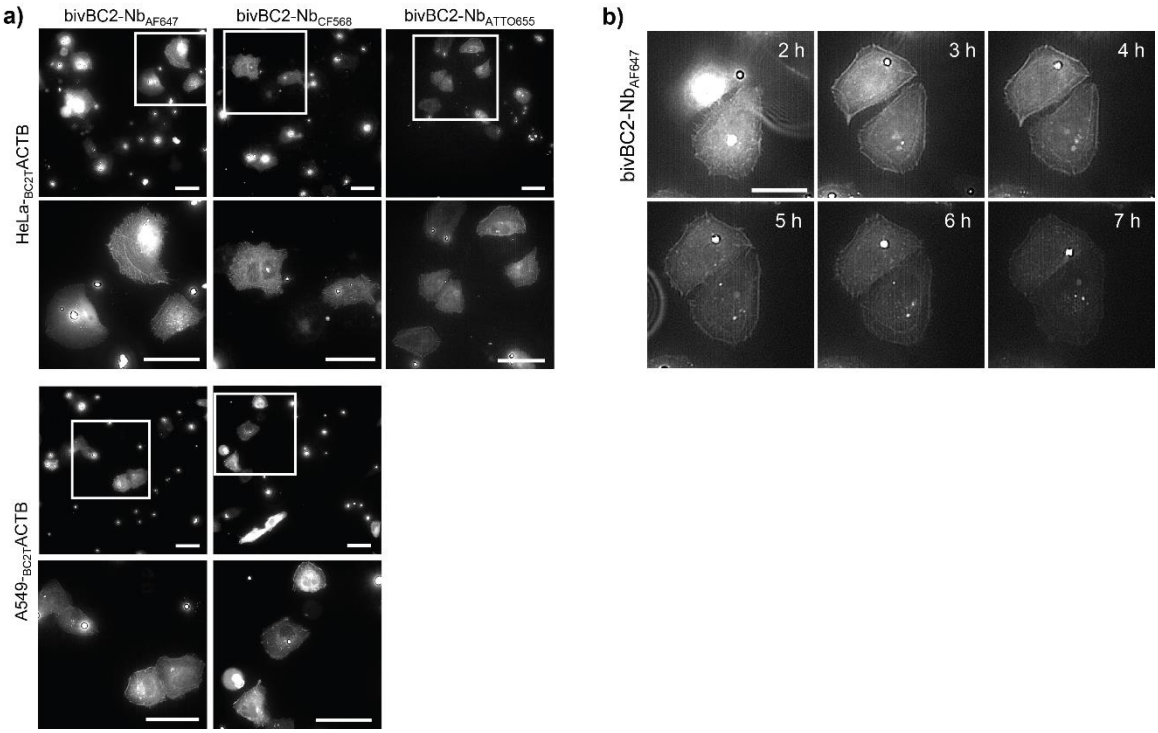

(**a**) Labeling of endogenous BC2-tagged actin upon transduction of bivBC2-Nb conjugated to different fluorescent dyes. Shown are representative images of living HeLa-$_{BC2T}$ACTB cells labeled either with bivBC2-Nb$_{AF647}$, bivBC2-Nb$_{CF568}$ or bivBC2-Nb$_{ATTO655}$ (upper panel) and A549-$_{BC2T}$ACTB cells labeled with either bivBC2-Nb$_{AF647}$ or bivBC2-Nb$_{CF568}$ (lower panel). Selected areas of transduced cells (indicated by white squares) are depicted as enlarged images. Scale bars, 50 µM. (**b**) Time lapse imaging of HeLa-$_{BCT2}$ACTB upon transduction of the bivBC2-Nb$_{AF647}$. Shown are representative images of two nanobody-transduced cells. Scale bar, 25 µm.

Supplementary Figure 15

a) chemically fixed HeLa-$_{BC2T}$ACTB/bivBC2-Nb$_{AF647}$

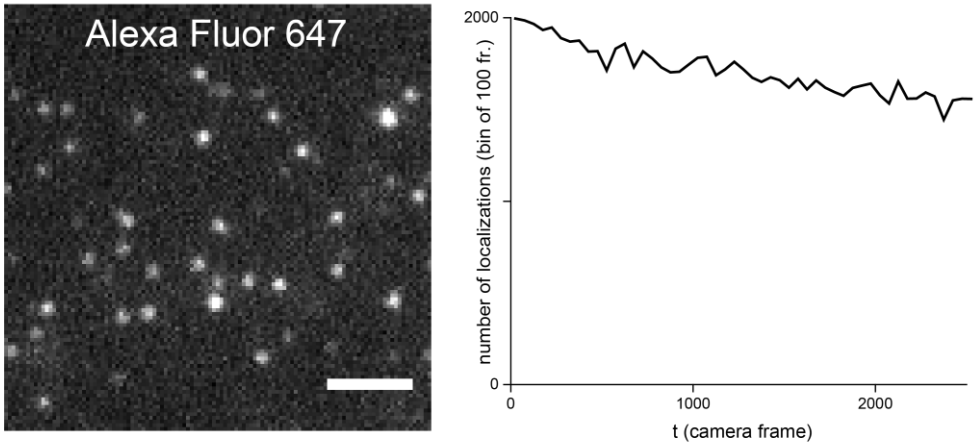

b) living HeLa-$_{BC2T}$ACTB/bivBC2-Nb$_{ATTO655}$

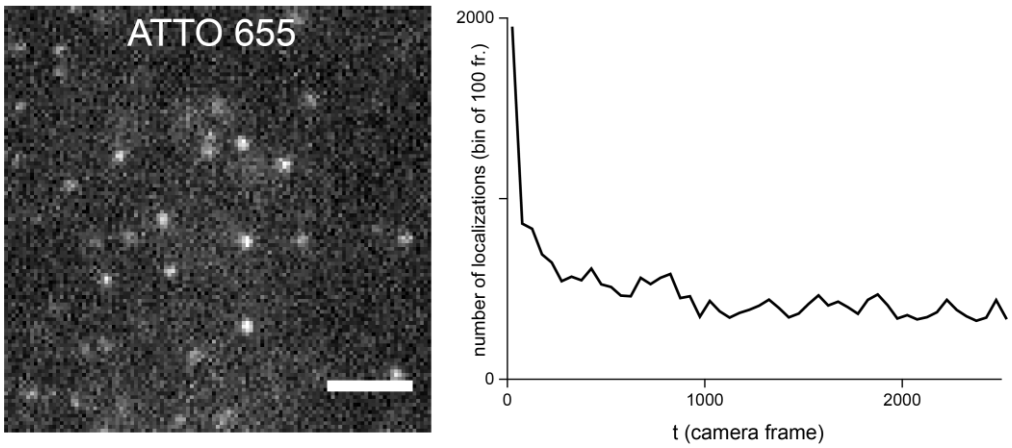

Comparison of ATTO655 and AF647 photophysics under dSTORM imaging conditions in living and chemically fixed cells. (**a**) Representative single imaging frame, extracted from a dSTORM movie of chemically fixed HeLa-$_{BC2T}$ACTB stained with the bivBC2-Nb$_{AF647}$, under standard dSTORM conditions (**Methods**). Line graph representing the absolute frequency count of localizations (y axis) at a bin size of 100 over the first 2500 frames of a 15 x 15 µm ROI of the movie (x axis). (**b**) Representative single imaging frame, extracted from a dSTORM movie of live HeLa-$_{BC2T}$ACTB stained with the bivBC2-Nb$_{ATTO655}$. Line graph representing the absolute frequency count of localizations (y axis) at a bin size of 100 over the first 2500 frames of a 15 x 15 µm ROI of the movie (x axis). Imaging sequences taken from raw data acquisitions of both conditions can be found in **Supplementary Movies 5 and 6.**

References

1. Nieuwenhuizen, R.P. et al. Measuring image resolution in optical nanoscopy. *Nature methods* **10**, 557-562 (2013).
2. Braun, M.B. et al. Peptides in headlock–a novel high-affinity and versatile peptide-binding nanobody for proteomics and microscopy. *Scientific reports* **6** (2016).

Bibliography

[1] P. Nurse, *Genetic control of cell size at cell division in yeast*, Nature **256** (1975) 547, URL: https://doi.org/10.1038/256547a0 (cit. on pp. 6, 146).

[2] H. Asakawa, T. Haraguchi and Y. Hiraoka, *Reconstruction of the kinetochore: a prelude to meiosis*, Cell Division **2** (2007), URL: https://doi.org/10.1186/1747-1028-2-17 (cit. on p. 6).

[3] T. Tomonaga et al., *Characterization of fission yeast cohesin: essential anaphase proteolysis of Rad21 phosphorylated in the S phase*, Genes Development **14** (2000) 2757, URL: https://doi.org/10.1101/gad.832000 (cit. on p. 6).

[4] Y. Kakui, A. Rabinowitz, D. J. Barry and F. Uhlmann, *Condensin-mediated remodeling of the mitotic chromatin landscape in fission yeast*, Nature Genetics **49** (2017) 1553, URL: https://doi.org/10.1038/ng.3938 (cit. on p. 6).

[5] C. L. Rieder, E. A. Davison, L. C. Jensen, L. Cassimeris and E. D. Salmon, *Oscillatory movements of monooriented chromosomes and their position relative to the spindle pole result from the ejection properties of the aster and half-spindle.*, Journal of Cell Biology **103** (1986) 581, URL: https://doi.org/10.1083/jcb.103.2.581 (cit. on p. 7).

[6] H. Ďúranová, M. Požgajová, M. Novotová, N. Lukáč and Z. Kňažická, *FISSION YEAST SCHIZOSACCHAROMYCES POMBE AS A MODEL SYSTEM FOR ULTRASTRUCTURAL INVESTIGATIONS USING TRANSMISSION ELECTRON MICROSCOPY*, Journal of microbiology, biotechnology and food sciences **9** (2019) 160, URL: https://doi.org/10.15414/jmbfs.2019.9.1.160-165 (cit. on p. 7).

[7] S. Tournier, Y. Gachet, V. Buck, J. S. Hyams and J. B. Millar, *Disruption of Astral Microtubule Contact with the Cell Cortex Activates a Bub1, Bub3, and Mad3-dependent Checkpoint in Fission Yeast*, Molecular Biology of the Cell **15** (2004) 3345, URL: https://doi.org/10.1091/mbc.e04-03-0256 (cit. on p. 7).

[8] G. Gay, T. Courtheoux, C. Reyes, S. Tournier and Y. Gachet, *A stochastic model of kinetochore–microtubule attachment accurately describes fission yeast chromosome segregation*, Journal of Cell Biology **196** (2012) 757, URL: https://doi.org/10.1083/jcb.201107124 (cit. on p. 7).

[9] J. C. Meadows et al., *Identification of a Sgo2-Dependent but Mad2-Independent Pathway Controlling Anaphase Onset in Fission Yeast*, Cell Reports **18** (2017) 1422, URL: https://doi.org/10.1016/j.celrep.2017.01.032 (cit. on p. 7).

[10] K. Tanaka and T. Kanbe, *Mitosis in the fission yeast Schizosaccharomyces pombe as revealed by freeze-substitution electron microscopy*, Journal of Cell Science **80** (1986) 253, URL: https://doi.org/10.1242/jcs.80.1.253 (cit. on p. 7).

[11] G. Dey et al., *Closed mitosis requires local disassembly of the nuclear envelope*, Nature **585** (2020) 119, URL: https://doi.org/10.1038/s41586-020-2648-3 (cit. on p. 7).

[12] S. Uzawa et al., *Spindle Pole Body Duplication in Fission Yeast Occurs at the G1/S Boundary but Maturation Is Blocked until Exit from S by an Event Downstream of Cdc10*, Molecular Biology of the Cell **15** (2004) 5219, URL: https://doi.org/10.1091/mbc.e04-03-0255 (cit. on pp. 7, 9).

[13] S. Burns et al., *Structured illumination with particle averaging reveals novel roles for yeast centrosome components during duplication*, eLife **4** (2015), URL: https://doi.org/10.7554/elife.08586 (cit. on p. 7).

[14] E. A. Nigg and A. J. Holland, *Once and only once: mechanisms of centriole duplication and their deregulation in disease*, Nature Reviews Molecular Cell Biology **19** (2018) 297, URL: https://doi.org/10.1038/nrm.2017.127 (cit. on p. 7).

[15] D. Virant et al., *Unraveling the kinetochore nanostructure in Schizosaccharomyces pombe using multi-color single-molecule localization microscopy*, (2021), URL: https://doi.org/10.1101/2021.12.01.469981 (cit. on pp. 8, 53, 152).

[16] C. Nabais, C. Peneda and M. Bettencourt-Dias, *Evolution of centriole assembly*, Current Biology **30** (2020) R494, URL: https://doi.org/10.1016/j.cub.2020.02.036 (cit. on p. 9).

[17] B. Byers and L. Goetsch, *Behavior of spindles and spindle plaques in the cell cycle and conjugation of Saccharomyces cerevisiae*, Journal of Bacteriology **124** (1975) 511, URL: https://doi.org/10.1128/jb.124.1.511-523.1975 (cit. on p. 9).

[18] R. Ding, R. R. West, D. M. Morphew, B. R. Oakley and J. R. McIntosh, *The spindle pole body of Schizosaccharomyces pombe enters and leaves the nuclear envelope as the cell cycle proceeds.*, Molecular Biology of the Cell **8** (1997) 1461, PMID: 9285819, URL: https://doi.org/10.1091/mbc.8.8.1461 (cit. on pp. 9–11).

[19] E. K. McCULLY and C. F. ROBINOW, *Mitosis in the Fission Yeast Schizosaccharomyces Pombe: A Comparative Study with Light and Electron Microscopy*, Journal of Cell Science **9** (1971) 475, URL: https://doi.org/10.1242/jcs.9.2.475 (cit. on p. 9).

[20] C. F. Robinow and J. Marak, *A FIBER APPARATUS IN THE NUCLEUS OF THE YEAST CELL*, Journal of Cell Biology **29** (1966) 129, ISSN: 0021-9525, URL: https://doi.org/10.1083/jcb.29.1.129 (cit. on p. 9).

[21] M. C. Ledbetter and K. R. Porter, *A "MICROTUBULE" IN PLANT CELL FINE STRUCTURE*, Journal of Cell Biology **19** (1963) 239, URL: https://doi.org/10.1083/jcb.19.1.239 (cit. on p. 9).

[22] M. Chalfie and J. N. Thomson,
Organization of neuronal microtubules in the nematode Caenorhabditis elegans.,
Journal of Cell Biology **82** (1979) 278, URL: https://doi.org/10.1083/jcb.82.1.278
(cit. on p. 9).

[23] R. C. Weisenberg,
Microtubule Formation in vitro in Solutions Containing Low Calcium Concentrations,
Science **177** (1972) 1104, URL: https://doi.org/10.1126/science.177.4054.1104
(cit. on p. 9).

[24] R. C. Weisenberg, W. J. Deery and P. J. Dickinson, *Tubulin-nucleotide interactions during the polymerization and depolymerization of microtubules*, Biochemistry **15** (1976) 4248,
URL: https://doi.org/10.1021/bi00664a018 (cit. on p. 9).

[25] R. Ding, K. L. McDonald and J. R. McIntosh, *Three-dimensional reconstruction and analysis of mitotic spindles from the yeast, Schizosaccharomyces pombe.*,
Journal of Cell Biology **120** (1993) 141,
URL: https://doi.org/10.1083/jcb.120.1.141 (cit. on p. 9).

[26] I. M. Cheeseman and A. Desai,
Molecular architecture of the kinetochore–microtubule interface,
Nature Reviews Molecular Cell Biology **9** (2008) 33,
URL: https://doi.org/10.1038/nrm2310 (cit. on p. 9).

[27] R. Wollman et al., *Efficient Chromosome Capture Requires a Bias in the 'Search-and-Capture' Process during Mitotic-Spindle Assembly*,
Current Biology **15** (2005) 828, URL: https://doi.org/10.1016/j.cub.2005.03.019
(cit. on p. 9).

[28] L. Bergen, R. Kuriyama and G. Borisy, *Polarity of microtubules nucleated by centrosomes and chromosomes of Chinese hamster ovary cells in vitro*,
Journal of Cell Biology **84** (1980) 151, URL: https://doi.org/10.1083/jcb.84.1.151
(cit. on p. 9).

[29] E. Kitamura et al., *Kinetochores Generate Microtubules with Distal Plus Ends: Their Roles and Limited Lifetime in Mitosis*, Developmental Cell **18** (2010) 248,
URL: https://doi.org/10.1016/j.devcel.2009.12.018 (cit. on p. 9).

[30] I. Kalinina et al.,
Pivoting of microtubules around the spindle pole accelerates kinetochore capture,
Nature Cell Biology **15** (2012) 82, URL: https://doi.org/10.1038/ncb2640
(cit. on p. 9).

[31] R. Blackwell et al., *Contributions of Microtubule Dynamic Instability and Rotational Diffusion to Kinetochore Capture*, Biophysical Journal **112** (2017) 552,
URL: https://doi.org/10.1016/j.bpj.2016.09.006 (cit. on p. 9).

[32] P. Lara-Gonzalez, F. G. Westhorpe and S. S. Taylor, *The Spindle Assembly Checkpoint*,
Current Biology **22** (2012) R966,
URL: https://doi.org/10.1016/j.cub.2012.10.006 (cit. on p. 9).

[33] K. Luger, A. W. Mäder, R. K. Richmond, D. F. Sargent and T. J. Richmond, *Crystal structure of the nucleosome core particle at 2.8 A resolution*, Nature **389** (1997) 251, URL: https://doi.org/10.1038/38444 (cit. on p. 9).

[34] R. C. Allshire and G. H. Karpen, *Epigenetic regulation of centromeric chromatin: old dogs, new tricks?*, Nature Reviews Genetics **9** (2008) 923, URL: https://doi.org/10.1038/nrg2466 (cit. on p. 10).

[35] B. E. Black and D. W. Cleveland, *Epigenetic Centromere Propagation and the Nature of CENP-A Nucleosomes*, Cell **144** (2011) 471, URL: https://doi.org/10.1016/j.cell.2011.02.002 (cit. on p. 10).

[36] D. Lando et al., *Quantitative single-molecule microscopy reveals that CENP-A Cnp1 deposition occurs during G2 in fission yeast*, Open Biology **2** (2012) 120078, URL: https://doi.org/10.1098/rsob.120078 (cit. on pp. 10, 11, 143, 148, 152).

[37] K. F. Sullivan, M. Hechenberger and K. Masri, *Human CENP-A contains a histone H3 related histone fold domain that is required for targeting to the centromere.*, Journal of Cell Biology **127** (1994) 581, URL: https://doi.org/10.1083/jcb.127.3.581 (cit. on p. 10).

[38] C. W. Carroll, K. J. Milks and A. F. Straight, *Dual recognition of CENP-A nucleosomes is required for centromere assembly*, Journal of Cell Biology **189** (2010) 1143, URL: https://doi.org/10.1083/jcb.201001013 (cit. on pp. 10, 13, 145).

[39] C. W. Carroll, M. C. Silva, K. M. Godek, L. E. Jansen and A. F. Straight, *Centromere assembly requires the direct recognition of CENP-A nucleosomes by CENP-N*, Nature Cell Biology **11** (2009) 896, URL: https://doi.org/10.1038/ncb1899 (cit. on p. 10).

[40] J. Fischböck-Halwachs et al., *The COMA complex interacts with Cse4 and positions Sli15/Ipl1 at the budding yeast inner kinetochore*, eLife **8** (2019), URL: https://doi.org/10.7554/elife.42879 (cit. on pp. 10, 13).

[41] L. Clarke and J. Carbon, *Isolation of a yeast centromere and construction of functional small circular chromosomes*, Nature **287** (1980) 504, URL: https://doi.org/10.1038/287504a0 (cit. on p. 10).

[42] R. Wevrick and H. F. Willard, *Long-range organization of tandem arrays of alpha satellite DNA at the centromeres of human chromosomes: high-frequency array-length polymorphism and meiotic stability.*, Proceedings of the National Academy of Sciences **86** (1989) 9394, URL: https://doi.org/10.1073/pnas.86.23.9394 (cit. on p. 10).

[43] P. S. Maddox, K. Oegema, A. Desai and I. M. Cheeseman, *"Holo"er than thou: Chromosome segregation and kinetochore function in C. elegans*, Chromosome Research **12** (2004) 641, URL: https://doi.org/10.1023/b:chro.0000036588.42225.2f (cit. on p. 10).

[44] V. Wood et al., *The genome sequence of Schizosaccharomyces pombe*, Nature **415** (2002) 871, URL: https://doi.org/10.1038/nature724 (cit. on p. 10).

[45] M. Murillo-Pineda and L. E. Jansen, *Genetics, epigenetics and back again: Lessons learned from neocentromeres*, Experimental Cell Research **389** (2020) 111909, URL: https://doi.org/10.1016/j.yexcr.2020.111909 (cit. on p. 10).

[46] S. Henikoff and T. Furuyama, *Epigenetic Inheritance of Centromeres*, Cold Spring Harbor Symposia on Quantitative Biology **75** (2010) 51, URL: https://doi.org/10.1101/sqb.2010.75.001 (cit. on p. 10).

[47] N. STEINER, *A novel epigenetic effect can alter centromere function in fission yeast*, Cell **79** (1994) 865, URL: https://doi.org/10.1016/0092-8674(94)90075-2 (cit. on pp. 10, 11).

[48] V. K. Ngan and L. Clarke, *The centromere enhancer mediates centromere activation in Schizosaccharomyces pombe*, Molecular and Cellular Biology **17** (1997) 3305, URL: https://doi.org/10.1128/mcb.17.6.3305 (cit. on pp. 10, 11).

[49] M. Winey et al., *Three-dimensional ultrastructural analysis of the Saccharomyces cerevisiae mitotic spindle.*, Journal of Cell Biology **129** (1995) 1601, URL: https://doi.org/10.1083/jcb.129.6.1601 (cit. on p. 10).

[50] W. D. Jiang and P. Philippsen, *Purification of a protein binding to the CDEI subregion of Saccharomyces cerevisiae centromere DNA*, Molecular and Cellular Biology **9** (1989) 5585, URL: https://doi.org/10.1128/mcb.9.12.5585-5593.1989 (cit. on p. 10).

[51] R. E. Baker and K. Rogers, *Genetic and Genomic Analysis of the AT-Rich Centromere DNA Element II of Saccharomyces cerevisiae*, Genetics **171** (2005) 1463, URL: https://doi.org/10.1534/genetics.105.046458 (cit. on p. 10).

[52] B. Jehn, R. Niedenthal and J. H. Hegemann, *In vivo analysis of the Saccharomyces cerevisiae centromere CDEIII sequence: requirements for mitotic chromosome segregation*, Molecular and Cellular Biology **11** (1991) 5212, URL: https://doi.org/10.1128/mcb.11.10.5212-5221.1991 (cit. on p. 10).

[53] U.-S. Cho and S. C. Harrison, *Ndc10 is a platform for inner kinetochore assembly in budding yeast*, Nature Structural & Molecular Biology **19** (2011) 48, URL: https://doi.org/10.1038/nsmb.2178 (cit. on p. 10).

[54] J. F. Partridge, K. S. Scott, A. J. Bannister, T. Kouzarides and R. C. Allshire, *cis-Acting DNA from Fission Yeast Centromeres Mediates Histone H3 Methylation and Recruitment of Silencing Factors and Cohesin to an Ectopic Site*, Current Biology **12** (2002) 1652, URL: https://doi.org/10.1016/s0960-9822(02)01177-6 (cit. on p. 10).

[55] T. A. Volpe et al.,
Regulation of Heterochromatic Silencing and Histone H3 Lysine-9 Methylation by RNAi,
Science **297** (2002) 1833, URL: https://doi.org/10.1126/science.1074973
(cit. on p. 10).

[56] E. S. Choi et al., *Factors That Promote H3 Chromatin Integrity during Transcription Prevent Promiscuous Deposition of CENP-ACnp1 in Fission Yeast*,
PLoS Genetics **8** (2012) e1002985, ed. by B. A. Sullivan,
URL: https://doi.org/10.1371/journal.pgen.1002985 (cit. on p. 11).

[57] A. G. Castillo et al.,
Telomeric Repeats Facilitate CENP-ACnp1 Incorporation via Telomere Binding Proteins,
PLoS ONE **8** (2013) e69673, ed. by B. A. Sullivan,
URL: https://doi.org/10.1371/journal.pone.0069673 (cit. on p. 11).

[58] O. Moreno-Moreno, M. Torras-Llort and F. Azorin, *Proteolysis restricts localization of CID, the centromere-specific histone H3 variant of Drosophila, to centromeres*,
Nucleic Acids Research **34** (2006) 6247, URL: https://doi.org/10.1093/nar/gkl902
(cit. on p. 11).

[59] P. Heun et al., *Mislocalization of the Drosophila Centromere-Specific Histone CID Promotes Formation of Functional Ectopic Kinetochores*, Developmental Cell **10** (2006) 303,
URL: https://doi.org/10.1016/j.devcel.2006.01.014 (cit. on p. 11).

[60] A. O. Bailey et al., *Posttranslational modification of CENP-A influences the conformation of centromeric chromatin*, Proceedings of the National Academy of Sciences **110** (2013) 11827,
URL: https://doi.org/10.1073/pnas.1300325110 (cit. on p. 11).

[61] A. J. Holland and D. W. Cleveland,
Losing balance: the origin and impact of aneuploidy in cancer, EMBO reports **13** (2012) 501,
URL: https://doi.org/10.1038/embor.2012.55 (cit. on pp. 11, 143).

[62] B. McClintock, *THE STABILITY OF BROKEN ENDS OF CHROMOSOMES IN ZEA MAYS*,
Genetics **26** (1941) 234, URL: https://doi.org/10.1093/genetics/26.2.234
(cit. on p. 11).

[63] J. S. Waye and H. F. Willard, *Human beta satellite DNA: genomic organization and sequence definition of a class of highly repetitive tandem DNA.*,
Proceedings of the National Academy of Sciences **86** (1989) 6250,
URL: https://doi.org/10.1073/pnas.86.16.6250 (cit. on p. 11).

[64] B. Vissel and K. Choo,
Human alpha satellite DNA - consensus sequence and conserved regions,
Nucleic Acids Research **15** (1987) 6751,
URL: https://doi.org/10.1093/nar/15.16.6751 (cit. on p. 11).

[65] L. Manuelidis, *Chromosomal localization of complex and simple repeated human DNAs*,
Chromosoma **66** (1978) 23, URL: https://doi.org/10.1007/bf00285813 (cit. on p. 11).

[66] B. F. McEwen et al., *CENP-E Is Essential for Reliable Bioriented Spindle Attachment, but Chromosome Alignment Can Be Achieved via Redundant Mechanisms in Mammalian Cells*,
Molecular Biology of the Cell **12** (2001) 2776, ed. by T. Salmon,
URL: https://doi.org/10.1091/mbc.12.9.2776 (cit. on p. 11).

[67] A. L. Pidoux and R. C. Allshire, *The role of heterochromatin in centromere function*, Philosophical Transactions of the Royal Society B: Biological Sciences **360** (2005) 569, URL: https://doi.org/10.1098/rstb.2004.1611 (cit. on p. 11).

[68] M. D. Blower, B. A. Sullivan and G. H. Karpen, *Conserved Organization of Centromeric Chromatin in Flies and Humans*, Developmental Cell **2** (2002) 319, URL: https://doi.org/10.1016/s1534-5807(02)00135-1 (cit. on p. 11).

[69] S. A. Ribeiro et al., *A super-resolution map of the vertebrate kinetochore*, Proceedings of the National Academy of Sciences **107** (2010) 10484, URL: https://doi.org/10.1073/pnas.1002325107 (cit. on p. 11).

[70] T. Hayashi et al., *Mis16 and Mis18 Are Required for CENP-A Loading and Histone Deacetylation at Centromeres*, Cell **118** (2004) 715, URL: https://doi.org/10.1016/j.cell.2004.09.002 (cit. on p. 11).

[71] T. Hayashi et al., *Schizosaccharomyces pombe centromere protein Mis19 links Mis16 and Mis18 to recruit CENP-A through interacting with NMD factors and the SWI/SNF complex*, Genes to Cells **19** (2014) 541, URL: https://doi.org/10.1111/gtc.12152 (cit. on p. 11).

[72] H. Hirai, K. Arai, R. Kariyazono, M. Yamamoto and M. Sato, *The Kinetochore Protein Kis1/Eic1/Mis19 Ensures the Integrity of Mitotic Spindles through Maintenance of Kinetochore Factors Mis6/CENP-I and CENP-A*, PLoS ONE **9** (2014) e111905, ed. by D. Cimini, URL: https://doi.org/10.1371/journal.pone.0111905 (cit. on p. 11).

[73] L. Subramanian, N. R. T. Toda, J. Rappsilber and R. C. Allshire, *Eic1 links Mis18 with the CCAN/Mis6/Ctf19 complex to promote CENP-A assembly*, Open Biology **4** (2014) 140043, URL: https://doi.org/10.1098/rsob.140043 (cit. on p. 11).

[74] E. M. Dunleavy et al., *A NASP (N1/N2)-Related Protein, Sim3, Binds CENP-A and Is Required for Its Deposition at Fission Yeast Centromeres*, Molecular Cell **28** (2007) 1029, URL: https://doi.org/10.1016/j.molcel.2007.10.010 (cit. on p. 11).

[75] D. R. Foltz et al., *Centromere-Specific Assembly of CENP-A Nucleosomes Is Mediated by HJURP*, Cell **137** (2009) 472, URL: https://doi.org/10.1016/j.cell.2009.02.039 (cit. on p. 11).

[76] E. M. Dunleavy et al., *HJURP Is a Cell-Cycle-Dependent Maintenance and Deposition Factor of CENP-A at Centromeres*, Cell **137** (2009) 485, URL: https://doi.org/10.1016/j.cell.2009.02.040 (cit. on p. 11).

[77] M. Shuaib, K. Ouararhni, S. Dimitrov and A. Hamiche, *HJURP binds CENP-A via a highly conserved N-terminal domain and mediates its deposition at centromeres*, Proceedings of the National Academy of Sciences **107** (2010) 1349, URL: https://doi.org/10.1073/pnas.0913709107 (cit. on p. 11).

[78] E. M. Dunleavy, G. Almouzni and G. H. Karpen, *H3.3 is deposited at centromeres in S phase as a placeholder for newly assembled CENP-A in G1 phase*, Nucleus **2** (2011) 146, URL: https://doi.org/10.4161/nucl.2.2.15211 (cit. on p. 11).

[79] R. C. Allshire and K. Ekwall, *Epigenetic Regulation of Chromatin States in Schizosaccharomyces pombe*, Cold Spring Harbor Perspectives in Biology **7** (2015) a018770, URL: https://doi.org/10.1101/cshperspect.a018770 (cit. on p. 11).

[80] A. L. Pidoux et al., *Fission Yeast Scm3: A CENP-A Receptor Required for Integrity of Subkinetochore Chromatin*, Molecular Cell **33** (2009) 299, URL: https://doi.org/10.1016/j.molcel.2009.01.019 (cit. on p. 11).

[81] J. S. Williams, T. Hayashi, M. Yanagida and P. Russell, *Fission Yeast Scm3 Mediates Stable Assembly of Cnp1/CENP-A into Centromeric Chromatin*, Molecular Cell **33** (2009) 287, URL: https://doi.org/10.1016/j.molcel.2009.01.017 (cit. on p. 11).

[82] P. Meraldi, A. McAinsh, E. Rheinbay and P. Sorger, Genome Biology **7** (2006) R23, URL: https://doi.org/10.1186/gb-2006-7-3-r23 (cit. on pp. 13, 146).

[83] J. J. Hooff, E. Tromer, L. M. Wijk, B. Snel and G. J. Kops, *Evolutionary dynamics of the kinetochore network in eukaryotes as revealed by comparative genomics*, EMBO reports **18** (2017) 1559, URL: https://doi.org/10.15252/embr.201744102 (cit. on pp. 13, 14, 146).

[84] S. D'Archivio and B. Wickstead, *Trypanosome outer kinetochore proteins suggest conservation of chromosome segregation machinery across eukaryotes*, Journal of Cell Biology **216** (2016) 379, URL: https://doi.org/10.1083/jcb.201608043 (cit. on pp. 13, 146).

[85] H. S. Malik and S. Henikoff, *Adaptive Evolution of Cid, a Centromere-Specific Histone in Drosophila*, Genetics **157** (2001) 1293, URL: https://doi.org/10.1093/genetics/157.3.1293 (cit. on pp. 13, 147).

[86] R. E. Baker and K. Rogers, *Phylogenetic Analysis of Fungal Centromere H3 Proteins*, Genetics **174** (2006) 1481, URL: https://doi.org/10.1534/genetics.106.062794 (cit. on pp. 13, 147).

[87] M. Ravi et al., *The Rapidly Evolving Centromere-Specific Histone Has Stringent Functional Requirements in Arabidopsis thaliana*, Genetics **186** (2010) 461, URL: https://doi.org/10.1534/genetics.110.120337 (cit. on pp. 13, 147).

[88] H. Saitoh et al., *CENP-C, an autoantigen in scleroderma, is a component of the human inner kinetochore plate*, Cell **70** (1992) 115, URL: https://doi.org/10.1016/0092-8674(92)90538-n (cit. on pp. 13, 147).

[89] M.-S. Kwon, T. Hori, M. Okada and T. Fukagawa, *CENP-C Is Involved in Chromosome Segregation, Mitotic Checkpoint Function, and Kinetochore Assembly*, Molecular Biology of the Cell **18** (2007) 2155, ed. by W. Bickmore, URL: https://doi.org/10.1091/mbc.e07-01-0045 (cit. on pp. 13, 147).

[90] K. Klare et al., *CENP-C is a blueprint for constitutive centromere-associated network assembly within human kinetochores*, Journal of Cell Biology **210** (2015) 11, URL: https://doi.org/10.1083/jcb.201412028 (cit. on pp. 13, 147).

[91] T. Nishino et al., *CENP-T-W-S-X Forms a Unique Centromeric Chromatin Structure with a Histone-like Fold*, Cell **148** (2012) 487, URL: https://doi.org/10.1016/j.cell.2011.11.061 (cit. on pp. 13, 14, 147).

[92] T. Hori, M. Okada, K. Maenaka and T. Fukagawa, *CENP-O Class Proteins Form a Stable Complex and Are Required for Proper Kinetochore Function*, Molecular Biology of the Cell **19** (2008) 843, ed. by T. Salmon, URL: https://doi.org/10.1091/mbc.e07-06-0556 (cit. on pp. 13, 147).

[93] T. K. Barth et al., *Identification of novel Drosophila centromere-associated proteins*, PROTEOMICS **14** (2014) 2167, URL: https://doi.org/10.1002/pmic.201400052 (cit. on p. 13).

[94] I. A. Drinnenberg, S. Henikoff and H. S. Malik, *Evolutionary Turnover of Kinetochore Proteins: A Ship of Theseus?*, Trends in Cell Biology **26** (2016) 498, URL: https://doi.org/10.1016/j.tcb.2016.01.005 (cit. on p. 13).

[95] S. Heeger et al., *Genetic interactions of separase regulatory subunits reveal the diverged Drosophila Cenp-C homolog*, Genes Development **19** (2005) 2041, URL: https://doi.org/10.1101/gad.347805 (cit. on p. 13).

[96] A. A. Ye, S. Cane and T. J. Maresca, *Chromosome biorientation produces hundreds of piconewtons at a metazoan kinetochore*, Nature Communications **7** (2016), URL: https://doi.org/10.1038/ncomms13221 (cit. on p. 13).

[97] E. Screpanti et al., *Direct Binding of Cenp-C to the Mis12 Complex Joins the Inner and Outer Kinetochore*, Current Biology **21** (2011) 391, URL: https://doi.org/10.1016/j.cub.2010.12.039 (cit. on pp. 13, 145).

[98] Y. N. Dimitrova, S. Jenni, R. Valverde, Y. Khin and S. C. Harrison, *Structure of the MIND Complex Defines a Regulatory Focus for Yeast Kinetochore Assembly*, Cell **167** (2016) 1014, URL: https://doi.org/10.1016/j.cell.2016.10.011 (cit. on pp. 13–15, 145, 148).

[99] K. Song, B. Gronemeyer, W. Lu, E. Eugster and J. E. Tomkiel, *Mutational Analysis of the Central Centromere Targeting Domain of Human Centromere Protein C, (CENP-C)*, Experimental Cell Research **275** (2002) 81, URL: https://doi.org/10.1006/excr.2002.5495 (cit. on p. 13).

[100] K. J. Milks, B. Moree and A. F. Straight, *Dissection of CENP-C–directed Centromere and Kinetochore Assembly*, Molecular Biology of the Cell **20** (2009) 4246, ed. by K. S. Bloom, URL: https://doi.org/10.1091/mbc.e09-05-0378 (cit. on p. 13).

[101] K. Tanaka, H. L. Chang, A. Kagami and Y. Watanabe, *CENP-C Functions as a Scaffold for Effectors with Essential Kinetochore Functions in Mitosis and Meiosis*, Developmental Cell **17** (2009) 334, URL: https://doi.org/10.1016/j.devcel.2009.08.004 (cit. on pp. 13, 14, 147).

[102] H. Kato et al., *A Conserved Mechanism for Centromeric Nucleosome Recognition by Centromere Protein CENP-C*, Science **340** (2013) 1110, URL: https://doi.org/10.1126/science.1235532 (cit. on p. 13).

[103] J. K. Chik et al., *Structures of CENP-C cupin domains at regional centromeres reveal unique patterns of dimerization and recruitment functions for the inner pocket*, Journal of Biological Chemistry **294** (2019) 14119, URL: https://doi.org/10.1074/jbc.ra119.008464 (cit. on pp. 13, 14, 147).

[104] R. L. Cohen et al., *Structural and Functional Dissection of Mif2p, a Conserved DNA-binding Kinetochore Protein*, Molecular Biology of the Cell **19** (2008) 4480, ed. by K. S. Bloom, URL: https://doi.org/10.1091/mbc.e08-03-0297 (cit. on p. 13).

[105] P. K. Allu et al., *Structure of the Human Core Centromeric Nucleosome Complex*, Current Biology **29** (2019) 2625, URL: https://doi.org/10.1016/j.cub.2019.06.062 (cit. on p. 13).

[106] S. Westermann et al., *Architecture of the budding yeast kinetochore reveals a conserved molecular core*, Journal of Cell Biology **163** (2003) 215, URL: https://doi.org/10.1083/jcb.200305100 (cit. on pp. 13, 14).

[107] D. Meeks-Wagner, J. S. Wood, B. Garvik and L. H. Hartwell, *Isolation of two genes that affect mitotic chromosome transmission in S. cerevisiae*, Cell **44** (1986) 53, URL: https://doi.org/10.1016/0092-8674(86)90484-8 (cit. on pp. 13, 14, 147).

[108] D.-U. Kim et al., *Analysis of a genome-wide set of gene deletions in the fission yeast Schizosaccharomyces pombe*, Nature Biotechnology **28** (2010) 617, URL: https://doi.org/10.1038/nbt.1628 (cit. on pp. 13, 14, 147).

[109] G. Giaever et al., *Functional profiling of the Saccharomyces cerevisiae genome*, Nature **418** (2002) 387, URL: https://doi.org/10.1038/nature00935 (cit. on pp. 13, 14, 147).

[110] G. E. Hamilton et al., *Reconstitution reveals two paths of force transmission through the kinetochore*, eLife **9** (2020), URL: https://doi.org/10.7554/elife.56582 (cit. on p. 13).

[111] P. Hornung et al., *A cooperative mechanism drives budding yeast kinetochore assembly downstream of CENP-A*, Journal of Cell Biology **206** (2014) 509, URL: https://doi.org/10.1083/jcb.201403081 (cit. on pp. 14, 147).

[112] F. Rago, K. E. Gascoigne and I. M. Cheeseman, *Distinct Organization and Regulation of the Outer Kinetochore KMN Network Downstream of CENP-C and CENP-T*, Current Biology **25** (2015) 671, URL: https://doi.org/10.1016/j.cub.2015.01.059 (cit. on pp. 14, 148).

[113] P. J. H. in 't Veld et al., *Molecular basis of outer kinetochore assembly on CENP-T*, eLife **5** (2016), URL: https://doi.org/10.7554/elife.21007 (cit. on pp. 14, 148).

[114] M. Hara, M. Ariyoshi, E.-i. Okumura, T. Hori and T. Fukagawa, *Multiple phosphorylations control recruitment of the KMN network onto kinetochores*, Nature Cell Biology **20** (2018) 1378, URL: https://doi.org/10.1038/s41556-018-0230-0 (cit. on pp. 14, 148).

[115] K. E. Gascoigne et al., *Induced Ectopic Kinetochore Assembly Bypasses the Requirement for CENP-A Nucleosomes*, Cell **145** (2011) 410, URL: https://doi.org/10.1016/j.cell.2011.03.031 (cit. on pp. 14, 148).

[116] T. Nishino et al., *CENP-T provides a structural platform for outer kinetochore assembly*, The EMBO Journal **32** (2013) 424, URL: https://doi.org/10.1038/emboj.2012.348 (cit. on pp. 14, 148).

[117] S. Kim and H. Yu, *Multiple assembly mechanisms anchor the KMN spindle checkpoint platform at human mitotic kinetochores*, Journal of Cell Biology **208** (2015) 181, URL: https://doi.org/10.1083/jcb.201407074 (cit. on pp. 14, 148).

[118] A. Suzuki, B. L. Badger and E. D. Salmon, *A quantitative description of Ndc80 complex linkage to human kinetochores*, Nature Communications **6** (2015), URL: https://doi.org/10.1038/ncomms9161 (cit. on pp. 14, 148).

[119] T. Hori et al., *CCAN Makes Multiple Contacts with Centromeric DNA to Provide Distinct Pathways to the Outer Kinetochore*, Cell **135** (2008) 1039, URL: https://doi.org/10.1016/j.cell.2008.10.019 (cit. on pp. 14, 148).

[120] G. E. Hamilton and T. N. Davis, *Biochemical evidence for diverse strategies in the inner kinetochore*, Open Biology **10** (2020) 200284, URL: https://doi.org/10.1098/rsob.200284 (cit. on pp. 14, 147).

[121] A. Schleiffer et al., *CENP-T proteins are conserved centromere receptors of the Ndc80 complex*, Nature Cell Biology **14** (2012) 604, URL: https://doi.org/10.1038/ncb2493 (cit. on pp. 14, 147).

[122] L. J. Bock et al., *Cnn1 inhibits the interactions between the KMN complexes of the yeast kinetochore*, Nature Cell Biology **14** (2012) 614, URL: https://doi.org/10.1038/ncb2495 (cit. on pp. 14, 147).

[123] P. D. Wulf, A. D. McAinsh and P. K. Sorger, *Hierarchical assembly of the budding yeast kinetochore from multiple subcomplexes*, Genes Development **17** (2003) 2902, URL: https://doi.org/10.1101/gad.1144403 (cit. on pp. 14, 147).

[124] T. Wang et al., *Identification and characterization of essential genes in the human genome*, Science **350** (2015) 1096, URL: https://doi.org/10.1126/science.aac7041 (cit. on p. 14).

[125] M. Okada et al., *The CENP-H–I complex is required for the efficient incorporation of newly synthesized CENP-A into centromeres*, Nature Cell Biology **8** (2006) 446, URL: https://doi.org/10.1038/ncb1396 (cit. on p. 14).

[126] M. E. Pesenti et al., *Reconstitution of a 26-Subunit Human Kinetochore Reveals Cooperative Microtubule Binding by CENP-OPQUR and NDC80*, Molecular Cell **71** (2018) 923, URL: https://doi.org/10.1016/j.molcel.2018.07.038 (cit. on p. 14).

[127] A. Suzuki, B. L. Badger, X. Wan, J. G. DeLuca and E. D. Salmon, *The Architecture of CCAN Proteins Creates a Structural Integrity to Resist Spindle Forces and Achieve Proper Intrakinetochore Stretch*, Developmental Cell **30** (2014) 717, URL: https://doi.org/10.1016/j.devcel.2014.08.003 (cit. on p. 14).

[128] M. Sipiczki, Genome Biology **1** (2000) reviews1011.1, URL: https://doi.org/10.1186/gb-2000-1-2-reviews1011 (cit. on p. 14).

[129] J. Hayles et al., *A genome-wide resource of cell cycle and cell shape genes of fission yeast*, Open Biology **3** (2013) 130053, URL: https://doi.org/10.1098/rsob.130053 (cit. on pp. 14, 147).

[130] A. Kerres et al., *Fta2, an Essential Fission Yeast Kinetochore Component, Interacts Closely with the Conserved Mal2 Protein*, Molecular Biology of the Cell **17** (2006) 4167, ed. by T. Salmon, URL: https://doi.org/10.1091/mbc.e06-04-0264 (cit. on pp. 14, 147).

[131] A. Petrovic et al., *Modular Assembly of RWD Domains on the Mis12 Complex Underlies Outer Kinetochore Organization*, Molecular Cell **53** (2014) 591, URL: https://doi.org/10.1016/j.molcel.2014.01.019 (cit. on pp. 15, 147).

[132] A. Petrovic et al., *The MIS12 complex is a protein interaction hub for outer kinetochore assembly*, Journal of Cell Biology **190** (2010) 835, URL: https://doi.org/10.1083/jcb.201002070 (cit. on pp. 15, 147).

[133] F. Malvezzi et al., *A structural basis for kinetochore recruitment of the Ndc80 complex via two distinct centromere receptors*, The EMBO Journal **32** (2013) 409, URL: https://doi.org/10.1038/emboj.2012.356 (cit. on p. 15).

[134] C. Ciferri et al., *Architecture of the Human Ndc80-Hec1 Complex, a Critical Constituent of the Outer Kinetochore*, Journal of Biological Chemistry **280** (2005) 29088, URL: https://doi.org/10.1074/jbc.m504070200 (cit. on pp. 15, 147).

[135] R. R. Wei, P. K. Sorger and S. C. Harrison, *Molecular organization of the Ndc80 complex, an essential kinetochore component*, Proceedings of the National Academy of Sciences **102** (2005) 5363, URL: https://doi.org/10.1073/pnas.0501168102 (cit. on pp. 15, 147).

[136] R. Valverde, J. Ingram and S. C. Harrison, *Conserved Tetramer Junction in the Kinetochore Ndc80 Complex*, Cell Reports **17** (2016) 1915, URL: https://doi.org/10.1016/j.celrep.2016.10.065 (cit. on p. 15).

[137] C. Ciferri et al., *Implications for Kinetochore-Microtubule Attachment from the Structure of an Engineered Ndc80 Complex*, Cell **133** (2008) 427, URL: https://doi.org/10.1016/j.cell.2008.03.020 (cit. on p. 15).

[138] K.-S. Hsu and T. Toda, *Ndc80 Internal Loop Interacts with Dis1/TOG to Ensure Proper Kinetochore-Spindle Attachment in Fission Yeast*, Current Biology **21** (2011) 214, URL: https://doi.org/10.1016/j.cub.2010.12.048 (cit. on p. 15).

[139] N. H. Tang, H. Takada, K.-S. Hsu and T. Toda, *The internal loop of fission yeast Ndc80 binds Alp7/TACC-Alp14/TOG and ensures proper chromosome attachment*, Molecular Biology of the Cell **24** (2013) 1122, ed. by K. S. Bloom, URL: https://doi.org/10.1091/mbc.e12-11-0817 (cit. on pp. 15, 145).

[140] A. Musacchio and A. Desai, *A Molecular View of Kinetochore Assembly and Function*, Biology **6** (2017) 5, URL: https://doi.org/10.3390/biology6010005 (cit. on p. 15).

[141] V. Krenn and A. Musacchio, *The Aurora B Kinase in Chromosome Bi-Orientation and Spindle Checkpoint Signaling*, Frontiers in Oncology **5** (2015), URL: https://doi.org/10.3389/fonc.2015.00225 (cit. on p. 15).

[142] S. Jenni and S. C. Harrison, *Structure of the DASH/Dam1 complex shows its role at the yeast kinetochore-microtubule interface*, Science **360** (2018) 552, URL: https://doi.org/10.1126/science.aar6436 (cit. on pp. 15, 147, 149, 153).

[143] J. ook Kim et al., *The Ndc80 complex bridges two Dam1 complex rings*, eLife **6** (2017), URL: https://doi.org/10.7554/elife.21069 (cit. on pp. 16, 149).

[144] J. F. Tien et al., *Cooperation of the Dam1 and Ndc80 kinetochore complexes enhances microtubule coupling and is regulated by aurora B*, Journal of Cell Biology **189** (2010) 713, URL: https://doi.org/10.1083/jcb.200910142 (cit. on p. 16).

[145] A. A. Jeyaprakash et al., *Structural and Functional Organization of the Ska Complex, a Key Component of the Kinetochore-Microtubule Interface*, Molecular Cell **46** (2012) 274, URL: https://doi.org/10.1016/j.molcel.2012.03.005 (cit. on p. 16).

[146] E. Abbe, *Beiträge zur Theorie des Mikroskops und der mikroskopischen Wahrnehmung*, Archiv für Mikroskopische Anatomie **9** (1873) 413, URL: https://doi.org/10.1007/bf02956173 (cit. on p. 19).

[147] L. Rayleigh, *On the Theory of Optical Images, with special reference to the Microscope*, Journal of the Royal Microscopical Society **23** (1903) 474, URL: https://doi.org/10.1111/j.1365-2818.1903.tb04831.x (cit. on p. 19).

[148] T. A. Klar and S. W. Hell, *Subdiffraction resolution in far-field fluorescence microscopy*, Optics Letters **24** (1999) 954, URL: https://doi.org/10.1364/ol.24.000954 (cit. on p. 19).

[149] M. G. L. Gustafsson, *Surpassing the lateral resolution limit by a factor of two using structured illumination microscopy. SHORT COMMUNICATION*, Journal of Microscopy **198** (2000) 82, URL: https://doi.org/10.1046/j.1365-2818.2000.00710.x (cit. on p. 19).

[150] E. Betzig et al., *Imaging Intracellular Fluorescent Proteins at Nanometer Resolution*, Science **313** (2006) 1642, URL: https://doi.org/10.1126/science.1127344 (cit. on p. 19).

[151] M. J. Rust, M. Bates and X. Zhuang, *Sub-diffraction-limit imaging by stochastic optical reconstruction microscopy (STORM)*, Nature Methods **3** (2006) 793, URL: https://doi.org/10.1038/nmeth929 (cit. on p. 19).

[152] M. Heilemann et al., *Subdiffraction-Resolution Fluorescence Imaging with Conventional Fluorescent Probes*, Angewandte Chemie International Edition **47** (2008) 6172, URL: https://doi.org/10.1002/anie.200802376 (cit. on p. 19).

[153] F. Chen, P. W. Tillberg and E. S. Boyden, *Expansion microscopy*, Science **347** (2015) 543, URL: https://doi.org/10.1126/science.1260088 (cit. on pp. 19, 52, 149).

[154] T. C. Murakami et al., *A three-dimensional single-cell-resolution whole-brain atlas using CUBIC-X expansion microscopy and tissue clearing*, Nature Neuroscience **21** (2018) 625, URL: https://doi.org/10.1038/s41593-018-0109-1 (cit. on p. 52).

[155] S. Truckenbrodt, C. Sommer, S. O. Rizzoli and J. G. Danzl, *A practical guide to optimization in X10 expansion microscopy*, Nature Protocols **14** (2019) 832, URL: https://doi.org/10.1038/s41596-018-0117-3 (cit. on p. 52).

[156] Y. S. Zhang et al., *Hybrid Microscopy: Enabling Inexpensive High-Performance Imaging through Combined Physical and Optical Magnifications*, Scientific Reports **6** (2016), URL: https://doi.org/10.1038/srep22691 (cit. on p. 52).

[157] Y. Lim et al., *Mechanically resolved imaging of bacteria using expansion microscopy*, PLOS Biology **17** (2019) e3000268, ed. by R. Parthasarathy, URL: https://doi.org/10.1371/journal.pbio.3000268 (cit. on p. 52).

[158] L. Chen et al., *Applications of Super Resolution Expansion Microscopy in Yeast*, Frontiers in Physics **9** (2021), URL: https://doi.org/10.3389/fphy.2021.650353 (cit. on p. 52).

[159] T. C. Kunz et al., *The Expandables: Cracking the Staphylococcal Cell Wall for Expansion Microscopy*, Frontiers in Cellular and Infection Microbiology **11** (2021), URL: https://doi.org/10.3389/fcimb.2021.644750 (cit. on p. 52).

[160] T. C. Kunz, R. Götz, M. Sauer and T. Rudel, *Detection of Chlamydia Developmental Forms and Secreted Effectors by Expansion Microscopy*, Frontiers in Cellular and Infection Microbiology **9** (2019), URL: https://doi.org/10.3389/fcimb.2019.00276 (cit. on p. 52).

[161] R. Gao et al., *A highly homogeneous polymer composed of tetrahedron-like monomers for high-isotropy expansion microscopy*, Nature Nanotechnology **16** (2021) 698, URL: https://doi.org/10.1038/s41565-021-00875-7 (cit. on pp. 52, 53, 153).

[162] P. Gorilak et al., *Expansion microscopy facilitates quantitative super-resolution studies of cytoskeletal structures in kinetoplastid parasites*, Open Biology **11** (2021) 210131, URL: https://doi.org/10.1098/rsob.210131 (cit. on p. 52).

[163] P. Kao and M. D. Nodine, "Application of expansion microscopy on developing Arabidopsis seeds", *Methods in Cell Biology*, Elsevier, 2021 181, URL: https://doi.org/10.1016/bs.mcb.2020.06.004 (cit. on p. 52).

[164] W. Nijenhuis et al., *Optical nanoscopy reveals SARS-CoV-2-induced remodeling of human airway cells*, (2021), URL: https://doi.org/10.1101/2021.08.05.455126 (cit. on p. 52).

[165] Y. Fan et al., "Mechanical expansion microscopy", *Methods in Cell Biology*, Elsevier, 2021 125, URL: https://doi.org/10.1016/bs.mcb.2020.04.013 (cit. on p. 52).

[166] S. Cheng and Y. Zhao, *Nanoscale imaging of E. coli cells by expansion microscopy*, Discoveries **7** (2019) e98, URL: https://doi.org/10.15190/d.2019.11 (cit. on p. 52).

[167] A. M. Rozario et al., *'Live and Large': Super-Resolution Optical Fluctuation Imaging (SOFI) and Expansion Microscopy (ExM) of Microtubule Remodelling by Rabies Virus P Protein*, Australian Journal of Chemistry **73** (2020) 686, URL: https://doi.org/10.1071/ch19571 (cit. on p. 52).

[168] Aho et al., *Quantitative Microscopy Reveals Stepwise Alteration of Chromatin Structure during Herpesvirus Infection*, Viruses **11** (2019) 935, URL: https://doi.org/10.3390/v11100935 (cit. on p. 52).

[169] C.-C. Yu et al., *Expansion microscopy of C. elegans*, eLife **9** (2020), URL: https://doi.org/10.7554/elife.46249 (cit. on p. 52).

[170] B. Liffner and S. Absalon, *Expansion Microscopy Reveals Plasmodium falciparum Blood-Stage Parasites Undergo Anaphase with A Chromatin Bridge in the Absence of Mini-Chromosome Maintenance Complex Binding Protein*, Microorganisms **9** (2021) 2306, URL: https://doi.org/10.3390/microorganisms9112306 (cit. on p. 52).

[171] E. Bertiaux et al., *Expansion microscopy provides new insights into the cytoskeleton of malaria parasites including the conservation of a conoid*, PLOS Biology **19** (2021) e3001020, ed. by M. Duffy, URL: https://doi.org/10.1371/journal.pbio.3001020 (cit. on p. 52).

[172] P. W. Tillberg et al., *Protein-retention expansion microscopy of cells and tissues labeled using standard fluorescent proteins and antibodies*, Nature Biotechnology **34** (2016) 987, URL: https://doi.org/10.1038/nbt.3625 (cit. on pp. 52, 53, 149).

[173] T. J. Chozinski et al., *Expansion microscopy with conventional antibodies and fluorescent proteins*, Nature Methods **13** (2016) 485, URL: https://doi.org/10.1038/nmeth.3833 (cit. on p. 52).

[174] H. G. Damstra et al., *Visualizing cellular and tissue ultrastructure using Ten-fold Robust Expansion Microscopy (TREx)*, eLife **11** (2022), URL: https://doi.org/10.7554/elife.73775 (cit. on p. 52).

[175] R. Götz et al., *Expansion Microscopy for Cell Biology Analysis in Fungi*, Frontiers in Microbiology **11** (2020), URL: https://doi.org/10.3389/fmicb.2020.00574 (cit. on pp. 52, 53).

[176] N. Trinks et al., *Subdiffraction-resolution fluorescence imaging of immunological synapse formation between NK cells and A. fumigatus by expansion microscopy*, Communications Biology **4** (2021), URL: https://doi.org/10.1038/s42003-021-02669-y (cit. on p. 52).

[177] T. Ku et al., *Multiplexed and scalable super-resolution imaging of three-dimensional protein localization in size-adjustable tissues*, Nature Biotechnology **34** (2016) 973, URL: https://doi.org/10.1038/nbt.3641 (cit. on p. 52).

[178] L. Drelich et al., *Toward High Spatially Resolved Proteomics Using Expansion Microscopy*, Analytical Chemistry **93** (2021) 12195, URL: https://doi.org/10.1021/acs.analchem.0c05372 (cit. on p. 52).

[179] O. M'Saad and J. Bewersdorf, *Light microscopy of proteins in their ultrastructural context*, Nature Communications **11** (2020), URL: https://doi.org/10.1038/s41467-020-17523-8 (cit. on p. 52).

[180] L. A. Campbell, K. E. Pannoni, N. A. Savory, D. Lal and S. Farris, *Protein-retention expansion microscopy for visualizing subcellular organelles in fixed brain tissue*, Journal of Neuroscience Methods **361** (2021) 109285, URL: https://doi.org/10.1016/j.jneumeth.2021.109285 (cit. on p. 52).

[181] I. Kubalová et al., *Prospects and limitations of expansion microscopy in chromatin ultrastructure determination*, Chromosome Research **28** (2020) 355, URL: https://doi.org/10.1007/s10577-020-09637-y (cit. on p. 52).

[182] M. Büttner et al., *Challenges of Using Expansion Microscopy for Super-resolved Imaging of Cellular Organelles*, ChemBioChem **22** (2020) 686, URL: https://doi.org/10.1002/cbic.202000571 (cit. on p. 52).

[183] C. Zhu et al., *Measurement of expansion factor and distortion for expansion microscopy using isolated renal glomeruli as landmarks*, Journal of Biophotonics (2021), URL: https://doi.org/10.1002/jbio.202100001 (cit. on p. 52).

[184] S. P. Pernal et al., *Nanoscale imaging using differential expansion microscopy*, Histochemistry and Cell Biology **153** (2020) 469, URL: https://doi.org/10.1007/s00418-020-01869-7 (cit. on p. 52).

[185] D. Gambarotto et al., *Imaging cellular ultrastructures using expansion microscopy (U-ExM)*, Nature Methods **16** (2018) 71, URL: https://doi.org/10.1038/s41592-018-0238-1 (cit. on pp. 52, 150).

[186] A. R. Halpern, G. C. M. Alas, T. J. Chozinski, A. R. Paredez and J. C. Vaughan, *Hybrid Structured Illumination Expansion Microscopy Reveals Microbial Cytoskeleton Organization*, ACS Nano **11** (2017) 12677, URL: https://doi.org/10.1021/acsnano.7b07200 (cit. on p. 53).

[187] R. Li, X. Chen, Z. Lin, Y. Wang and Y. Sun, *Expansion enhanced nanoscopy*, Nanoscale **10** (2018) 17552, URL: https://doi.org/10.1039/c8nr04267e (cit. on p. 53).

[188] H. Xu et al., *Molecular organization of mammalian meiotic chromosome axis revealed by expansion STORM microscopy*, Proceedings of the National Academy of Sciences **116** (2019) 18423, URL: https://doi.org/10.1073/pnas.1902440116 (cit. on pp. 53, 152).

[189] F. U. Zwettler et al., *Molecular resolution imaging by post-labeling expansion single-molecule localization microscopy (Ex-SMLM)*, Nature Communications **11** (2020), URL: https://doi.org/10.1038/s41467-020-17086-8 (cit. on pp. 53, 152).

[190] J. Tam and D. Merino, *Stochastic optical reconstruction microscopy (STORM) in comparison with stimulated emission depletion (STED) and other imaging methods*, Journal of Neurochemistry **135** (2015) 643, URL: https://doi.org/10.1111/jnc.13257 (cit. on p. 53).

[191] R. Götz et al., *Nanoscale imaging of bacterial infections by sphingolipid expansion microscopy*, Nature Communications **11** (2020), URL: https://doi.org/10.1038/s41467-020-19897-1 (cit. on p. 53).

[192] I. Vojnovic, *Spatial and temporal organization of the kinetochore proteins sad1, cut12 and cnp1 in Schizosaccharomyces pombe studied by fluorescence single molecule methods at a nanometer resolution*, Master thesis (2016) (cit. on p. 144).

[193] I. Vojnovic and U. Endesfelder, *Beginner's guide to producing super-resolved images on a widefield fluorescence microscope*, The Biochemist **42** (2020) 52, URL: https://doi.org/10.1042/bio20200045 (cit. on p. 144).

[194] I. Vojnovic, J. Winkelmeier and U. Endesfelder, *Visualizing the inner life of microbes: practices of multi-color single-molecule localization microscopy in microbiology*, Biochemical Society Transactions **47** (2019) 1041, URL: https://doi.org/10.1042/bst20180399 (cit. on p. 144).

[195] R. C. Allshire, *Elements of chromosome structure and function in fission yeast*, Seminars in Cell Biology **6** (1995) 55, URL: https://doi.org/10.1016/1043-4682(95)90001-2 (cit. on p. 144).

[196] B. Levenberg and J. M. Buchanan, *BIOSYNTHESIS OF THE PURINES*, Journal of Biological Chemistry **224** (1957) 1005, URL: https://doi.org/10.1016/s0021-9258(18)64992-0 (cit. on p. 144).

[197] B. Turkowyd, D. Virant and U. Endesfelder, *From single molecules to life: microscopy at the nanoscale*, Analytical and Bioanalytical Chemistry **408** (2016) 6885, URL: https://doi.org/10.1007/s00216-016-9781-8 (cit. on p. 144).

[198] X. Sun et al.,
Development of SNAP-Tag Fluorogenic Probes for Wash-Free Fluorescence Imaging,
ChemBioChem **12** (2011) 2217, URL: https://doi.org/10.1002/cbic.201100173
(cit. on p. 144).

[199] G. V. Los et al.,
HaloTag: A Novel Protein Labeling Technology for Cell Imaging and Protein Analysis,
ACS Chemical Biology **3** (2008) 373, URL: https://doi.org/10.1021/cb800025k
(cit. on p. 144).

[200] M. Zhang et al.,
Rational design of true monomeric and bright photoactivatable fluorescent proteins,
Nature Methods **9** (2012) 727, URL: https://doi.org/10.1038/nmeth.2021
(cit. on p. 145).

[201] B. Turkowyd et al.,
A General Mechanism of Photoconversion of Green-to-Red Fluorescent Proteins Based on Blue and Infrared Light Reduces Phototoxicity in Live-Cell Single-Molecule Imaging,
Angewandte Chemie International Edition **56** (2017) 11634,
URL: https://doi.org/10.1002/anie.201702870 (cit. on p. 145).

[202] F. V. Subach et al.,
Photoactivatable mCherry for high-resolution two-color fluorescence microscopy,
Nature Methods **6** (2009) 153, URL: https://doi.org/10.1038/nmeth.1298
(cit. on pp. 145, 152).

[203] D. Virant, B. Turkowyd, A. Balinovic and U. Endesfelder,
Combining Primed Photoconversion and UV-Photoactivation for Aberration-Free, Live-Cell Compliant Multi-Color Single-Molecule Localization Microscopy Imaging,
International Journal of Molecular Sciences **18** (2017) 1524,
URL: https://doi.org/10.3390/ijms18071524 (cit. on p. 145).

[204] D. S. Bindels et al.,
mScarlet: a bright monomeric red fluorescent protein for cellular imaging,
Nature Methods **14** (2016) 53, URL: https://doi.org/10.1038/nmeth.4074
(cit. on p. 145).

[205] B. E. Black et al., *Centromere Identity Maintained by Nucleosomes Assembled with Histone H3 Containing the CENP-A Targeting Domain*, Molecular Cell **25** (2007) 309,
URL: https://doi.org/10.1016/j.molcel.2006.12.018 (cit. on p. 145).

[206] A. Guse, C. W. Carroll, B. Moree, C. J. Fuller and A. F. Straight,
In vitro centromere and kinetochore assembly on defined chromatin templates,
Nature **477** (2011) 354, URL: https://doi.org/10.1038/nature10379 (cit. on p. 145).

[207] I. Sanchez-Perez et al., *The DASH complex and Klp5/Klp6 kinesin coordinate bipolar chromosome attachment in fission yeast*, The EMBO Journal **24** (2005) 2931,
URL: https://doi.org/10.1038/sj.emboj.7600761 (cit. on p. 145).

[208] K. Griffiths, H. Masuda, S. Dhut and T. Toda,
Fission yeast dam1-A8 mutant is resistant to and rescued by an anti-microtubule agent,
Biochemical and Biophysical Research Communications **368** (2008) 670,
URL: https://doi.org/10.1016/j.bbrc.2008.01.156 (cit. on p. 146).

[209] I. Loïodice et al., *Ase1p Organizes Antiparallel Microtubule Arrays during Interphase and Mitosis in Fission Yeast*, Molecular Biology of the Cell **16** (2005) 1756,
URL: https://doi.org/10.1091/mbc.e04-10-0899 (cit. on p. 146).

[210] L. K. Krüger, J.-L. Sanchez, A. Paoletti and P. T. Tran,
Kinesin-6 regulates cell-size-dependent spindle elongation velocity to keep mitosis duration constant in fission yeast, eLife **8** (2019), URL: https://doi.org/10.7554/elife.42182
(cit. on p. 146).

[211] K. Finan, A. Raulf and M. Heilemann,
A Set of Homo-Oligomeric Standards Allows Accurate Protein Counting,
Angewandte Chemie International Edition **54** (2015) 12049,
URL: https://doi.org/10.1002/anie.201505664 (cit. on p. 146).

[212] D. Virant et al.,
A peptide tag-specific nanobody enables high-quality labeling for dSTORM imaging,
Nature Communications **9** (2018),
URL: https://doi.org/10.1038/s41467-018-03191-2 (cit. on p. 146).

[213] K. Yan et al.,
Structure of the inner kinetochore CCAN complex assembled onto a centromeric nucleosome,
Nature **574** (2019) 278, URL: https://doi.org/10.1038/s41586-019-1609-1
(cit. on p. 146).

[214] K. Cieslinski et al.,
Nanoscale structural organization and stoichiometry of the budding yeast kinetochore, (2021),
URL: https://doi.org/10.1101/2021.12.01.469648 (cit. on p. 146).

[215] A. P. Joglekar, K. Bloom and E. Salmon,
In Vivo Protein Architecture of the Eukaryotic Kinetochore with Nanometer Scale Accuracy,
Current Biology **19** (2009) 694, URL: https://doi.org/10.1016/j.cub.2009.02.056
(cit. on p. 147).

[216] P. Aravamudhan, I. Felzer-Kim, K. Gurunathan and A. P. Joglekar, *Assembling the Protein Architecture of the Budding Yeast Kinetochore-Microtubule Attachment using FRET*,
Current Biology **24** (2014) 1437, URL: https://doi.org/10.1016/j.cub.2014.05.014
(cit. on p. 147).

[217] A. Petrovic et al., *Structure of the MIS12 Complex and Molecular Basis of Its Interaction with CENP-C at Human Kinetochores*, Cell **167** (2016) 1028,
URL: https://doi.org/10.1016/j.cell.2016.10.005 (cit. on p. 147).

[218] D. P. Maskell, X.-W. Hu and M. R. Singleton,
Molecular architecture and assembly of the yeast kinetochore MIND complex,
Journal of Cell Biology **190** (2010) 823,
URL: https://doi.org/10.1083/jcb.201002059 (cit. on p. 147).

[219] E. M. Kudalkar et al., *Regulation of outer kinetochore Ndc80 complex-based microtubule attachments by the central kinetochore Mis12/MIND complex*, Proceedings of the National Academy of Sciences **112** (2015), URL: https://doi.org/10.1073/pnas.1513882112 (cit. on p. 147).

[220] E. Roscioli et al., *Ensemble-Level Organization of Human Kinetochores and Evidence for Distinct Tension and Attachment Sensors*, Cell Reports **31** (2020) 107535, URL: https://doi.org/10.1016/j.celrep.2020.107535 (cit. on p. 147).

[221] A. P. Joglekar et al., *Molecular architecture of the kinetochore-microtubule attachment site is conserved between point and regional centromeres*, Journal of Cell Biology **181** (2008) 587, URL: https://doi.org/10.1083/jcb.200803027 (cit. on p. 147).

[222] Y. Zahedi, M. Durand-Dubief and K. Ekwall, *High-Throughput Flow Cytometry Combined with Genetic Analysis Brings New Insights into the Understanding of Chromatin Regulation of Cellular Quiescence*, International Journal of Molecular Sciences **21** (2020) 9022, URL: https://doi.org/10.3390/ijms21239022 (cit. on p. 147).

[223] M. J. Ohira, D. G. Hendrickson, R. S. McIsaac and N. Rhind, *An estradiol-inducible promoter enables fast, graduated control of gene expression in fission yeast*, Yeast **34** (2017) 323, URL: https://doi.org/10.1002/yea.3235 (cit. on p. 148).

[224] W. Zhang et al., *Centromere and kinetochore gene misexpression predicts cancer patient survival and response to radiotherapy and chemotherapy*, Nature Communications **7** (2016), URL: https://doi.org/10.1038/ncomms12619 (cit. on p. 148).

[225] N. H. Tang and T. Toda, *MAPping the Ndc80 loop in cancer: A possible link between Ndc80/Hec1 overproduction and cancer formation*, BioEssays **37** (2015) 248, URL: https://doi.org/10.1002/bies.201400175 (cit. on p. 148).

[226] C. Featherstone and P. Russell, *Fission yeast p107wee1 mitotic inhibitor is a tyrosine/serine kinase*, Nature **349** (1991) 808, URL: https://doi.org/10.1038/349808a0 (cit. on p. 148).

[227] P. Russell and P. Nurse, *Negative regulation of mitosis by wee1+, a gene encoding a protein kinase homolog*, Cell **49** (1987) 559, URL: https://doi.org/10.1016/0092-8674(87)90458-2 (cit. on p. 148).

[228] P. Pérez, J. C. Cortés, J. Cansado and J. C. Ribas, *Fission yeast cell wall biosynthesis and cell integrity signalling*, The Cell Surface **4** (2018) 1, URL: https://doi.org/10.1016/j.tcsw.2018.10.001 (cit. on p. 149).

[229] J. C. G. Cortés, M. Ramos, M. Osumi, P. Pérez and J. C. Ribas, *The Cell Biology of Fission Yeast Septation*, Microbiology and Molecular Biology Reviews **80** (2016) 779, URL: https://doi.org/10.1128/mmbr.00013-16 (cit. on p. 149).

[230] D.-Q. Ding et al., *Large-scale screening of intracellular protein localization in living fission yeast cells by the use of a GFP-fusion genomic DNA library*, Genes to Cells **5** (2000) 169, URL: https://doi.org/10.1046/j.1365-2443.2000.00317.x (cit. on p. 149).

[231] A. R. Bowen et al., *Classification of fungal chitin synthases.*, Proceedings of the National Academy of Sciences **89** (1992) 519, URL: https://doi.org/10.1073/pnas.89.2.519 (cit. on p. 149).

[232] Y. MATSUO, K. TANAKA, T. NAKAGAWA, H. MATSUDA and M. KAWAMUKAI, *Genetic Analysis of chs1+ and chs2+ Encoding Chitin Synthases from Schizosaccharomyces pombe*, Bioscience, Biotechnology, and Biochemistry **68** (2004) 1489, URL: https://doi.org/10.1271/bbb.68.1489 (cit. on p. 149).

[233] R. Martin-Garcia, A. Duran and M.-H. Valdivieso, *In Schizosaccharomyces pombe chs2p has no chitin synthase activity but is related to septum formation*, FEBS Letters **549** (2003) 176, URL: https://doi.org/10.1016/s0014-5793(03)00812-3 (cit. on p. 149).

[234] M. Arellano, H. Cartagena-Lirola, M. A. N. Hajibagheri, A. Duran and M. H. Valdivieso, *Proper ascospore maturation requires the chs1+ chitin synthase gene in Schizosaccharomyces pombe*, Molecular Microbiology **35** (2000) 79, URL: https://doi.org/10.1046/j.1365-2958.2000.01678.x (cit. on p. 149).

[235] K. Hinterndorfer et al., *Ultrastructure Expansion Microscopy reveals the nanoscale cellular architecture of budding and fission yeast*, (2022), URL: https://doi.org/10.1101/2022.05.16.492060 (cit. on p. 150).

[236] I. Flor-Parra, J. Zhurinsky, M. Bernal, P. Gallardo and R. R. Daga, *A Lallzyme MMX-based rapid method for fission yeast protoplast preparation*, Yeast **31** (2013) 61, URL: https://doi.org/10.1002/yea.2994 (cit. on p. 150).

[237] C. Cupp-Enyard, *Sigmas Non-specific Protease Activity Assay - Casein as a Substrate*, Journal of Visualized Experiments (2008), URL: https://doi.org/10.3791/899 (cit. on p. 150).

[238] O. Lowry, N. Rosebrough, A. L. Farr and R. Randall, *PROTEIN MEASUREMENT WITH THE FOLIN PHENOL REAGENT*, Journal of Biological Chemistry **193** (1951) 265, URL: https://doi.org/10.1016/s0021-9258(19)52451-6 (cit. on p. 150).

[239] S. Osburn et al., *Structure and Reactivity of the Glutathione Radical Cation: Radical Rearrangement from the Cysteine Sulfur to the Glutamic Acid alpha-Carbon Atom*, ChemPlusChem **78** (2013) 970, URL: https://doi.org/10.1002/cplu.201300057 (cit. on p. 151).

[240] R. Ramis et al., *Modelling the repair of carbon-centred protein radicals by the antioxidants glutathione and Trolox*, New Journal of Chemistry **43** (2019) 2085, URL: https://doi.org/10.1039/c8nj05544k (cit. on p. 151).

[241] S. A. McKinney, C. S. Murphy, K. L. Hazelwood, M. W. Davidson and L. L. Looger, *A bright and photostable photoconvertible fluorescent protein*, Nature Methods **6** (2009) 131, URL: https://doi.org/10.1038/nmeth.1296 (cit. on p. 151).

[242] U. Endesfelder et al., *Multiscale Spatial Organization of RNA Polymerase in Escherichia coli*, Biophysical Journal **105** (2013) 172, URL: https://doi.org/10.1016/j.bpj.2013.05.048 (cit. on p. 152).

[243] M. J. Mlodzianoski et al.,
Sample drift correction in 3D fluorescence photoactivation localization microscopy,
Optics Express **19** (2011) 15009, URL: https://doi.org/10.1364/oe.19.015009
(cit. on p. 152).

[244] B. C. Campbell, M. G. Paez-Segala, L. L. Looger, G. A. Petsko and C. F. Liu,
Chemically stable fluorescent proteins for advanced microscopy,
Nature Methods **19** (2022) 1612,
URL: https://doi.org/10.1038/s41592-022-01660-7 (cit. on p. 153).

[245] B. C. Campbell et al., *mGreenLantern: a bright monomeric fluorescent protein with rapid expression and cell filling properties for neuronal imaging*,
Proceedings of the National Academy of Sciences **117** (2020) 30710,
URL: https://doi.org/10.1073/pnas.2000942117 (cit. on p. 153).

List of Figures

List of Tables

Acronyms

3C triple-color. 145–148, 153

APC anaphase promoting complex. 7

APS ammonium persulfate. 151

CATD CENPA targeting domain. 10, 11, 145

CCAN constitutive centromere associated network. 11, 13, 14

CH calponin homology. 15

cnt centromere core domain. 10, 11

dSTORM direct stochastic optical reconstruction microscopy. 53

EF expansion factor. 2, 52, 149, 151, 152

EM electron microscopy. 1, 8, 11, 15, 143, 147, 149, 153

Ex-SMLM expansion single-molecule localization microscopy. 53, 152

ExM expansion microscopy. 2, 4, 5, 19, 52, 53, 109, 149, 150, 152

ExPALM expansion photoactivated localization microscopy. 152, 153

ExSIM expansion structured illumination microscopy. 53

ExSTORM expansion stochastic optical reconstruction microscopy. 53, 152

FP fluorescent protein. 1, 2, 53, 144–146, 148, 150–153

FRET Förster resonance energy transfer. 13, 147

GSH glutathione. 151

HAT hydrogen-atom transfer. 151

imr imperfect repeat region. 10

kMT kinetochore microtubule. 1, 6, 8–13, 15, 16, 143, 146, 149, 153

KT kinetochore. 1, 2, 5, 6, 8–15, 26, 54, 55, 109, 143–149, 153

MAP microtubule-associated protein. 9, 15

MT microtubule. 5–9, 13, 15, 16, 145, 153

MTOC microtubule organizing center. 9

NA numerical aperture. 19

NE nuclear envelope. 7–9

otr outer repeat. 10, 11

PAA poly-acrylamide. 52, 151–153

PALM photoactivated localization microscopy. 2, 11, 53, 109, 143, 145, 148, 149, 152, 153

PC-PALM primed conversion photoactivated localization microscopy. 145

PMSF phenylmethylsulfonylfluorid. 150, 151

POI protein of interest. 1, 2, 52–55, 143–148, 153

proExM protein retention expansion microscopy. 149, 150, 152

PSF point spread function. 19

ROI region of interest. 148

RWD RING finger, WD repeat, DEAD-like helicases. 15

SAC spindle assembly checkpoint. 7, 9, 15

SDS sodium dodecyl sulfate. 151

SExY single-molecule expansion microscopy in fission yeast. 2, 4, 109, 149–153

SIM structured illumination microscopy. 19, 53

SMLM single-molecule localization microscopy. 1, 2, 5, 19, 20, 26, 53–55, 143, 144, 146, 149, 153, 157

SPB spindle pole body. 1, 5–9, 143–145, 153

sptPALM single-particle tracking photoactivated localization microscopy. 157

SRM super-resolution microscopy. 19, 53, 152

STED stimulated emission depletion. 19, 53

TBZ thiabendazole. 145, 146, 148

TEMED tetramethylethylenediamine. 151

TIP plus-end tracking protein. 9, 15

U-ExM ultrastructure expansion microscopy. 52, 150

UV-PALM ultra-violet photoactivated localization microscopy. 145

Acknowledgements

First and foremost I would like to thank Prof. Dr. Ulrike Endesfelder for not only the great opportunity to do my PhD in her group, but also her continuous support during this time, especially during the COVID-19 pandemic, where she showed amazing crisis management skills. She helped me stay motivated when I hit a roadblock, encouraged me to visit international conferences and gave me the room to grow scientifically. For all of that I am very grateful!

I would also like to thank my fission yeast buddies Jannik Winkelmeier and David Virant for all the brain storming, late imaging days and incedibly well timed jokes when I was feeling down. We were a great team!

Furthermore, big thanks belongs to Marc Endesfelder and Dr. Bartosz Turkowyd for being the coding crisis managers for the kinetochore project, Dr. Oliver Caspari for his help with the SExY project and the whole Endesfelder group for their cheer and support. Mountaineering and soccer golf will never be the same without all of you!

Additionally, I would like to thank Prof. Dr. Victor Sourjik for his financing help during the first critical months of the COVID-19 pandemic while we could not move to the US and my thesis advisory committee consisting of Prof. Dr. Ulrike Endesfelder, Prof. Dr. Martin Thanbichler and Dr. Andreas Diepold for their great advice and keeping me on track during my PhD. I would also like to thank my examination comission consisting of Prof. Dr. Ulrike Endesfelder, Prof. Dr. Martin Thanbichler, Prof. Dr. Victor Sourjik and Prof. Dr. Lennart Randau for agreeing and finding the time to grade my thesis work.

Alex, my best friend, partner in crime and fiancé, you know that without you I would be lost. I cannot thank you enough for being beside me through all this. You are my rock and I cannot wait to start some new adventures with you soon! ♡

Finally, I would like to thank my family for their unconditional love and support even through tough times! Whenever I was doubting myself you were there for me. I especially want to thank my parents for teaching me to never give up and the huge package of German sweets you sent us to the US when I missed home, my sister for her constant phone therapy sessions and my grandma for the constant supply of homemade cookies. Last but not least, I want to thank my family in the US who helped me get acclimated to another country and never let me feel alone. Sve vas volim!